Division of Orthopaedic & Accident Surgery

School of Medical & Surgical Sciences

University of Nottingham

Quantitative Stereophotogrammetric and MRI Evaluation of Ankle Articular Cartilage and Ankle Joint Contact Characteristics

A Doctoral Thesis

Submitted in partial fulfilment of the requirements for the award of

Doctor of Philosophy of the University of Nottingham

2007

Table of Contents

Table of Contents

Table of Contents

Declaration

This work has been carried out while I was in the post of Orthopaedic Research Fellow at the Center for Applied Biomechanics, University of Virginia, USA and the Frank Stronach Institute, Technical University of Graz, Austria. During this time I registered as a PhD student in the department of Orthopaedic and Accident Surgery at the University of Nottingham, under the supervision of Professor W A Wallace.

I declare that no part of this work has been presented, whether in the same or a different form, to this or any other university in support of an application for any degree. The studies described and presented in this thesis are the original work of the author except where otherwise stated in the text.

S A. Millington BMedSci BMBS MRCS(Ed)

Date 11/07/2007

Acknowledgments

I would like to acknowledge the important contribution of a number of colleagues who have assisted me in the studies reported in this thesis.

Firstly I thank Prof Scott Acton from the University of Virginia, USA who has become a good friend during the last 3 years, for showing initial interest and belief in my ideas for cartilage mapping from MR images. Moreover I would like to thank Dr Jinshan Tang and Bing Li for writing and refining the 2D semi-automated image segmentation algorithms which I used for the MRI studies.

I express my thanks to Prof Milan Sonka, at the University of Iowa, USA, and his graduate student Kang Li, for their hard work and rapid development of the 3D automated segmentation algorithm for use on cartilage sensitive MR images.

With regard to the stereophotography and joint contact area studies, I acknowledge and thank Dr Markus Grabner at the Technical University of Graz, Austria and his graduate student Ralph Wozelka for their contribution in writing the algorithms which I used for post processing of huge volumes of geometric data.

Throughout the time I have been performing the research for this thesis and writing it up a number of people have acted as mentors to me giving excellent support and sound advice. To this end I thank Professors Jeff Crandall and Shep Hurwitz at the University of Virginia, USA; Professor Siegfried Trattnig at the Medical University of Vienna, Austria and Professor Angus Wallace at the University of Nottingham, UK.

Finally, and most importantly I must thank my wife Christina for her unending support, understanding and patience whilst I have been writing this thesis, without her it would not have been possible.

Funding

I am grateful for the financial support from the following funding agencies that made it possible to perform the research presented in this thesis.

- DePuy, USA, for the DePuy University of Virginia foot & ankle surgery fellowship, which provided salary support during my studies in Virginia

- The National Highway and Traffic Safety Administration, USA – provided support for the biomechanical testing aspects of the studies

- Zimmer inc. USA provided an industrial grant that helped to fund in part the semi-automated segmentation studies and cartilage stiffness studies.

- National Institute for Health, USA. SBIR grant number – 1R43AR052983-01: which supported the pilot work and initial testing for the 3D automated cartilage segmentation algorithms

List of Tables

List of Figures

List of Figures

List of Abbreviations

ACI	Autologous Chondrocyte Implantation
ATOS™	Advance TOpographic Sensor
BCI	Bone Cartilage Interface
CV	Coefficient of Variation
dGVF	Directional Gradient vector Flow
dGEMRIC	Delayed Gadolinium Enhanced MRI of Cartilage
ECM	Extracellular Matrix
FCD	Fixed Charge Density
FLASH	Fast Low Angle Shot
FOM	Figure of Merit
GAG	Glycosaminoglycan
GRE	Gradient Recalled Echo
MRI	Magnetic Resonance Imaging
PBS	Phosphate Buffered Saline
PG	Proteoglycan
PMMA	Polymethylmetharcrylate
RMS	Root Mean Square
ROI	Region of Interest
s.d.	Standard Deviation
T1	T1 Relaxation time
T2	T2 Relaxation time
TE	Echo Time
TR	Relaxation Time

Research Publications Related to this Thesis

[1] Li K, Millington SA, Wu X, Chen DZ, Sonka M. Simultaneous segmentation of multiple closed surfaces using optimal graph searching. Inf Process Med Imaging 2005; 19 :406-17.

[2] Millington SA, Li B, Tang J, Trattnig S, Crandall JR, Hurwitz SR, Acton ST Quantitative and topographical evaluation of ankle articular cartilage using high resolution MRI. J Orthop Res 2007 Feb; 25(2) 143-151.

[3] Millington SA, Grabner M, Wozelka R, Anderson DD, Hurwitz SR, Crandall JR. Quantification of ankle articular cartilage topography and thickness using a high resolution stereophotography system. Osteoarthritis Cartilage 2007 Feb; 15(2); 205-211.

[4] Millington SA, Grabner M, Wozelka R, Hurwitz SR, Crandall JR. A stereophotographic study of ankle joint contact area. J Ortho. Res. (Epub ahead of print) 2007 Jun, DOI 10.1002/jor.20425.

[5] Rudd R, Crandall J, Millington SA, Hurwitz SR, Hoglund N. Injury Tolerance and Response of the Ankle Joint in Dynamic Dorsiflexion. Stapp Car Crash Journal 2004;48:1-26.

[6] Tang J, Millington SA, Acton ST, Crandall JR, Hurwitz SR. Surface Extraction and Thickness measurement of the articular Cartilage from MR images using Directional Gradient Vector Flow Snakes. IEEE transaction on biomedical engineering 2006 May;53(5):896-907.

Abstract

Osteoarthritis and degenerative cartilage diseases affect millions of people. Therefore, there is huge interest in developing new therapies to repair, replace and/or regenerate cartilage. This necessitates advances in techniques which make earlier non-invasive diagnosis and objective quantitative evaluations of new therapies possible. Most previous research has focused on the knee and neglected the ankle joint. Hence, the aims of this thesis are to describe and quantify the geometric properties of ankle cartilage, to evaluate joint contact characteristics and develop techniques which allow quantitative measurements to be made in vivo.

Chapters 3 and 6 describe the application of a high resolution stereophotography system for making highly accurate 3-D geometric models from which quantitative measurements of cartilage parameters and joint area contact can be made. Chapters 4 and 5 report the testing of image analysis algorithms designed to segment cartilage sensitive MR images. Work focused on initially on a semi-automated 2-D segmentation approach and subsequently on a pilot study of 3-D automated segmentation algorithm.

The stereophotographic studies were highly accurately and demonstrated that ankle cartilage thickness is greater than previously reported with the thickest cartilage occurring where cartilage injuries are most commonly seen. Furthermore, joint contact area is larger than previously believed and corresponds to the regions of the thickest cartilage over the talar shoulders. The image analysis studies show that it is possible to accurately and reproducibly segment the thin cartilage layers of the ankle joint using a semi-automated approach. The feasibility of a fully automated 3D method for future clinical use is also shown.

In conclusion this thesis presents novel methods for examining ankle articular cartilage in vitro and in vivo, showing that the thickest cartilage occurs in highly curved regions over the shoulders of the talus which correspond to regions of greatest contact. Importantly, the image analysis techniques may be used for future clinical monitoring of patients sustaining cartilage injuries or undergoing cartilage repair therapies.

Chapter 1. Introduction

The articular cartilage of the ankle joint may be injured without an associated fracture or ligamentous injury occurring and damage to the articular surface in some instances may lead to progressive joint degeneration. Articular cartilage repair and techniques to stimulate articular cartilage regeneration are currently extremely topical areas of research; however, there is little well defined experimental data on the 3D topographical distribution and mechanical properties of the articular cartilage of the ankle especially joint under high rate loading. In order for clinicians to evaluate and appropriately treat patients with articular cartilage injuries they require an understanding of the injury mechanisms and the typical natural history of such injuries. Researchers need to have an understanding of cartilage injury mechanisms and properties under varied loading conditions if they are to develop new treatment methods and develop safety systems to prevent such injuries. Knowledge of the topographical distribution and variation in mechanical properties of the ankle articular cartilage are essential if, in future, we are to ensure that articular cartilage repair produces tissue with properties similar to the native articular cartilage. Limited awareness of articular cartilage injury, difficulty in diagnosis and lack of suitable methods for evaluating outcomes of cartilage repair and cartilage restorative techniques pose significant obstacles in a rapidly expanding area of research.

The majority of research relating to articular cartilage properties and injury has understandably focused on the knee joint due to the high incidence of injury and osteoarthritis, thick articular cartilage layers and relatively simple surgical access which makes the knee more amenable to study than other joints. The articular cartilage of the ankle joint has been less extensively studied and although similarities do exist between the articular cartilages of the knee and the ankle there are important and significant differences between the articular cartilages of these joints(Treppo et al., 2000) including cartilage thickness, joint congruency, cartilage stiffness, and mechanical forces.

1.1. Ankle anatomy

The ankle is a modified hinge joint consisting of three bones (tibia, fibula, and talus); the ligaments bind these bones into a single functional unit, allowing motion to occur. The distal inferior articular surface of the tibia is referred to as the tibial plafond and is concave antero-posteriorly and medio-laterally. The tibial plafond is wider along its anterior boarder than its posterior boarder and the lateral side of the plafond is longer than the medial side.

The medial malleolus represents the most distal projection of the tibia whereas the lateral malleolus is the terminal extension of the fibula. The lateral malleolus has a broad medial surface for articulation with the lateral facet of the talus. Characteristically the fibula extends approximately 1 cm more distally and posterior than the medial malleolus, figure 1.1.

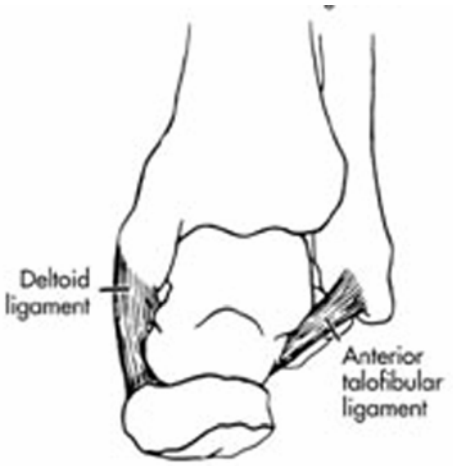

Figure 1.1 Anterior view of the left ankle

A coronal schematic of a left ankle viewed from anteriorly. The fibula is positioned slightly posterior to the tibia and extends approximately 1cm more distally. (Adapted from Chapman MW: sprains of the ankle instr course lect. 1975; 24; 294-308.)

The bones forming the articular surfaces of the ankle are held in place by strong ligamentous support. Medially, by the deltoid ligament, figures 1.1 and 1.2, which is divided into two portions: The superficial deltoid runs from the tip of the medial

malleolus distally as a broad ligament inserting onto the navicular, sustentaculum tali, and the talus. The deep deltoid is the very strong condensation of capsular fibres that extend from the intercollicular notch to the medial surface of the talus as the anterior and posterior tibiocalcaneal ligiaments.

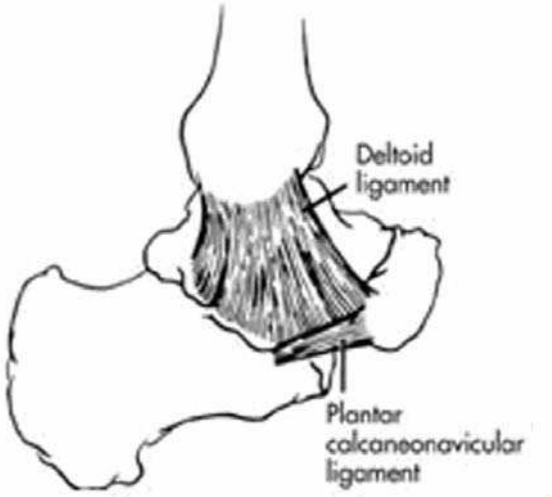

Figure 1.2 Medial view of the ankle ligamentous structures.

The broad, strong deltoid ligament extending from the medial malleolus to the navicular, sustentaculum tali, and the talus. (Adapted from Chapman MW: sprains of the ankle instr course lect. 1975; 24; 294-308.)

The lateral ligaments, figure 1.3, are typically not as strong as those on the medial side of the ankle; they consist of three components: the anterior talofibular ligament (ATFL), calcaneofibular ligament (CFL), and the posterior talofibular ligament (PTFL).

A number of anatomical features help to maintain the rotatory stability of the ankle joint: firstly the collateral and syndesmosis ligaments, secondly, the fit of the talus in the mortise and the shape of the articular surfaces under loading conditions; and thirdly the ATFL, CFL and PTFL in the loaded ankle.

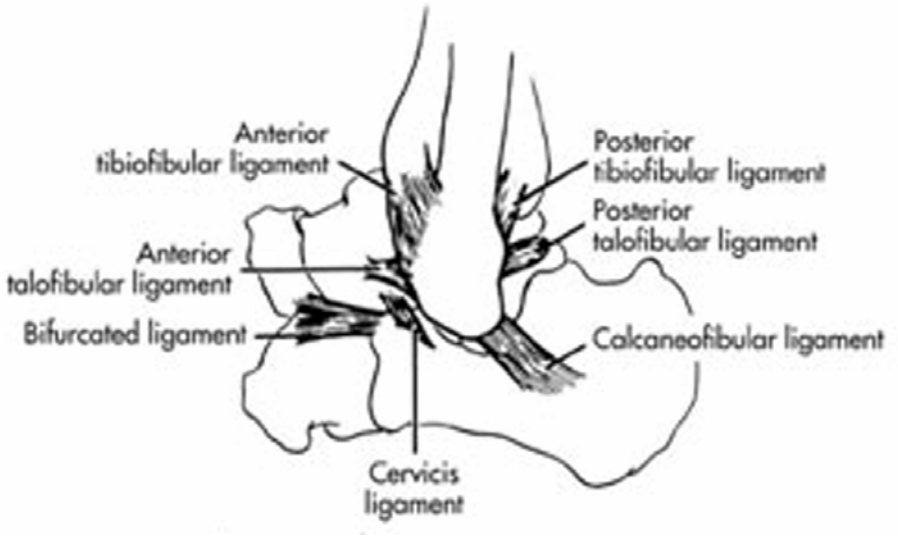

Figure 1.3 Lateral view of the ankle ligamentous structures

There are a larger number of ligamentous structures on the lateral aspect of the ankle but they are not as strong as those on the medial aspect. The three main components are the the anterior talofibular ligament (ATFL), calcaneofibular ligament (CFL), and the posterior talofibular ligament (PTFL) (Adapted from Chapman MW: sprains of the ankle instr course lect. 1975; 24; 294-308.)

The talus has five articular surfaces, all of which have a weight-bearing function, figure 1.4. Two thirds of the talar surface is covered with articular cartilage, and the bone has no muscle attachments. Principally, the talus consists of three parts, the head, neck, and body, the two processes, the lateral and posterior may be considered extra. The head is the portion that articulates mostly with the navicular. The body includes the dome of the talus articulating in the ankle joint and the posterior facet articulating in the subtalar joint. Between the head and the body is the neck, which does not articulate with the ankle and sits over the sinus tarsi below.

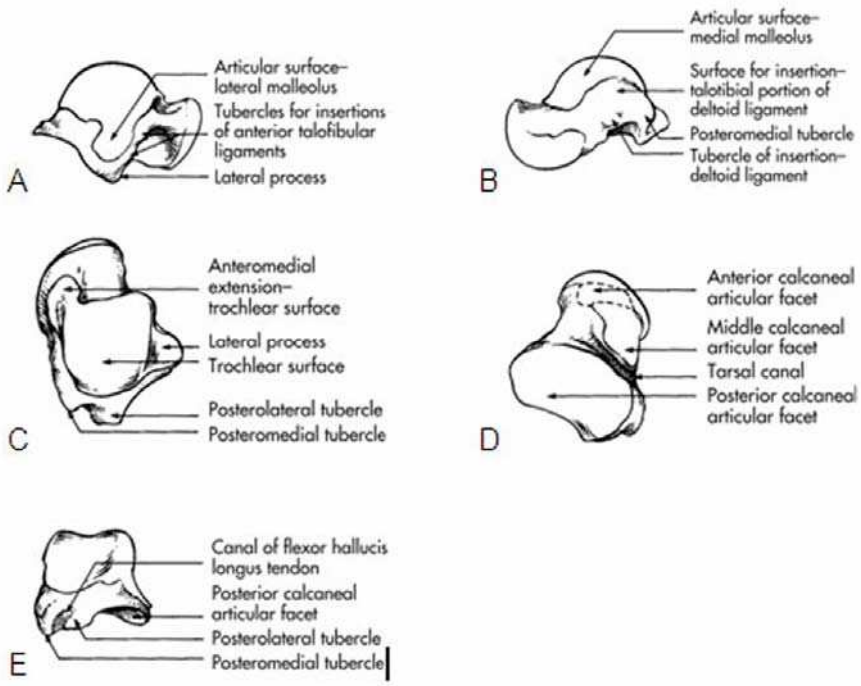

Figure 1.4 Anatomical features of the talus.

The characteristic anatomical features of the talus from five views: a) Laterally, b) medially, c) superiorly d) inferiorly and e) posteriorly. The talus is predominantly covered by articular cartilage and has no muscle attachments. (Adapted from www.orthoteers.com)

The body of the talus is arbitrarily divided into five surfaces: lateral, medial, superior, inferior, and posterior. The lateral surface consists of the lateral facet which articulates with the distal fibula. The lateral facet lies over the lateral process which is a non-articular component of the talus. The lateral talocalcaneal ligament inserts at the inferior tip of the lateral process. Along the anterior border of the triangular lateral process are two tubercles for insertion of the anterior talofibular ligament. Along the posteroinferior border of this lateral surface lies a groove for the attachment of the posterior talofibular ligament. The medial surface of the body presents two areas, superior and inferior. The superior portion is occupied by the articular facet which is shaped like a comma, with the long axis oriented anteroposteriorly. The inferior portion is non-articular and the site of insertion for the deep component of the deltoid ligament. The superior surface of the talar body is completely covered with articular cartilage and is shaped like a pulley,

with the groove of the pulley (trochlea) slightly closer to the medial border. The transverse diameter of the superior surface is greater anteriorly than posteriorly and is classically said to resemble a keystone. The inferior surface of the talar body consists of the facies articularis calcanea posterior tali. This articular surface is quadrilateral in shape and is concave in the long axis while being flat transversely. It articulates with the posterior facet of the calcaneus. The posterior surface of the talar body consists of posterolateral and posteromedial tubercles that flank the sulcus for the flexor hallucis longus tendon. The posterolateral tubercle is larger and more prominent than the posteromedial tubercle. An accessory bone, the os trigonum, is sometimes found in connection with the posterolateral tubercle.

1.2. Articular cartilage structure

Articular cartilage is a highly specialised tissue suited to withstanding high levels of repeated loading throughout an average persons life time. Articular cartilage is an avascular, aneural tissue with no lymphatic channels and a low cellular density (Stockwell, 1979). In fact chondrocytes account for less than 10% of the cartilage volume (Stockwell, 1979), however, the cell are synthetically active producing and maintaining the organic part of the extracelluar matrix (ECM). The ECM is composed of a collagen fibre network, mainly type II collagen, embedded in proteoglycans (PG) (Eyre, 1980; Muir, 1983). Typically collagen account for 15 – 22% of cartilage by wet weight, PG's account for 4 – 7 % by wet weight, with the remaining 60 – 85% being accounted for mainly by water and inorganic salts (Mow and Ratcliffe, 1997). Collagen and PG's are the main components supporting the mechanical stresses applied to articular cartilage and in combination with water they determine the biomechanical behaviour of articular cartilage(Ateshian et al., 1997; Maroudas, 1979; Mow and Ateshian, 1997; Mow et al., 1980; Mow et al., 1984).

The collagen within articular cartilage has a highly organised structure that provides a fibrous scaffold for the cartilage; it is inhomogeneously distributed which produces the layered appearance of articular cartilage (Lane and Weiss, 1975; Mow and Ratcliffe, 1997). Typically, cartilage is accepted as having 3 zones: the superficial tangential zone;

the middle zone and the deep zone, figures 1.5. In the superficial tangential zone the collagen fibres are tightly packed and run parallel to the cartilage surface, this layer typically accounts for 10 – 20% of the total thickness of the cartilage layer. In the transitional (or middle) zone the collagen fibres are more randomly orientated, often running obliquely to the cartilage surface, and are less tightly packed. The transitional zone forms 40 – 60% of the total cartilage thickness. The radial (or deep) zone accounts for approximately 30% of the total cartilage thickness and the collagen fibres are radially orientated; this zone includes the calcified cartilage and the tidemark which represents the interface between articular cartilage and the calcified cartilage. The radially orientated fibres which pass into the calcified cartilage help to securely anchor the cartilage to the underlying bone (Bullough and Jagannath, 1983), figure 1.6. The varying orientation of the collagen fibres plays an important role by distributing different applied stresses evenly over the loaded region of the cartilage (Setton et al., 1995). The functional integrity of cartilage depends on its biochemical composition. The collagen component of the structure is largely responsible for the tensile stiffness of articular cartilage during loading (Poole et al., 2001), but collagen fibres provide little resistance to compressive loading. The varying orientation of the collagen fibres is believed to be partly responsible for the anisotropic material properties of articular cartilage (Kempson, 1979; Mow and Ratcliffe, 1997; Woo et al., 1987).

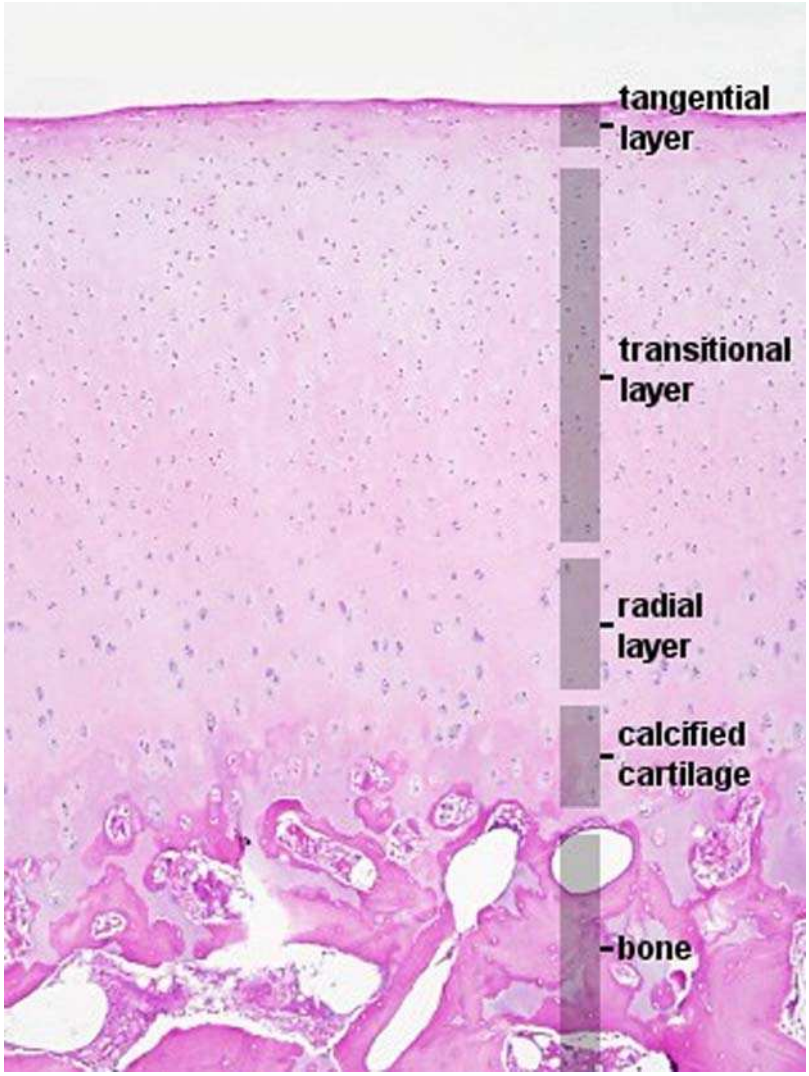

Figure 1.5 A photomicrograph of articular cartilage with H & E staining.

The characteristic zones of articular cartilage are highlighted. In the tangential zone fibres run parallel to the surface and chondrocytes are oblong with their long axis parallel to the surface. Chondrocytes are 'round' and randomly distributed whilst in the radial layer they are more columnar and orientated perpendicular to the tidemark. (Mag.x 10)

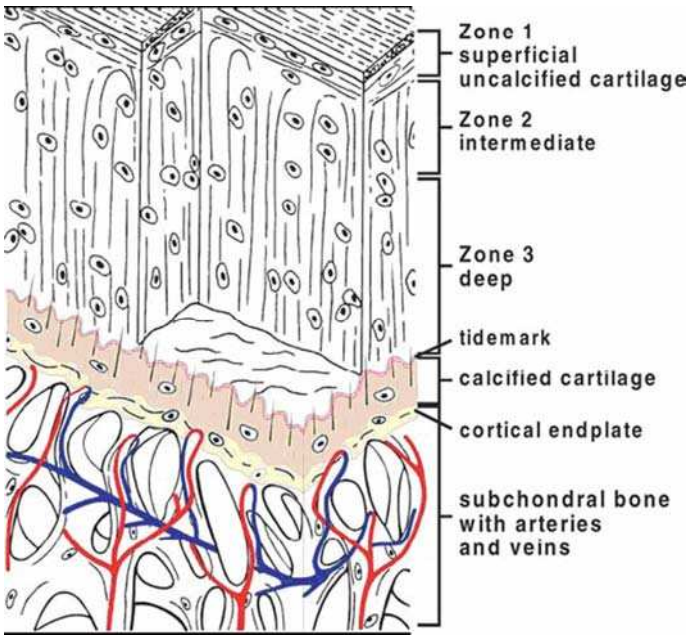

Figure 1.6 Schematic representation of articular cartilage structure.

A characteristic representation of articular cartilage structure and subchondral bone showing the layers and variation in collagen orientation from the joint surface to the subchondral bone. Adapted with permission from (Imhof et al., 2002)

Proteoglycans found within articular cartilage are large protein-polysaccharide molecules composed of a protein core to which glycosaminoglycans (GAG) molecules are attached, figures 1.7 and 1.8. It is the GAG content of articular cartilage which is largely responsible for its compressive stiffness(Poole et al., 2001). PG's form large aggregates by binding to a Hyaluronan molecule; these aggregates immobilise the PG's within the collagen network so providing the ECM with more stability and rigidity(Muir, 1983; Ratcliffe et al., 1986).

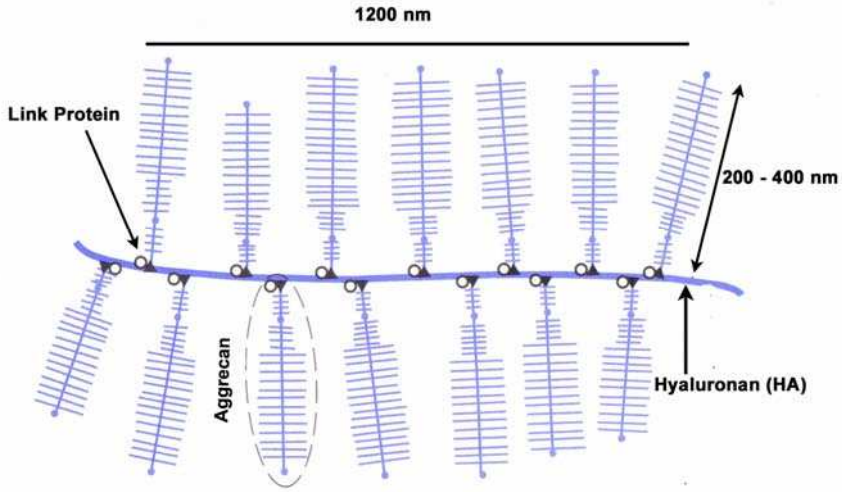

Figure 1.7 Schematic of a proteoglycan macromolecule.

Aggrecans non-covalently bind to HA, stabilised by link proteins to form the proteoglycan macromolecule which help to give articular cartilage its compressive stiffness. (Adapted from Nordin & Franklin: Basic biomechanics of the musculoskeletal system 3rd Edition Lippincott, Williams and Wilkins, 2001)

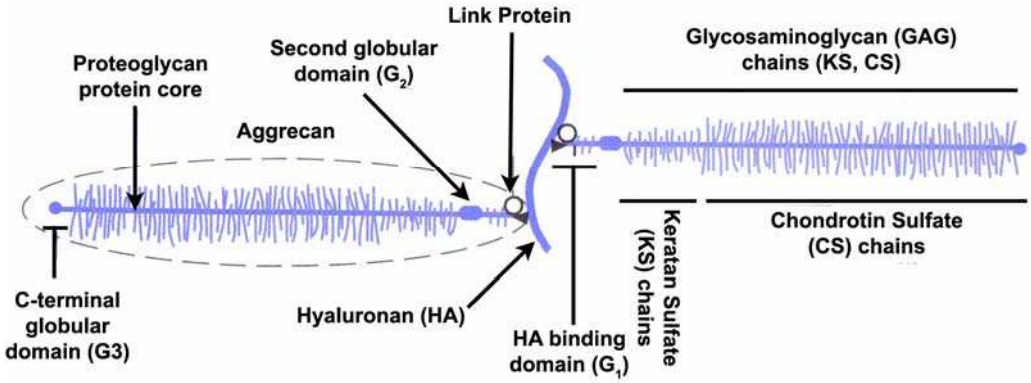

Figure 1.8 Schematic of the structure of an aggrecan.

The negatively charged glycosaminoglycans (chondrotin sulphate and keratin sulphate chains) covalently bind to the proteoglycan core protein. (Adapted from Nordin & Franklin: Basic biomechanics of the musculoskeletal system 3rd Edition Lippincott, Williams and Wilkins, 2001)

Water is the largest component of articular cartilage and it is mostly concentrated near the cartilage surface. Water within the articular cartilage plays an essential role as it

allows diffusion of gas and nutrients to the chondrocytes within the avascular cartilage. Moreover, water plays a significant role in the biomechanical response of articular cartilage. The interaction of water with the collagen and PG's via the Donnan osmotic pressure regulates the swelling properties of cartilage(Maroudas, 1968; Maroudas, 1975). Under load a large proportion of the water within the cartilage may be moved and it is the control of this movement which is highly important in determining the mechanical behaviour of the cartilage(Ateshian et al., 1997; Hlavacek, 1995).

1.3. Articular cartilage injury

The articular cartilage of diarthrodial joints has unique properties which allow the smooth, painless movement of synovial joints. However, the articular cartilage may be injured by acute impact and/or torsional loading or less severe repetitive loading; cartilage injury can in turn lead to degenerative change in the articular cartilage with associated joint pain and decreased movement(Buckwalter et al., 2000). The mechanisms of articular cartilage injury; the frequency with which they occur and their natural progression is poorly understood by researchers and clinicians alike(Buckwalter, 1992; Buckwalter, 1995; Buckwalter and Mankin, 1997). In many cases articular cartilage injuries are associated with another injury which distracts attention from the articular cartilage injury e.g. meniscal injury, ligamentous injury, joint capsule injury, synovial injury or intra-articular fracture. Buckwalter(Buckwalter, 2002) describes three broad classes of severity of articular cartilage injury: 1) damage to the joint surface that does not cause visible mechanical disruption of the articular cartilage, but does cause chondral damage and may cause subchondral bone injury; 2) Mechanical disruption of the articular surface limited to the articular cartilage and 3) mechanical disruption of the articular cartilage and bone. Repo and Finlay(Repo and Finlay, 1977) studied articular cartilage injuries in explants from renal transplant donors they showed that articular cartilage could withstand loads in excess of 25 MPa without injury and suggested that a stress greater than that necessary to fracture the femur would be required to produce injury. However evidence to support the importance of the first two classes described above is provided by several authors(Borrelli, Jr. et al., 2003; Haut, 1989; Haut et al.,

1995; Rudd et al., 2004). Between them they have demonstrated that articular cartilage injury due to impact loading can occur at sub-fracture levels in a variety of joints including the knee and ankle. Others have demonstrated that single impact loading above physiological levels but below levels required to produce surface disruption can damage chondrocytes and have a detrimental effect on the cartilage matrix(Borrelli, Jr. et al., 2003; Donohue et al., 1983; Torzilli et al., 1999). The initial effects following impact loading are chondrocytes apoptosis and a decrease in the proteoglycan (PG) content followed by decreased stiffness and increase permeability of the articular cartilage(Borrelli, Jr. et al., 2003; Buckwalter, 1992; Chen et al., 2001; Donohue et al., 1983; Han et al., 2002; Jeffrey et al., 1997; Loening et al., 2000; Thompson, Jr. et al., 1991). A causal link between chondrocyte apoptosis and osteoarthritis has been suggested by Kim et al(Kim et al., 2000) who found increased numbers of apoptotic cells with increasing severity of osteoarthritis.

Most studies of acute articular cartilage injury have examined the effects of impact force or energy; however, Atkinson et al(Atkinson et al., 1998) suggest that shear stresses occurring in the articular cartilage may be more significant indicators of cartilage injury than impact energy and impact force.

Chondrocytes have the ability to repair the macromolecular structure of articular cartilage through synthesis of new molecules when they sense a change in the cartilage matrix(Martin and Buckwalter, 2000), but the repair response of the articular cartilage is limited and often fails to completely heal the defect in the articular cartilage surface; the point at which damage becomes irreversible is unclear. In most cases large areas of chondral repair begin to degenerate relatively rapidly with a decrease in PG content, surface fibrillation increased permeability and decreased cell content. The contribution of each of these responses to injury in the development and progression of post traumatic osteoarthritis remain to be determined.

1.4. Ankle injury and osteoarthritis

Primary osteoarthritis (OA) of the ankle is relatively rare(Dieppe and Kirwan, 1994; Funk, 1976), with radiographic changes of osteoarthritis being nearly 10 times more frequent in the knee than the ankle, in patients seeking treatment(Cushnaghan and Dieppe, 1991; Wilson et al., 1990). The sex distribution of ankle osteoarthritis also differs from knee osteoarthritis as ankle OA occurs slightly more frequently in men than women as opposed to knee OA which is more common in women(Cushnaghan and Dieppe, 1991). The major cause of ankle osteoarthritis is secondary post traumatic osteoarthritis which commonly occurs after high energy tibial plafond fractures(Buckwalter and Saltzman, 1999; Walter, Jr. and Spector, 1991). This is in keeping with the finding of Brown et al(Brown et al., 1988) who reported that the sensitivity of a joint to a step off in the articular cartilage was inversely proportional to the thickness of the articular cartilage layer of the injured surface. As the ankle joint has thin articular cartilage layers it is sensitive to small step off's and therefore prone to post traumatic osteoarthritis. There are also other significant factors in a joints susceptibility to the effects of surface incongruity including the modulus of elasticity of the articular cartilage, the global congruity of the joint(Huber-Betzer et al., 1990) and the age of the patient(Martin et al., 1997; Martin and Buckwalter, 2001). The ability of the articular surfaces of the human ankle joint to remodel incongruities is unclear, but several animal models have demonstrated a remarkable potential for remodelling incongruities in joint surfaces(Llinas et al., 1993; Lovasz et al., 1998).

For rotational intra-articular ankle fractures (typically lower energy fractures) the rate of post traumatic osteoarthritis is substantially increased if ankle mortise widening due to the fracture is not adequately corrected(Michelson, 1995). The author speculated that the heightened risk of post traumatic osteoarthritis was due to altered joint loading characteristics. However, subsequent cadaveric studies have demonstrated that relatively normal joint loading occurs under static loading conditions with 50% of the tibial surface (posterior malleolus) removed(Macko et al., 1991). The dynamic loading characteristics also remain relatively unchanged with large posterior tibial plafond

defects(Fitzpatrick et al., 2001). It would therefore seem that altered contact characteristics do not fully explain the increased prevalence of osteoarthritis following intra-articular fracture of the ankle.

Axial compression loading of the ankle joint; such as occurs in falls from a height or footwell intrusion in motor vehicle collisions; more commonly results in high energy fractures of the tibial plafond. Typically these injuries are more challenging to treat and have a worse outcome. In assessing the outcomes of intra-articular ankle fractures, it is extremely difficult, if not impossible to separate the effect of the injury to the articular cartilage at the time of impact from the effects of the treatment. Several studies have demonstrated that injury severity is closely correlated with the quality of the surgical reduction, i.e. the most severe fractures had the worst reductions(DeCoster et al., 1999; Marsh et al., 1997). As it is not possible to separate these two variables there is currently no way to know whether it is the initial injury or the quality of the reduction of the articular surface that leads to the development of posttraumatic osteoarthritis. As a result of this lack of clarity and understanding a report from American Orthopaedic Association(Marsh et al., 2002), has called for research into a number of areas including methods to measure the accuracy of joint surface reduction; methods to measure the severity of injury to the articular cartilage and the effects of acute damage versus chronic effects of altered contact stresses. Greater knowledge in these areas will help direct future treatment and determine whether it is better to focus research on attempts to improve joint mechanics or to improve the biological environment of the damaged cartilage.

1.5. Cartilage MRI

Magnetic resonance imaging (MRI) of articular cartilage is becoming an increasingly useful tool for the assessment and monitoring of articular cartilage injury and degeneration. It is an excellent research instrument and there is considerable potential for expansion of the role of MRI in clinical practice as it becomes more widely available and cost efficient to use(Recht et al., 2001). Magnetic resonance imaging is a non invasive, non contact, multi-planar technique capable of producing high resolution,

high contrast images in serial contiguous slices. In recent years there has been considerable development in the field of articular cartilage imaging and refinement of imaging sequences to enhance the visualization of articular cartilage and hence the accuracy of quantitative measurements. Extensive work by Eckstein et al(Al Ali et al., 2002; Eckstein et al., 1994; Eckstein et al., 1995; Glaser et al., 2001; Graichen et al., 2000) has shown spoiled 3D gradient echo (FLASH) sequences with water excitation to be particularly useful, giving high resolution high contrast images of the articular cartilage. These images work by selectively obtaining signal from only the protons on water, resulting in a "fat suppressed" image, which helps to delineate cartilage from bone(Burstein and Gray, 2003). Trattnig et al(Trattnig et al., 1998) and Ba-Ssalamah et al(Ba-Ssalamah et al., 2002) have developed sequences with the potential to reduce image acquisition time by a factor of 4; however, these sequences currently lack the resolution for precise quantitative measurements. Most articular cartilage imaging work has concentrated on the knee joint(Cohen et al., 1999; Eckstein et al., 1994; Eckstein et al., 2005b; Eckstein et al., 2005c; Faber et al., 2001; Lukasz et al., 1998; Peterfy et al., 1994; Pilch et al., 1994; Schnier et al., 1997) which displays the thickest articular cartilage layers in the human body. However there have been a few notable exceptions(Al Ali et al., 2002; Graichen et al., 2000; Nishii et al., 2004; Peterfy et al., 1995) which have quantitatively examined joints with thinner articular cartilage layers (<2mm thick) which are more typical in most joints of the human body.

Accurate quantification of thin cartilage layers has become possible firstly because the development of more powerful magnets has meant higher resolution images can be acquired in a given time. Without these developments doubling the resolution in all three dimensions would require a 64 fold increase in imaging time if all other parameters were to remain the same(Wehrli et al., 1998). Secondly there has been a parallel improvement in image analysis and processing techniques. Image interpolation means that the sub-pixel resolution inherent in MR images(Seul et al., 2000) can be utilised to reduce the percentage error in measurements from MRI data, which is essential when working with thin cartilage layers. A variety of image segmentation techniques have been used previously including: manual segmentation(Cohen et al.,

1999; Eckstein et al., 1994; Jonsson et al., 1992; Peterfy et al., 1994; Pilch et al., 1994); seed point and region growing algorithms(Eckstein et al., 1998a; Haubner et al., 1997; Losch et al., 1997); fully automated 2D shape recognition techniques(Robson et al., 1995; Solloway et al., 1997); interpolated B splines(Cohen et al., 1999) and most recently B-spline snakes(Stammberger et al., 1999b). Other more primitive methods for making point measurements have been simple point to point measurements and thresholding along a line perpendicular to a surface(Tan et al., 1996). Many of these techniques have limitations especially in the noisy images of thin articular cartilage layers of highly congruent joints. The B-spline snake approach, is a semi-automated technique which appears to be superior to the other techniques used so far. It is precise and reproducible(Eckstein et al., 2001a) and hence avoids the subjectivity and labour intensiveness of manual segmentation techniques and the inability of fully automated processes to detect indistinct boundaries.

Ba-Ssalamah et al(Ba-Ssalamah et al., 2002) used a fat suppressed multi-shot echo planar imaging sequence, to image the ankles of patients with ankle symptoms. They showed that the sequence was comparable to fat suppressed gradient recalled images for detection of lesions and reduced the image acquisition times by a factor of 4. Unfortunately the resolution of this particular sequence (0.5 x 0.5 mm in plane resolution) suffered from insufficient resolution for precise quantification of cartilage thickness and volume. Similarly the sequence used by Tan et al(Tan et al., 1996) (0.63 x 0.63 mm in plane resolution) lacked sufficient resolution; this combined with the use of a thresholding technique to measure thickness led to errors of ± 100% in their measurements.

Al-Ali et al(Al Ali et al., 2002) have performed high resolution MRI imaging (FLASH sequence with water excitation) of the ankle joint and utilised a B-spline snake image segmentation program to segment and reconstruct the cartilage layers after interpolation of the images to an in plane resolution of 0.125 x 0.125 mm. However, the image data was not isotropic (1 mm slice thickness) and the images were acquired sagittally; therefore, the authors were unable to produce suitable images or reconstructions of the

talar shoulders or malleolar cartilage; additionally the acquisition times for these image sequences were very long limiting their application in clinical practice.

Standard MRI techniques, described above, can be used to provide excellent anatomical analysis; however, more advanced techniques are currently being developed which allow biochemical and functional imaging of articular cartilage in clinical practice(Burstein and Gray, 2003; Kim et al., 2003). Contrast agents such as Gd-DTPA are negatively charged and when administered intravenously penetrate articular cartilage. As glycosaminoglycans (GAG's) are also negatively charged the Gd-DTPA concentrates in areas of low GAG concentration and is relatively excluded from regions of high GAG concentration. Gadolinium Enhanced MRI of Cartilage (dGEMRIC) utilises these differences in Gd-DTPA distribution and has been shown to be the "gold standard" for measurement of GAG content(Bashir et al., 1999; Trattnig et al., 1999). These techniques are still experimental and there are several methodological issues to resolve; however, the possibility of combining high quality anatomical and functional MRI data could produce a paradigm shift in the diagnosis, monitoring and timing of intervention for degenerative conditions of articular cartilage.

1.6. Quantitative Cartilage Measurements

In order to characterise the mechanical properties of a diarthrodial joint it is essential to have accurate measurements of the articular cartilage thickness and the variation in thickness across the surface of the joint. It is also essential to know the range of quantitative metrics of the articular cartilage of healthy joints if we are to use cartilage thickness and cartilage volume etc. as longitudinal quantitative measures of joint degeneration such as occurs in osteoarthritis.

Most investigations of articular cartilage thickness have dealt with the knee and there have been relatively few studies of the ankle and other joints with thin articular cartilage layers. A variety of methods have been used to measure the thickness with varying accuracy both in vitro and in vivo. In vitro methods include anatomical sections(Jurvelin et al., 1987); needle probe measurements(Shepherd and Seedhom,

1999); stereophotographic techniques(Ateshian et al., 1991) and ultrasound(Adam et al., 1998a; Jurvelin et al., 1995). In vivo methods include: X-ray measurements(Hall and Wyshak, 1980; Karvonen et al., 1994); computer tomography sections(Eckstein et al., 1998a); and magnetic resonance imaging(Al Ali et al., 2002; Cohen et al., 1999). The in vitro techniques require disarticulation of the joint and/or may alter the thickness due to deformation during contact. Whereas, the in vivo techniques with the exception of MRI rely on indirect measurement techniques or can only make measurements at a discrete number of points.

Early studies of cartilage thickness often failed to make allowance for the out of plane surface curvature of the joint when using 2 dimensional techniques such as anatomical sections and X-ray studies. The error in these oblique measurements meant that the thickness of the articular layers may have been over-estimated. More recent studies have utilised advanced 3D reconstruction techniques which allow precision thickness measurements to be made at a perpendicular to the joint surface, hence allowing for curvature in all directions and giving true thickness measurements.

With specific regard to the ankle joint, Athanasiou et al(Athanasiou et al., 1995) took osteochondral cores; at 8 sites on the talar surface, 5 sites on the distal tibial surface and 1 site on the distal fibula from each of 14 cadaveric ankles; they measured the thickness at the edge of each core and reported a maximum and mean thickness for the talus of 1.45mm and 1.22 mm respectively. For the tibia the maximum and mean were 1.3 mm and 1.14 mm respectively, the distal fibula was reported to have the thinnest cartilage, 0.95 mm. The measurements made by Athanasiou et al(Athanasiou et al., 1995) are not measurements of the true thickness perpendicular to the surface and may be affected by the harvesting process. Shepherd and Seedhom(Shepherd and Seedhom, 1999) used a needle probe attached to a load cell displaced at a constant rate; they reported mean tibial and talar thicknesses of 1.35 mm and 1.16 mm respectively. Unfortunately the needle probe technique is a destructive technique which ruptures the surface preventing further testing and Jurvelin et al(Jurvelin et al., 1995) previously reported the change in force signal was not very sharp and a subjective evaluation was required; furthermore, only discrete individual measurements can be made so it is not possible to produce

continuous topographical maps. Adam et al(Adam et al., 1998a) dissected 20 cadaveric ankle joints and used A-mode ultrasound (12MHz) to measure cartilage thickness over the joint surfaces and provided an example of a thickness distribution map over the talar dome. The accuracy of measurements made using this approach is dependent on the assumption that sound travelled at a uniform speed through all layers of the articular cartilage. Considerable variation in the velocity of sound in human articular cartilage has been shown by Yao and Seedhom(Yao and Seedhom, 1999) and similar concerns have also been previously expressed by Jurvelin et al(Jurvelin et al., 1995) who saw large scatter in their results especially in thin cartilage layers. Using ultrasound Adam et al(Adam et al., 1998a) reported a maximum and mean talar cartilage thickness of 1.73±0.21 mm and 0.93±0.16 mm respectively; in the distal tibia the measurements were 1.5±0.19 mm and 1.0±0.17 mm respectively.

Ateshian et al(Ateshian et al., 1994) developed an analytical stereophotographic technique for measuring the thickness of articular cartilage and have applied the technique to the knee, but not to thin articular layers such as the ankle joint. This technique is a non contact method with which Ateshian et al have been able to make very precise measurements (± 90 μm). Unfortunately this method is destructive to the cartilage, requires complete dissection of the joint and using the method they described it is not possible to make measurements over the entire surface. The stereophotographic method described by Ateshian et al(Ateshian et al., 1994) requires the application of complex mathematical techniques, including fitting B-splines through the digitised points to produce a 3D reconstruction of the surface(Ateshian, 1993) and then calculate thickness measurement perpendicular to the joint surface. Despite these limitations the stereophotogrammetric analysis approach is an extremely useful method providing a gold standard for validating other measurement techniques such as MRI(Cohen et al., 1999) as well as generating detailed geometric data for input into computational models(Anderson et al., 2006).

MRI is becoming more widely available and offers many benefits over other methods for measuring thickness. It is a non contact 3D technique capable of high resolution which can be used in vivo. Using surface reconstruction techniques MRI can be used to

longitudinally measure changes in thickness and volume in a patient as well as producing 3D topographical distribution maps. Initial attempts to make cartilage thickness measurements were applied to the knee joint which has the thickest cartilage in the body and is relatively easy to segment as it does not have large congruent areas(Eckstein et al., 1996; Eckstein et al., 1997; Peterfy et al., 1994).

The ankle joint represents a greater technical challenge than the knee joint as the cartilage layers are thinner, the joint is more congruent and there is a sharp curvature of the surfaces at the medial and lateral edges of the talar dome. Attempts to utilise MRI to measure the thickness of the cartilage layers of the ankle were firstly limited by the achievable resolution of the images and secondly by the techniques for determining the cartilage boundaries(Tan et al., 1996). The work of Eckstein and colleagues has been essential to the development of quantitative MRI measurements. Al-Ali et al(Al Ali et al., 2002) have applied these developments to the human hind foot including the ankle joint. Following segmentation they used a Euclidean distance transformation to calculate thickness at every voxel on the cartilage surface. In 16 healthy volunteers they reported a maximum and mean thickness of the talar dome cartilage of 1.56±0.35 mm and 0.89±0.19 mm respectively, and for the distal tibial cartilage 1.54±0.34 mm and 0.82±0.15 mm respectively. Unfortunately, as mentioned in section 1.5, the imaging sequence used by Al-Ali et al(Al Ali et al., 2002) was rather long for clinical practice and did not acquire isotropic data; therefore, their measurements do not include the malleolar surfaces and a subjective decision was required to determine the edges of the talar dome.

1.7. Ankle joint contact area

In order to develop a model to help understand the effects of loading on articular cartilage and be able to calculate stress within articular cartilage it is essential to determine the contact area of the joint. Ankle joint contact area experiments have been particularly challenging, as the ankle joint is highly congruent, and has only limited access. There have been several reported experimental studies of ankle joint contact characteristics with wide variations in methodology and loading conditions resulting in

varying reports of the extent and location of the contact area(Calhoun et al., 1994; Driscoll et al., 1994; Greenwald et al., 1977; Kimizuka et al., 1980; Kura et al., 1998; Macko et al., 1991; Yao and Seedhom, 1991). Techniques applied to measuring human ankle joint contact area include; dye injection(Black et al., 1981); silicone moulding(Kimizuka et al., 1980); the '3S technique'(Yao and Seedhom, 1991); stereophotographic proximity analysis(Ateshian et al., 1994), Fuji film(Calhoun et al., 1994; Christensen et al., 1994) and more recently roentgen stereophotography(Corazza et al., 2005). The most widely used technique for measuring joint contact area in the ankle has been Fuji film(Calhoun et al., 1994; Choung and Christensen, 2002; Christensen et al., 1994; Driscoll et al., 1994; Macko et al., 1991). Ateshian et al(Ateshian et al., 1994) published an elegant study comparing a number of different techniques for measuring joint contact area in an incongruent and a congruent joint. They reported that the dye staining technique consistently overestimated the contact area especially in the congruent joint; this may be attributable to surface tension effects of the dye, additionally air bubbles may lead to erroneous areas of contact. Silicone casting produced the smallest contact areas and this probably occurs for two reasons, firstly the silicone 'film' cannot be squeezed out of the contact area in a finite time, secondly the viscosity of the silicone rapidly increases as it turn from the liquid to solid state relatively rapidly. Dye staining and silicone moulding also require extensive joint dissection prior to testing which may significantly affect joint stability and hence joint contact area. Fuji Film and stereophotography proximity techniques produced consistent results in both the congruent and incongruent joints. Fuji film gives the benefit of also allowing pressure measurement, but suffers from several problems. 1) It requires the insertion of the film which has a finite thickness; 2) it can only measure the contact area on one side of the joint i.e. it is difficult to normalise the contact area to the entire joint surface area; 3) crinkling and crimping of the film occur and 4) slippage and shearing of the film can produce spurious results. Stereophotography proximity experiments do not require disruption of the joint prior to testing or during the loading phase and the experiments can be performed relatively quickly. Unfortunately this technique requires expensive testing equipment and a considerable amount of complex post processing of the data is required.

Several of the techniques outlined above have been applied to the ankle joint: including reversible cartilage staining (Black et al., 1981), Silicone oil-carbon black powder suspension squeeze, known as the '3S' technique(Yao and Seedhom, 1993), dye injection(Yao and Seedhom, 1991), silicone rubber moulding(Kimizuka et al., 1980), and more recently roentgen stereophotography(Corazza et al., 2005). Unfortunately, the wide variation in the joint positioning and the loading conditions make direct comparison between studies difficult.

Previous studies of ankle joint contact area have used a range of different joint load magnitudes varying from to 490N to 3200 N(Calhoun et al., 1994; Yao and Seedhom, 1993) and have measured contact area with the ankle joint in variety of positions(Calhoun et al., 1994; Christensen et al., 1994; Kimizuka et al., 1980) which has substantially influenced the results previously reported. However, these earlier studies have not assessed the joint contact area under load at the extremes of ankle movement where injury may be more likely to occur

Calhoun *et al*(Calhoun et al., 1994) and Driscoll *et al*(Driscoll et al., 1994), using Fuji film, reported that the contact area of the ankle joint was distributed over the central region of the talar dome; Kimizuka *et al.*(Kimizuka et al., 1980) reported a similar distribution from silicone rubber moldings. In contrast, studies using reversible staining(Greenwald et al., 1977) and roentgen stereophotography combined with a 3-D digitiser(Corazza et al., 2005) reported the ankle joint contact area to be located over the lateral and medial margins of the talus.

Unfortunately, these earlier ankle studies were unable to reliably evaluate highly curved areas over the shoulders of the talus and accurately quantify the total surface area of the joint.

Chapter 2. Aims of the thesis

The purpose of this thesis is to characterise the geometrical and joint contact properties of the articular cartilage layers of the ankle joint in order to further understanding of ankle cartilage injuries. Furthermore, this thesis seeks to develop and validate methods for in vivo quantification of articular cartilage parameters using magnetic resonance imaging and image analysis.

The specific aims of the thesis are:

- To describe and test a high resolution stereophotogrammetry system for quantifying the geometric parameters of the ankle articular cartilage layers in vitro which can be used as an independent standard to validate in vivo techniques.

- To illustrate the topographical distribution of ankle articular cartilage across the surface of the talus, tibia and fibula.

- To test and validate image processing algorithms on high resolution cartilage sensitive MR images which can be used for in vivo quantification of articular cartilage parameters.

- To quantify the ankle joint contact area under compressive load throughout the range of movement using a stereophotogrammetric system which does not require introduction of material, such as Fuji film, into the joint during the loading process.

The studies which make up this thesis will improve understanding of the geometry, thickness distribution and variation in contact area distribution of cartilage across the ankle joint. Moreover, the results will provide essential experimental results which can be used to enhance computational models of the ankle joint which are used to study ankle joint injury and development of degenerative conditions such as post traumatic osteoarthritis.

Chapter 3. Stereophotography experiments

3.1. Introduction

As outlined in section 1.6 a variety of techniques have been applied, with varying success, to make quantitative measurements of articular cartilage in diarthrodial joints. Such quantitative measurements are required in order to characterise the mechanical properties of joint articular cartilage, improve the accuracy of computational models, such as finite element models, and to provide baseline measurements of metrics which may potentially be used to monitor degenerative change such as occur in osteoarthritis.

In the ankle joint a limited number of studies of the cartilage thickness and other quantitative parameters have been performed. These earlier studies have used microscope measurements on osteochondral cores(Athanasiou et al., 1995), needle force probes(Shepherd and Seedhom, 1999), A mode ultrasound(Adam et al., 1998a) and MRI(Al Ali et al., 2002; Tan et al., 1996) to make quantitative measurements. Unfortunately these studies provide data on only a small number of discrete sites across the joint surface or exclude large areas of the surface which are of considerable clinical interest such as the shoulders and malleolar facets of the talus.

The experiments reported in this chapter seek to address some of the shortcomings identified in earlier studies. Therefore, the objectives of this study were first, to describe a high resolution stereophotographic technique for quantifying the thin cartilage layers of the ankle joint, providing a method to validate other techniques; second, to describe the topographical variation of ankle joint articular cartilage across the joint surface; and finally, to provide baseline measurements of quantitative parameters of ankle cartilage in with joints with no visual signs of degeneration or cartilage defects.

3.2. Materials & methods

3.2.1. Ethical approval

All specimens used in this set of experiments were acquired in accordance with US state and federal laws. Ethical approval for the study was provided by the University of Virginia institutional review board and human usage review panel.

3.2.2. Specimen preparation

Twelve fresh frozen foot and ankle specimens were harvested from 12 male cadavers, with a mean age of 61.5 years (range 51-75 years). From the available medical histories there were no reports of trauma to the lower limbs or musculoskeletal disease in the ankle(s) of the subjects tested. The specimens were stored at -25ºC. Prior to testing, each specimen was allowed to thaw at room temperature for 24 hours. After thawing, the ankle joints were disarticulated, and soft tissues were removed from around the tibia-fibula complex and the talus. The syndesmosis was left intact. Each specimen was visually examined by and stained using the India ink technique to assess for cartilage surface lesions and/or degeneration. No cartilage lesions were seen in any of the specimens tested, minor localised surface fibrillation was seen in 2 ankles, which is in keeping with the findings of Meachim et al(Meachim, 1975) in autopsy specimens.

The bones were then potted in custom potting cups using a fast-setting resin (R1 Fastcast, Goldenwest manufacturing inc. CA, USA) taking care to ensure that the articular surface was above the level of the potting material, figure 3.1. The talus was elevated above the potting material by inserting 3 screws into the inferior surface of the talus, leaving part of the screw shafts projecting into the potting material so that the screws became rigidly embedded into the resin and fixed the talus in position. During preparation the specimens were kept hydrated with phosphate buffered saline containing protease inhibitor (Sigma-Aldrich, USA). The potting cups incorporated a flange at their rim with photo targets fixed to it, the rigid fixation of the specimen ensured that there was no motion of the specimen relative to these targets, figure 3.1.

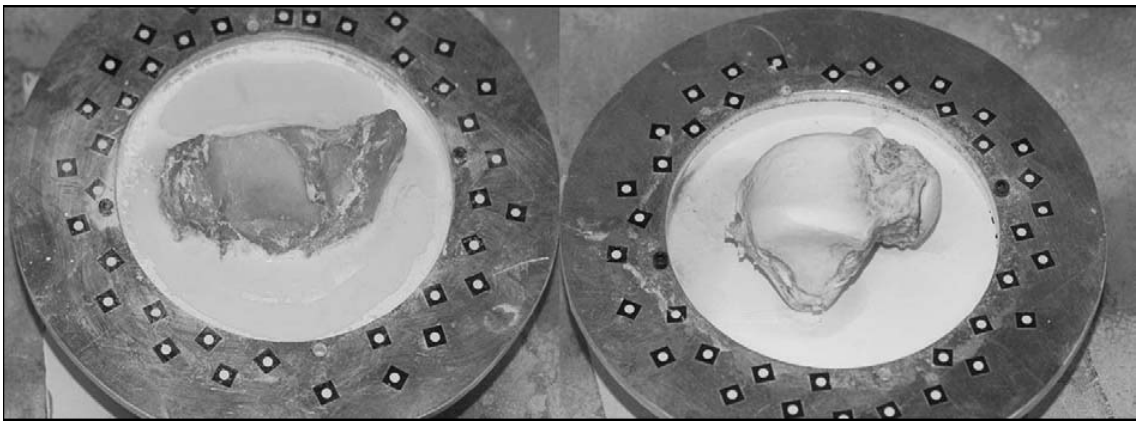

Figure 3.1 Potted tibia- fibula complex and talus specimens

Representative tibia-fibula and talus specimens rigidly fixed into the custom made potting cups. The articular surface of the talus has been prepared with a fine white power to improve image contrast and optimise the performance of the ATOS system. Black and white photo targets are fixed to the flange on the potting cup.

3.2.3. Advanced Topographic Sensor (ATOS™)

Figure 3.2 The ATOS™ system

The major components of the ATOS™ system are shown in this photograph including the fringe pattern projector, the CCD cameras, the 6 degrees of freedom mounting system and the computer processing unit

The Stereophotogrammetric system (Advanced TOpometric System - ATOS II SO, Capture 3-d, CA, USA), consists of two high resolution CCD cameras, a fringe pattern projector and digital image processing software, figure 3.2. The ATOS™ system has a

measurement noise (accuracy) of ± 2μm and point spacing of 0.03 mm (http://www.gom.com/EN/measuring.systems/atos/system/variations).

The system functions by projecting a fringe pattern onto the specimen and the fixed photo targets; the system then uses triangulation and digital image post processing to assign 3D coordinates to each pixel, thereby generating a dense point cloud. By combining multiple point clouds taken from different views, a full detailed 3D model of each surface can be generated, typically yielding on the order of 70,000 points for each cartilage or bone surface, figure 3.3. In order to improve image contrast and optimise the performance of the ATOS™ system a fine coating of white powder was sprayed onto the surface being imaged, figure 3.1.

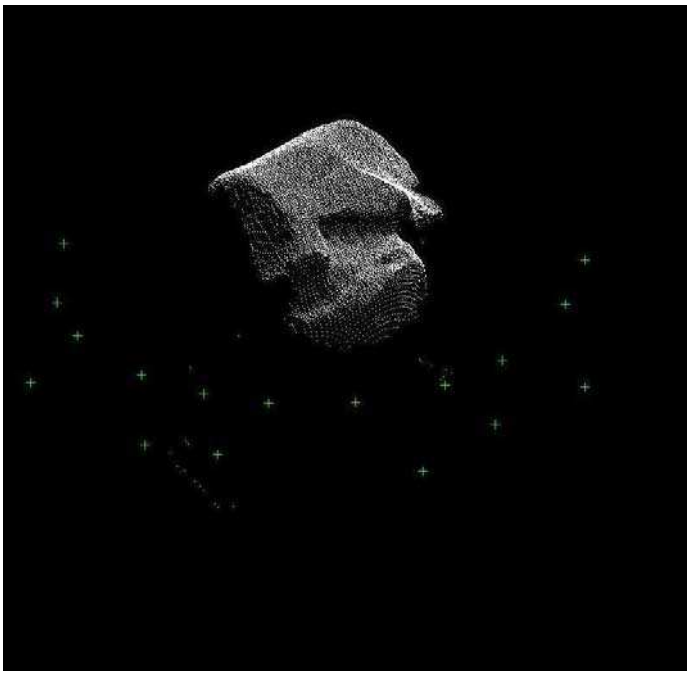

Figure 3.3 A typical talar data point cloud

A typical point cloud of the talar surface generated through combination of multiple point clouds. The green crosses mark the location of photo targets automatically detected by ATOS™ and used to register the point clouds together

3.2.4. Data Acquisition

Each cartilage surface was imaged, and the point cloud data were saved to disk. The articular cartilage was then dissolved by submerging the specimen in a 5% sodium hypochlorite solution for 6-8 hours to reveal the intact subchondral bone(Ateshian et al., 1991), figure 3.4. During this process the specimen was not allowed to move relative to the photo targets due to the rigid fixation. After removal from the 5% sodium hypochlorite the specimen was again visually examined to ensure that all the cartilage had been removed. The imaging process was then repeated for the subchondral bone surfaces. Finally, the common photo targets were defined and used to spatially register the cartilage and subchondral bone surfaces together using software incorporated in the ATOS™ system which performs a rigid body rotation and transformation of the cartilage surface onto the bone.

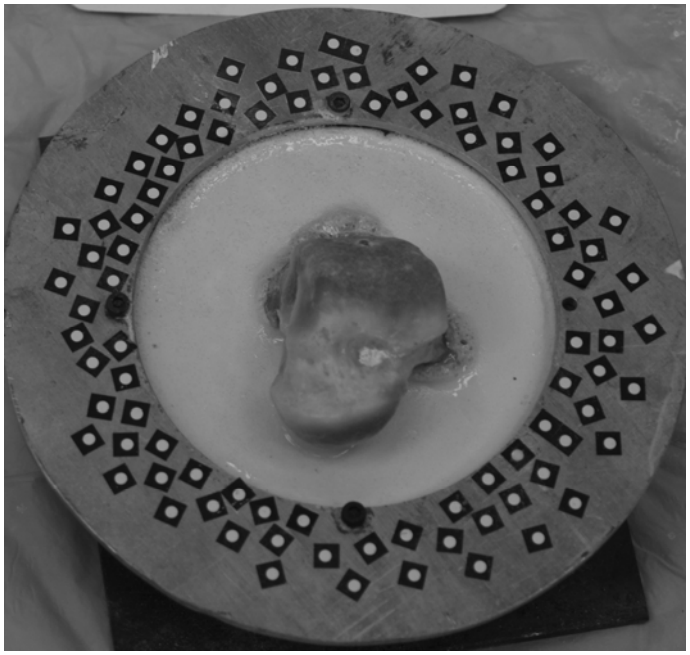

Figure 3.4 Talar subchondral bone surface after removal of the articular cartilage.

A potted talus specimen following immersion in 5% sodium hypochlorite; the articular cartilage has been dissolved to reveal the intact subchondral bone surface.

3.2.5. Post Processing Technique

In order to handle the large quantities of point cloud data in an efficient manner it was necessary to develop a custom written post processing algorithm. To achieve this it was necessary to establish collaboration with Dr Markus Grabner and Mag. Ralph Wozelka at the Technical University of Graz, Austria; and I thank them for performing the necessary programming and "bug fixing" to develop a suitable algorithm.

Briefly, the cartilage thickness was measured by performing an octree-based search for every point on the cartilage surface to find its nearest neighbour on the corresponding bone surface. This is a reasonable approximation since the average distance between adjacent points on any surface is small, typically less than 40 micrometers. However, care had to be taken at the edges of the surfaces because although the cartilage and bone surfaces were registered to each other, their borders did not necessarily match identically, since the surfaces were imaged independently. If the boundary of one of the meshes were to extend beyond the other, as depicted in, figure 3.5, an incorrectly large thickness would be reported for the extended part of the surface. These offending regions were identified by inspecting a triangle $T = (v_1,v_2,v_3)$ on M and the nearest neighbors v_i' of v_i ($i = 1. . . 3$) on M', see figure 3.5, (v_3 is not shown in this 2D sketch). If all v_i', $i = 1. . . 3$, lie on the boundary of M', triangle T is discarded, steps 1 and 2 in figure 3.5. Additionally, in some specimens small amounts of periarticular tissue, e.g. fat, joint capsule and/or ligamentous tissue, which could not be completely removed caused artefacts, making the cartilage layer appear thicker along parts of the boundary figure 3.5. Therefore, any extraneous parts at the periphery had to be identified post hoc and repaired To alleviate this problem, we define a maximum thickness d_0 and shrink both meshes M and M' until the distance between them is not larger than d_0 anywhere at the boundary.

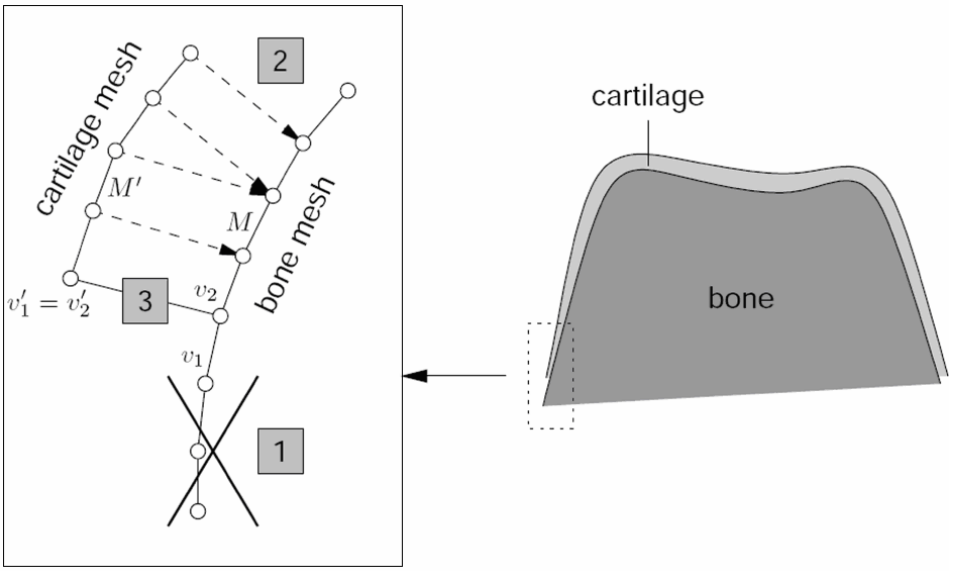

a) different mesh extents

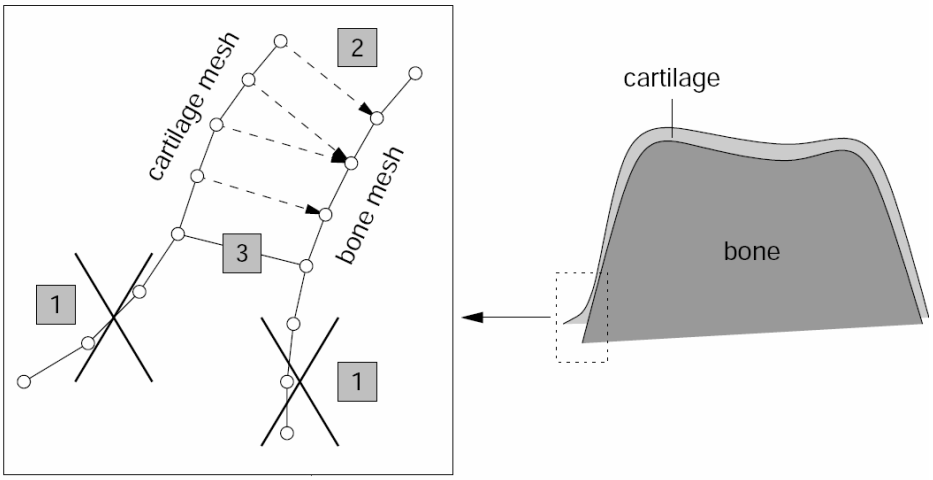

b) diverging meshes

Figure 3.5 Schematic of the corrective post processing procedure.

a) Different mesh extents. b) Diverging meshes. Step 1, removal of non-corresponding regions; step 2, for each vertex on the cartilage surface the nearest neighbour on the bone surface is found; step 3 the edges of the meshes are "stitched" together.

The final step was to "stitch" the cartilage and bone meshes together to form a closed volume. Note that these corrective procedures had no impact on the more central portions of the surface models, as they only occur at the periphery.

The processed triangulated meshes for each cartilage layer were used to measure the cartilage surface areas and the bone cartilage interface (BCI) areas. The cartilage volumes were determined from the closed polyhedra formed by the combined cartilage and bone meshes. In addition, the coefficient of variation was calculated for each cartilage layer in order to provide a description of the variation of thickness within a cartilage layer.

3.2.6. Statistical analysis

The coefficient of variation was calculated for each cartilage layer in order to provide a description of the variation of thickness within a cartilage layer. Quantitative parameters were statistically analysed for differences between the talar, tibial and fibula layers using an ANOVA with a post hoc Tukey test, $p < 0.05$ was considered significant.

3.3. Results

Precise 3-D geometric models and thickness distribution maps were generated for each articular cartilage layer, providing complete geometric data including the highly curved regions and the peripheries of the surfaces. Representative examples of the 3-D thickness distribution maps of the talus, tibia and fibula are shown in figures 3.6, 3.7 and 3.8. The 3-D models faithfully reproduce the keystone shape of the talus with a central groove running anterior-posterior over the superior surface and the concavity of the distal tibial surface. Moreover, the thickness distribution maps reveal several characteristic patterns. The talus maps displayed two distinct areas over the talar shoulders, one anterior-laterally and one posterior medially, where the thickest cartilage occurred, figure 3.6.

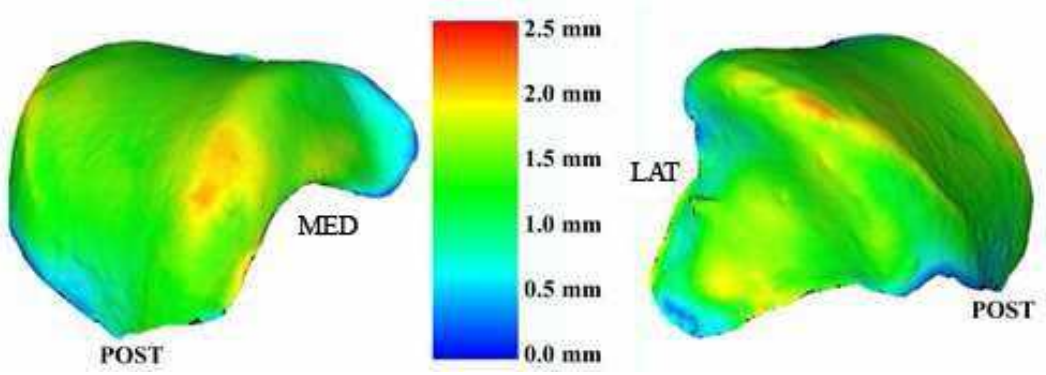

Figure 3.6 Stereophotographic 3-D talus cartilage thickness maps

Representative 3-D thickness distribution maps of the talar articular cartilage layer, viewed from the medial (left) and lateral aspect (right) of a left talus.

The tibial cartilage thickness was more evenly distributed; however, the thickest cartilage typically occurred in two areas; the central part of the anterior tibial plafond and the curved region at the transition between the tibial plafond on the medial malleolus, figure 3.7.

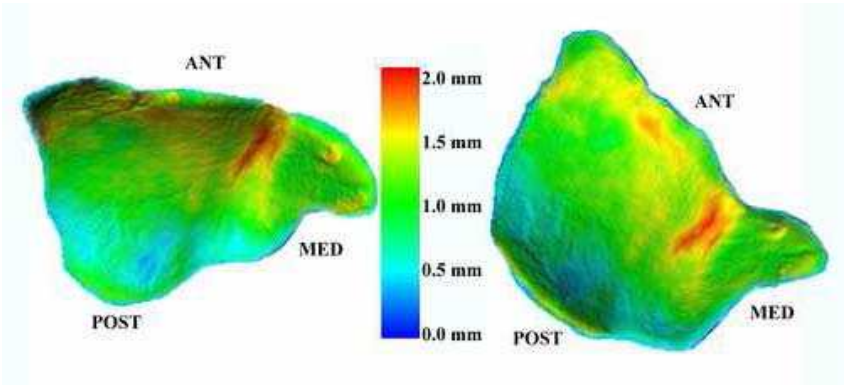

Figure 3.7 Stereophotographic 3-D tibial cartilage thickness maps

Representative 3-D thickness distribution maps of the tibial articular cartilage layer, viewed from the inferior aspect of a right tibia.

The fibula showed a characteristic valgus angulation of the distal articular surface and had the most homogeneous cartilage thickness of the ankle cartilage layers, figure 3.8.

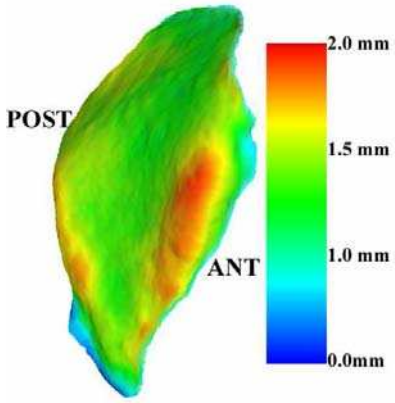

Figure 3.8 A stereophotographic 3-D fibula cartilage thickness maps

A representative 3-D thickness distribution map of the fibula articular cartilage layer, viewed from the anterior aspect of a left fibula.

The articular cartilage thickness was measured at every point on the articular cartilage surface; the mean number of measurements per surface was 73236. The mean and standard deviations (across the 12 specimens) of spatial mean thickness, maximum thickness, cartilage surface area, bone cartilage interface area and volume are shown in table 3.1. Since the surface areas and volumes are measured from the triangulated mesh, created from the point cloud data, noise in the vertex locations could result in local variations in the surface normals which may subsequently affect the measurements. While this effect is small for any given vertex the cumulative effect across the total surface area maybe considerable; however, the area error is small if the vertex displacement is small compared to the triangle edge length. Table 3.2, shows the results for different numbers of iterations of a previously described denoising method(Fleishman et al., 2003). The results show that while the surface area error due to vertex noise is larger than volume error it is still negligibly low; therefore mesh denoising was not used for the purposes of these tests.

N=12	Talus	Tibia	Fibula
Mean thickness (mm)	1.10 ± 0.18	1.16 ± 0.14	0.85 ± 0.13
Max thickness (mm)	2.38 ± 0.4	2.18 ± 0.19	2.06 ± 0.08
Cartilage surface area (cm^2)	21.56 ± 2.14	13.45 ± 1.28	4.30 ± 0.79
Bone-cartilage interface area (cm^2)	23.6 ± 1.67	12.57 ± 0.79	3.67 ± 0.63
Volume (ml)	2.44 ± 0.48	1.50 ± 0.28	0.32 ±0.08

Table 3.1 Stereophotographically determined quantitative cartilage parameters.

Mean values (± S.D.) for each of the quantitative parameters measured from 12 ankle specimens.

There was no significant difference between the mean articular cartilage thickness of talar and tibial cartilage layers. The talar ($p<0.01$) and the tibial cartilage ($p<0.001$) spatial mean thickness values were significantly greater than the fibula cartilage. For maximum cartilage thickness the only significant difference was between the talus and the fibula ($p < 0.05$).

Number of iterations	% Reduction of total surface area	% Reduction in volume
1	0.23	0.01
2	0.30	0.02
3	0.36	0.03
4	0.40	0.04
5	0.44	0.05

Table 3.2 Impact on area and volume of the denoising algorithm

The effect of different iterations of the denoising algorithm. Reduction in area and volume measurements are given in percentage relative to the original unsmoothed mesh.

Cartilage surface area and BCI area measurements showed clear significant differences. The talus had a significantly larger surface area than both the tibia ($p<0.001$) and the fibula ($p<0.001$). Even when the tibia and fibula were combined, representing the superior half of the ankle joint, the talus had a significantly larger surface area ($p<0.001$).

The talar cartilage volume was also significantly greater than the combined tibia-fibula cartilage volume ($p<0.001$) and the tibia had a significantly greater volume than the fibula ($p<0001$). This is a clear reflection of the larger area covered by articular cartilage on the talus compared with the tibia and fibula.

As an assessment of the homogeneity/inhomgeneity of the cartilage thickness across the joint surface the coefficient of variation was calculated for the superior part of the joint (tibia-fibula complex) and the inferior part of joint (the talus). The coefficients of variation were very similar for both halves of the joint, 30.21% over the tibia-fibula complex cartilage and 30.54% over the talar cartilage.

3.4. Discussion

In this study a highly accurate technique for generating 3-D geometric models and making quantitative measurements in thin cartilage layers, based on a commercially available stereophotography system, ATOS™, has been described. The system allows rapid acquisition and processing of large volumes of geometric data with a measurement noise (accuracy) of ± 2 μm. The versatility and accuracy of the technique have made it possible to study geometrical parameters of thin highly curved cartilage layers to a level of detail that has not been previously possible.

The results show that the mean cartilage thickness ranged from 0.85 ± 0.13 mm in the fibula to 1.16 ± 0.14 mm in the tibia, and maximum thickness ranged from 2.06 ± 0.08 mm in the fibula to 2.38 ± 0.4 mm in the talus. The coefficients of variation show that that ankle cartilage thickness has a relatively consistent level of homogeneity throughout the joint; the values are lower than those reported in the knee joint(Ateshian

et al., 1991), but consistent with other results reported in the ankle joint(Adam et al., 1998a).

A variety of techniques have been used previously to measure cartilage thickness in the ankle. Using the in vitro needle force probe technique(Athanasiou et al., 1995; Shepherd and Seedhom, 1999), mean cartilage thickness values have been reported as 1.22 mm and 1.16mm for the talus, 1.18 mm and 1.35 mm for the tibia and 0.95 mm for the fibula. Using A-mode ultrasound in an in vitro study the reported mean thickness values were lower; 0.95 mm and 1.0 mm for the talus and tibia, respectively. In an MRI based study of volunteers(Al Ali et al., 2002) the mean cartilage thickness was at the lower limit of values reported in the literature; 0.89 mm and 0.82 mm in the talus and the tibia, respectively.

Unfortunately each of the above techniques has limitations. The needle probe technique can only be used at a number of discrete points over the surface and ruptures the surface limiting the usefulness of further testing. Furthermore, Jurvelin *et al*(Jurvelin et al., 1995) previously reported the change in force signal was not very sharp and a subjective evaluation was required when using a needle probe. The accuracy of ultrasound measurements is dependent on the assumption that sound travels at a uniform speed through all layers of the articular cartilage. However, previous studies(Jurvelin et al., 1995; Yao and Seedhom, 1999) have shown considerable variation in the velocity, especially in thin cartilage layers, which may help to explain the lower mean values seen with ultrasonic measurements.

MRI can avoid many of these limitations, allowing measurements at every voxel and calculation of surface areas and volumes. Unfortunately, the earlier MRI study(Al Ali et al., 2002) excluded the talar shoulders and malleolar facets as well as the tibial medial malleolar and fibular surfaces, because non-isotropic sagittally acquired data were used. Therefore, a direct comparison of volume and surface area measurements with the current study is not possible.

During the disarticulation and potting of the specimens they were kept hydrated with phosphate buffered saline which theoretically may result in some swelling of the

articular cartilage; however, if the cartilage was left untreated it would potentially become dehydrated by exposure to the atmosphere and the surface preparation. The relatively short preparation time and the rapid data acquisition process for the cartilage surface by the ATOS™ system helped to minimise these effects; therefore, it is reasonable to believe that the results of the present study realistically represents the thickness of the cartilage in the *in vivo* state.

Although the reported stereophotography technique is destructive to articular cartilage, and thus can only be performed *in vitro* it is still a very useful technique as it provides an independent gold standard for validating the accuracy of other measurement techniques, such as MRI(Cohen et al., 1999), which may also be used for *in vivo* studies.

In the talus the thickness distribution maps indicate the thickest cartilage region occurs anterior-laterally and posterior-medially over the shoulders of the talus. This is in contrast to earlier studies, which were unable to assess the highly curved regions of the joint surfaces, and reported the thickest cartilage to occur in the central region of the talar dome(Adam et al., 1998a; Athanasiou et al., 1995; Shepherd and Seedhom, 1999). The findings in this set of experiments are in keeping with those of Muller-Gerbl *et al*(Muller-Gerbl and Putz, 1995) who described findings from anatomical sections. The results reported here clearly show that the regions of greatest thickness on the talus correspond to the most common site of osteochondritis dissecans (OCD) lesions in the ankle(O'Farrell and Costello, 1982). Furthermore, the thick cartilage over the anterior border of the tibia corresponds to cartilage injury sites seen in the dorsiflexion tests(Rudd et al., 2004) which provided a stimulus for developing the experimental studies which make up this thesis. It is also interesting to note that the regions of greatest cartilage thickness in the ankle joint correspond to regions on the talus and tibia where the subchondral bone is most dense(Muller-Gerbl and Putz, 1995). These finding may be a response to the prevailing mechanical conditions occurring in the ankle joint.

Understanding the behaviour of ankle articular cartilage requires a true understanding of the 3-D anatomy, including the distribution of cartilage thickness across the joint

surface. Additionally, biomechanical knowledge of the joint contact pattern and cartilage stiffness distribution across the joint surface is important. As the results of this study show that the thickest cartilage occurs where cartilage injuries are most commonly seen, investigation of the joint contact characteristics and cartilage mechanical properties in these regions is of significant interest.

Changes in quantitative geometric parameters have been suggested as potentially sensitive measures of degenerative change in cartilage layers (Burgkart et al., 2003; Gray et al., 2004). The described stereophotography technique offers the possibility to validate MRI derived measurement for surface areas and volumes, in addition to thickness in thin cartilage layers. Validated MRI techniques offer a powerful tool for detecting and monitoring cartilage injury and degenerative change

The geometric data generated using this technique can be used as input to finite element (FE) computational models. As a result the geometric database created from this study may be used to generate a representative geometry of the ankle joint and it cartilage layers(Cohen et al., 2003). FE models based on representative geometry can be of significant benefit for stress and strain analysis(Fitzpatrick et al., 2004) and to aid development of improved ankle prostheses (Cheung and Zhang, 2005).

3.5. Conclusions

In this chapter a highly accurate technique for acquiring geometric data and making quantitative measurements of thin articular cartilage layers has been described and applied to the ankle joint. The reported stereophotographic technique may be used as an independent standard for validation of the accuracy of in vivo measurements in thin cartilage layers using MRI. Furthermore, the 3-D geometric ankle cartilage data will help to produce more realistic computational models for biomechanical analysis. Finally, the thickness distribution maps produced show that the thickest articular cartilage in the ankle occurs at the clinically relevant regions where cartilage lesions most commonly occur(O'Farrell and Costello, 1982).

Chapter 4. 2-D Semi-automated cartilage segmentation study

4.1. Introduction

In the western world, osteoarthritis is the most common form of disability. The socio-economic impact of degenerative joint diseases is huge, in the United States alone the cost was approximately $65 billion per year during the 1990's (Yelin and Callahan, 1995). This cost is only set to rise with an aging population and rising drug costs. The potential impact of chondro-protective treatments and articular cartilage restoration techniques are significant.

Unlike other major joints of the lower limb, the ankle is rarely affected by primary osteoarthritis. However, the ankle appears to have a greater predisposition to the development of post traumatic osteoarthritis than the hip and knee joints(Marsh et al., 2002; Marsh et al., 2003). Furthermore, ankle post traumatic osteoarthritis often develops in a younger population and more rapidly than in other joints(Buckwalter and Saltzman, 1999; Dieppe and Kirwan, 1994; Funk, 1976). Another challenging problem in the ankle is osteochondritits dissecans (OCD) of the talar body, which typically occurs over the anterior-lateral or posterior-medial shoulders of the talus(O'Farrell and Costello, 1982).

Currently precise evaluation of a patients' degenerative joint(s), qualitatively and quantitatively both pre- and post treatment is technically demanding, especially in highly congruent joints with thin articular cartilage, e.g. the ankle joint. However, in order to clinically evaluate present and future treatments we must be able to precisely and reproducibly image and quantify the articular cartilage of these joints (Burgkart et al., 2001; Burgkart et al., 2003; Eckstein et al., 2001a; Eckstein et al., 2002; Peterfy and Genant, 1996), especially because quantitative geometric measurements of cartilage parameters such as cartilage thickness and volume, have been suggested as sensitive

image based biomarkers for detecting and monitoring cartilage degeneration in osteoarthritis(Gray et al., 2004).

Accurate assessment of articular cartilage layers requires the use of three-dimensional reconstruction of joints in order to quantify the cartilage parameters independently of slice location or orientation. Three dimensional reconstructions are particularly important for longitudinal studies of patients in which measurements must be reproducible.

The objectives of the experiments reported in this chapter were firstly to evaluate quantitative parameters of the cartilage layers of the entire ankle joint using high resolution MRI. Secondly, to test the precision (reproducibility) of the quantitative measurements made using a semi-automated directional gradient vector flow (dGVF) snake segmentation algorithm which was developed during the course of this thesis in collaboration with Prof Scott Acton, Dr Jinshan Tang and Bing Li of the University of Virginia, department of Electrical and Electronic Engineering. The final aim was to describe the topographical distribution of articular cartilage over the surfaces of the ankle joint from the 3D reconstructions generated from the segmented MRI data sets.

4.2. Material & methods

4.2.1. Ethical approval

Ethical approval for this study was provided by the University of Virginia institutional review board and human usage review panel. All the experimental components of the study were performed at the University of Virginia, Charlottesville, VA, USA; therefore, all human cadaveric specimens used in the studies presented in this thesis were acquired in accordance with Virginia state law and US federal laws.

4.2.2. Specimen preparation

Eight fresh frozen human, male cadaveric lower leg and foot complexes harvested from five cadavers, were studied. The mean age was 52.3 years. From the available medical

histories there were no reports of trauma to the lower limbs or musculoskeletal disease in the ankle(s) of the subjects. Each lower leg specimen was stored at -25ºC. Prior to MRI examination, the specimen to be evaluated was removed from the freezer and allowed to thaw at room temperature for 24 hours. All specimens were thoroughly defrosted so that all water molecules were freely mobile and MRI examinations could be performed without difficulty.

4.2.3. Magnetic Resonance Imaging protocol

The MR images were acquired using a 1.5 T MR scanner (Magnetom vision, Siemens, Erlangen, Germany) with a circularly polarized transmit and receive extremity coil. A sagittal spoiled 3D gradient echo sequence, fast low angle shot (FLASH), with selective water excitation imaging sequence used was, TR of 18 ms, TE 7.65 ms, flip angle 25°, in-plane resolution 0.3 mm x 0.3 mm, slice thickness 0.3 mm, field of view 160 mm, and a 512^2 matrix. The acquisition time was 17 mins 14 secs. As the image resolution was isotropic we were able to reconstruct the images in three perpendicular planes (sagittal, coronal and axial).

In five cadaveric ankles six repeated data sets were acquired with repositioning of the ankle and re-shimming of the magnet between acquisitions. In all other specimens, a single data set was acquired.

4.2.4. 2-D Cartilage segmentation algorithm

Since there are no suitably accurate and reliable image analysis software programs commercially available for the purpose of segmenting articular cartilage surfaces it was necessary to develop a custom written image segmentation algorithm. To this end I am deeply grateful to Prof Scott Acton, Dr Jinshan Tang and Bing Li from the Virginia image and video analysis (VIVA) laboratory at the University of Virginia department of electrical and electronic engineering for their considerable effort in programming the Matlab based image segmentation algorithm. I worked in close collaboration with the members of the VIVA team on the algorithm and user interface which went through a

number of stages of development in order to make it stable, user friendly, versatile and semi-automated. The work presented in appendix 2 describes the directional Gradient Vector Flow (dGVF) snake and anisotropic noise reduction algorithms in detail. The algorithm was subsequently improved to allow the snake to curve under itself so overcoming a major limitation of the initial version of the program which occasionally failed when used for segmenting coronal image of the ankle joint.

The snake is an active contour that is optimized with respect to curve smoothness and collocation with the strong image edges.

Following image acquisition all image data sets were transferred to and stored on a desktop work station for post processing and segmentation. In the initial experiments, reported in appendix 2, sagittal images were segmented since the tibia and talar cartilage layers surfaces do not have any "over hanging" regions when viewed in this plane; however, this meant that the shoulders and malleolar surfaces were excluded from analysis. Following further modification of the algorthim so that the dGVF snake could handle "overhanging" regions, coronal images were segmented since they allow visualisation of all the relevant cartilage, appendix 3.

4.2.5. Anisotropic diffusion – noise reduction algorithm

The post processing and segmentation procedure consist of a number of steps. First, the image volume is cropped to a smaller volume containing all the cartilage layers of the ankle, but excluding unnecessary image data such as from the distal tibial shaft. Secondly, the images are linearly interpolated (doubling the number of voxels in each row and column of each slice) to an in-plane resolution of 0.15 mm x 0.15 mm. The third step was to run an anisotropic diffusion 'de-noising' algorithm(Tang et al., 2004). For a detailed description of the anisotropic noise reduction algorithm see appendix 2. Briefly, the anisotropic diffusion technique preserves the quality of edges within the images by using a non linear filtering method that encourages smoothing in homogeneous regions, e.g. bone and cartilage substance, while inhibiting smoothing across the edges i.e. at the boundaries between cartilage and bone or apposing cartilage

surfaces. The anisotropic diffusion algorithm increases the robustness of the dGVF snake to noise. In the presence of noise the dGVF snake may produce a boundary which requires considerable manual editing. However, the use of the anisotropic diffusion algorithm prior to segmentation improves the performance of the dGVF snake by enhancing the cartilage and bone boundaries and reduces the need for manual editing, figure 4.1.

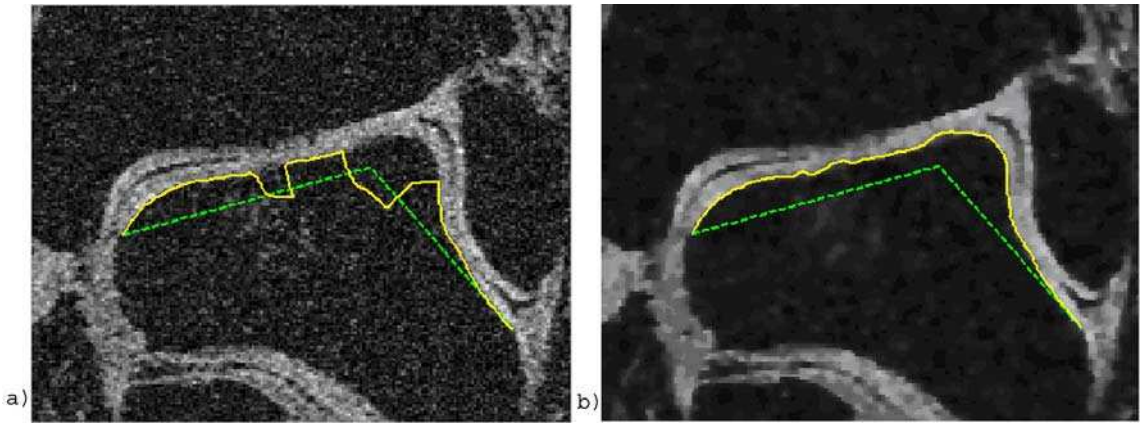

Figure 4.1 Enhanced segmentation performance due to the anisotropic diffusion noise reduction algorithm

A typical coronal MRI slice acquired using the isotropic cartilage sequence. a) Before noise reduction and b) after noise reduction using the anisotropic diffusion denoising algorithm. The dashed green line represents a very simple approximate initialisation for the bone boundary and the solid yellow line represents the boundary detected by the dGVF snake

The fourth step was to segment the talar, tibia and fibula cartilage layers using the semi-automated directional gradient vector flow (dGVF) snake algorithm(Tang et al., 2004). Briefly, a manual initialisation is required for each border in the first image segmented, the dGVF snake algorithm is then applied and the resulting contours serve as the initialisation for the borders in the next image. This approach takes account of the 3D context of the image data and facilitates segmentation in regions where the cartilage surfaces are closely apposed. The system is interactive and allows manual editing of the segmentation lines in each image if required. After completing the full segmentation the final step was to interpolate the data to an isotropic resolution of $0.15mm^3$ and generate 3D reconstructions of each cartilage layer.

4.2.6. Data analysis

For ground truth data manual tracings were used in order to evaluate the border positioning of the computer aided segmentation. The Pratt figures of merit (FOM)(Pratt, 1978), calculated using equation 4.1, were computed to assess the computer aided border positioning compared to manual segmentation. The FOM is given by

$$FOM = \frac{\sum_{i=1}^{I_A} \frac{1}{1+\alpha(d(i)^2)}}{\max(I_A, I_M)}$$

Equation 4.1 Pratt figures of merit (FOM)

In equation 1, I_A is the number of boundary pixels delineated by the computer-aided segmentation method, I_M is the number of boundary pixels delineated by manual segmentation. $d(i)$ is the Euclidean distance(Stammberger et al., 1999a) between a boundary pixel delineated by the expert and the nearest boundary pixel delineated by the dGVF snake segmentation algorithm and α is a scaling constant, with a suggested value of 1/9(Pratt, 1978). A FOM = 1 represents a perfect match between the boundary pixels delineated by computer-aided segmentation method and the boundary pixels delineated by manual segmentation. The relationship between the FOM and the average distance between the computer-aided segmentation boundary and a ground truth derived boundary is shown in figure 4.2.

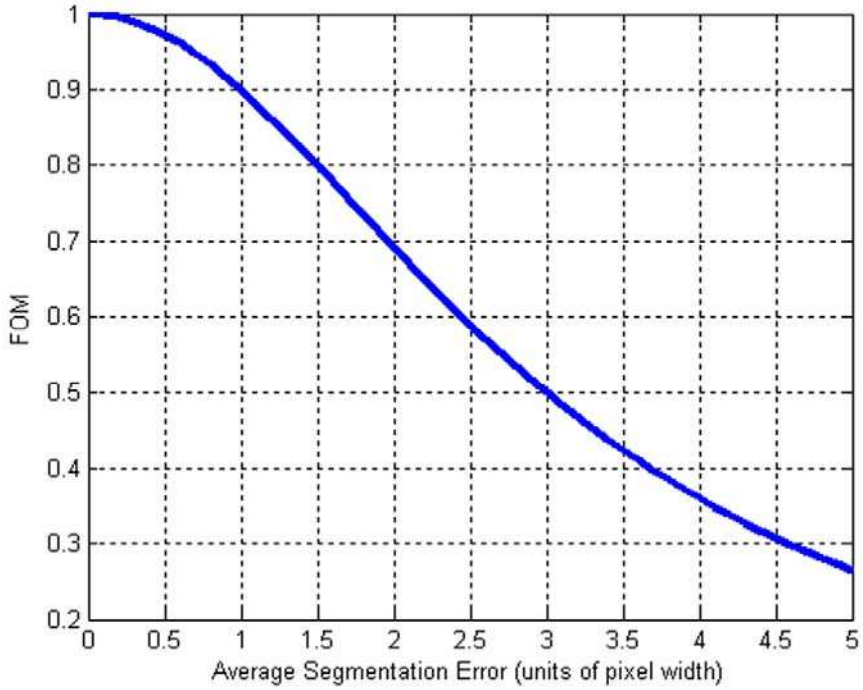

Figure 4.2 A plot of Pratt figure of merit (FOM) vs. "average segmentation error" in units of pixel width

The segmentation error is defined here as the average distance between the computed boundary and the ground truth boundary. The error units are pixel widths

Two image stacks each containing 20 contiguous image slices through the middle of the talus in the region of cartilage to cartilage contact were selected from the image data set. Each image stack was manually segmented and a 2 week interval lapsed before performing the segmentation with the dGVF snake algorithm, in order to ensure there was no "training effect". The FOM values were then calculated using equation 4.1.

The sagittal image segmentation experiments were performed using the initial version of the dGVF snake algorithm which was unable to deal with overhangs; therefore a limited subset of the data was segmented. For these experiments four repeated data sets from four ankles were segmented as a pilot study of the usability and reproducibility of the approach.

2-D Semi-automated cartilage segmentation study

The coronal image segmentation experiments were performed using the finalised version of the dGVF snake algorithm which is capable of dealing with overhanging regions. In these experiments the full MRI data set was segmented.

3D reconstructions were used to make quantitative measurements and visualize the thickness distribution of the articular cartilage. Using 3D reconstructions of the cartilage layers for thickness calculations ensures measurements are independent of section orientation and allow for out-of-plane curvature. Thickness was determined at each voxel on the cartilage surface (4444 sites/cm^2) using a 3D Euclidean distance transformation(Stammberger et al., 1999a). Cartilage surface area and bone cartilage interface (BCI) area were measured from the triangulated mesh(Eckstein et al., 2001b) and the cartilage volume of each layer was determined by integration of the voxels(Peterfy et al., 1994)

In order to evaluate the precision (reproducibility) of the dGVF approach the mean, standard deviation (s.d.) and coefficients of variation (CV%), for each of the quantitative parameters studied from the six repeated data sets in five ankles were determined. The root mean square (RMS) average(Gluer et al., 1995) of the CV's and s.d. from the individual joints were calculated for each of the parameters measured in the talar, tibia and fibula cartilage layers.

The performance of the anisotropic diffusion algorithm was evaluated quantitatively by measuring variance reduction ratio (Acton et al., 1999; Acton and Bovik, 1998). The variance reduction ratio is defined as the ratio of variance reduction following noise reduction and the original variance in a defined region of interest. A value of 0 means no noise reduction and a value of 1 means perfect noise reduction. This test is used in order to quantify the improvement given by the anisotropic diffusion process, thus avoiding absolute computation of signal and noise power for a given image. For these variance reduction computations, five contiguous slices from the central part of the joint were selected from every data set. The variance reduction was calculated for two regions of interest (ROI's), one in the bone, one in the cartilage. A total of 165 images were evaluated.

4.2.7. Statistical analysis

Statistical analysis was performed using an analysis of variance (ANOVA) with repeated measures (mixed model) and post hoc Tukey tests. Results were considered significant at the $p < 0.05$ level.

4.3. Results

4.3.1. Sagittal image segmentation experiments

The precision (reproducibility) of the MRI based cartilage measurements was determined by calculating the root mean square average (RMS thickness), standard deviation (STD) and coefficient of variation of mean thickness (CV) were determined for the tibia and talar cartilage layers from the four repeated image data sets for each of the four specimens individually; the results are shown in tables 4.1 and 4.2, respectively.

Specimen No.	**1**	**2**	**3**	**4**
RMS Thickness (mm)	1.28	1.44	1.03	1.22
STD of RMS Thickness (mm)	0.05	0.02	0.03	0.04
CV of Mean Thickness (%)	4.28	1.24	3.16	3.17

Table 4.1 Tibial cartilage thickness measurement results

The RMS mean thickness, STD of the RMS thickness and coefficient of variation from four repeated measurements in four different tibia specimens

Specimen No.	**1**	**2**	**3**	**4**
RMS Thickness (mm)	1.31	1.41	1.12	1.36
STD of RMS Thickness (mm)	0.09	0.05	0.11	0.06
CV of Mean Thickness (%)	7.00	3.33	10.13	4.34

Table 4.2 Talar cartilage thickness measurement results

The RMS mean thickness, STD of the RMS thickness and coefficient of variation from four repeated measurements in four different talus specimens. The malleolar surfaces were excluded from segmentation using the initial dGVF snake.

When considering all four ankles together the RMS CV of mean thickness for cartilage thickness was 2.96% and 6.20%, for the tibia and talus, respectively. For cumulative values (tibia and talus combined), the RMS CV mean thickness was < 4.6%. The mean RMS thickness was 1.24 ± 0.17 mm in the tibia and 1.30 ± 0.13 mm in the talus, table 4.3.

	Tibia	**Talus**
RMS CV of Mean Thickness (%)	2.97	6.20
Mean RMS Thickness (mm)	1.24	1.30
STD of Mean RMS thickness	0.17	0.13
RMS STD	0.04	0.08
Inter-subject variability/Technical precision	4.42	1.56

Table 4.3 Mean morphological values for all specimens

Mean morphological values and inter-subject variability / technical precision ratios for all talus and tibia specimens. The malleolar surfaces were excluded from segmentation using the initial dGVF snake.

The inter-subject variability (i.e. the STD of mean RMS thickness across the four specimens) was compared to the technical precision(Gluer et al., 1995), (i.e. the RMS

STD for repeated thickness measurements in all specimens), of the segmentation approach; the ratios were 1.56 and 4.42 for the talus and tibia, respectively, table 4.3. The ratios reflect that the mean articular cartilage thickness has a relatively low inter-subject variability, particularly for talar cartilage.

4.3.2. Coronal image segmentation experiments

Once the dGVF snake algorithm had been modified to handle overhanging regions the finalised version was used to segment coronal images from all MRI sets. Segmentation of coronal images allowed all region of ankle cartilage to be segmented including the malleolar surfaces and the highly curved regions over the talar shoulders.

The mean number of images segmented (± s.d.) per data set was 110 ± 6. From the eight ankles imaged, the mean values (± s.d.) for thickness, maximum thickness, cartilage surface area, cartilage bone interface area and volume are shown in table 4.4. The results show that for each of the parameters measured the talar cartilage had the largest values and the fibula cartilage gave the lowest values

	Mean thickness (mm ± s.d.)	**Max thickness (mm ± s.d.)**	**Cartilage area (cm^2 ± s.d.)**	**BCI area (cm^2 ± s.d.)**	**Cartilage volume (ml ± s.d.)**
Talus	1.34 ± 0.14	2.67 ± 0.25	28.03 ± 2.56	24.53 ± 2.16	3.32 ± 0.55
Tibia	1.21 ± 0.14	2.44 ± 0.58	15.30 ± 1.69	14.87 ± 1.48	1.72 ± 0.25
Fibula	0.91 ± 0.08	1.68 ± 0.18	4.21 ± 0.63	3.75 ± 0.56	0.35 ± 0.06

Table 4.4 Quantitative cartilage measurements using the final dGVF snake

Absolute mean values (± S.D.), from the eight subjects, for each of the quantitative parameters measured for the talar, tibial and fibula cartilage layers. Measurements made using the final dGVF snake include all parts of the ankle cartilage layers

There were significant differences between the talus, tibia and fibula for all quantitative parameters: mean thickness $p < 0.001$, maximum thickness $p < 0.005$, cartilage surface area $p < 0.001$, cartilage bone interface area $p < 0.001$ and cartilage volume $p < 0.001$.

In order to compare the superior part of the ankle joint (tibia-fibula complex) to the inferior part of the ankle joint, with which it articulates, the values for surface areas and volume in the talar cartilage were compared to the combined tibia and fibula values. The talar cartilage layer has a significantly larger cartilage surface area $p < 0.001$, cartilage bone interface $p < 0.001$ and cartilage volume $p = 0.002$, than the superior part of the joint with which it is articulated.

The mean FOM value for the border positioning between the manually defined borders and the borders obtained with dGVF snake segmentation algorithm was 0.88 ± 0.06. From figure 4.2 it can be seen that a FOM = 0.9 represents approximately a one pixel (0.15 mm) "average" Euclidean distance between the boundary pixels delineated by computer-aided segmentation method and the boundary pixels delineated by manual segmentation. Figure 4.3 shows a sample image with an expert traced border and the corresponding border detected by the dGVF snake algorithm.

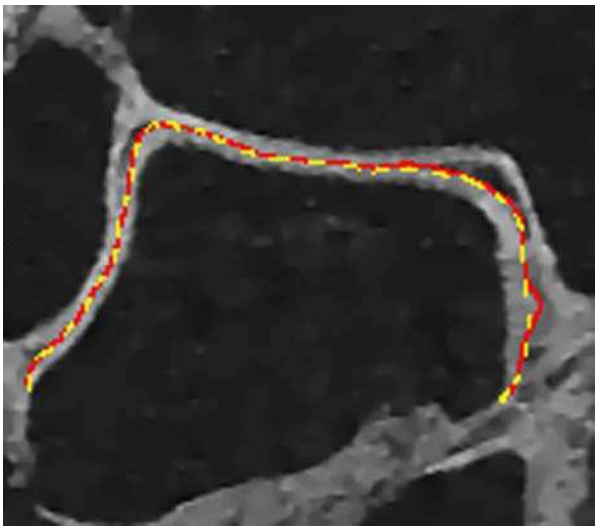

Figure 4.3 dGVF snake vs manual segmentation

Talar cartilage borders detected by the dGVF snake (solid red line) and manual segmentation (dashed yellow line), with an FOM value of 0.937.

When evaluating the precision of the approach using the six repeated data sets from five ankles, table 4.5 the RMS average coefficient of variation (min – max) ranged from 2.82% (1.21% – 4.21%) for the talar cartilage bone interface area to 9.62% (5.08% -

12.0%) for the fibula volume. Segmentation of the talar cartilage was the most precise in terms of all measured parameters followed by the tibial cartilage; the fibula gave the largest mean CV's for all the parameters assessed.

	Mean thickness %	**Max thickness %**	**Cartilage area %**	**BCI area %**	**Volume %**
Talus	3.49 (2.67 – 4.75)	4.47 (3.26 – 6.24)	3.23 (2.01 – 4.48)	2.82 (1.21 – 4.21)	4.95 (2.57 – 7.48)
Tibia	4.57 (3.26 – 5.75)	6.33 (3.77– 11.35)	4.51 (2.41 – 7.71)	3.99 (2.27 – 6.96)	5.04 (3.29 – 6.98)
Fibula	4.67 (2.62 – 7.40)	7.44 (4.14 – 9.51)	9.28 (7.29– 11.96)	9.46 (8.21– 11.10)	9.62 (5.08– 12.00)

Table 4.5 Reproducibility of segmentation using the dGVF snake algorithm

Mean coefficients of variation (min – max) from the six repeated measurements in five subjects for each of the quantitative parameters.

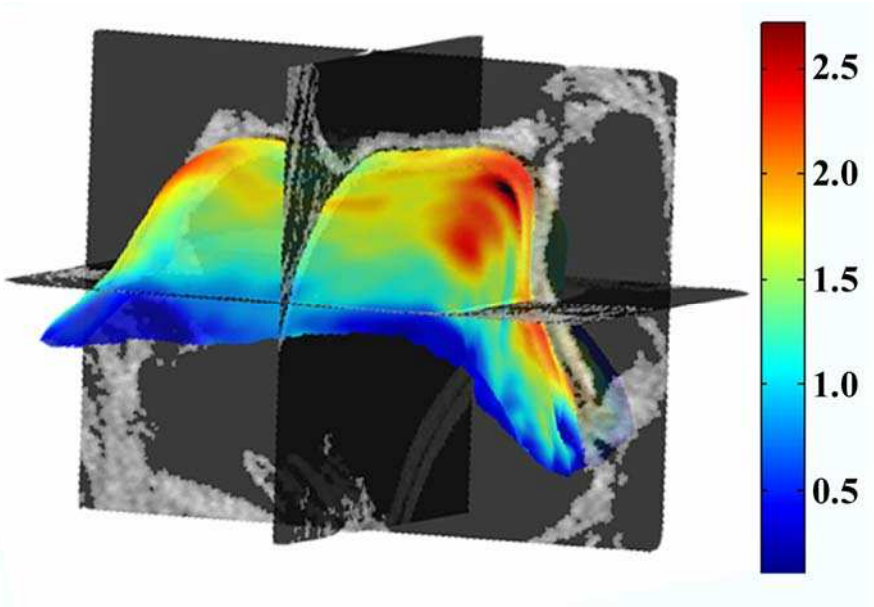

Figure 4.4 Talus thickness distribution map generated from MRI segmentation

A typical 3D thickness distribution map of a talar cartilage layer in context with the original 3D MRI data.

The colour 3D thickness distribution maps of each segmented cartilage layer show, clear characteristic thickness distributions. In all the tali studied there were two distinct areas, one anterior-laterally and one posterior-medially, over the talar shoulders where the thickest cartilage occurred, figure 4.4. For the tibial cartilage layers the cartilage thickness appeared to be more evenly distributed; however, two areas, the central part of the anterior tibial plafond and the curved region at the transition between the tibial plafond on the medial malleolus, were typically thicker than the other regions, figure 4.5. The fibula cartilage was typically more homogeneous, but slight valgus angulation of the distal articular surface was seen, as shown in figure 4.6.

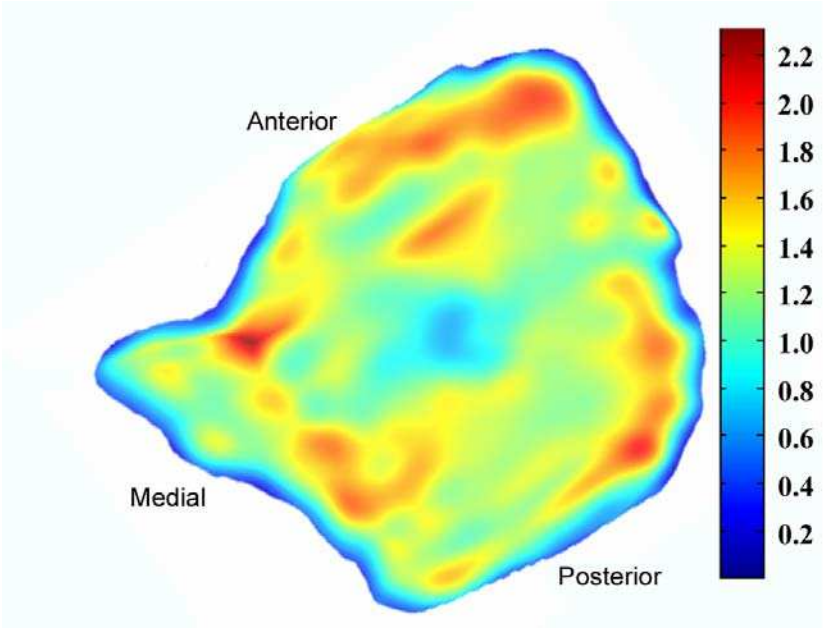

Figure 4.5 A tibia thickness map derived from MR segmentation

A typical tibial cartilage 3D thickness distribution map generated from MRI segmentation using the dGVF snake algorithm

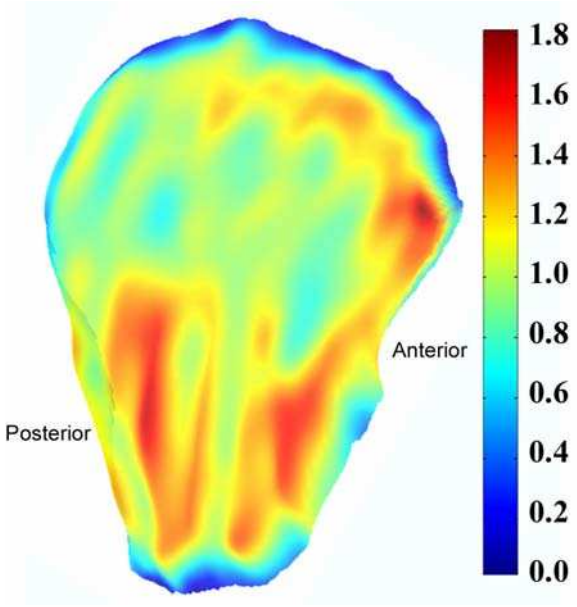

Figure 4.6 A tibia thickness map derived from MR segmentation

A typical tibial cartilage 3D thickness distribution map generated from MRI segmentation using the dGVF snake algorithm

The evaluation of the anisotropic diffusion denoising algorithm showed that the technique produced marked enhancement of the images with a clear improvement in the definition of the edges in the images, as can be clearly seen in figure 4.1. The variance reduction ratios were 0.98 ± 0.01 and 0.74 ± 1.38 for the bone and cartilage, respectively.

4.4. Discussion

The objectives of this study were to: evaluate the quantitative geometric parameters of the cartilage layers of the ankle joint; test the precision of our segmentation technique and describe the topographic distribution of the cartilage over the ankle joint surfaces. This is the first study to quantify the articular cartilage of the entire ankle joint, including the fibula and highly curved regions over the talar shoulders and the medial malleolus, using MRI.

When studying the entire cartilage layers from the coronal segmentation experiments the results showed that the mean thickness ranged from 0.91 ± 0.08 mm in the fibula to

1.35 ± 0.14 mm in the talus and maximum thickness ranged from 1.68 ± 0.18 mm in the fibula to 2.69 ± 0.25 mm in the talus. The figure of merit values show that the border positioning achieved with the dGVF snake, relative to manual segmentation, is better than the border positioning obtained with standard snake techniques(Tang et al., 2006). Furthermore, the high FOM values obtained are encouraging since the images analysed were in the middle of the joint and showed extensive cartilage to cartilage contact which represents some of the most challenging regions to segment in the ankle joint, figure 4.3. However, in some images the dGVF snake failed and it was necessary to manually edit the borders detected by the dGVF snake; this typically occurred where there were large areas of continuous cartilage to cartilage contact with indistinct borders.

The results show that the coefficients of variation for the quantitative geometric parameters studied varied from 2.82% - 9.62% in the different cartilage layers. The inter-subject variability in this study was slightly smaller than reported by Al Ali et al(Al Ali et al., 2002); what is more, it was notably larger than the variability seen in the serial measurements.

Quantitative MRI of thin congruent cartilage layers has, to date, been challenging because of the trade-off between maintaining an acceptable scan time and signal to noise ratio (SNR) whilst obtaining a sufficient resolution required for accurate quantitative measurements. The scan time, 17 mins 14 secs, used for this set of experiments is relatively long; however, Al Ali et al used a longer sequence on volunteers and reported no motion artefacts and suggested that the scan time is acceptable for routine in vivo use(Al Ali et al., 2002). It is reasonable to believe the scan time used in this study is acceptable for research use; however it is unclear whether this would be well tolerated by symptomatic patients, who may experience discomfort and have difficultly remaining motionless. After discussion with a number of colleagues and musculoskeletal radiologist it was felt that it was acceptable to sacrifice some of the SNR by using one image acquisition in order to obtain high resolution, isotropic image data and maintain a suitable scan time. By using isotropic image data reconstructions can be made in all three planes whilst the resolution was sufficiently high to avoid partial volume effects. Furthermore, the variance reduction ratio values show that it is

possible to effectively counteract the reduced SNR by applying the anisotropic diffusion algorithm to enhance the images whilst preserving edges with the image. Through the combination of the anisotropic diffusion algorithm and the dGVF snake segmentation algorithm it has been possible to segment images that others believed lacked sufficient definition for reliable segmentation(Al Ali et al., 2002).

The coefficients of variation achieved in this set of experiments are approaching those observed in quantitative studies of knee articular cartilage(Eckstein et al., 1998b; Hyhlik-Durr et al., 2000; Kshirsagar et al., 1998; Peterfy et al., 1994; Stammberger et al., 1999a), which is very encouraging. Unfortunately, the CV values for the fibula are slightly higher due to the much smaller area and thickness of the layer which makes measurements more sensitive to small variations.

Further improvements in precision will be possible in the future through a number of technological advancements. Current and ongoing development of higher field strength can be observed and a new clinical standard at 3.0 Tesla seems to be being established(Craig et al., 2005; Eckstein et al., 2005a; Eckstein et al., 2005c; Schibany et al., 2005; Schmitt et al., 2004). High-field MRI allows increased resolution while maintaining the same scan time. In addition, the development of parallel imaging allows shorter scan times. Multi-element coils can reduce the scan time by a factor of 2-4(Heidemann et al., 2004). Furthermore, there has been renewed interest in SNR efficient imaging sequences for cartilage, including forms of steady-state precession as well as driven equilibrium and TSE imaging. These new sequences offer the possibility to acquire 3D data sets with isotropic voxels, which provides excellent segmentation possibilities(Hargreaves et al., 2003; Menzel and et al, 2005).

The values for mean and maximum cartilage thickness of the talus, tibia and fibula measured using this approach are greater than those previously reported using a number of different techniques including A-mode ultrasound(Adam et al., 1998a), MRI(Al Ali et al., 2002; Tan et al., 1996) and force-needle probes(Athanasiou et al., 1995; Shepherd and Seedhom, 1999). However it is important to note that these studies excluded the highly curved regions over the talar shoulders, which have been shown to be the site of

maximum cartilage thickness in anatomical sections(Muller-Gerbl and Putz, 1995) as well as in the stereophotography experiments(Millington et al., 2004), chapter 3. Notably, the values obtained using this MRI segmentation approach are in keeping with values found using the high resolution stereophotography technique that should be considered as a reference standard for the "true" cartilage thickness (Millington et al., 2004), chapter 3.

The 3D thickness distribution maps demonstrate a characteristic distribution pattern which is most marked in the talus. It is widely believed that the thickest cartilage in the ankle occurs at the centre of the talar dome and tibial plafond(Adam et al., 1998b; Athanasiou et al., 1995; Shepherd and Seedhom, 1999), but MRI segmentation generated thickness maps clearly show the thickest cartilage occurred over the anterior-lateral and posterior-medial shoulders of the talus which corresponds to the most common site of OCD lesions in the ankle joint (O'Farrell and Costello, 1982) and corresponds to measurements from anatomical sections(Muller-Gerbl and Putz, 1995) and those from the stereophotography experiments in chapter 3. Furthermore, the thick cartilage over the anterior border of the tibia corresponds to cartilage injury sites seen in dorsiflexion testing(Rudd et al., 2004), which formed part of the rational for this thesis.

4.5. Conclusions

These 2-D semi-automated cartilage segmentation studies have quantified the geometric parameters of the talar, tibial and fibula cartilage layers. They have demonstrated that the mean and maximum thickness of each layer of ankle cartilage exceed the measurements previously reported(Adam et al., 1998a; Al Ali et al., 2002; Athanasiou et al., 1995; Shepherd and Seedhom, 1999; Tan et al., 1996). Additionally, it has been shown that by using the dGVF snake segmentation algorithm combined with the anisotropic diffusion denoising algorithm it is possible to extract the cartilage layers more precisely than previously achieved(Al Ali et al., 2002) in the ankle joint. Finally, the 3D thickness distribution maps generated from the segmentation have shown a characteristic pattern with the thickest cartilage occurring over the anterior-lateral and

posterior-medial talar shoulders, where OCD lesions commonly occur(O'Farrell and Costello, 1982).

Chapter 5. Preliminary 3-D fully automated cartilage segmentation study

5.1. Introduction

As outlined in section 4.1 osteoarthritis and degenerative cartilage diseases affect millions of people and the treatment and socio-economic costs are enormous(Yelin and Callahan, 1995). As a result, new articular cartilage therapies have very significant practical implications and applications for future patient management and care. Therefore there is huge research and commercial interest in developing new therapies to repair, replace and/or regenerate injured or degenerate cartilage. This drive to develop new therapies necessitates advances in techniques which make earlier non-invasive diagnosis possible and allow objective and quantitative evaluation of new therapies. Gray et al.(Gray et al., 2004) have suggested that quantitative geometric measurements of cartilage parameters such, as cartilage thickness and volume, are potentially sensitive image based biomarkers for detecting and monitoring cartilage degeneration in osteoarthritis. This belief forms the basis for one of the major study areas in the National Institute of Health (NIH), USA osteoarthritis initiative (http://www.niams.nih.gov/ne/oi/). However; to date all techniques used, including the dGVF snake reported in Chapter 4, have been limited, being tedious and labour intensive, requiring slice by slice and border by border segmentation or editing. As such the previously reported 2D approaches are impractical for routine clinical use and have only been utilised in a research setting.(Cohen et al., 1999; Eckstein et al., 2005c; Eckstein and Glaser, 2004; Solloway et al., 1997)

A clinically useable, accurate and reproducible quantitative 3-D analysis tool for cartilage images has the potential to produce a paradigm shift in the early diagnosis and detection of osteoarthritis, degenerative diseases and cartilage injury. Non-invasive monitoring methods will be particularly useful for clinical trials yielding new treatments developed by the pharmaceutical and biotechnology industries. Furthermore, automated quantitative analysis of 3-D cartilage images has the potential to significantly enhance

large epidemiological trials, such as the Osteoarthritis Initiative, which seek to identify risk factors for osteoarthritis and cartilage degenerative diseases. What is more, the development of automated 3D cartilage image analysis with quantitative measurements and 3D mapping of cartilage layers has the potential to significantly aid pre-operative planning and post operative monitoring of patients undergoing cartilage reparative and restorative therapies.

The specific objectives of this study were first to demonstrate that a 3D graph search algorithm can detect multiple cartilage surfaces automatically and simultaneously; second to assess segmentation errors and demonstrate sub-pixel accuracy of the cartilage segmentation and morphological measurements compared to existing independent standards and finally to evaluate the reproducibility of the algorithm.

5.2. Material & methods

5.2.1. Ethical approval

Ethical approval for this study was provided by the University of Virginia institutional review board and human usage review panel. All the MR images used in this study were acquired at the University of Virginia, Charlottesville, VA, USA; therefore, all human cadaveric specimens used in the study were acquired in accordance with Virginia state law and US federal laws. Furthermore, ethical approval was also provided by the University of Iowa USA for the use of the anonymous MR data in the development of the automated 3D image analysis algorithm.

5.2.2. MRI data sets

The MRI data sets acquired for the 2-D segmentation studies reported in chapter 4 were re-used for this study. To recap, the MR images were acquired using a 1.5 T MR scanner (Magnetom vision, Siemens, Erlangen, Germany) with a circularly polarized transmit and receive extremity coil. A sagittal spoiled 3D gradient echo sequence, fast low angle shot (FLASH), with selective water excitation imaging sequence used was,

TR of 18 ms, TE 7.65 ms, flip angle 25°, in-plane resolution 0.3 mm x 0.3 mm, slice thickness 0.3 mm, field of view 160 mm, and a 512^2 matrix, figure 5.1. The acquisition time was 17 mins 14 secs. As the image resolution was isotropic we were able to reconstruct the images in three perpendicular planes (sagittal, coronal and axial).

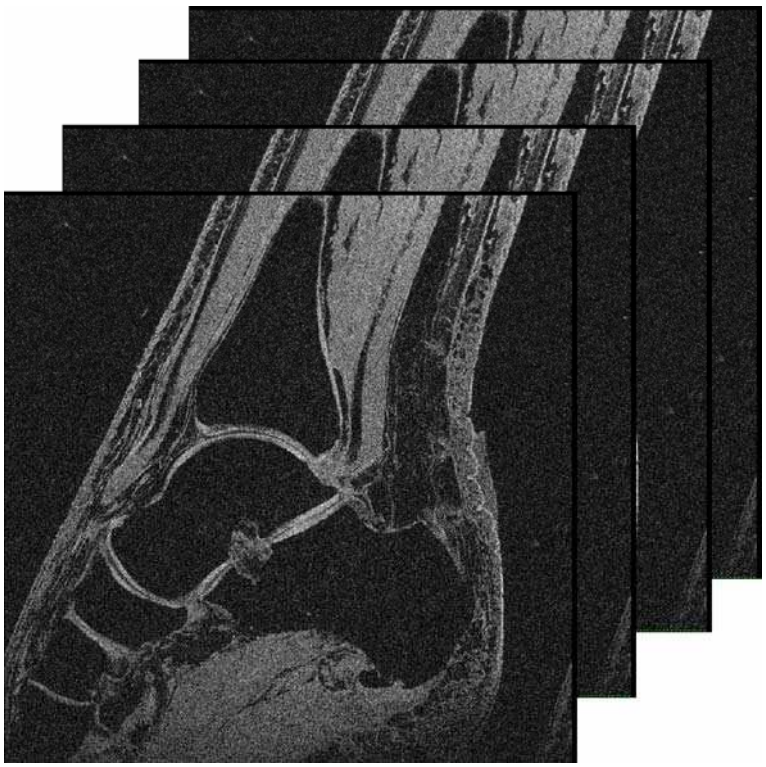

Figure 5.1 A high resolution isotropic cartilage sensitive MR image stack

A sample image stack acquired using the sagittal 3D gradient echo sequence, fast low angle shot (FLASH), with selective water excitation. Since the images have isotropic voxels 3D reconstructions can be made in the coronal and axial planes

5.3. 3-D segmentation algorithm

The 3-D segmentation algorithm used in this study was developed by Prof Milan Sonka and his graduate student Kang Li at the University of Iowa. The basis for this collaboration originated from a meeting with Prof Sonka at which I presented my earlier 2-D segmentation work and outlined ongoing and future projects related to articular cartilage imaging.

3-D fully-automated cartilage segmentation study

The proposed algorithm used in this study represents a non-trivial modification and advancement of a 3-D approach previously developed at the University of Iowa for segmenting tubular structures in medical images, e.g. blood vessels (Li et al., 2004).

The proposed algorithm is described in greater detail in appendix 4. Briefly, the method allows segmenting multiple interrelated surfaces in volumetric images and facilitates subsequent quantitative analysis. The general strategy of the method is to achieve the final segmentation in two stages. The initial stage provides approximate segmentation of the three dimensional object, in this case the subchondral bone, and the final segmentation is achieved by accurate and simultaneous segmentation of the multiple surfaces of interest i.e. the subchondral bone and cartilage surfaces. The outputs of the algorithm are triangulated meshes that are ready for visualization and quantitative measurement, figure 5.2.

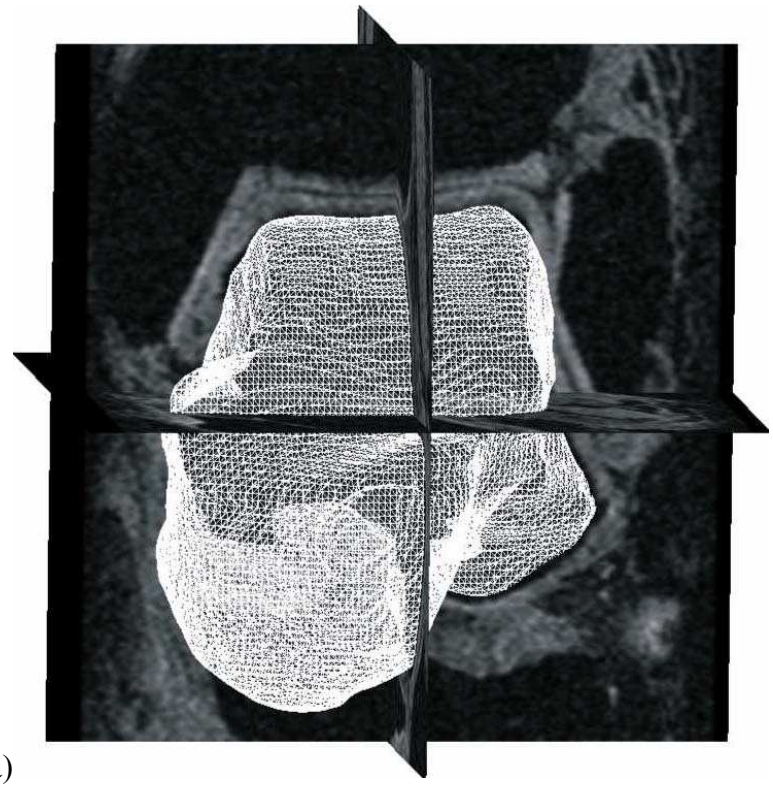

a)

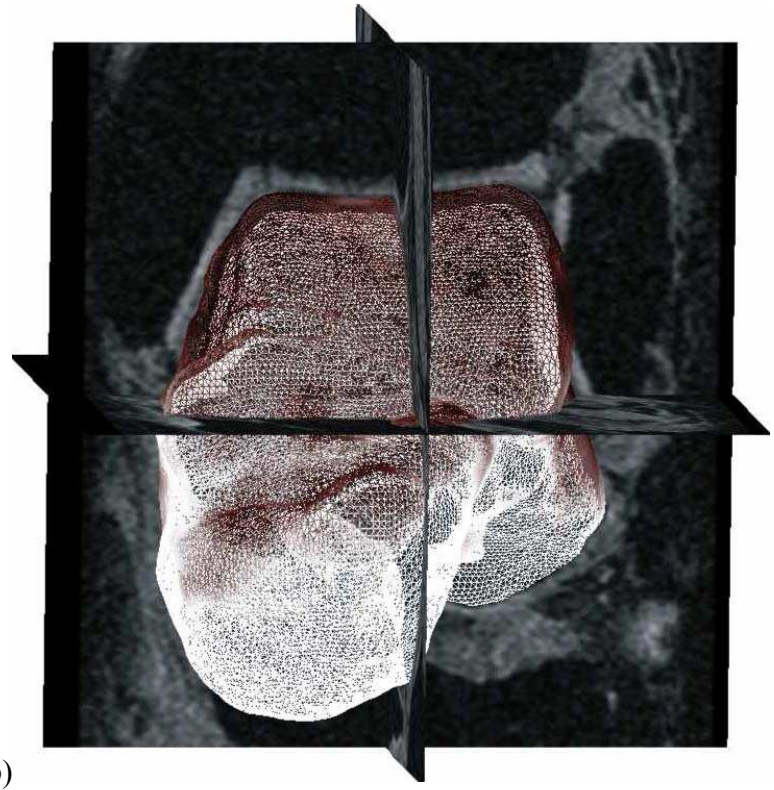

b)

Figure 5.2 Triangulated output meshes

a) Presegmentation triangulated mesh generated using the level set methods this serves as the initialisation for the 3D automated segmentation algorithm. b) Segmentation triangulated mesh, the bone surface mesh is shown in white and the cartilage mesh is shown in red

The method consists of the following three main steps, figures 5.3 and 5.4:

1. Bone surface pre-segmentation. A level set based algorithm is used. Starting from several seed spheres placed within the bone of interest, the method uses the image derived edge and regional information to evolve a smooth surface toward the bone boundary. The pre-segmented subchondral bone surface serves as an initialization to the subsequent segmentation.

2. Mesh generation and optimization. The pre-segmentation results in an implicit surface that is the zero level set of a 4-D function embedded in a volumetric digital grid. An iso-surfacing algorithm (e.g., marching cubes) is used to convert the implicit surface into an explicit triangulated mesh. The mesh is optimized by

removing or merging isolated and redundant triangles. The resolution of the mesh can be increased or decreased using progressive level of detail approaches when necessary.

3. Co-segmentation of the cartilage and bone surfaces. The mesh generated by the second step is used to initialize a graph in a narrow band around the pre-segmented bone surface. The novel multi-surface graph search algorithm, appendix 4, is used to simultaneously obtain the precise positions of the bone and cartilage surfaces based on two cost functions separately designed for the two surfaces while considering specific geometric constraints.

Steps 1 and 3 represent innovative approaches within the field of medical image analysis, in particular articular cartilage segmentation; step 2 utilises well established standard techniques in the field of graphics, therefore only steps 1 and 3 are outlined in more detail in appendix 4.

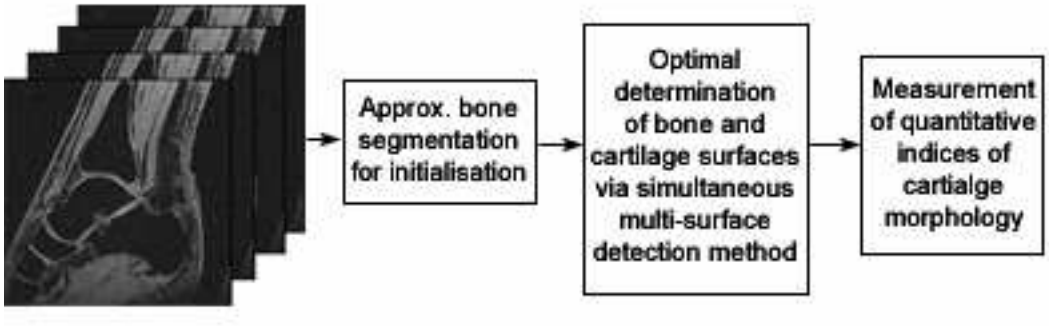

Figure 5.3 Processing blocks of the automated 3D segmentation approach

5.3.1. Independent Standard.

In order to assess the accuracy of the proposed approach we compared the results of the computer segmentation to two different independent standards: 1) phantom images with different levels of noise and 2) comparison to manual tracing.

Noisy phantom image data modelling cartilage layers across a joint were generated to allow validation of the quantitative indices in a phantom environment for which the

ground truth was known. Three volumetric phantoms were generated containing a simplified rendering of a bone and its cartilage. Each 3-D phantom data set consisted of 20 image slices. Three different levels of Gaussian noise were introduced (none, medium, high). Thus, a total of 9 phantoms (3x3) consisting of 180 image slices were used. In the data sets, all parameters were known by design and so the output of the segmentation algorithm could be easily compared to the true result.

From the 8 MR image data sets, 55 coronal or sagittal slices were randomly selected for manual tracing. The selection of coronal as well as sagittal slices allows assessment the performance of the inherently 3D segmentation method using 2D manual tracings.

5.3.2. Comparisons with the Independent Standard.

Computer segmentation of the talus bone and its cartilage surfaces was initialised and performed on the entire 3D volume for each data set, image phantoms and ankle MRI volumes. Consequently, the segmented surfaces were available for the entire closed 3D object. The automated borders detected in the 55 slices where manual tracings were available were further analysed.

The automated segmentation method locally failed in 5 of the 55 image slices due to local pre-segmentation errors. The segmentation accuracy was assessed in the remaining 50 image slices by computing signed, unsigned, and RMS surface positioning errors. The positioning errors were defined as the shortest distances between the manually traced borders and the computer determined surfaces in the coronal and sagittal MR slices for which the independent standard was available. The errors are reported on a per slice basis as mean ± standard deviation.

5.3.3. Reproducibility

To assess the reproducibility of the 3D automated cartilage segmentation, the method was independently initialized 5 times in each joint and the mean and maximum cartilage thicknesses were determined for each of the 8 talus cartilage layers. The reproducibility

was assessed by calculating mean ± standard deviation of differences between the average values obtained in the 5 reproducibility runs and the individual results.

5.4. Validation Indices

To assess the performance of this proof-of-concept implementation of the algorithm we used the following validation indices:

5.4.1. Approximate Bone Segmentation Indices.

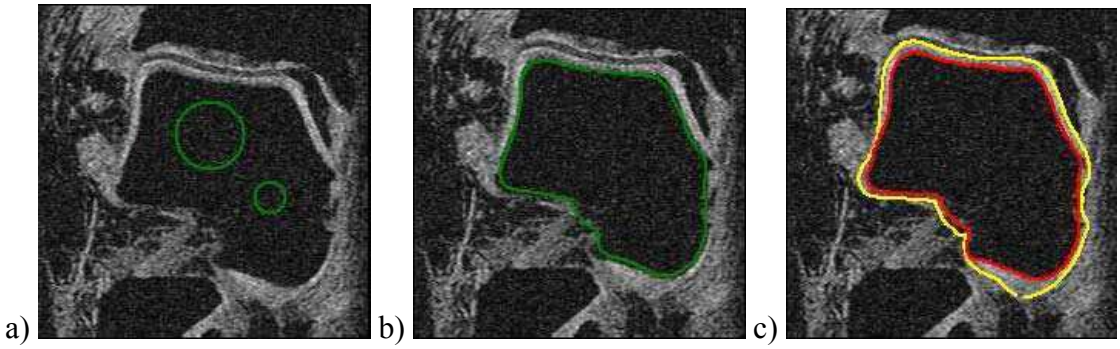

Figure 5.4 Visualisation of the 3D automated segmentation processing steps

a) Interactive initialization of the bone segmentation – defining which bone(s) shall be segmented using seed spheres. b) Result of the approximate bone segmentation (green). c) Accurate bone and cartilage surfaces of an ankle obtained by simultaneous optimal detection of two surfaces in 3D (red and yellow, respectively). Note that during development optimisation concentrated on the ankle joint, not on the sub-talar joint.

As outlined in figures 5.2 and 5.3 approximate bone segmentation is necessary for automated initialization of the multiple-surface segmentation method. Therefore, the mean and maximum unsigned distances between the approximate bone segmentation surface and the true bone surface known from the independent standard was determined for each segmented bone and reported in mm. Similarly, the agreement between the normals of the manually-traced and automatically determined bone surfaces were assessed at 1 mm intervals along the manually traced independent standard borders of the respective bone. Mean and standard deviation, as well as maximum difference between the directions of the border normals are reported in degrees.

5.4.2. Surface Positioning Errors.

The signed and unsigned mean surface positioning errors of the identified surfaces were determined between the corresponding points – the first point being from a computer detected surface and the second point from the independent standard surface, that were closest to each other using the Euclidean metric. The positioning errors were determined for each point on the computer-detected surfaces as the distances between corresponding surface points. These errors were determined across the talar dome surface, the sub-talar cartilage surface regions were excluded from analysis as the segmentation algorithm was not optimised to segment these regions. The surface positioning errors are reported as means ± standard deviations in pixels and in mm.

5.4.3. Cartilage Morphology Indices.

Similarly, the signed and unsigned mean measurement errors of the morphologic indices were determined in comparison to the indices derived from the independent standard. The errors of cartilage thickness are reported as means ± standard deviation in pixels as well as in mm.

5.5. Results

All experiments were performed on a workstation with dual 3.0GHz processors and 4GB of RAM. For each data set, we used 3 seed-spheres inside the bone region to initialize the pre-segmentation.

The phantom experiments showed that the proposed algorithm was able to accurately detect the bone and cartilage surfaces. The segmentation was successful in all 9 phantoms; the achieved segmentation performance is shown in tables 5.1 and 5.2

	Distance Mean	Distance Maximum	Mean Angular Difference	Maximum Angular Difference
Approximate Bone segmentation	1.69 ± 0.31 pixels	2.09 ± 0.24 pixels	1.16 ± 1.03º	3.13 ± 1.23º

Table 5.1 Performance of approximate segmentation used for initialisation in phantoms

To make the segmentation process more efficient, the MR volume was cropped to include only the talus and unnecessary regions such as the distal tibial shaft so forming smaller volumes of approximately 250×250×150 voxels each. The pre-segmentation was performed on 2-times down-sampled copies of the cropped images, while the final segmentation was performed on the original full-resolution images, figure 5.4.

Mean error	Bone surface	Cartilage surface	Cartilage thickness
Signed	- 0.06 ± 0.35 pixels	0.04 ± 0.41 pixels	0.24 ± 0.22 pixels
Unsigned	0.33 ± 0.13 pixels	0.37 ± 0.17 pixels	0.27 ± 0.19 pixels

Table 5.2 Performance of the 3D graph searching segmentation algorithm in phantoms

For each ankle data set, the average execution times of the pre-segmentation and segmentation stages were about 200 seconds and 70 seconds, respectively. The surface positioning errors (distance and angular) of the approximate computer-segmentation, which served as the initialisation, compared to the manual tracings are shown in table 5.3. The surface positioning errors and cartilage thickness errors of the final segmentation of the talus bone and its cartilage surface are shown in table 5.4.

Approximate Bone segmentation	Distance Mean	Distance Maximum	Mean Angular Difference	Maximum Angular Difference
Pixels	1.35 ± 0.88	2.26 ± 1.08	4.65 ± 4.54º	11.11 ± 6.27º
mm	0.41 ± 0.26	0.68 ± 0.33 mm	--	--

Table 5.3 Performance of approximate segmentation used for initialisation on ankle MR data sets

Mean error	Bone surface	Cartilage surface	Cartilage thickness
Signed (pixels)	0.12 ± 1.04	0.41 ± 1.27	- 0.20 ± 1.11
Unsigned (pixels)	0.86 ± 0.60	1.00 ± 0.89	0.85 ± 0.74
Signed (mm)	0.04 ± 0.31	0.12 ± 0.38	- 0.06 ± 0.33
Unsigned (mm)	0.26 ± 0.18	0.30 ± 0.27	0.26 ± 0.22

Table 5.4 Performance of the 3D graph searching segmentation algorithm on ankle cartilage MR data sets

Error measurements reported in pixels and mm, compared to ground truth manual segmentation. Unsigned values indicated the sub-pixel accuracy of the method, whilst the signed values indicated that the method is unbiased.

Examples of the achieved computer-segmentation are shown in figure 5.5 and a comparison between the computer segmentation and manually-traced bone and cartilage contours are shown in figure 5.6.

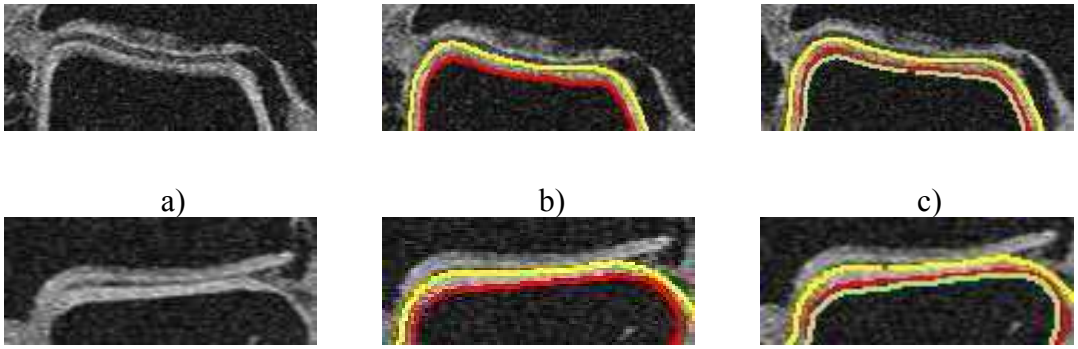

Figure 5.5 Examples of segmentation in the talo-tibia joint contact region

a) Original image (enlarged portion shown). b) Accurate bone and cartilage surfaces of an ankle obtained by simultaneous optimal detection of two surfaces in 3D (red and yellow, respectively). c) Comparison of the approximate segmentation (green) and the final accurate bone segmentation (red) shows the segmentation improvement achieved by the optimal border detection step. In this figure, only the talus bone and cartilage borders are shown for clarity.

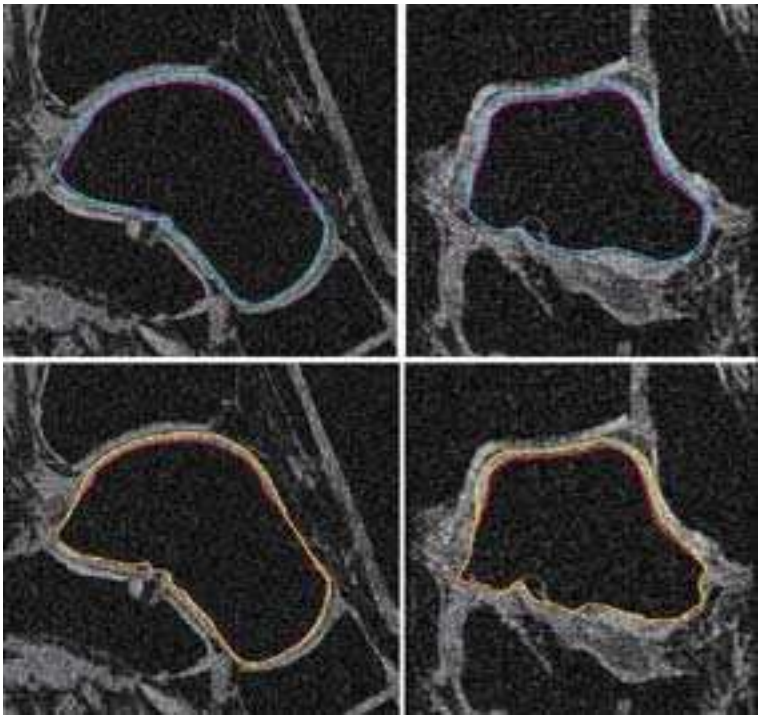

Figure 5.6 A comparison of 3D automated and manual segmentation

Typical borders detected by automated (purple and blue) and manual segmentation (red and yellow). Sagittal and coronal ankle MR images are shown in order to allow a comparison between the 2D manual segmentation and the optimal graph searching algorithm which is inherently 3D.

The mean cartilage thickness measurements achieved a signed error of 0.08 ± 0.07mm, and an unsigned error of 0.09 ± 0.06mm. All border positioning errors show sub-voxel accuracy (voxel size 0.3 x 0.3 x 0.3 mm^3).

In the reproducibility experiment, the initializing spheres were modified from the original settings by adding up to 10% of random variation to their radii and 2 to 5 voxels of random translations to each coordinate of their positions. The Bland-Altman plots of the signed differences between each individual measurement and the average measurements are shown in figure 5.7 demonstrating that repeated measurement of cartilage thickness with varying initialisation is unbiased and reproducible.

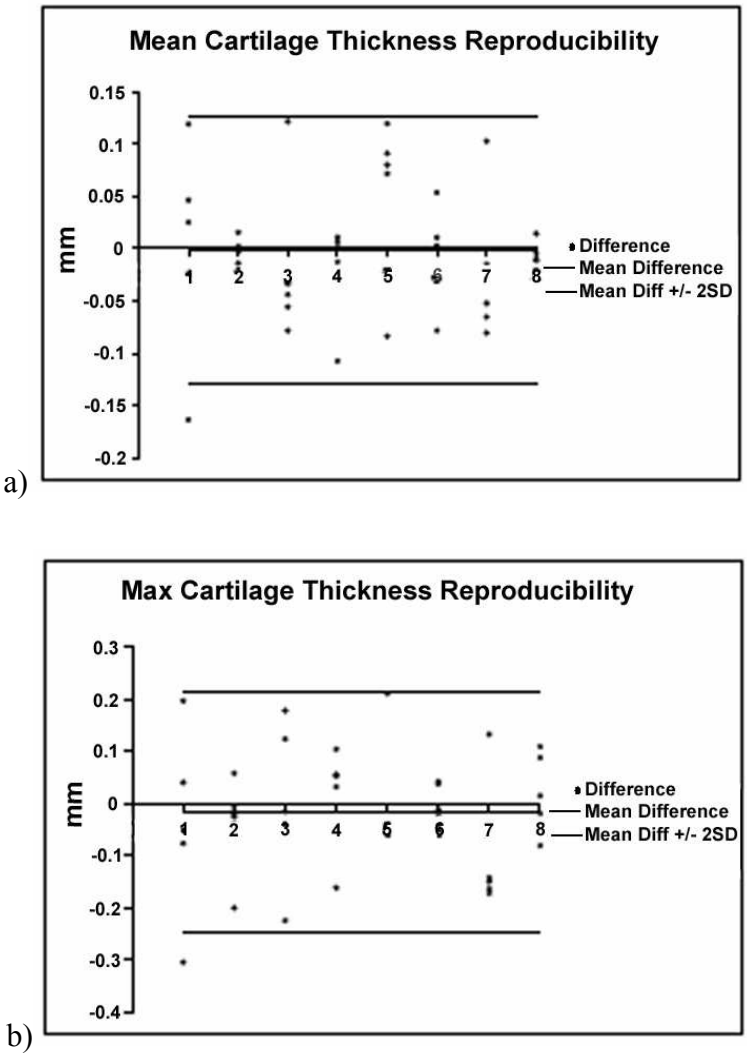

Figure 5.7 Bland-Altman plots of cartilage thickness measurement reproducibility.

5.6. Discussion

The Bland Altman plots from the reproducibility tests of the segmentation algorithm following repeated initialisations using different seed sphere sizes and positions clearly display that the approach is both reproducible and unbiased.

Traditional approaches to the problem of cartilage segmentation, such as, manual segmentation(Cohen et al., 1999; Eckstein et al., 1994; Jonsson et al., 1992; Peterfy et al., 1994) , seed and region growing algorithms(Eckstein et al., 1998b; Haubner et al., 1997; Losch et al., 1997), b-splines(Cohen et al., 1999) and b-spline snakes(Al Ali et al., 2002; Graichen et al., 2000) are not suitable for clinical use as they are slow, labour intensive and potentially prone to error. The 3D graph searching method used in this study has been shown to be fully automated, fast, accurate and reproducible.

A drawback of the algorithm described is the need to set the size and position of the seed sphere and the necessity to perform the pre-segmentation step. However in the algorithms current format this is essential to ensure the algorithm produces good accurate results; moreover, even when this step is included the whole process is significantly faster and less labour intensive than earlier methods. Additionally, further work is required to optimise the system for use in other joints such as the hip and shoulder and to develop a user interface that is widely acceptable and easy for clinicians to use.

Over the past decade a number of surgical interventions have been developed in an attempt to produce a durable cartilage repair(Brittberg et al., 1994; Hangody et al., 1998; Minas and Nehrer, 1997). In parallel there have been considerable advances in anatomical and functional MRI, such that MRI can provide information regarding the biochemical and biomechanical status of articular cartilage, including the glycosaminoglycan content and collagen organisation(Bashir et al., 1997; Mosher et al., 2000; Nieminen et al., 2004; Trattnig et al., 1999). However, until now accurate 3D visualisation and objective measurement of articular cartilage properties, in a clinically useable timeframe, at injury sites and the properties of repair/graft sites has not been

possible. The ability to combine these new functional techniques with the reported algorithm offers a potentially powerful set of tools for pre-operative assessment of cartilage injuries sites as well as the post operative monitoring of patients undergoing cartilage repair and restorative therapies. This area holds a lot of promise for cartilage repair surgery planning; with on going work to co-register biochemical and biomechanical sequences, such as dGEMRIC, with high resolution 3D sequences.

5.7. Conclusions

This study evaluates the feasibility with regard to accuracy and reproducibility of a fully automated 3D multi-surface segmentation algorithm on cartilage sensitive MRI images. The results indicate that both the pre-segmentation steps and the final segmentation process are fast, accurate and reproducible.

The reported 3D approach addresses a number of the existing challenges in articular cartilage segmentation and quantification; what is more this approach carries substantial promise for the future utility for automated quantitative 3D analysis of articular cartilage in a clinical setting.

Chapter 6. Ankle joint contact area measurement study

6.1. Introduction

Knowledge of the joint contact area under physiological loads and throughout the range of motion is essential for understanding the biomechanics of the ankle joint, furthermore it is beneficial for understanding the pathogenesis of joint degeneration as well as improving prosthetic design and ligament reconstruction surgery**.** Importantly, cartilage restoration and repair therapies, such as mosaicoplasty and autologous chondrocyte implantation (ACI), are becoming more common for talar articular cartilage lesions(Hangody et al., 2001; Hangody, 2003; Mandelbaum et al., 2003; Whittaker et al., 2005). Lesions occurring on the talus that are amenable to surgical treatment commonly occur over the anterior-laterally or posterior-medial talar shoulders(O'Farrell and Costello, 1982); therefore the joint contact characteristics in these regions under different loading conditions are of particular interest.

As highlighted in section 1.7 there have been several reported experimental studies of ankle joint contact characteristics with wide variations in methodology and loading conditions resulting in varying reports of the extent and location of the contact area(Calhoun et al., 1994; Corazza et al., 2005; Driscoll et al., 1994; Greenwald et al., 1977; Kimizuka et al., 1980; Kura et al., 1998; Macko et al., 1991; Yao and Seedhom, 1991).

The most common approach to measuring ankle joint contact area has been Fuji film. Calhoun *et al*(Calhoun et al., 1994) and Driscoll *et al*(Driscoll et al., 1994) used Fuji film and reported that the contact area of the ankle joint was located over the central region of the talar dome; Kimizuka *et al.*(Kimizuka et al., 1980) reported a similar distribution from silicone rubber mouldings. In contrast, studies using reversible staining(Greenwald et al., 1977) and roentgen stereophotography combined with a 3-D

digitiser(Corazza et al., 2005) reported the ankle joint contact area to be located over the lateral and medial margins of the talus.

There has been considerable variation in parameters during joint contact area tests, most notable has been variation in the joint load magnitudes ranging from to 490N to 3200 N(Calhoun et al., 1994; Yao and Seedhom, 1993) and variation in the joint loading positions(Calhoun et al., 1994; Christensen et al., 1994; Kimizuka et al., 1980) these factors have substantially influenced the results previously reported. However, these earlier studies have not assessed the joint contact area under load at the extremes of ankle movement where injury may be more likely to occur.

The specific objectives of this study were first to measure the joint contact area in intact ankle joints under a physiological load in a variety of positions including neutral and the extremes of dorsiflexion, supination, pronation and plantar flexion. Second, to describe the distribution of the contact area across the joint surfaces and last, to demonstrate a technique which allows analysis of the entire ankle joint surface with greater accuracy and fewer limitations than other techniques.

6.2. Materials & methods

6.2.1. Ethical approval

Ethical approval for each of the sets of experiments reported in this thesis study was provided by the University of Virginia institutional review board and human usage review panel. All the experimental components of my research were performed at the University of Virginia, Charlottesville, VA, USA; therefore, all human cadaveric specimens used in the studies presented in this thesis were acquired in accordance with Virginia state law and US federal laws.

6.2.2. Specimen preparation

10 lower leg specimens (6 right and 4 left legs) were obtained from 9 fresh frozen cadavers, mean age 64.6 years (6 male, 3 female). From the available medical histories there were no reports of trauma to the lower limbs or musculoskeletal disease in the ankle(s) of the subjects. The specimens were stored at -25ºC; prior to testing each specimen was allowed to thaw at room temperature for 24 hours. A normal range of movement and ligamentous stability were confirmed by physical examination prior to testing.

Each lower leg specimen was transected approximately 20 cm proximal to the ankle joint. The soft tissues were stripped from the proximal tibia and fibula and the two bones were then rigidly fixed into a potting cup using a fast setting resin (R1 Fastcast, Goldenwest manufacturing inc. CA, USA) with the leg in an anatomically neutral position.

Two Steinmann pins were inserted into the tibia approximately 1 cm proximal to the joint line, via minimal incisions, a further two pins were inserted into each of the talar neck and the distal fibula. 45º bevelled frames with mounted photo targets were then rigidly fixed to Steinmann pins using polymethylmetharcrylate (PMMA). The range of movement was once again examined to ensure that the reference frames did not come into contact with each other or impinge the range of motion at the ankle joint. The foot was then rigidly mounted to a foot plate using three screws into the calcaneous, one screw into the distal part of the first metatarsal, and taping across the forefoot, figure 6.1

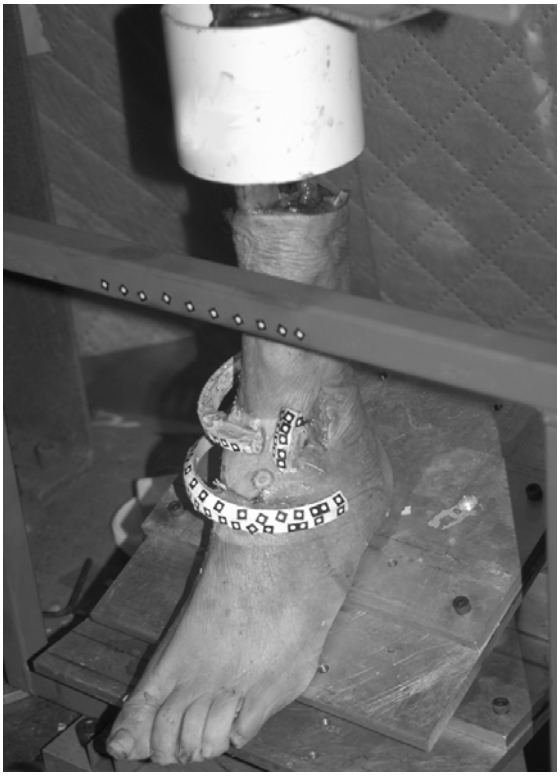

Figure 6.1 A lower leg specimen mounted in the test rig in 20˚ plantarflexion.

Bevelled frames with the mounted photo targets are rigidly attached to each of the bones. The foot is rigidly attached to the foot plate by screws in the calcaneus the first metatarsal Additionally, the forefoot was tapped to the foot plate prior to the application of load.

6.2.3. Specimen Loading

In the next step the foot plate was rigidly fixed to the base of the test fixture. The actuator of the hydraulic materials testing machine (Tinius Olson, USA) was lowered and the base of the potting cup was positioned flat against the actuator plate. This configuration ensured that the axial compressive load was applied along the vertical axis of the tibia and fibula. For testing in positions other than neutral, a 20º angled aluminium block was incorporated between the foot plate and the base of the test rig, figure 6.1

Each ankle was tested in five positions: neutral, 20º plantar flexion, 20º supination, 20º pronation, and 20º dorsiflexion which reflect the more extreme ends of movement. The

specimen was steadily loaded over 3 minutes to a peak load of 1000N, the actuator was then held in a stationary position, for approximately 20 secs whilst the photo targets were imaged using the stereophotogrammatric system. The load was then released and the specimen was repositioned. The process was repeated for each of the joint positions studied.

6.2.4. Modification of the Stereophotography Technique

At peak load the photo targets were imaged and formed the spatial co-ordinate frame for the subsequent registration of the tibia, talus and fibula surfaces together. Once the loading studies were completed the ankle joint was disarticulated and the joint surfaces were examined for signs of surface fibrillation or degeneration using the India ink technique. Each articular surface was then imaged relative to the photo targets rigidly fixed to the relevant bone, using the ATOS™ system.

The surfaces of the three ankle bones were then realigned into the positions assumed in each of the joint loading configurations. This was performed using software incorporated into the ATOS™ system. First the photo targets associated with an individual cartilage surface were identified and then the same photo targets in the loaded configuration were identified. An automated transformation to position the photo targets and the associated surface into the loaded joint position was performed and the point cloud data was saved. The procedure was performed for each bone hence, providing the relative positions of the joint surfaces when under load. The procedure was repeated for each of the five joint positions evaluated.

6.2.5. Post Processing Technique

The force applied to the cartilage layers during the loading phase causes cartilage deformation to occur; however, the force is then removed, the ankle joint is disarticulated and the joint surfaces are independently imaged with the stereophotography system in the undeformed state. When the undeformed surfaces of the talus, tibia and fibula are transformed into the common co-ordinate system formed

by the photo targets in the loaded state the undeformed cartilage surfaces overlap. This overlapping region is a good approximation of the true contact area according to the Winkler elastic foundation model (Johnson, 1985). However, determining the overlapping regions is not straightforward since the surfaces are not closed, so heuristics must be applied to decide which part of the surface should be considered in contact (i.e., overlapping) with the opposite surface.

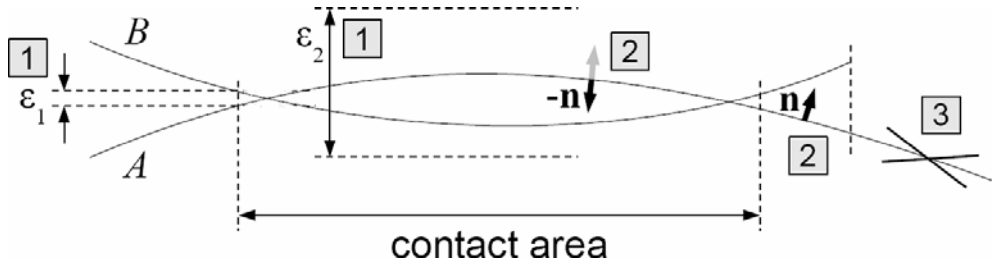

Figure 6.2 Contact area post processing steps.

1) Values of ε_1 and ε_2 are set to allow for the surface uncertainty and the maximum deformation; 2) the direction from one surface to the other is determined, which is the surface normal vector (n) in non-overlapping regions and (-n) in overlapping regions; 3) Regions of the surface extending beyond the border of the opposing surface are excluded.

We define two constants ε_1 and ε_2 and treat all triangles on mesh *A* with a distance of less than ε_1 from the corresponding triangle on the opposite mesh *B* as part of the contact area. Moreover, overlapping regions are considered in contact for distances up to ε_2 to account for a certain amount of deformation, figure 6.2. We set $\varepsilon_1 > 0$ since in the deformed state a greater area of cartilage will be in contact with its opposing surface than compared to the overlap of undeformed surfaces; furthermore ε_1 allows for a small amount of uncertainty in the surface due to the surface preparation. To ensure that only valid solutions are yielded, and erroneous results at the peripheries of the joint surfaces are avoided, the value of ε_2 should not exceed the maximum expected value of overlap. The values of ε_2 may theoretically be up to the combined cartilage thickness of the opposing surfaces. For this study the parameters are set as ε_1=0.03mm and ε_2=1mm. To distinguish overlapping and non-overlapping regions, the surface normal vector **n** is examined. In the non-overlapping case, **n** points towards the opposite surface, while the opposite surface is found in the negative direction **-n** in the overlapping case, figure 6.2.

Finally, to make the processing more efficient regions that extend beyond the opposite surface's border and therefore cannot be in contact with each other are disregarded, as previously described(Millington et al., 2007b), figure 6.2.

Since the surface areas and contact areas are measured from the triangulated mesh, created from the point cloud data, noise in the vertex locations could result in local variations in the surface normals which may subsequently increase the size of the measured area. While this effect is small for any given vertex the cumulative effect across the total surface area or joint contact area maybe considerable; however the area error is small if the vertex displacement is small compared to the triangle edge length. To assess whether vertex location noise produced a marked effect on the joint contact area measurement the change in joint contact area following consecutive iterations of a previously described denoising method(Fleishman et al., 2003) was assessed

6.3. Results

The results of multiple iterations of the denoising method show that the contact area error due to vertex location noise is negligibly low; therefore mesh denoising was not used for the purposes of these tests, table 6.1.

Number of iterations	% Reduction of total surface area	Normalised contact area (%)
0	-	39.86
1	0.23	39.83
2	0.30	39.83
3	0.36	39.84
4	0.40	39.82
5	0.44	39.83

Table 6.1 Impact of the denoising algorithm on surface area and normalised contact area measurements.

The effect of noise reduction on surface area and normalised contact area measurements for consecutive iterations of the noise reduction algorithm. Reductions in total surface area a reported relative to the initial mesh.

The absolute size of the joint surface area for each bone, the talo-tibia joint contact area, talo-fibula contact area and total joint contact area were calculated for each joint position. In order to compensate for variations in the size of the joint contact area caused by differences in the size of the limbs of the specimen donors the normalised joint contact area was also calculated.

The joint surface area measurements are shown in table 6.2. The mean talo-tibia contact area was greatest in dorsiflexion 7.34 cm^2 ± 1.69 cm^2 and was significantly larger than in plantar flexion ($P < 0.05$) which showed the smallest joint contact area 4.39 cm^2 ± 1.41 cm^2. When considering the talo-fibula contact area, the maximum joint contact occurred in dorsiflexion, 2.02 cm^2 ± 0.78 cm^2, and the minimum joint contact area occurred in pronation, 0.77 cm^2 ± 0.49 cm^2, respectively ($P<0.05$). Mean total talar, tibia and fibula contact areas for the different loading positions are shown in figure 6.3. The total talar contact area in dorsiflexion and neutral were both significantly larger than the total contact area in plantarflexion, $P < 0.005$ and $P < 0.05$, respectively. Furthermore, the total contact area in dorsiflexion was significantly larger than in pronation, $P < 0.05$.

Bone	**Mean surface area, cm^2**	**Standard deviation, cm^2**	**Minimum surface area, cm^2**	**Maximum surface area, cm^2**
Talus	20.0	2.3	16.3	24.1
Tibia	10.4	1.2	8.7	12.8
Fibula	3.0	0.5	2.4	4.0

Table 6.2 Absolute joint surface area measurements

Mean, standard deviation and range of joint surface areas for each bone in the ankle joint, N=10

The joint contact area for each measurement was normalised to the joint surface area appropriate bone i.e. the talus, tibia or fibula of the respective specimen. The mean normalised total talar, tibia and fibula contact areas for the different loading positions are shown in figure 6.4. The normalised plantarflexion contact area was significantly smaller than in dorsiflexion, $P < 005$, neutral, $P< 0.05$ and supination, $P < 0.05$. The

normalised dorsiflexion contact area was also significantly greater than in pronation, P< 0.05.

The results show that as the ankle joint rotated in the sagittal plane and moved from plantar flexion to dorsiflexion the tibio-talar normalised contact area increased by 15.74% ± 7.95%; whereas, when the ankle rotated in the coronal plane moving from pronation to supination the tibio-talar normalised contact area increased by only 5.02% ± 6.86%

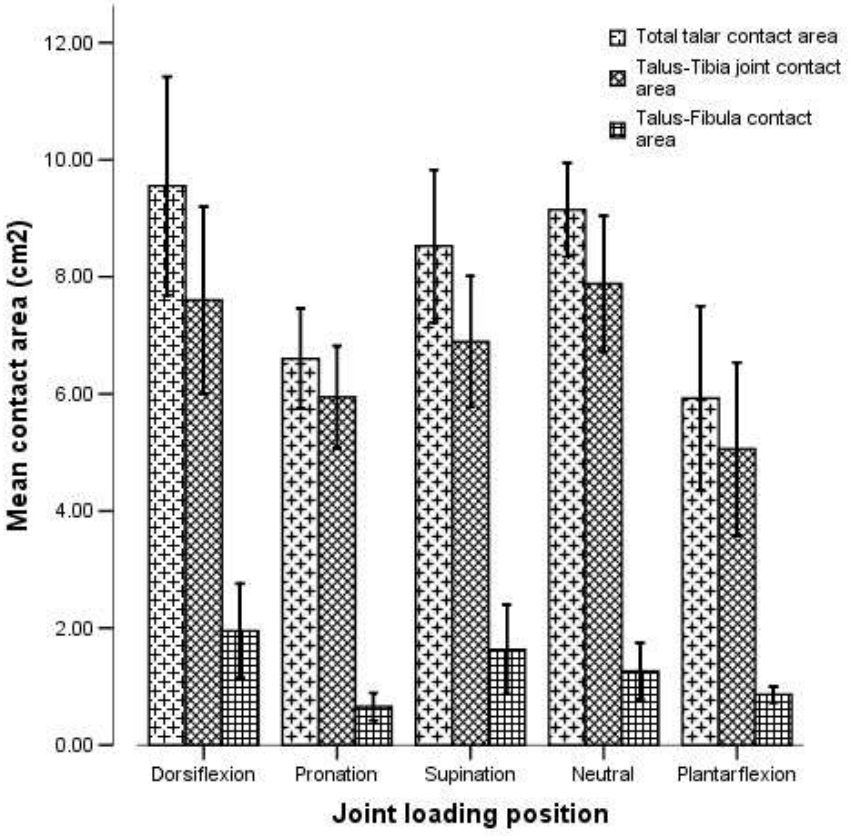

Figure 6.3 Bar chart of the mean joint contact area (cm^2)

The mean joint contact area (cm^2) over the surface of each of the talus, tibia and fibula in the five different loading positions tested. Error bars represent ± 1 S.D.

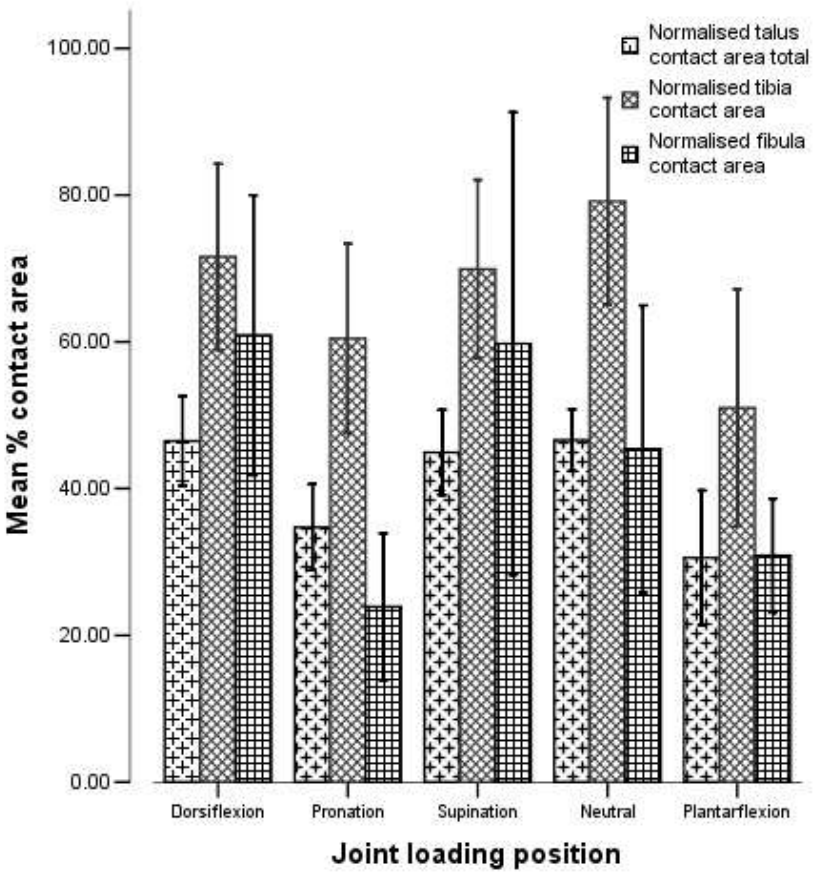

Figure 6.4 Bar chart of mean normalised joint contact area.

Mean normalised joint contact area over the surface of the talus, tibia and fibula in each of the five loading positions tested. Error bars represent ± 1 S.D.

Characteristic patterns of joint contact were seen in each of the respective loading positions; typical examples of the shape and location of the joint contact area in each of the five positions tested are shown in figure 6.5 Notable features are the broad contact area in dorsiflexion distributed over the especially over the medial and lateral talar shoulders. However, in 20˚ plantarflexion the contact area on the tibia is narrower and more centrally located as the talus is narrower posteriorly. When the limbs were loaded in supination typically the area where the greatest overlap of the surfaces and therefore the region of greatest deformation under load occurred at the site where the medial talar shoulder contacts the tibial plafond. In supination the contact area was more medially located than in neutral or pronation, figure 6.5. In contrast the region of maximum

cartilage surface overlap in pronation occurred at the site corresponding to the contact between the lateral talar shoulder and the tibial plafond. The region of contact in eversion was clearly more laterally located than in neutral loading, figure 6.5.

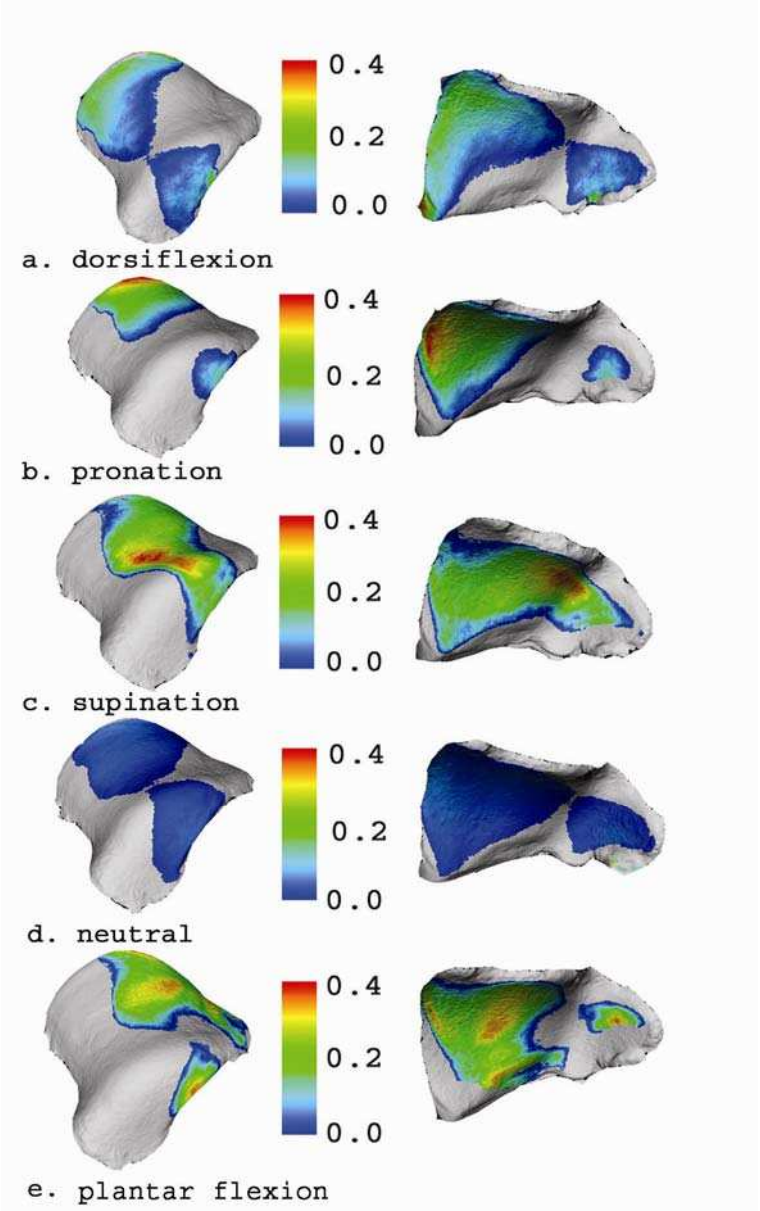

Figure 6.5 Typical talar-tibia joint contact distribution patterns.

Representative examples of talar-tibia joint contact distribution patterns displayed on the talar and tibial surfaces in each of the five loading positions tested. a) dorsiflexion, b) pronation, c) supination, d) neutral and e) plantarflexion. Colour coding shows the extent of overlap, in mm, of the surfaces in the loaded position indicating the areas of greatest cartilage deformation

The contact pattern between the talus and fibula displayed a relatively consistent pattern; there was noticeable difference, as anticipated, between pronation and supination. Under loading in 20º of supination the contact area occurred over the proximal part of the fibula surface, mainly centrally and anteriorly, figure 6.6. The corresponding contact on the talar surface over the anterior superior aspect of the lateral talar facet, figure 6.6. When the specimens were loaded in the pronated position the contact area was distributed over the inferior part of the fibula surface where it has a valgus angulation figure 6.7. The corresponding contact area on the talar surface occurred slightly posteriorly over the distal valgus angulated part of the lateral talar facet, figure 6.7.

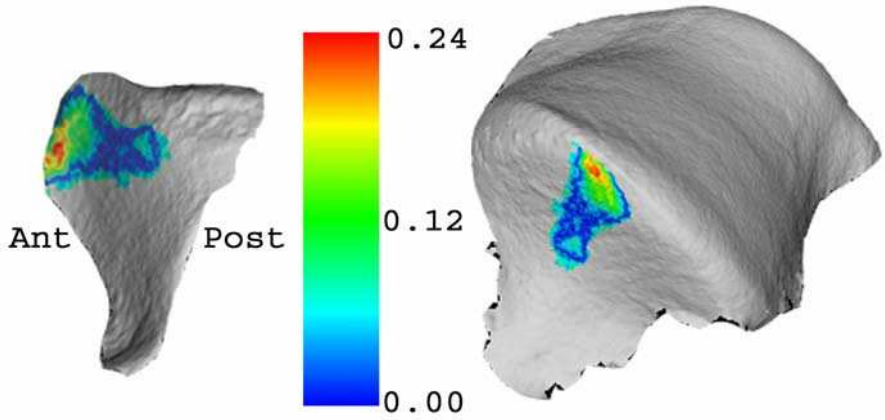

Figure 6.6 Talo-fibula contact distribution in 20˚ supination.

Characteristic joint contact distribution pattern between the talus and fibula in 20˚ supination displayed on the talar and fibula surfaces.

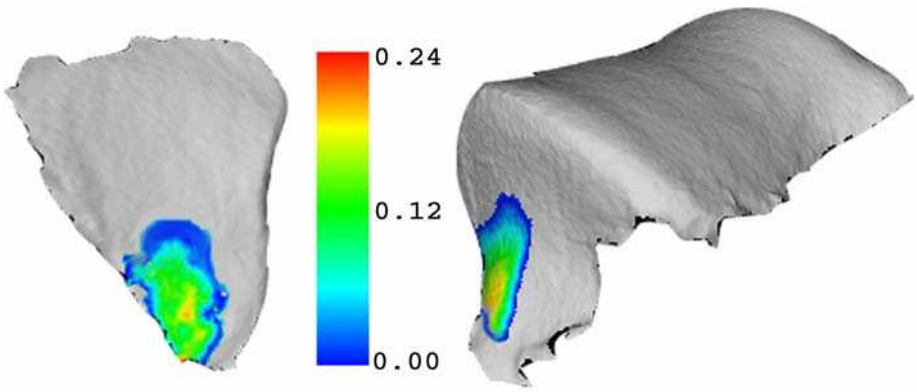

Figure 6.7 Talo-fibula contact distribution in 20˚ pronation.

A representative example of the joint contact between the talus and fibula in 20˚ pronation, displayed on the talar and fibula surfaces

6.4. Discussion

In this study a modification of the stereophotogrammetric technique, previously used to determine cartilage thickness and distribution, is reported for measuring and describing joint contact area in the ankle joint. The objective of the study was to quantitatively evaluate the joint contact area under loading in different joint positions and to describe the joint contact area distribution across the joint surfaces in neutral, dorsiflexion, plantarflexion, pronation and supination. The system allows rapid acquisition and processing of large volumes of geometric data with high measurement accuracy (± 2 μm). The versatility and accuracy of the technique has enabled us to study the joint contact characteristics of the highly congruent ankle joint without having to disrupt the joint integrity prior to the loading phase

The results show that the largest talo-tibia and talo-fibula contact area occurred in dorsiflexion, 7.34 cm^2 ± 1.69 cm^2 and 2.02 cm^2 ± 0.78 cm^2, respectively. The smallest talo-tibia contact area occurred in plantarflexion, 4.39 cm^2 ± 1.41 cm^2 and the smallest talo-fibula contact area occurred in pronation, 0.77 cm^2 ± 0.49 cm^2; both are significantly smaller than in dorsiflexion ($P < 0.05$)

Direct comparison to earlier studies is difficult due to the variety of load magnitudes and joint positions used. The mean normalised total talar contact area was considerably higher than in the study by Calhoun *et al*(Calhoun et al., 1994) who reported the maximum normalised contact as 15% at 10º dorsiflexion. Moreover the total talar contact area measured in this study exceeds values reported using the '3S technique'(Yao and Seedhom, 1991) and Fuji film(Christensen et al., 1994). Unfortunately the earlier techniques have a limited ability to accurately measure the contact area over a surface with a complex 3D topography; where as the stereophotography approach allows easy evaluation of the entire surface and measurement of surface and contact areas by triangulation.

In comparison to the knee joint the total talar contact area is greater than that seen in the patello-femoral joint(Gold et al., 2004; Nakagawa et al., 2003; Patel et al., 2003), but smaller than in the tibio-femoral joint(Fukubayashi and Kurosawa, 1980; Kurosawa et al., 1980); however, the differences are not so pronounced as previously believed.

In pronation it was found that the mean talo-fibula contact area was significantly smaller than in dorsiflexion. In contrast to earlier studies(Calhoun et al., 1994; Kura et al., 1998) the talo-fibula contact area in pronation was smaller than in supination; however, the difference was not statistically significant. This was an unexpected finding, but is explained by examining the distribution pattern of the talo-fibula contact area over the joint surfaces. When the ankle joint is loaded in pronation the fibula tip comes into contact with the distal angulated section of the lateral talar facet which forces the distal fibula more laterally. This results in a small localised contact between the distal part of the fibula surface and the distal part of the lateral talar facet, figure 6.7. In supination the distal part of the lateral talar facet assumes a more vertical orientation, this combined with the compressive load and the ligamentotaxis pulling the fibula inferiorly result in a larger contact area between the lateral talar shoulder region and the broader proximal part of the fibula joint surface, figure 6.6

The regions where the greatest surface overlap were measured, corresponding to the regions where the greatest cartilage deformation occurred and therefore presumably the

greatest load transfer, correspond to the shoulders of the talar cartilage. This is interesting as the cartilage thickness and the subchondral bone mineral density are highest over the talar shoulders(Millington et al., 2007b; Millington et al., 2007c; Muller-Gerbl and Putz, 1995) and these findings may be a response to the prevailing mechanical conditions occurring in the ankle joint.

The distribution of the contact area over the joint surfaces seen in this study support the finding of earlier studies using roentgen stereophotography and reversible staining(Corazza et al., 2005) and reversible staining(Greenwald et al., 1977) which indicated that joint contact was predominantly over the margins of the talar dome. However, our results differ from studies which required the insertion of Fuji film into the joint space and reported that the contact area to be over the central talar dome(Calhoun et al., 1994; Driscoll et al., 1994; Kimizuka et al., 1980). Fuji film studies of highly curved and congruent joints must be interpreted with caution as the Fuji film itself can alter the joint mechanics and is prone to crinkling in highly curved areas, such as the talar shoulders.

It is important to bear in mind that in this study, as in many of the earlier studies, the fixation of the foot and the tibia constrain movements in particular rotation of the tibia which occurs during dorsiflexion and plantar flexion in the gait cycle(Mann, 1993). This restriction of rotation could have prevented the ankle joint from obtaining maximal congruence in dorsiflexion and plantar flexion; hence, the joint contact area reported my still be an under estimation of the in vivo situation.

Given that cartilage surfaces deform in regions of contact it should be appreciated that the "true" *in vivo* contact area is not directly measured by this technique since a proximity analysis of the non-deformed surfaces is used to determine the joint contact area. However, by varying the surface proximity value which is considered to represent joint contact between zero and the maximum cartilage thickness it theoretically possible to determine the full range of possible contact areas. Additionally, the technique used in this study can only be used in vitro and it is important to appreciate that in cadaveric

experiments there is no muscle tension and the stiffness of ligamentous tissue is different from that of living people.

Despite these shortcomings, the reported stereophotogrammetric technique has the advantage that during the loading phase of the study no extensive dissection of the joint structures is required and no foreign material is inserted into the joint, which may alter the joint contact pattern. Moreover, the described method allows accurate 3-D reconstructions of the entire articular surface of each bone in the joint, facilitating joint contact analysis in highly curved regions and automating quantitative measurements. The versatility of the technique addresses many of the difficulties associated with previous methods used for measuring ankle joint contact area.

The in vitro method described in this study will be helpful for comparative studies and validation of loading devices and image analysis algorithms which are being developed for measuring joint contact area from MR images. In future it will be particularly interesting to remove the constraints on tibial rotation during loading and assess the effect on contact area. Furthermore, it will be interesting to assess sex differences as it has been show there are differences in the bone sizes and radii of curvature between men and women, with a greater potential for adduction in women(Ferrari et al., 2004); unfortunately this was not possible in this study due to the small numbers of specimens and is beyond the scope of this thesis. Importantly this method provides useful input data for computational models of the ankle joint which facilitate in depth analysis of joint biomechanics.

6.5. Conclusions

This study has demonstrated a modification of the high resolution stereophotographic technique reported in Chapter 3, that does not violate the joint structures or require insertion of foreign material into the joint during loading and allows analysis of the entire ankle joint surface. The finding of the study show that the largest contact area occurred in dorsiflexion, the smallest contact area occurred in plantarflexion, but in all cases the contact area appears to be larger than previously reported. Furthermore, the

contact distribution was located more over the talar shoulders where the cartilage is thickest, see Chapter 3 and Chapter 4(Millington et al., 2007b; Millington et al., 2007c) the subchondral bone most dense and OCD lesions most commonly occur(O'Farrell and Costello, 1982) as opposed to contact over the centre of the talar dome and tibial plafond as reported in some earlier studies.

Chapter 7. General discussion

The impetus to undertake the research presented in this thesis came from a series of high rate forced dorsiflexion tests of cadaveric ankle joints to evaluate fracture tolerance(Rudd et al., 2004). In a number of the ankles tested articular cartilage surface injuries were seen in the absence of a fracture. As a result it was decided that it would be interesting and beneficial to assess and validate methods which would allow in vivo assessment and quantification of ankle articular cartilage using MRI. Additionally, it was felt that an evaluation of ankle joint contact area would offer insights which would improve our current understanding of joint contact characteristics.

This thesis has sought to characterise the geometrical and joint contact properties of the articular cartilage layers of the ankle joint in order to further our understanding of ankle mechanics and ankle cartilage injuries. There has been a particular emphasis on the development and testing of methods forming the basis for in vivo quantification of articular cartilage parameters using magnetic resonance imaging and image analysis.

More specifically the research presented in this thesis aimed to 1) Describe and test a high resolution stereophotogrammetry system for quantifying the geometric parameters of the ankle articular cartilage layers in vitro which can be used as an independent standard to validate in vivo techniques. 2) Illustrate the topographical distribution of articular cartilage across the surface of the talus, tibia and fibula. 3) Test and validate image processing algorithms on high resolution cartilage sensitive MR images which can be used for in vivo quantification of articular cartilage parameters and 4) Quantify the ankle joint contact area under compressive load throughout the range of movement using a stereophotogrammetric system which does not require introduction of material, such as Fuji film, into the joint during the loading process.

Chapter 3 reports the use of a highly accurate stereophotography system for making morphometric measurements of ankle articular cartilage; chapter 4 used a 2-D semi-automated dGVF snake segmentation algorithm on cartilage sensitive MR images in

order to make similar morphometric measurements. In both studies 3-D thickness distribution maps were generated.

The stereophotography results showed the mean thickness of the talar and tibial cartilage to be 1.1 ± 0.18 mm and 1.16 ± 0.14 mm, respectively; whilst the maximum talar and tibial cartilage thickness was 2.38 ± 0.4 and 2.18 ± 0.19, respectively. Segmentation of the MRI data sets using the 2-D semi-automated dGVF snake algorithm measured the mean thickness of the talar and tibial cartilage as 1.34 ± 0.14 mm and 1.21 ± .014, respectively; the maximum thickness of the talar and tibial cartilage was 2.67 ± 0.25 mm and 2.44 ± 0.58 mm, respectively. The average MRI based mean and maximum thickness measurements were greater than those made using the stereophotography method, but the difference is not statistically significant, additionally the differences were sub-voxel in size. The results of both studies, in particular the MRI segmentation study results, represent the upper part of the range of results reported in the literature(Adam et al., 1998a; Al Ali et al., 2002; Athanasiou et al., 1995; Shepherd and Seedhom, 1999; Tan et al., 1996). However, these earlier studies did not examine the entire cartilage surface and notably excluded the highly curved regions which the studies in this thesis have identified as the regions of greatest thickness.

Thickness distribution maps generated using both stereophotography and MRI segmentation, consistently showed the maximum sites of cartilage thickness on the talus occurring over the talar shoulders where as in the tibia the maximum thickness was along the anterior border and in the region between the tibial plafond and the medial malleolus. These finding correlate with the sites identified as having the highest density subchondral bone(Muller-Gerbl and Putz, 1995), the most common site of OCD lesions in the ankle joint(O'Farrell and Costello, 1982) and being major joint contact regions(Millington et al., 2007a). A number of earlier studies indicated that the greatest cartilage thickness occurs over the centre of the talar dome(Adam et al., 1998a; Athanasiou et al., 1995; Shepherd and Seedhom, 1999), but these studies did not analyse the highly curved regions of the ankle joint bones.

General discussion

With regard to the reproducibility of the MRI segmentation algorithms both the 2-D semi-automated dGVF snake algorithm and the 3-D graph search algorithm have been show to be very reproducible and unbiased. Specifically, the 2-D algorithm has demonstrated coefficients of variation approaching those achieved in studies of knee articular cartilage(Eckstein et al., 1998b; Hyhlik-Durr et al., 2000; Kshirsagar et al., 1998; Peterfy et al., 1994; Stammberger et al., 1999a) which is thicker and less challenging to segment than ankle cartilage.

The measurements of ankle joint contact area reported in chapter 6 follow a similar pattern to previous studies when considering contact area with respect to joint position(Calhoun et al., 1994; Corazza et al., 2005; Driscoll et al., 1994). Tibio-talar contact area was largest in dorsiflexion and smallest in plantar flexion; however, direct comparison with previous studies is difficult due to the variety of load magnitudes, joint positions and methods for reporting the measurements. Nonetheless the contact areas measured appear to be larger than previously reported in each of the joint position studied. The existing literature provides a spectrum of opinion in relation to the distribution of the joint contact area, some studies report the contact area to be located over the central talar dome(Calhoun et al., 1994; Driscoll et al., 1994; Kimizuka et al., 1980), where as others report the contact area to be mainly over the medial and lateral margins of the talus(Corazza et al., 2005; Greenwald et al., 1977). The reported stereophotographic method for measuring joint contact area supports the finding of the latter studies, indicating that the major regions of joint contact area occur over the edges and shoulders of the talar dome. As highlighted earlier the distribution corresponds to the regions with the highest subchondral bone density(Muller-Gerbl and Putz, 1995) and greatest cartilage thickness(Millington et al., 2007b; Millington et al., 2007c) which may be a reflection of prevailing mechanical conditions in the ankle joint.

During the course of this research a number of novel techniques and solutions to problems have been developed which have useful applications within the fields of articular cartilage, ankle biomechanics and image analysis research.

General discussion

The stereophotography based experiments represent a modification of techniques used in many industrial processes (http://www.gom.com); therefore the approaches described in Chapters 3 and 6 benefit from the availability of commercially available systems which are extremely versatile and highly accurate (www.capture3d.com). An important benefit of using this approach is that it allows a full geometric assessment of the entire joint surface and the subchondral bone and a full set of morphological measurements, which is not possible with many previously described techniques. The versatility and accuracy of the approach means it can be used as a gold standard against which to compare MRI. Furthermore, the format in which the data is acquired is easily exportable and can be converted to other standard formats for use with other software.

The anisotropic diffusion, noise reduction algorithm used in the 2-D semi automated segmentation process is an important step in the area of articular cartilage segmentation. Previously the low SNR achieved with high resolution isotropic MRI data meant that they were considered unsuitable for segmentation and quantitative measurement(Al Ali et al., 2002). Therefore, larger voxel sizes were used to improve SNR, but this potentially sacrifices the accuracy and increases the error in quantitative measurements made from the data. By using an anisotropic diffusion noise reduction algorithm the image quality can be enhanced without losing the anatomical features of the cartilage layers, so allowing successful segmentation of high resolution isotropic image data sets. The ability to use these higher resolution isotropic data sets potentially reduces error in quantitative measurements and means that partial volume effects are smaller and 3-D multi-planar reconstructions can be properly utilised.

The image analysis algorithms used in chapters 4 & 5, provide progressive steps in automation of the cartilage segmentation process. Notably, these algorithms function in thin articular cartilage layers, even in congruent joints with extensive cartilage to cartilage contact. Additionally; the 2-D semi-automated algorithm, in particular, has enhanced the reproducibility of cartilage segmentation, the fully automated 3-D approach has the possibility to further improve reproducibility by reducing the variability associated with user input.

Whilst appreciating the benefits of the methods and results reported it is important to acknowledge the limitations of the techniques used and the results obtained in these studies. The limitations of the individual studies have been discussed in each of the relevant chapters, but are summarised here.

The stereophotography based techniques for studying ankle cartilage geometry and ankle joint contact area can, unfortunately, only be used in vitro as they ultimately require disarticulation of the joint in order to make morphometric measurements of cartilage volume etc. require the cartilage to be dissolved to reveal the subchondral bone. A generally limiting feature restricting the wider use of this technique is the considerable expense of high spec commercial stereophotography systems, or the need to collaborate with experts in the field who are capable of building a customised individual system as well as performing the programming required to calibrate the system and handle the data processing. The technique described for imaging the surface requires that they be prepared with a fine white powder and it is extremely difficult to exactly quantify the effects this has on the true measurements, but it is believed to be negligible, and since both the cartilage and bone are treated in the same fashion the effects on thickness measurements should be negated. This could potentially be avoided by using a laser scanning system which does not require routine surface preparation, but laser scanners may suffer from scatter on “glistening” surfaces. A potentially greater problem may result if delays occur in the experimental process as the cartilage layer may become dehydrated, despite protective measures, so altering quantitative measurements.

A notable drawback of the work presented in this thesis is the lack of spatial registration of the stereophotography generated models of the cartilage layers and the MRI segmentation derived models. As a result it is has not been possible to determine surface positioning error for the segmentation lines, which would allow exact quantification of surface errors and identify regions in which the segmentation algorithms consistently perform well or poorly. However, the development of a suitable reliable, automated spatial registration algorithm is beyond the scope of this thesis, but is a major area of

interest for future developments, since such an algorithm will enhance studies of cartilage changes in patients over time which requires repeated longitudinal imaging.

With regard to the MRI image analysis based studies the imaging sequenced used is rather long, 17 mins 14 s; whilst being suitable for research purposes it is likely to be too long for routine clinical use. Nevertheless, being able to acquire high resolution isotropic image data that is suitable for segmentation is an important advance and with the continuing rapid development in MRI technology acquisition times will be significantly reduced.

Whilst isotropic data sets allow multi-planar reconstructions when using the 2-D semi-automated algorithm not all the image plane are suitable for complete segmentation and in the ankle joint it was only the coronal images which allowed full segmentation to be performed. Sagittal and axial films experience noticable partial volume effects at sites of marked curvature which make it impossible to perform complete, accurate segmentation. An additional limitation of the 2-D semi-automated approach is the need for high performance processors as well as the CPU required to run the Matlab™ based code and calculate the morphometric parameters from the reconstructions of the cartilage layers. This could potentially be improved by programming the algorithm in a different computer language. Furthermore, although the algorithm represents an improvement on earlier methods, it is still slow, tedious and, in challenging cases, rather labour intensive which limits its widespread usability. Hence, the pilot study in chapter 5 was performed in the hope of addressing some of these concerns.

The automated 3-D graph searching algorithm is an exciting advance in the field of cartilage image analysis, but it must be remembered that the work presented in chapter 5 is only a pilot study. Again, as with the 2-D semi-automated algorithm, the 3-D approach requires a computer with a high performance processor and considerable CPU in order to function appropriately. However, with further development and better optimisation of the algorithm parameters alongside to continuous improvements in computer technology, this is does not represent a significant obstacle. In its current format the algorithm parameters have only been optimised to the basic shape of the

ankle joint bones i.e. talus, tibia and fibula, therefore, unlike the 2-D dGVF snake algorithm, it is not immediately transferable for use in other joints such as the knee. Again, with further development work this limitation will be relatively straightforward to overcome. As only basic optimisation has been carried out so far the algorithm user must carefully select the position of the initialising seed spheres in order to ensure the algorithm functions correctly and this is further hampered as the program only has a rudimentary user interface which must be significantly enhanced before it will be suitable for widespread use.

The modified stereophotography technique used for the joint contact studies, in Chapter 6, is affected by many of the technical limitations previously highlighted. When considering the modification for the joint contact study a key point to realize is that the technique makes an indirect measurement of the joint contact area. Since the photo targets are imaged in the loaded position, when the articular cartilage is deformed due to load, the load is then removed, the joint disarticulated and the surfaces re-imaged in the non-deformed state; therefore, the contact area is determined indirectly from the area of surface overlap.

Specific limitations of the study reported in Chapter 6, as opposed to limitations of the stereophotographic technique, include: The fixation of the tibia, fibula and foot during loading which constrains the rotation of the bones that occurs during movement of the ankle joint and so may prevent the bones reaching maximal congruity leading to an underestimation of the true contact area. The absence of muscle tension or loading, which would occur in the in vivo situation, may subtly alter the relative position of the bones in a given foot position. These two points can be addressed relatively easily in future studies by modifying the test rig, using specimens with an intact knee joint and using mechanical pulley systems to tension relevant muscles.

One final general limitation of the studies presented in this thesis is the relatively small numbers of specimens used in the studies; however, this is a well established, longstanding problem in research of this nature due to the limited supply of suitable cadaveric specimens.

Each of the studies carried out for this thesis are interlinked as each represents a step in the process of developing and validating MRI based, non invasive, in vivo methods for objectively evaluating geometrical, biochemical and biomechanical properties of articular cartilage. The work presented here focuses on initial image analysis algorithm testing and the development of methods which may act as independent gold standards for validating MRI measurements.

The stereophotography based study, Chapter 3, provides baseline data with regard to ankle articular cartilage geometric parameters. This links to subsequent studies as the method allows validation of MRI image analysis algorithms since cadaveric specimens can be imaged and the segmentation data compared to stereophotographic reconstructions once they have been spatially registered.

The image analysis studies, Chapters 4 & 5, represent advances on previous methods used to segment articular cartilage in 3-D MR data sets. Validated 2-D segmentation allows quantitative in vivo assessment of articular cartilage and provides an essential stepping stone in the development of fully automated 3-D segmentation methods. The ability to accurately segment cartilage layers provides the possibility to longitudinally monitor geometric parameters and to create to 3-D reconstructions of cartilage layers which can enhance the clinical assessment of a cartilage lesion.

The joint contact area study in Chapter 6 is a novel modification of the method reported in Chapter 3 and has made it possible to study joint contact area without disrupting the joint prior to or during loading. It provides new information about the distribution of contact across the joint surfaces in the ankle which is useful for development of realistic computational models of the ankle for predictive studies. More importantly, the method offers an independent standard for the initial validation of MRI based measurements, which is vital in view of the development of MR compatible joint loading devices.

In summary each of the studies presented represents a small advance in the current knowledge. The cartilage thickness maps generated from stereophotography and MRI show that the maximum thickness occurs at the edges of the talar dome over the shoulders of the bone, helping to clarify the variable picture obtained from reviewing

earlier studies which were unable to accurately analyse highly curved regions. The image analysis methods applied and tested are a progression on previously reported 2-D segmentation methods. The combined noise reduction and 2-D semi automated approach demonstrated that it is possible to precisely segment high resolution isotropic MR images which have an SNR previously believed to be too low for segmentation purposes(Al Ali et al., 2002). The 3-D fully automated study is a further step in the field of cartilage image analysis and highlighted the unique potential of using an optimised graph searching algorithm for articular cartilage segmentation; it represents a significant step in the development of a clinically applicable suite of tools for analysing articular cartilage in vivo using MRI. Finally, by using a stereophotography based technique which allowed assessment of the entire joint surface without having to disrupt the joint before or joint loading, we have established that ankle joint contact area is notably larger than previously reported and that the major areas of contact correspond to the areas of thickest cartilage and most dense subchondral bone.

Chapter 8. Thesis conclusions

Ankle articular cartilage injuries can occur at sub-fracture load magnitude(Rudd et al., 2004) and may lead to subsequent joint degeneration. Articular cartilage repair and techniques to stimulate articular cartilage regeneration are extremely topical areas of research. However, there is little well defined experimental data on the 3-D topographical distribution and mechanical properties of the articular cartilage of the ankle. This knowledge is essential so that cartilage repair and/or regeneration techniques can be successfully implemented and monitored non-invasively in the ankle joint. The studies reported in this thesis represent a small step forward in our understanding of ankle cartilage geometry and the development of techniques for making accurate non-invasive quantitative measurements using MRI. Furthermore the data generated provides a baseline geometric dataset which can be used to enhance computational models of the ankle joint for studying ankle biomechanics and injury.

The experimental studies reported in this thesis have achieved the intended aims and provide information which helps to improve our current understanding of the geometry, cartilage thickness distribution and variation in contact area across the ankle joint.

A highly accurate stereophotography technique for acquiring geometric data and making quantitative measurements of thin articular cartilage has been described and applied to the ankle joint. A further modification of the stereophotography experimental technique has also been reported which allows measurement of ankle joint contact area under load in a number of positions without disrupting the joint before or during loading. These stereophotography methods provide an independent standard against which MRI measurements can subsequently be compared.

With regard to image analysis techniques for making MRI based measurements, the development and testing of a semi-automated 2-D directional gradient vector flow snake has been reported. Subsequent attempts have been made to increase the degree of automation and speed of the image segmentation process and pilot testing of a fully automated 3-D graph searching algorithm has been reported.

Thesis conclusions

In the stereophotography experiments reported in chapter 3 quantitative measurements of thin articular cartilage layers indicate that ankle cartilage is thicker than previously believed and the thickness distribution maps show that the thickest articular cartilage in the ankle occurs over the talar shoulders where cartilage lesions most commonly occur(O'Farrell and Costello, 1982). The accuracy of the stereophotographic technique means it may be used as an independent gold standard for validation of the accuracy of in vivo measurements in thin cartilage layers using MRI.

The 2-D semi-automated cartilage segmentation studies, in chapter 4, quantified the geometric parameters of the talar, tibial and fibula cartilage layers from non-invasive MRI scans of intact ankle joints. These studies showed that by using the dGVF snake segmentation algorithm combined with an anisotropic diffusion denoising algorithm it is possible to extract the cartilage layers more precisely than previously achieved(Al Ali et al., 2002) in the ankle joint. In keeping with the stereophotography studies in chapter 3 the mean and maximum thickness of each layer of ankle cartilage exceeded the measurements previously reported and the same characteristic cartilage thickness distribution was observed.

The image segmentation study reported in chapter 5 evaluates the feasibility with regard to accuracy and reproducibility of a fully automated 3D multi-surface segmentation algorithm on cartilage sensitive MRI images. The results indicate that both the pre-segmentation steps and the final segmentation process are fast, accurate and reproducible.

The reported 3D approach addresses a number of the existing challenges in articular cartilage segmentation and quantification; what is more, this approach carries substantial promise as a future utility for automated quantitative 3D analysis of articular cartilage in a clinical setting.

Finally, in Chapter 6, a modification of the high resolution stereophotographic technique reported earlier in Chapter 3, was developed and used to study ankle joint contact area across the entire joint surface in a variety of positions. The technique offers an advantage over other techniques in that it does not violate the joint structures or

require insertion of foreign material into the joint during loading. The results of the joint contact measurement experiments show that the largest contact area occurred in dorsiflexion whilst the smallest contact area occurred in plantarflexion. Importantly the study showed that in all joint positioins the contact area appears to be larger than previously reported. Furthermore, the contact distribution was located more extensively over the talar shoulders where the cartilage is thickest, see Chapter 3 and Chapter 4(Millington et al., 2007b; Millington et al., 2007c) and the subchondral bone most dense. This also coincides with the location where clinically most talar OCD lesions occur(O'Farrell and Costello, 1982) as opposed to contact over the centre of the talar dome and tibial plafond as reported in some earlier studies.

As with the results from the stereophotography experiments in Chapter 3, the results provide essential experimental data which again can be used to enhance computational models of the ankle joint which are used to study ankle joint injury, development of degenerative conditions such as post traumatic osteoarthritis, ankle biomechanics and potential effects of new therapies

Chapter 9. Future work

The research presented in this thesis shows the development of a series of new techniques and tools for analysing articular cartilage. Furthermore it has sought to answer a number of points regarding the cartilage distribution and joint contact characteristics of the ankle. By addressing these questions and through the development of new approaches a number of new and interesting research areas have been highlighted. The in vitro techniques reported in this thesis may be used for the future validation of in vivo techniques which are clinically useful. Moreover, the results of this thesis have helped to form the basis of a number of successful grant applications which will fund on going research into the following areas.

1. Further development of 3D automated segmentation
2. *In vivo* joint contact area measurement
3. Development of automated spatial registration tools
4. Evaluation of the NIH osteoarthritis initiative data set
5. Mechanical cartilage stiffness mapping
6. Validation of functional MRI measurements
7. Follow-up and monitoring of cartilage lesion and cartilage repair tissue
8. Pre-operative planning for autologous chondrocyte transplantation
9. Development and refinement of ankle finite element models

Appendix 1. Stereophotography study

OsteoArthritis and Cartilage (2007) **15**, 205–211

doi:10.1016/j.joca.2006.07.008

Osteoarthritis and Cartilage

International Cartilage Repair Society

OARSI OSTEOARTHRITIS RESEARCH SOCIETY INTERNATIONAL

Quantification of ankle articular cartilage topography and thickness using a high resolution stereophotography system

S. A. Millington B.M.B.S., M.R.C.S. (Ed.)†‡*, M. Grabner Ph.D.§, R. Wozelka Mag.§, D. D. Anderson Ph.D.‖, S. R. Hurwitz M.D.¶ and J. R. Crandall Ph.D.†

† *Center for Applied Biomechanics, The University of Virginia, Charlottesville, VA, USA*
‡ *Department of Traumatology, Medical University of Vienna, Austria*
§ *Department of Computer Graphics and Vision, Technical University of Graz, Austria*
‖ *Orthopaedic Biomechanics Laboratory, University of Iowa, Iowa City, IA, USA*
¶ *Department of Orthopaedic and Trauma Surgery, Foot and Ankle Division, The University of Virginia, Charlottesville, VA, USA*

Summary

Objective: To describe the topography and to measure thicknesses, surface areas and volumes in the cartilage layers of the ankle.

Methods: Twelve cadaveric ankle joints were disarticulated and the cartilage surfaces of each bone were imaged with a highly accurate (± 2 μm) stereophotography system (ATOS™). The cartilage was then dissolved and the subchondral bone imaged. The geometric data were then used to measure the quantitative parameters in each cartilage layer.

Results: The mean cartilage volume across the 12 specimens ranged from 0.32 ± 0.08 ml for the fibula to 2.44 ± 0.48 ml for the talus. The mean thickness of both the talar (1.1 ± 0.18 mm) and tibial (1.16 ± 0.14 mm) cartilage was significantly thicker than the fibula (0.85 ± 0.13 mm). The talus had the greatest mean maximum cartilage thickness (2.38 ± 0.4 mm).

Conclusions: The reported stereophotographic technique may be used as an independent gold standard for validation of the accuracy of quantitative cartilage measurements made using magnetic resonance imaging. The thickness distribution maps show that the thickest articular cartilage occurs over the talar shoulders where osteochondral lesions commonly occur and not in the centre of the talar dome as commonly believed.

Key words: Ankle, Articular cartilage, Cartilage thickness, Cartilage volume, Stereophotography.

Introduction

Accurate quantitative descriptions of the surface geometry of articular joints are essential for validating the accuracy of measurements made using advanced 3-D magnetic resonance imaging (MRI) techniques and the development of computational models.

In order to characterise the mechanical properties of a diarthrodial joint, accurate measurements of the articular cartilage thickness and the variation in thickness across the surface of the joint are required. It is also essential to have baseline measurements of quantitative geometric parameters of cartilage, such as thickness and volume in healthy joints, if we are to use non-invasive imaging-based biomarkers to monitor the progression of degenerative joint diseases[1], such as osteoarthritis.

Most previous investigations of articular cartilage thickness have dealt with the knee. There have been relatively few studies of the ankle and other joints possessing thinner articular cartilage layers[2–5].

*Address correspondence and reprint requests to: Dr Steven A. Millington, B.M.B.S., M.R.C.S. (Ed.), Department of Traumatology, Medical University of Vienna, Leitermayergasse 31/20, A-1180 Vienna, Austria. Tel: 43-650-962-0402; Fax: 43-1-40400-7631; E-mail: steven.millington@meduniwien.ac.at
Received 6 April 2006; revision accepted 23 July 2006.

A variety of methods have been used to measure the thickness of cartilage in different joints both *in vitro* and *in vivo* with varying accuracy; *in vitro* methods include: anatomical sections[6]; needle probe measurements[7]; stereophotographic techniques[8] and A-mode ultrasound[9,10]. *In vivo* methods for measuring cartilage thickness include: X-ray measurements[11,12]; computer tomography sections[13]; and MRI[2,14]. *In vitro* techniques require disarticulation of the joint and/or may alter the thickness due to deformation during contact. Several of the *in vivo* techniques use indirect methods to make measurements of cartilage thickness e.g., X-ray and contrast-enhanced computer tomography (CT).

Early studies in this area were limited to using 2-D techniques such as anatomical sections and plain radiographs, failing to account for out-of-plane surface curvature of the joint. The resulting oblique measurements tend to over-estimate the thickness of the cartilage layer. More recent studies using advanced 3-D reconstruction techniques allowed precise thickness measurements to be made perpendicular to the joint surface, hence accommodating curvature in all directions and giving true thickness measurements at an increased number of points.

Ateshian *et al.*[8] developed an analytical stereophotographic technique for measuring the thickness of articular cartilage and applied the technique to the knee, but not to thin articular layers such as the ankle joint. The reported

Appendix 1

technique was a non-contact method which allowed precise measurements (±90 μm). Unfortunately the process was slow, labour intensive and allowed only a discrete number of points to be digitised; furthermore, it was not possible to reconstruct the entire joint surface from one data set, as the cameras and specimen were fixed in one position.

MRI is becoming more widely available and offers many benefits over other methods for measuring articular surface geometry. Using modern segmentation algorithms and 3-D reconstruction techniques, MRI can be used to longitudinally measure changes in parameters such as cartilage thickness and volume, *in vivo*. Initial research along these lines has focused on the knee joint[14–19], which has the thickest cartilage in the body and is relatively easy to segment, as it does not have large congruent areas. However, attempts to utilise MRI for quantitative measurements of the cartilage layers of the ankle have been limited by the achievable image resolution and the techniques for detecting cartilage boundaries[20]. With the exception of the efforts of Eckstein and co-workers, there have been few attempts to establish the accuracy of MRI measurements of cartilage specifically in thin congruent cartilage layers[2–5]. Moreover, the accuracy of MRI-based quantitative measurements in thin congruent cartilage layers has not been validated against an independent gold standard.

The objectives of this study were first, to describe a high resolution stereophotographic technique for quantifying the thin cartilage layers of the ankle joint, providing a method to validate other techniques; second, to describe the topographical variation of ankle joint articular cartilage; and finally, to provide baseline measurements of quantitative parameters of ankle cartilage in joints with no visual signs of degeneration or cartilage defects.

Materials and methods

Twelve fresh frozen foot and ankle specimens were harvested from 12 male cadavers, with a mean age of 61.5 years (range 51–75 years). All specimens were acquired in accordance with state and federal laws. Ethical approval for the study was provided by the University of Virginia Institutional Review Board and human usage review panel. From the available medical histories there were no reports of trauma to the lower limbs or musculoskeletal disease in the ankle(s) of the subjects.

The specimens were stored at −25°C. Prior to testing, each specimen was allowed to thaw at room temperature for 24 h. After thawing, the ankle joints were disarticulated, and soft tissues were removed from around the tibia–fibula complex and the talus, leaving the syndesmosis intact. Each specimen was visually examined by an orthopaedic surgeon and stained using the India ink technique to assess for cartilage surface lesions and degeneration. No cartilage lesions were seen in any of the specimens tested, minor localised surface fibrillation was seen in two ankles, which is in keeping with the findings of Meachim[21] in autopsy specimens. The bones were then potted in custom potting cups using a fast-setting resin (R1 Fastcast, Goldenwest Manufacturing Inc., CA, USA) taking care to ensure that the articular surface was above the level of the potting material (Fig. 1). The talus was elevated above the potting material by inserting three screws into the inferior surface of the talus, leaving part of the screw shafts projecting into the potting material so that the screws became rigidly embedded into the resin and fixed the talus in position. During preparation the specimens were kept hydrated with phosphate buffered saline containing protease inhibitor (Sigma–Aldrich, USA). The potting cups incorporated a flange at their rim with photo targets fixed to it, the rigid fixation of the specimen ensured that there was no motion of the specimen relative to these targets (Fig. 1).

The Stereophotogrammetric system (Advanced TOpometric System – ATOS II SO, Capture 3-d, CA, USA) consists of two high resolution CCD cameras, a fringe pattern projector and digital image processing software. The ATOS system has a measurement noise (accuracy) of ±2 μm and a point spacing of 0.03 mm (http://www.gom.com/EN/measuring.systems/atos/system/variations). The system functions by projecting a fringe pattern onto the specimen and the fixed photo targets; the system then uses triangulation and digital image post processing to assign 3-D coordinates to each pixel, thereby generating a dense point cloud. By combining multiple point clouds taken from different views, a full detailed 3-D model of each surface can be generated, typically yielding on the order of 70,000 points for each cartilage or bone surface. In order to improve image contrast and optimise the performance of the ATOS system a fine coating of white powder was sprayed onto the surface being imaged.

Each cartilage surface was imaged, and the point cloud data were saved to disk. The articular cartilage was then dissolved by submerging the specimen in a 5% sodium hypochlorite solution for 6–8 h to reveal the intact subchondral bone[8]. During this process the specimen was not allowed to move relative to the photo targets due to the rigid fixation. After removal from the 5% sodium hypochlorite the specimen was again visually examined by an orthopaedic

Fig. 1. A potted tibia–fibula complex and a talus specimen are shown in this picture. The articular surface of the talus has been prepared with a fine white power to improve image contrast and optimise the performance of the ATOS system. Black and white photo targets are fixed to the flange on the potting cup.

Appendix 1

surgeon to ensure that all the cartilage had been removed. The imaging process was then repeated for the subchondral bone surfaces. Finally, the common photo targets were defined and used to spatially register the cartilage and subchondral bone surfaces together using software incorporated in the ATOS system which performs a rigid body rotation and transformation of the cartilage surface onto the bone.

POST PROCESSING TECHNIQUE

Cartilage thickness was measured by performing an octree-based search for every point on the cartilage surface to find its nearest neighbour on the corresponding bone surface. This is a reasonable approximation since the average distance between adjacent points on any surface is small, typically less than 40 μm. However, care had to be taken at the edges of the surfaces because although the cartilage and bone surfaces were registered to each other, their borders did not necessarily match identically, since the surfaces were imaged independently. If the boundary of one of the meshes were to extend beyond the other, as depicted in Fig. 2(a), an incorrectly large thickness would be reported for the extended part of the surface. These offending regions were identified by inspecting a triangle $T=(v_1,v_2,v_3)$ on M and the nearest neighbours v_i' of v_i $(i=1\ldots3)$ on M', see Fig. 2(a), (v_3 is not shown in this 2-D sketch). If all v_i', $i=1\ldots3$, lie on the boundary of M', triangle T is discarded, steps 1 and 2 in Fig. 2(a). Additionally, in some specimens small amounts of periarticular tissue, e.g., fat, joint capsule and/or ligamentous tissue, which could not be completely removed caused artefacts, making the cartilage layer appear thicker along parts of the boundary [Fig. 2(b)]. Therefore, any extraneous parts at the periphery had to be identified *post hoc* and repaired. To alleviate this problem, we define a maximum thickness d_0 and shrink both meshes M and M' until the distance between them is not larger than d_0 anywhere at the boundary.

The final step was to "stitch" the cartilage and bone meshes together to form a closed volume. Note that these corrective procedures had no impact on the more central portions of the surface models, as they only occur at the periphery.

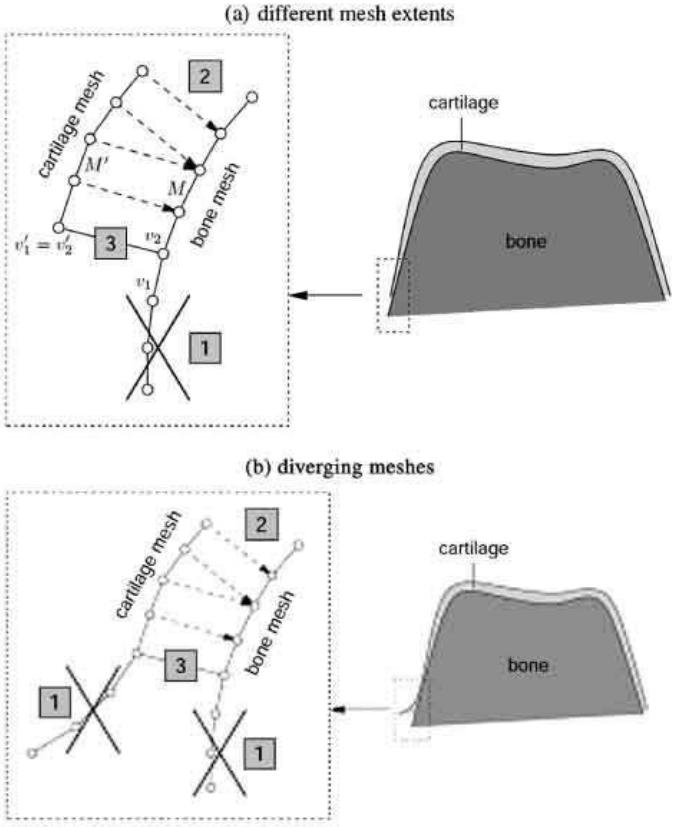

Fig. 2. Schematic of the corrective post processing procedure. (a) Different mesh extents. (b) Diverging meshes. Step 1, removal of non-corresponding regions; step 2, for each vertex on the cartilage surface the nearest neighbour on the bone surface is found; step 3, the edges of the meshes are "stitched" together.

Appendix 1

The processed triangulated meshes for each cartilage layer were used to measure the cartilage surface areas and the bone cartilage interface (BCI) areas. The cartilage volumes were determined from the closed polyhedra formed by the combined cartilage and bone meshes. In addition, the coefficient of variation was calculated for each cartilage layer in order to provide a description of the variation of thickness within a cartilage layer.

Quantitative parameters were statistically analysed for differences between the talar, tibial and fibula layers using an ANOVA with a *post hoc* Tukey test, $P < 0.05$ was considered significant.

Results

Precise 3-D geometric models and thickness distribution maps were generated for each articular cartilage layer, providing complete geometric data including the highly curved regions and the peripheries of the surfaces. Representative examples of the 3-D thickness distribution maps are shown in Figs. 3–5. The 3-D models faithfully reproduce the sellar shape of the talus and the concavity of the distal tibial surface, and the thickness distribution maps reveal several characteristic patterns. The talus maps displayed two distinct areas over the talar shoulders, one anterior-laterally and one posterior-medially, where the thickest cartilage occurred (Fig. 3). The tibial cartilage thickness was more evenly distributed; however, the thickest cartilage typically occurred in two areas; the central part of the anterior tibial plafond and the curved region at the transition between the tibial plafond and the medial malleolus (Fig. 4). The fibula showed a characteristic valgus angulation of the distal articular surface and had the most homogeneous cartilage thickness of the ankle cartilage layers (Fig. 5).

The articular cartilage thickness was measured at every point on the articular cartilage surface; the mean number of measurements per surface was 73,236. The mean and standard deviations (across the 12 specimens) of spatial mean thickness, maximum thickness, cartilage surface area, BCI area and volume are shown in Table I.

There was no significant difference between the mean articular cartilage thickness of talar and tibial cartilage layers. The talar ($P < 0.01$) and the tibial cartilage ($P < 0.001$) spatial mean thickness values were significantly greater than the fibula cartilage. For maximum cartilage thickness the only significant difference was between the talus and the fibula ($P < 0.05$).

Cartilage surface area and BCI area measurements showed clear significant differences. The talus had a significantly larger surface area than both the tibia ($P < 0.001$) and the fibula ($P < 0.001$). Even when the tibia and fibula were combined, representing the superior half of the ankle joint, the talus had a significantly larger surface area ($P < 0.001$).

The talar cartilage volume was also significantly greater than the combined tibia–fibula cartilage volume ($P < 0.001$) and the tibia had a significantly greater volume than the fibula ($P < 0001$). This is a clear reflection of the larger area covered by articular cartilage on the talus compared with the tibia and fibula.

As an assessment of the homogeneity/inhomogeneity of the cartilage thickness across the joint surface the coefficient of variation was calculated for the superior part of the joint (the tibia–fibula complex) and the inferior part of joint (the talus). The coefficients of variation were very similar for both halves of the joint, 30.21% over the tibia–fibula complex cartilage and 30.54% over the talar cartilage.

Discussion

In this study we have described a highly accurate technique for generating 3-D geometric models and making quantitative measurements in thin cartilage layers, based on a commercially available stereophotography system, ATOS™. The system allows rapid acquisition and processing of large volumes of geometric data with a measurement noise (accuracy) of ± 2 μm. The versatility and accuracy of the technique have enabled us to study geometrical parameters of thin highly curved cartilage layers to a level of detail that has not been previously possible.

Our results show that the spatial mean cartilage thickness ranged from 0.85 ± 0.13 mm in the fibula to 1.16 ± 0.14 mm in the tibia, and maximum thickness ranged from 2.06 ± 0.08 mm in the fibula to 2.38 ± 0.4 mm in the talus. The coefficients of variation show that ankle cartilage thickness has a relatively consistent level of homogeneity throughout the joint; the values are lower than those reported in the knee joint[8], but consistent with results reported in the ankle joint[9].

A variety of techniques have been used previously to measure ankle cartilage thickness in the ankle. Using the *in vitro* needle force probe technique[7,22], mean cartilage thickness values have been reported as 1.22 mm and 1.16 mm for the talus, 1.18 mm and 1.35 mm for the tibia and 0.95 mm for the fibula. Using A-mode ultrasound in an *in vitro* study the reported mean thickness values were lower; 0.95 mm and 1.0 mm for the talus and tibia, respectively. In an MRI-based study of volunteers[2] the mean

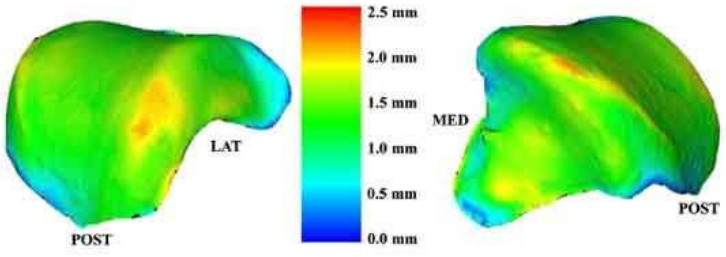

Fig. 3. Representative 3-D thickness distribution maps of the talar articular cartilage layer, viewed from the lateral (left) and medial aspects (right) of a right talus.

Appendix 1

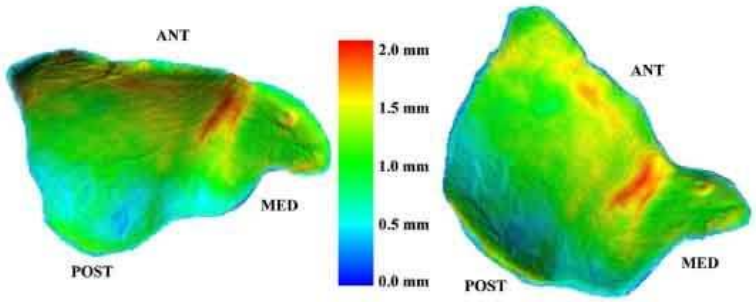

Fig. 4. Representative 3-D thickness distribution maps of the tibial articular cartilage layer, viewed from the inferior aspect of a right tibia.

cartilage thickness was at the lower limit of values reported in the literature; 0.89 mm and 0.82 mm in the talus and the tibia, respectively.

Unfortunately each of the above techniques has limitations. The needle probe technique can only be used at a number of discrete points over the surface and ruptures the surface limiting the usefulness of further testing. Furthermore, Jurvelin *et al.*[10] previously reported the change in force signal was not very sharp and a subjective evaluation was required when using a needle probe. The accuracy of ultrasound measurements is dependent on the assumption that sound travels at a uniform speed through all layers of the articular cartilage. However, previous studies[10,23] have shown considerable variation in the velocity, especially in thin cartilage layers, which may help to explain the lower mean values seen with ultrasonic measurements.

MRI can avoid many of these limitations, allowing measurements at every voxel and calculation of surface areas and volumes. Unfortunately, the earlier MRI study[2] excluded the talar shoulders and malleolar facets as well as the tibial medial malleolar and fibular surfaces, because non-isotropic sagittally acquired data were used. Therefore, a direct comparison of volume and surface area measurements with the current study is not possible.

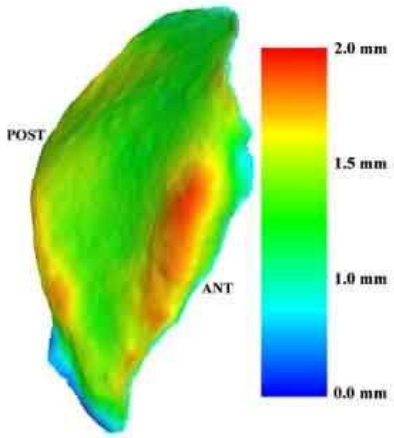

Fig. 5. A representative 3-D thickness distribution map of the fibula articular cartilage layer, viewed from the anterior aspect of a left fibula.

During the disarticulation and potting the specimens were kept hydrated with phosphate buffered saline which theoretically may result in some swelling of the articular cartilage; however, if the cartilage was left untreated it would potentially become dehydrated by exposure to the atmosphere and the surface preparation. The relatively short preparation time and the rapid data acquisition process for the cartilage surface by the ATOS™ system helped to minimise these effects; therefore, we believe that the results of the present study realistically represent the thickness of the cartilage in the *in vivo* state.

Although the reported stereophotography technique is destructive to articular cartilage, and thus can only be performed *in vitro* it is still a very useful technique as it provides an independent gold standard for validating the accuracy of other measurement techniques, such as MRI[14], which may also be used for *in vivo* studies.

In the talus the thickness distribution maps indicate the thickest cartilage region occurs anterior-laterally and posterior-medially over the shoulders of the talus. Earlier studies, unable to assess the highly curved regions of the joint surfaces, reported the thickest cartilage to occur in the central region of the talar dome[7,9,22]. Our findings are in keeping with those of Muller-Gerbl and Putz[24] who described findings from anatomical sections. The results of this study clearly show that the regions of greatest thickness on the talus correspond to the most common site of Osteochondritis dissecans (OCD) lesions in the ankle[25]. Furthermore, the thick cartilage over the anterior border of the tibia corresponds to cartilage injury sites seen in dorsiflexion testing[26]. It is also interesting to note that the regions of greatest cartilage thickness in the ankle joint correspond to regions on the talus and tibia where the subchondral bone is most dense[24]. These finding may be a response to the prevailing mechanical conditions occurring in the ankle joint.

Understanding the behaviour of ankle articular cartilage requires a true understanding of the 3-D anatomy, including

Table I
Mean values (±S.D.) for each of the quantitative parameters measured from 12 ankle specimens

$N=12$	Talus	Tibia	Fibula
Mean thickness (mm)	1.10 ± 0.18	1.16 ± 0.14	0.85 ± 0.13
Max thickness (mm)	2.38 ± 0.4	2.18 ± 0.19	2.06 ± 0.08
Cartilage surface area (mm^2)	21.56 ± 2.14	13.45 ± 1.28	4.30 ± 0.79
BCI area (mm^2)	23.6 ± 1.67	12.57 ± 0.79	3.67 ± 0.63
Volume (ml)	2.44 ± 0.48	1.50 ± 0.28	0.32 ± 0.08

Appendix 1

the distribution of cartilage thickness across the joint surface. Additionally, biomechanical knowledge of the cartilage stiffness distribution across the joint surface is important. As the results of this study show that the thickest cartilage occurs where cartilage injuries are most commonly seen, future studies of the cartilage mechanical properties in these regions will be of significant interest.

Changes in quantitative geometric parameters have been suggested as potentially sensitive measures of degenerative change in cartilage layers[1,27]. The described stereophotography technique offers the possibility to validate MRI derived measurement for surface areas and volumes, in addition to thickness in thin cartilage layers. Validated MRI techniques offer a powerful tool for detecting and monitoring cartilage injury and degenerative change.

The geometric data generated using this technique can be used as input to finite element (FE) computational models. As a result the geometric database created from this study may be used to generate a representative geometry of the ankle joint and its cartilage layers[28]. FE models based on representative geometry can be of significant benefit for stress and strain analyses[29] and to aid development of improved ankle prostheses[30].

Conclusions

We have reported a highly accurate technique for acquiring geometric data and making quantitative measurements of thin articular cartilage layers. The reported stereophotographic technique may be used as an independent gold standard for validation of the accuracy of *in vivo* measurements in thin cartilage layers using MRI. Furthermore, the 3-D geometric ankle cartilage data will help to produce more realistic computational models for biomechanical analysis. Finally, the thickness distribution maps produced show that the thickest articular cartilage in the ankle occurs at the clinically relevant regions where cartilage lesions most commonly occur[25].

References

1. Gray ML, Eckstein F, Peterfy C, Dahlberg L, Kim YJ, Sorensen AG, *et al.* Toward imaging biomarkers for osteoarthritis. Clin Orthop Relat Res 2004;(427 Suppl):S175–81.
2. Al Ali D, Graichen H, Faber S, Englmeier KH, Reiser M, Eckstein F. Quantitative cartilage imaging of the human hind foot: precision and inter-subject variability. J Orthop Res 2002;20(2):249–56.
3. Graichen H, Springer V, Flaman T, Stammberger T, Glaser C, Englmeier KH, *et al.* Validation of high-resolution water-excitation magnetic resonance imaging for quantitative assessment of thin cartilage layers. Osteoarthritis Cartilage 2000;8(2):106–14.
4. Peterfy CG, van Dijke CF, Lu Y, Nguyen A, Connick TJ, Kneeland JB, *et al.* Quantification of the volume of articular cartilage in the metacarpophalangeal joints of the hand: accuracy and precision of three-dimensional MR imaging. AJR Am J Roentgenol 1995;165(2): 371–5.
5. Nishii T, Sugano N, Sato Y, Tanaka H, Miki H, Yoshikawa H. Three-dimensional distribution of acetabular cartilage thickness in patients with hip dysplasia: a fully automated computational analysis of MR imaging. Osteoarthritis Cartilage 2004;12(8):650–7.
6. Jurvelin J, Kiviranta I, Arokoski J, Tammi M, Helminen HJ. Indentation study of the biochemical properties of articular cartilage in the canine knee. Eng Med 1987;16(1):15–22.
7. Shepherd DE, Seedhom BB. Thickness of human articular cartilage in joints of the lower limb. Ann Rheum Dis 1999;58(1):27–34.
8. Ateshian GA, Soslowsky LJ, Mow VC. Quantitation of articular surface topography and cartilage thickness in knee joints using stereophotogrammetry. J Biomech 1991;24(8):761–76.
9. Adam C, Eckstein F, Milz S, Putz R. The distribution of cartilage thickness within the joints of the lower limb of elderly individuals. J Anat 1998;193(Pt 2):203–14.
10. Jurvelin JS, Rasanen T, Kolmonen P, Lyyra T. Comparison of optical, needle probe and ultrasonic techniques for the measurement of articular cartilage thickness. J Biomech 1995;28(2):231–5.
11. Hall FM, Wyshak G. Thickness of articular cartilage in the normal knee. J Bone Joint Surg 1980;62(3): 408–13.
12. Karvonen RL, Negendank WG, Teitge RA, Reed AH, Miller PR, Fernandez-Madrid F. Factors affecting articular cartilage thickness in osteoarthritis and aging. J Rheumatol 1994;21(7):1310–8.
13. Eckstein F, Schnier M, Haubner M, Priebsch J, Glaser C, Englmeier KH, *et al.* Accuracy of cartilage volume and thickness measurements with magnetic resonance imaging. Clin Orthop Relat Res 1998; (352):137–48.
14. Cohen ZA, McCarthy DM, Kwak SD, Legrand P, Fogarasi F, Ciaccio EJ, *et al.* Knee cartilage topography, thickness, and contact areas from MRI: *in-vitro* calibration and *in-vivo* measurements. Osteoarthritis Cartilage 1999;7(1):95–109.
15. Faber SC, Eckstein F, Lukasz S, Muhlbauer R, Hohe J, Englmeier KH, *et al.* Gender differences in knee joint cartilage thickness, volume and articular surface areas: assessment with quantitative three-dimensional MR imaging. Skeletal Radiol 2001;30(3):144–50.
16. Raynauld JP, Kauffmann C, Beaudoin G, Berthiaume MJ, de Guise JA, Bloch DA, *et al.* Reliability of a quantification imaging system using magnetic resonance images to measure cartilage thickness and volume in human normal and osteoarthritic knees. Osteoarthritis Cartilage 2003;11(5):351–60.
17. Raynauld JP, Martel-Pelletier J, Berthiaume MJ, Labonte F, Beaudoin G, de Guise JA, *et al.* Quantitative magnetic resonance imaging evaluation of knee osteoarthritis progression over two years and correlation with clinical symptoms and radiologic changes. Arthritis Rheum 2004;50(2):476–87.
18. Eckstein F, Charles HC, Buck RJ, Kraus VB, Remmers AE, Hudelmaier M, *et al.* Accuracy and precision of quantitative assessment of cartilage morphology by magnetic resonance imaging at 3.0 T. Arthritis Rheum 2005;52(10):3132–6.
19. Eckstein F, Hudelmaier M, Wirth W, Kiefer B, Jackson R, Yu J, *et al.* Double echo steady state (DESS) magnetic resonance imaging of knee articular cartilage at 3 Tesla – a pilot study for the osteoarthritis initiative. Ann Rheum Dis 2005;26(8).
20. Tan TC, Wilcox DM, Frank L, Shih C, Trudell DJ, Sartoris DJ, *et al.* MR imaging of articular cartilage in the ankle: comparison of available imaging sequences and methods of measurement in cadavers. Skeletal Radiol 1996;25(8):749–55.

Appendix 1

21. Meachim G. Cartilage fibrillation at the ankle joint in Liverpool necropsies. J Anat 1975;119(3):601–10.
22. Athanasiou KA, Niederauer GG, Schenck RC Jr. Biomechanical topography of human ankle cartilage. Ann Biomed Eng 1995;23(5):697–704.
23. Yao JQ, Seedhom BB. Ultrasonic measurement of the thickness of human articular cartilage *in situ*. Rheumatology (Oxford) 1999;38(12):1269–71.
24. Muller-Gerbl M, Putz R. Functional Anatomy of the Ankle Joint. The Tibial Pilon Fracture 1995, 1st edn[1], 3–25.
25. O'Farrell TA, Costello BG. Osteochondritis dissecans of the talus. The late results of surgical treatment. J Bone Joint Surg Br 1982;64(4):494–7.
26. Rudd R, Crandall J, Millington SA, Hurwitz SR, Hoglund N. Injury tolerance and response of the ankle joint in dynamic dorsiflexion. Stapp Car Crash Journal 2004;48:1–26.
27. Burgkart R, Glaser C, Hinterwimmer S, Hudelmaier M, Englmeier KH, Reiser M, *et al.* Feasibility of *T* and *Z* scores from magnetic resonance imaging data for quantification of cartilage loss in osteoarthritis. Arthritis Rheum 2003;48(10):2829–35.
28. Cohen ZA, Mow VC, Henry JH, Levine WN, Ateshian GA. Templates of the cartilage layers of the patellofemoral joint and their use in the assessment of osteoarthritic cartilage damage. Osteoarthritis Cartilage 2003;11(8):569–79.
29. Fitzpatrick DC, Otto JK, McKinley TO, Marsh JL, Brown TD. Kinematic and contact stress analysis of posterior malleolus fractures of the ankle. J Orthop Trauma 2004;18(5):271–8.
30. Cheung JT, Zhang M. A 3-dimensional finite element model of the human foot and ankle for insole design. Arch Phys Med Rehabil 2005;86(2):353–8.

Appendix 2. 2-D segmentation algorithm development

895 IEEE TRANSACTIONS ON BIOMEDICAL ENGINEERING, VOL. 53, NO. 5, MAY 2006

Surface Extraction and Thickness Measurement of the Articular Cartilage From MR Images Using Directional Gradient Vector Flow Snakes

Jinshan Tang, *Senior Member, IEEE*, Steven Millington, Scott T. Acton*, *Senior Member, IEEE*, Jeff Crandall, and Shepard Hurwitz

***Abstract*—The accuracy of the surface extraction of magnetic resonance images of highly congruent joints with thin articular cartilage layers has a significant effect on the percentage errors and reproducibility of quantitative measurements (e.g., thickness and volume) of the articular cartilage. Traditional techniques such as gradient-based edge detection are not suitable for the extraction of these surfaces. This paper studies the extraction of articular cartilage surfaces using snakes, and a gradient vector flow (GVF)-based external force is proposed for this application. In order to make the GVF snake more stable and converge to the correct surfaces, directional gradient is used to produce the gradient vector flow. Experimental results show that the directional GVF snake is more robust than the traditional GVF snake for this application. Based on the newly developed snake model, an articular cartilage surface extraction algorithm is developed. Thickness is computed based on the surfaces extracted using the proposed algorithm. In order to make the thickness measurement more reproducible, a new thickness computation approach, which is called T-norm, is introduced. Experimental results show that the thickness measurement obtained by the new thickness computation approach has better reproducibility than that obtained by the existing thickness computation approaches.**

***Index Terms*—B-splines, cartilage surface extraction, gradient vector flow, segmentation, snakes.**

I. Introduction

IN THE western world, osteoarthritis is the most common form of disability. The socio-economic impact of degenerative joint diseases is huge; in the United States alone the cost was approximately $65 billion per year during the 1990s [1]. This cost is only set to rise with an aging population and rising drug costs. The potential impact of chondro-protective treatments and articular cartilage restoration techniques are significant. Currently, precise evaluation of a patients' degenerative joint(s), qualitatively and quantitatively both pretreatment and post-treatment, is technically demanding, especially in highly congruent joints with thin articular cartilage, e.g., the ankle joint. However, in order to clinically evaluate present and future treatments we must be able precisely and reproducibly image and quantify the articular cartilage of these joints [2]–[6].

Accurate assessment of articular cartilage layers requires the use of three-dimensional (3-D) reconstruction of joints in order to quantify the cartilage parameters independently of slice location or orientation. Three-dimensional reconstructions are particularly important for longitudinal studies of patients in which measurements must be reproducible.

Magnetic resonance imaging is a multiplanar imaging technique capable of producing high resolution, high-contrast images in serial contiguous slices. In recent years there has been considerable development in the field of articular cartilage imaging and refinement of imaging sequences to enhance the visualization of articular cartilage. Extensive work by Eckstein *et al.* [7]–[10] has shown spoiled 3-D gradient echo (FLASH) sequences with water excitation to be particularly useful. However, most articular cartilage imaging work has concentrated on the knee joint [8], [9], [11]–[16], which displays the thickest articular cartilage layers in the human body. There have been a few notable exceptions [7], [10] that have examined joints with thinner articular cartilage layers (<3 mm thick), which are more typical in most joints of the human body.

The accuracy of the surface extraction and segmentation of highly congruent joints with thin articular cartilage layers can have a significant effect on the percentage errors and reproducibility of quantitative measurements (e.g., thickness and volume) of the articular cartilage. Fully manual surface extraction and segmentation [8], [11], [14], [15], [17], [18] is labor intensive, prone to error and subject to subjective judgment of an observer leading to interobserver variability. Fully automated processes [19], [20] at present cannot accurately and reproducibly extract and segment articular cartilage layers in areas where the boundary is not sufficiently distinct or in noisy images.

Previous studies have performed segmentation using a variety of techniques including: manual segmentation [8], [11], [14], [15], [17], [18], seed point and region growing algorithms [21]–[23], and edge detection followed by spline-based smoothing [11], all of which have limitations in noisy images of thin cartilage layers of highly congruent joints.

Manuscript received July 27, 2004; revised October 1, 2005. *Asterisk indicates corresponding author.*

J. Tang is with the Department of Electrical and Computer Engineering, University of Virginia, Charlottesville, VA 22903 USA.

S. Millington is with the Center for Applied Biomechanics and the Department of Orthopaedic Surgery, University of Virginia, Charlottesville, VA 22903 USA.

*S. T. Acton is with the Department of Electrical and Computer Engineering and the Department of Biomedical Engineering, University of Virginia, Charlottesville, VA 22903 USA. (e-mail: acton@virginia.edu).

J. Crandall is with the Center for Applied Biomechanics and the Department of Biomedical Engineering, University of Virginia, Charlottesville, VA 22903 USA.

S. Hurwitz is with the Department of Orthopaedic Surgery, University of Virginia, Charlottesville, VA 22903 USA.

Digital Object Identifier 10.1109/TBME.2006.872816

Appendix 2

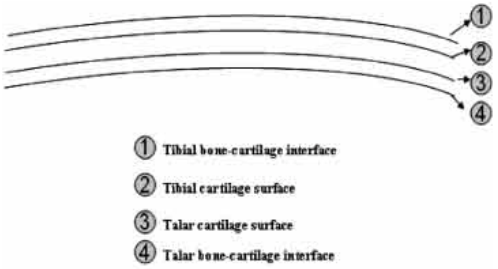

Fig. 1. Diagram depicting articular cartilage.

We hypothesize an appropriate algorithm for this application is the active contour model or *snake* [24]. A snake is a parameterized contour [24] that translates and deforms on the image plane according to the strength of the image edges and the internal properties of the contour such as smoothness. Since the original snake was introduced by Kass *et al.* [24], many additional snakes have been proposed [25]–[27]. This paper adopts a GVF snake originally developed and discussed in [25]. The advantage of a GVF snake is its robustness to the initialization of the snake [25]. Considering that the cartilage boundaries are smooth curves, we use B-splines to represent the active contours. A B-spline has several characteristics that make it suitable for describing the cartilage boundary as well as being suitable for snake evolution. The B-spline implicitly incorporates contour smoothness and avoids the ad hoc tension and rigidity parameters of the traditional parametric snake [28]–[30]. In addition, the B-spline permits the local control of the curve by controlling individual control points, which makes it useful for human adjustment. In fact, human adjustment is one of the necessary steps in the cartilage surface extraction [11].

Because the cartilage of the ankle is very thin and the surfaces are closely located with respect to each other (less than 3 mm) (see Fig. 1), the current GVF snake model is ineffective in the tracking of the surface. In order to track the cartilage surfaces effectively, we provided a modification of the current GVF snake model to improve its performance by incorporating gradient direction information into the GVF model. This additional information will make the snake more stable and converge to the correct surface.

Additionally in the study we introduce a new thickness computation approach. In the past, several thickness computation approaches have been proposed [20], [31]: 1) vertical distance: z-directional distance between points on the two different surfaces on the same cartilage; 2) proximity method: closest neighbor on corresponding surface; 3) normal distance: length of surface normal vectors between the two surfaces; 4) thickness computation developed in [20], which we call M-norm distance in this paper. However, the reproducibility of all of the existing thickness computation approaches limits their use for longitudinal monitoring of changes in thin cartilage layers. In order to obtain a more reproducible measurement, a new thickness computation approach, which is based on the M-norm approach in [20], is developed in this paper.

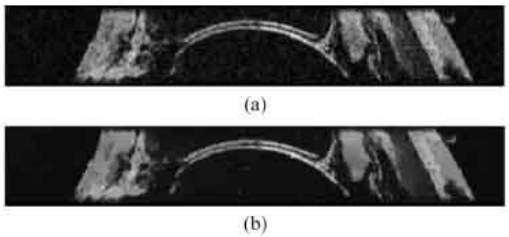

Fig. 2. Noise reduction using anisotropic diffusion. (a) Original image; (b) image after anisotropic diffusion.

II. Materials and Methods

A. Image Acquisition

Four foot and ankle complexes were harvested from three male human cadavers (age 51–59 years, mean 54.7 years). Only a limited medical history was available for each cadaver; however, there were no reports of trauma to the lower limbs or musculoskeletal disease.

The MR images were acquired using a 1.5 T MR scanner (Magneton vision, Siemens, Erlahgen, Germany) and a circularly polarized transmit receive extremity coil. The imaging sequence used was a sagittal spoiled 3-D gradient-echo sequence, fast low angle shot (FLASH), with selective water excitation, TR of 18 ms, TE of 7.65 ms, flip angle of 25°, in-plane resolution of 0.3 mm × 0.3 mm, slice thickness of 0.3 mm, field of view (FOV) of 160 mm, and a matrix of 512^2 pixels. The acquisition time was 17 min, 14 s. As the images were acquired using isotropic voxels we were able to reconstruct the images in three perpendicular planes (sagittal, coronal and axial). All image data were then transferred to a desktop work station for surface extraction and segmentation. Fig. 2(a) shows one slice from a 3-D MR image.

B. Noise Reduction

The image data obtained by magnetic resonance imaging (MRI) are typically noisy; thus, a noise reduction technique is needed to improve the tracking accuracy of the snake. In some tracking algorithms using a snake model [25], [26], a Gaussian filter is used to reduce the noise before a snake is used for tracking. However, the Gaussian filter is not a good edge preserving noise reduction technique. Application of a Gaussian filter to these images will blur the edges in the images. We need a noise reduction technique that can preserve the quality of the edges of the images. One such technique is anisotropic diffusion [32]. Anisotropic diffusion has been applied to reduce the noise in MRI images and has produced good results [32]. Anisotropic diffusion is a nonlinear filtering method, which encourages diffusion in the homogeneous region while inhibiting diffusion

Appendix 2

at edges. The partial differential equation (PDE) of anisotropic diffusion is given as follows in continuous domain [33]

$$\begin{cases} \frac{\partial I}{\partial t} = div\left[c\left(|\nabla I|\right)\nabla I\right] \\ I(t=0) = I_0 \end{cases} \tag{1}$$

where ∇ is the gradient operator, div is the divergence operator, $|\ |$ denotes the magnitude, I_0 is the initial image and $c()$ is the diffusion coefficient, which can be given by

$$c(x,y) = \exp\left(-\left[\frac{\nabla I(x,y)}{k}\right]^2\right). \tag{2}$$

Fig. 2(b) shows an image processed by anisotropic diffusion. This figure demonstrates the noise reduction and the edge preservation of the anisotropic diffusion technique. We use the anisotropic diffusion as a preprocessing step for segmentation by the directional GVF snakes.

C. Cartilage Surface Extraction Using Directional GVF Snake

In this subsection, we will first introduce the traditional GVF model, and then introduce the modification of the current GVF model for cartilage surface extraction which is based on directional gradient and B-spline.

1) Traditional GVF External Forces: Kass *et al.* [24] define a snake as a controlled continuity contour that is attracted to salient image features. However, there are some disadvantages related to the original model. One of the disadvantages of the snake defined in [24] is the sensitivity to the initialization of the snake. The initial contour must be close to the actual object boundary because the capture range of the image gradient is small. To alleviate this problem, a gradient vector flow (GVF) is proposed in [25], [26] as an external force to attract the snake to actual boundary of the objects. GVF fields are computed by another diffusion process, which can be implemented by minimizing the following energy function [25], [26]:

$$E_{\mathrm{GGVF}}(u,v) = \frac{1}{2}\int\int g\left(|\nabla f|\right)\left(u_x^2+u_y^2+v_x^2+v_y^2\right) + \left(1-g\left(|\nabla f|\right)\right)\left((u-f_x)^2+(v-f_y)^2\right)dxdy \tag{3}$$

where g is a decreasing function of the edge-force magnitude and is defined as follows:

$$g\left(|\nabla f|\right) = \exp\left(-\left(\frac{|\nabla f|}{k}\right)\right) \tag{4}$$

Here k is a nonnegative smoothing parameter for the field (u,v). The functional described by (3) smoothes the force field (u,v) only when the edge strength is low. From (3), the following Euler equations can be obtained [26]:

$$g\nabla^2 u - (1-g)(u-f_x) = 0 \tag{5}$$

$$g\nabla^2 v - (1-g)(v-f_y) = 0. \tag{6}$$

The GVF field can be obtained by solving the following partial differential equations:

$$u_t = g\nabla^2 u - (1-g)(u-f_x) \tag{7}$$

$$v_t = g\nabla^2 v - (1-g)(v-f_y). \tag{8}$$

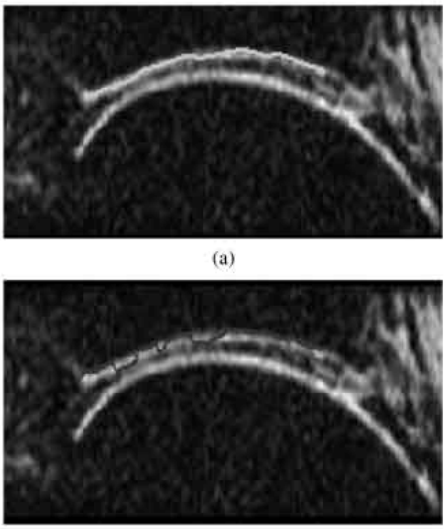

(a)

(b)

Fig. 3. Example of tracking results using GVF Bspline snake. (a) Initialization of the snake; (b) tracking results.

Solving (7), (8), we can obtain the generalized gradient vector flow vectors, which can be used as external forces that attract the snake to the cartilage boundary [25], [26].

2) Directional Gradient Vector Flow (DGVF) External Forces: With the GVF snake, only the gradient magnitude is used to compute the gradient vector flow. Thus, the traditional GVF snake may be attracted to strong edges that have the opposite gradient direction with respect to the intended boundary.

Fig. 3 demonstrates this point. In Fig. 3, the image includes four boundaries (from top to bottom) corresponding to four surfaces: tibial bone-cartilage interface, tibial cartilage surface, talar cartilage surface and talar bone-cartilage interface. In the example of Fig. 3, we hope to capture the boundary corresponding to the tibial bone-cartilage interface. If we initialize the snake as shown in Fig. 3, then we find that a portion of the snake converges to the boundary corresponding to the tibial bone-cartilage interface, while another portion converges to the boundary corresponding to the tibial cartilage surface.

In order to utilize the edge direction information in tracking the cartilage boundaries, we use an edge map function that incorporates gradient direction information, which is computed by

$$D_{\mathbf{n}}(I) = \nabla I \bullet \mathbf{n} \tag{9}$$

where I is the original image, ∇I is the gradient and $\mathbf{n}$ is a two-dimensional (2-D) vector which represents the direction of the edge, which can be specified by the user (and is known *a priori* for the ankle cartilage application).

Appendix 2

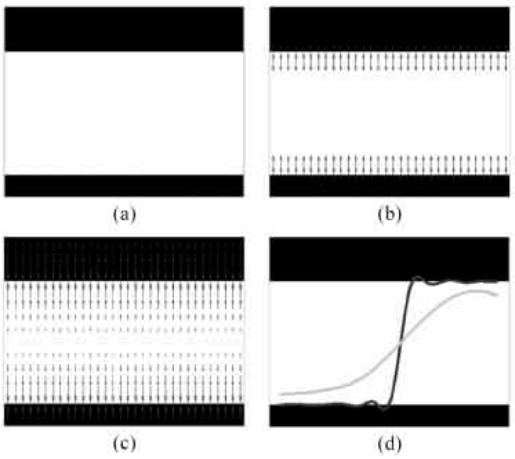

Fig. 4. Example of tracking results using GVF snake. (a) Original synthetic image; (b) gradient flow without direction information; (c) gradient vector flow without direction information produced from Fig. 3(b). (d) Tracking results using GVF; the smooth curve is the initial curve and the step-like curve is the final contour.

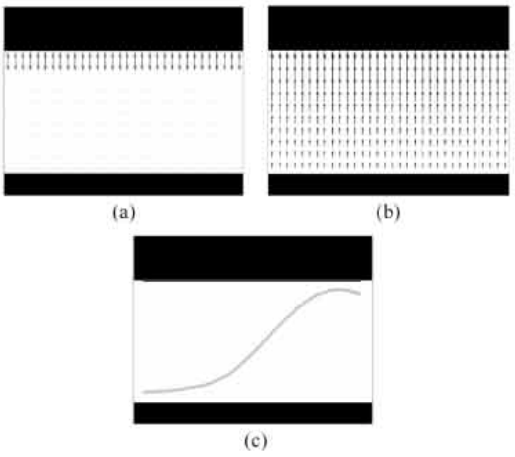

Fig. 5. Directional gradient flow and its corresponding directional gradient vector flow. (a) Gradient flow with direction information; (b) gradient vector flow with direction information; (c) tracking results using DGVF, the lower line is the initial curve and the upper line is the final contour.

Let

$$F = \begin{cases} D_{\mathbf{n}}(I), & D_{\mathbf{n}}(I) > 0 \\ 0, & \text{otherwise} \end{cases}. \tag{10}$$

Replacing f by F in (3), we obtain the directional gradient vector flow (DGVF) of the image by minimizing the following equation

$$E_{\mathrm{GGVF}}(u,v) = \frac{1}{2}\int\int g\left(|\nabla F|\right)\left(u_x^2+u_y^2+v_x^2+v_y^2\right) + \left(1-g\left(|\nabla F|\right)\right)\left((u-F_x)^2+(v-F_y)^2\right)dxdy \tag{11}$$

Solving (11) we can obtain GVF using directional gradient, which has the similar format to (5) and (6)

$$g\nabla^2 u - (1-g)(u-F_x) = 0 \tag{12}$$

$$g\nabla^2 v - (1-g)(v-F_y) = 0. \tag{13}$$

Fig. 4(b) shows the gradient flow field for the synthetic image shown in Fig. 4(a). Fig. 4(c) shows the gradient vector flow field and Fig. 4(d) shows the tracking results using the traditional GVF model (here, the aim is to capture the top boundary in the image). In Fig. 4(d), the lower (lighter) curve is the initial curve, and the upper (darker) curve is the final contour. From Fig. 4(d), it may be observed that the traditional snake failed to capture the top boundary because of the initialization. Fig. 5(b) shows that the enhanced directional gradient vector flow field, and Fig. 5(c) shows the tracking results using the directional GVF (DGVF) snake. Fig. 5(c) demonstrates that the improved GVF snake captures the boundary as intended. Fig. 6 shows the tracking results using the initialization in Fig. 3(a).

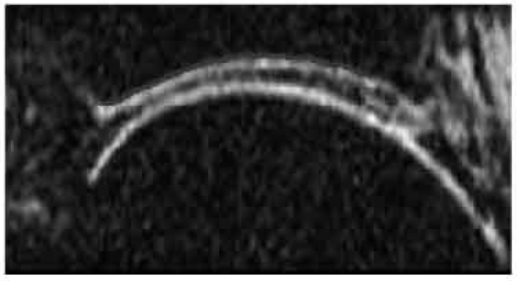

Fig. 6. Cartilage boundary tracking using directional gradient vector flow snake on the same image as in Fig. 1(a) and using the same initialization as in Fig. 1(b).

3) B-Spline Representation of the Active Contour and Snake Evolution:

a) Active contour representation using B-spline: There are many advantages in using a B-spline to represent the contour [28]–[30]. Because of the smoothness of a B-spline, we can avoid the choice of parameters in the traditional snake models [28]; the B-spline also assists our adjustment of the contour due to its local properties, without affecting the whole contour. We know that human adjustment is an important step in the tracking of cartilage boundary because of less than ideal imaging conditions [11]. Manual adjustment is particularly important for the cases in which cartilage defects or image noise cause the segmentation to fail. In these regions human interaction is required to adjust the contour to the correct boundary.

The B-spline used in this paper is a nonuniform, nonrational cubic B-spline [34]. The intervals between successive knot values in the nonuniform, nonrational B-spline need not be uniform [34]. The nonuniform B-spline has the following two

Appendix 2

properties that uniform B-splines do not have [34]: 1) The start and end points can be easily interpolated. 2) Additional knot and control points can be added to nonuniform B-splines so that the resulting curve can be easily reshaped. These two properties allow for human adjustment which is important in our application, see Section II-C4.

Let the control points be denoted by P_0 through P_m. The knot-value sequence is a nondecreasing sequence of knot values t_0 through t_{m+4}, and Q_i is a curve segment defined by control points P_{i-3}, P_{i-2}, P_{i-1}, P_i and blending functions $B_{i-3,4}$, $B_{i-2,4}$, $B_{i-1,4}$, $B_{i,4}(t)$ as follows [34]:

$$Q_i(t) = P_{i-3}\cdot B_{i-3,4} + P_{i-2}\cdot B_{i-2,4} + P_{i-1}\cdot B_{i-1,4} + P_i \cdot B_{i,4}(t) \tag{14}$$

where $3 \le i \le m$ and $t_i \le t \le t_{i+1}$. The blending functions can be obtained using recursion as follows [34]:

$$B_{i,1}(t) = \begin{cases} 1, & if\ t_i \le t < t_{i+1} \\ 0, & \text{elsewhere} \end{cases} \tag{15}$$

and

$$B_{i,p}(t) = \frac{t - t_i}{t_{i+p-1} - t_i} B_{i,p-1}(s) + \frac{t_{i+p} - t}{t_{i+p} - t_{i+1}} B_{i+1,p-1}(t). \tag{16}$$

When $p = 4$, we obtained the blending function of cubic splines. In this paper, we adopt the cubic B-spline for the representation of the active contour.

b) Open B-spline GVF snake: Now let us introduce the B-spline open snake algorithm used for cartilage surface extraction in Section II-C4. The external force used in our B-spline open snake utilizes the directional gradient vector flow obtained in Section II-C2. Instead of using the internal forces discussed in [24], we use the B-spline described in Section II-C3 to represent the active contour. The B-spline open snake algorithm can be described by several steps. First, we initialize the active contour, which can be performed manually or automatically. Second, we sample the active contour as follows: the active contour is segmented into many segments uniformly, and in each segment, the point with the largest contrast is selected as the sample point (for convenience, we denote the obtained samples by $(x_0, y_0), \ldots, (x_{n-1}, y_{n-1})$, where n is the number of the sample points). Third, we compute the gradient vector flow field described in Section II-C2 and to evolve the contour using the obtained directional gradient vector flow, starting from initial samples. After the evolution converges, the obtained points are denoted by $(\bar{x}_0, \bar{y}_0), \ldots, (\bar{x}_{n-1}, \bar{y}_{n-1})$. Fourth, we represent the active contour using a B-spline. To achieve this representation, we first use the least squares method [34] to estimate control points from the sample points $(\bar{x}_0, \bar{y}_0), \ldots, (\bar{x}_{n-1}, \bar{y}_{n-1})$. The control points are used to build a new active contour using (14). After the fourth step is finished, the same processing steps will be performed on the next slice for which the initial contour is the resultant contour of the previous slice.

4) Cartilage Surface Extraction:

a) Framework for the cartilage surface segmentation: The algorithm for the extraction of cartilage boundary is semi-automatic. For the first slice, we initialize each surface/interface manually, for subsequent slices we use the tracking results from the previous slice. Then the B-spline directional GVF snake model is used to refine the initialization result. After the automatic tracking is finished, we allow adjustment of the contour where necessary via human interaction (see Section II-C4). The obtained contours are then used as the initial contours for the next slice. To summarize, Fig. 7 shows the framework of our surface extraction algorithm.

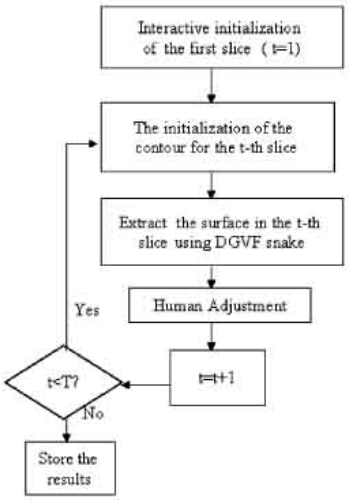

Fig. 7. Algorithm flow diagram.

b) Human adjustment: There are two approaches to human adjustment. The first involves adjustment of the control points. After the control points are moved to the new positions, and are treated as new control points, the new control points are used to construct the corresponding segments using the algorithm in Section II-C3. In the articular cartilage application, it is sufficient to adjust two or three control points. The second approach is to correct the original sample points. This is done by selecting the region to be corrected and deleting it. The operator then defines new points which are part of the correct boundary. This approach is more tedious than the first, but allows finer adjustment.

Fig. 8 shows an example of cartilage surface extraction (in a specimen with an articular cartilage defect) using the B-spline DGVF snake without human adjustment and with human adjustment, respectively. The human adjustment was to reposition two control points in the region of the cartilage defect. Fig. 8 demonstrates that while the selected region was adjusted all other parts of the contour remain unchanged.

D. Cartilage Surface Reconstruction and Thickness Measurement

From the extraction stage, we use the resultant contours to reconstruct the four surfaces and compute the average thickness of the two cartilage layers. When we reconstruct the 3-D surfaces, we use the B-spline to interpolate the slice thickness to match the in-plane resolution, that was interpolated in an earlier step; the final resolution in 0.15 mm.

Appendix 2

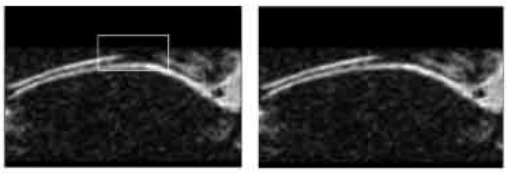

Fig. 8. Local adjustment of the contour by an operator. (a) Contour before adjustment; (b) contour after adjustment.

For thickness computation, we investigated three distinct approaches. The first technique utilizes the normal distance [31], the second technique for thickness computation was developed in [20], which we call M-norm and the third technique for thickness computation is what we developed in this paper, which is called T-norm.

In order to compute the thickness between two surfaces, the M-norm method first obtains an average surface of the two surfaces, then for each point, (x_i, y_i, z_i) in the average surface, the normal vector $(A_i, B_i, C_i)^T$, where T is the vector transpose, is computed. Using (x_i, y_i, z_i) and $(A_i, B_i, C_i)^T$, a line is obtained. The two points, (x_i^u, y_i^u, z_i^u) and (x_i^d, y_i^d, z_i^d), from the intersection of the line to the upper surface and the lower surface respectively, are used to compute the thickness of the point (x_i, y_i, z_i) according to

$$t_i = \sqrt{\left(x_i^u - x_i^d\right)^2 + \left(y_i^u - y_i^d\right)^2} \tag{17}$$

and the average thickness $\bar{t}$ is given by

$$\bar{t} = \frac{1}{K}\sum_{i=1}^{K} t_i \tag{18}$$

where K is the number of points on the average surface.

In the discrete space, the norm vector can be computed by

$$A_i = \frac{(z(y_i, x_i) - z(y_i - 1, x_i) + z(y_i + 1, x_i) - z(y_i, x_i))}{2} \tag{19}$$

$$B_i = \frac{(z(y_i, x_i) - z(y_i, x_i - 1) + z(y_i, x_i + 1) - z(y_i, x_i))}{2} \tag{20}$$

$$C_i = -1. \tag{21}$$

Considering the possible instability of one point, we used the norm vector of the plane obtained by the point (x_i, y_i, z_i) and its nearest points on the medial surface. The norm vector $(\overline{A}_i, \overline{B}_i, \overline{C}_i)^T$ of the plane is obtained by minimizing the following function:

$$\mathbf{Q}(\overline{A}_i, \overline{B}_i, \overline{C}_i) = \frac{1}{2}\sum_{t=1}^{N}(\overline{A}_i\Delta x_t + \overline{B}_i\Delta y_t + \overline{C}_i\Delta z_t)^2 + \left(\overline{A}_i^2 + \overline{B}_i^2 + \overline{C}_i^2 - 1\right)^2 \tag{22}$$

where

$$\Delta x_t = x_t - x_{t-1} \tag{23}$$

$$\Delta y_t = y_t - y_{t-1} \tag{24}$$

$$\Delta z_t = z_t - z_{t-1} \tag{25}$$

and (x_t, y_t, z_t) are the points required to compute the norm vector. The second term in (22) is to normalize the norm vector and avoid the answer degrading to zero vector. From (22), we have (26), shown at the bottom of the page. Equation (26) can be written in matrix form as follows:

$$\frac{\partial \mathbf{Q}(\mathbf{H})}{\partial \mathbf{H}} = \mathbf{M}\mathbf{H} + 2\mathbf{H}^{\mathbf{T}}\mathbf{H}\mathbf{H} - \mathbf{2H} \tag{27}$$

where

$$\mathbf{M} = \begin{pmatrix} \sum_{t=1}^{N}\Delta x_t^2 & \sum_{t=1}^{N}\Delta x_t\Delta y_t & \sum_{t=1}^{N}\Delta x_t\Delta z_t \\ \sum_{t=1}^{N}\Delta x_t\Delta y_t & \sum_{t=1}^{N}\Delta y_t^2 & \sum_{t=1}^{N}\Delta y_t\Delta z_t \\ \sum_{t=1}^{N}\Delta x_t\Delta z_t & \sum_{t=1}^{N}\Delta y_t\Delta z_t & \sum_{t=1}^{N}\Delta z_t^2 \end{pmatrix} \tag{28}$$

$$\mathbf{H} = \begin{pmatrix} \overline{A}_i \\ \overline{B}_i \\ \overline{C}_i \end{pmatrix}. \tag{29}$$

Equation (22) can be solved using the simple iteration method as follows:

$$\mathbf{H}_n = \mathbf{H}_{n-1} - \lambda_{n-1}\left(\mathbf{M}\mathbf{H}_{\mathbf{n-1}} + 2\mathbf{H}_{n-1}^{\mathbf{T}}\mathbf{H}_{n-1}\mathbf{H}_{\mathbf{n-1}} - 2\mathbf{H}_{n-1}\right) \tag{30}$$

where n is the iteration and λ_{n-1} is the step length. We use fixed step length of 0.05 in this paper for convenience. When the

$$\begin{cases} \dfrac{\partial \mathbf{Q}(\overline{A}_i, \overline{B}_i, \overline{C}_i)}{\partial \overline{A}_i} = \overline{A}_i\displaystyle\sum_{t=1}^{N}\Delta x_t^2 + \overline{B}_i\sum_{t=1}^{N}\Delta x_t\Delta y_t + \overline{C}_i\sum_{t=1}^{N}\Delta x_t\Delta z_t + 2\overline{A}_i\left(\overline{A}_i^2 + \overline{B}_i^2 + \overline{C}_i^2 - 1\right) \\ \dfrac{\partial \mathbf{Q}(\overline{A}_i, \overline{B}_i, \overline{C}_i)}{\partial \overline{B}_i} = \overline{A}_i\displaystyle\sum_{i=1}^{N}\Delta x_t\Delta y_t + \overline{B}_i\sum_{i=1}^{N}\Delta y_t^2 + \overline{C}_i\sum_{i=1}^{N}\Delta y_t\Delta z_t + 2\overline{B}_i\left(\overline{A}_i^2 + \overline{B}_i^2 + \overline{C}_i^2 - 1\right) \\ \dfrac{\partial \mathbf{Q}(\overline{A}_i, \overline{B}_i, \overline{C}_i)}{\partial \overline{C}_i} = \overline{A}_i\displaystyle\sum_{i=1}^{N}\Delta x_t\Delta z_t + \overline{B}_i\sum_{i=1}^{N}\Delta z_t\Delta y_t + \overline{C}_i\sum_{i=1}^{N}\Delta z_t^2 + 2\overline{C}_i\left(\overline{A}_i^2 + \overline{B}_i^2 + \overline{C}_i^2 - 1\right) \end{cases} \tag{26}$$

Appendix 2

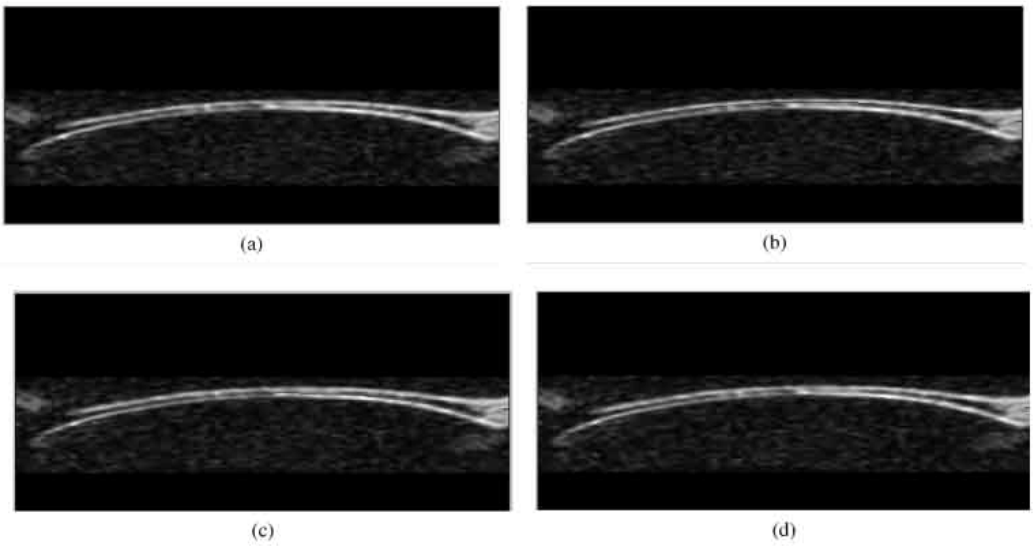

Fig. 9. Examples of contour results using the proposed algorithm.

TABLE I
FOM VALUES OBTAINED FOR THE SEVENTH, ELEVENTH, AND FIFTEENTH SLICES OF TWO IMAGE STACKS USING THE DGVF SNAKE AND THE TRADITONAL GVF SNAKE, RESPECTIVELY

Image Stack	Technique	Frame 7th	11th	15th
1	DGVF	0.87	0.83	0.79
	GVF	0.84	0.67	0.54
2	DGVF	0.93	0.89	0.95
	GVF	0.86	0.74	0.62

iteration converges, we obtain a solution to (30). The M-norm that uses the norm vector obtained by (27)–(30) is the *T-norm*.

III. EXPERIMENTAL RESULTS

A. Comparison of Automatic Segmentation Results

Ground truth data are collected for comparison. We use the manual outlines from an experienced technician as ground truth against which the computer-aided delineation is evaluated. The metric adopted in this paper for comparison is Pratt's figure of merit (FOM) [35].

$$\mathrm{FOM} = \frac{\sum_{i=1}^{I_A} \frac{1}{1+\alpha(d(i)^2)}}{\mathbf{max}(I_A, I_I)} \tag{31}$$

where I_A is the number of boundary pixels delineated by the computer-aided segmentation method, I_I is the number of boundary pixels delineated by the technician. $d(i)$ is the Euclidean distance between a boundary pixel delineated by the technicians and the nearest boundary pixel delineated by computer-aided segmentation and α is a scaling constant, with a suggested value of 1/9 [35]. A perfect match between the boundary pixels delineated by computer-aided segmentation method and the boundary pixels delineated by the technician yields $F = 1$ in (33).

Two image stacks were used to compare the tracking performance of the two external forces: the traditional GVF external forces and the directional GVF external forces. Each image stack contains 20 contiguous image slices from a cartilage sensitive MRI volume. For convenient discussion, we named one image stack as image stack 1 and the other image stack as image stack 2. Fig. 9(a)–(d) shows the tracking results, using the DGVF, for the eleventh frame of image stack 1; for the tibial bone cartilage interface, tibial cartilage surface, talar cartilage surface and talar bone cartilage interface, respectively. The seventh, eleventh, and fifteenth frames of the image stacks were selected to compute the FOM using (31). Table I shows the FOM values computed between the ground truth data and the results obtained with the DGVF and the traditional GVF for the seventh, eleventh, and fifteenth frames of the two image stacks. The results show the directional GVF snake provides higher FOM values compared to those of the standard GVF snake for this sequence.

Appendix 2

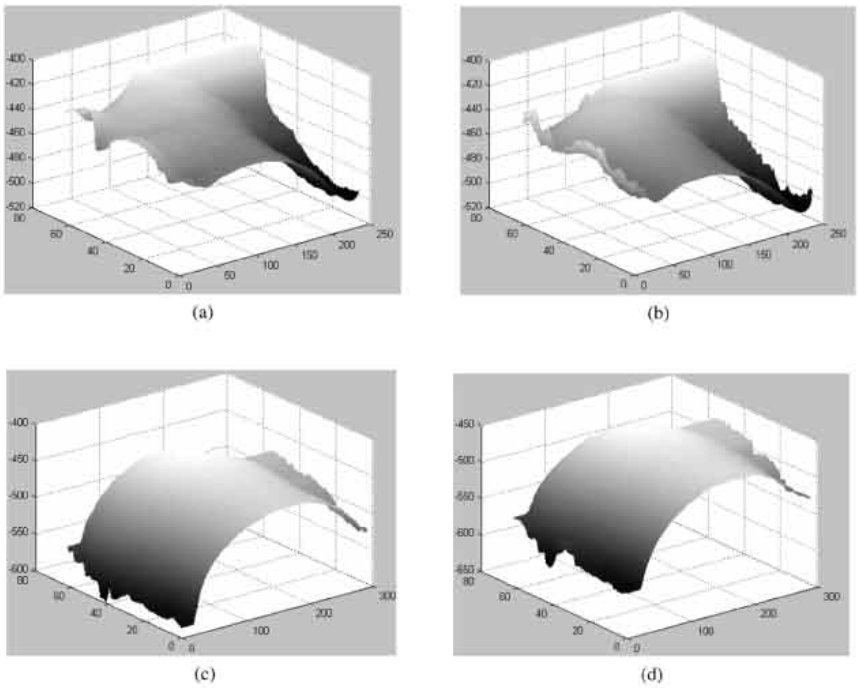

Fig. 10. Surface reconstructed from the boundary extracted from the 2-D slices. (a) Tibial bone-cartilage interface; (b) tibial cartilage surface; (c) talar cartilage surface; (d) talar bone-cartilage interface.

TABLE II
TIBIAL CARTILAGE THICKNESS MEASUREMENT RESULTS FROM FOUR REPEATED MEASUREMENTS (WITH JOINT REPOSITIONING) IN FOUR INDIVIDUAL SPECIMENS

Talus Specimen number		**2**	**3**	**4**
T-norm				
RMS Thickness	1.89	1.92	1.71	1.84
STD of RMS thickness (mm)	0.06	0.02	0.01	0.02
CV of mean thickness (%)	3.00	1.04	0.26	1.05
Normal distance				
RMS Thickness	1.28	1.44	1.03	1.22
STD of RMS thickness (mm)	0.05	0.02	0.03	0.04
CV of mean thickness (%)	4.28	1.24	3.16	3.17
M-norm				
RMS Thickness	1.80	1.84	1.51	1.71
STD of RMS thickness (mm)	0.07	0.02	0.01	0.03
CV of mean thickness (%)	3.95	0.96	0.57	1.71

B. Experimental Results on Surface Reconstruction and Thickness Computation

For cartilage thickness measurements we used images from four human cadaveric ankle joints; each ankle was imaged four times with repositioning of the joint and re-shimming of the magnet between acquisitions. The images were acquired at an isotropic resolution of $0.3 \times 0.3 \times 0.4$ mm, (FOV 160 mm, matrix 512 mm^2). Approximately 30 min elapsed between image acquisitions.

Following completion of the imaging the image data was transferred to a desktop workstation for further processing. Images were linearly interpolated by a factor of 2 to an in-plane resolution of 0.15×0.15 mm, and then noise-reduction was performed on the images. Subsequently, the images were segmented using the DGVF snake method described in Section II-C. The contours generated by segmentation were subsequently used to produce a 3-D reconstruction of the articular cartilage layers with interpolation to an isotropic resolution of 0.15 mm. Fig. 10 shows an example of a 3-D reconstruction of an articular cartilage layer, generated from the segmentation results.

Using the 3-D reconstructions of the cartilage layers for thickness calculations ensures measurements are independent of section orientation and allow for out-of-plane curvature. Cartilage

Appendix 2

TABLE III
TALAR CARTILAGE THICKNESS MEASUREMENT RESULTS FROM FOUR REPEATED MEASUREMENTS (WITH JOINT REPOSITIONING) IN FOUR INDIVIDUAL SPECIMENS

Talus Specimen number	1	2	3	4
T-norm				
RMS Thickness	1.82	1.84	1.70	1.83
STD of RMS thickness (mm)	0.07	0.02	0.04	0.02
CV of mean thickness (%)	3.58	0.99	2.61	0.86
Normal distance				
RMS Thickness	1.31	1.41	1.12	1.36
STD of RMS thickness (mm)	0.09	0.05	0.11	0.06
CV of mean thickness (%)	7.00	3.33	10.13	4.34
M-norm				
RMS Thickness	1.72	1.75	1.57	1.75
STD of RMS thickness (mm)	0.08	0.02	0.13	0.03
CV of mean thickness (%)	4.39	1.21	8.23	1.68

TABLE IV
MEAN VALUES OF TIBIAL CARTILAGE MORPHOLOGY AND THE RATIO OF INTERSUBJECT VARIABILITY VERSUS TECHNICAL PRECISION, FOR ALL SPECIMENS

Talar cartilage thickness	T-norm	Normal distance	M-norm
RMS CV(%) of mean thickness – all specimens	1.34	2.97	1.80
Mean RMS thickness – all specimens (mm)	1.84	1.24	1.72
STD of mean RMS thickness – all specimens (mm)	0.09	0.17	0.15
RMS STD – all specimens (mm)	0.03	0.04	0.04
Intersubject variability/Technical precision	2.93	4.42	3.70

TABLE V
MEAN VALUES OF TALAR CARTILAGE MORPHOLOGY AND THE RATIO OF INTERSUBJECT VARIABILITY VERSUS TECHNICAL PRECISION, FOR ALL SPECIMENS

Talar cartilage thickness	T-norm	Normal distance	M-norm
RMS CV(%) of mean thickness – all specimens	2.01	6.20	3.88
Mean RMS thickness – all specimens (mm)	1.80	1.30	1.70
STD of mean RMS thickness – all specimens(mm)	0.06	0.13	0.09
RMS STD – all specimens (mm)	0.04	0.08	0.08
Intersubject variability/Technical precision	1.54	1.56	1.17

thickness of the tibia and talus was calculated for each specimen using the three methods described in Section II (T-norm, M-norm and normal distance). Thickness measurements were made at every voxel on the cartilage surface (4444 $\mathrm{sites/cm^2}$).

To determine the precision (reproducibility) of the MRI-based cartilage measurements the root-mean square average (RMS thickness), standard deviation (SD) and coefficient of variation of mean thickness (CV) were determined from the four repeated image data sets for each of the four specimens for the individual tibia and talar cartilage layers; the results are shown in Tables II and III, respectively.

The RMS CV of mean thickness—all specimens for cartilage thickness ranged from 1.34% (tibia T-norm) to 6.20% (talus normal distance). For cumulative values (tibia and talus combined), the RMS CV mean thickness—all specimens was <4.6% in the worst case. The mean RMS thickness—all specimens from the four repeated measurements in each of the four specimens ranged from 1.24 ± 0.17 mm (normal distance) to 1.84 ± 0.09 mm (T-norm) in the tibia, see Table IV, and 1.30 ± 0.13 mm (normal distance) to 1.80 ± 0.06 mm (T-norm) in the talus, see Table V.

Comparing the intersubject variability (SD of mean RMS thickness—all specimens) to the technical precision [36](RMS SD—all specimens) of the segmentation, the ratios ranged from 1.17 (talus m-norm, Table IV) to 4.42 (tibial normal distance, Table V). The ratios reflect that the mean articular cartilage thickness has a relatively low intersubject variability, particularly for talar cartilage.

IV. DISCUSSION

The objective of this study was to develop a reliable, reproducible and robust segmentation algorithm for surface tracking of the thin articular cartilage layers of a highly congruent joint, i.e., the ankle joint. To our knowledge this is the first study to investigate the application of a directional gradient vector flow snake for segmenting thin congruent cartilage layers. We have experimentally tested the performance of the segmentation algorithm and 3-D reconstruction method developed in this study, and compared three methods for making thickness computations.

The average coefficients of variation for the thickness of all cartilage layers was 1.7% using the T-norm; 2.8% using the M-norm and 4.6% using the normal distance. The coefficients of variation achieved using the normal distance are slightly greater than those seen in the knee joint, which are typically 2.0%–3.4%, where as the coefficients of variation using the T-norm method are slightly better than those seen in the knee

Appendix 2

joint [14], [21], [37], [38]. When compared to the earlier studies which have attempted to make quantitative measurement of the ankle cartilage we have shown better accuracy and reproducibility [7], [39]. These results are very encouraging given that the mean ankle cartilage thickness is on the order 1.2 mm (normal distance) to 1.8 mm (T-norm) compared to the much thicker cartilage layers (4–5 mm) seen in the knee joint. By comparing the intersubject variability to technical precision we have also shown that using the T-norm and normal distance measurement techniques individual cartilage layers with a high or low mean thickness can be reliably discriminated.

Our technical precision data demonstrates that the RMS average SD ranged from 0.032 mm (tibia, T-norm) to 0.082 mm (talus, normal distance), which far exceeded the resolution ($0.3\ \mathrm{mm}^3$) of the scan. However, we must be aware that when an interpolation is applied to the original data set that potentially, sensitivity to small focal defects (<0.3 mm) is lost; but for assessing global longitudinal variability in cartilage thickness interpolation helps to improve accuracy.

The MRI sequence used in this study is relatively long (17 min, 25 s) and represents the upper time limit for use on patients; however, Al Ali *et al.* [7] used a nonisotropic sagittal sequence with a scan time of 19 min, 40 s on volunteers. They reported no motion artifacts and suggested that the imaging time was acceptable for *in vivo* use. Moreover, as the sequence they used was nonisotropic because they felt they could not achieve sufficient image quality for reliable segmentation with a single image acquisition, as a result they were unable to make accurate 3-D reconstructions and advocated performing a repeat scan in the coronal plane to acquire full 3-D reconstructions. In the future, scan times will can be halved as 3T MRI scanners are becoming more widely available for clinical use.

We have compared three different techniques for computing the thickness of the articular cartilage. The normal distance technique provides a measurement of the true normal thickness of the cartilage from one surface (bone surface) to another (cartilage surface). The T-norm method generates a normal to the 'average' surface and calculates the distance between two points where the vector intersects the cartilage and bone surfaces; hence, the T-norm does not provide a true normal thickness. The M-norm is a simplified 2-D measurement that does take account of any out of plane curvature of the surfaces and, therefore, is not suitable for longitudinal studies. However, the M-norm is useful for comparing our results to those of other investigators, e.g., [20].

Since the most important factor in a tool for detecting injury and degeneration is the ability to detect change in thickness over time rather than measure the true thickness at any point in time we would advocate the use of the T-norm thickness computation method. The results from the T-norm computations demonstrate a superior technical precision and lower CV making it more useful for longitudinal studies of articular cartilage degeneration than the normal distance method. Where the true normal thickness of the cartilage is required, such as user defined regions of interest, the normal distance technique could be substituted for the T-norm method.

The results of the four repeated measurements in each specimen demonstrate the reproducibility of the segmentation and reconstruction method presented in this paper. The process described offers a useful tool for early diagnosis and monitoring of degenerative change occurring in the thin articular cartilage layer of highly congruent joints; i.e., if we serially image a patient's ankle using MRI at 6 month intervals following an injury, we can reliably detect degenerative change and thinning of the articular cartilage layers. As the intersubject variability exceeds the technical precision of technique, we are able to use our method to perform longitudinal studies of the ankle joint articular cartilage.

V. Conclusion

This paper studies ankle articular cartilage surface tracking using GVF B-spline snake. Because the cartilage is very thin and the layers are closely apposed to each other, the traditional GVF B-spline snake is not suitable for accurate tracking of the cartilage surface. Thus, we have developed a directional GVF snake for tracking the surface of the articular cartilage of the ankle. We have compared our algorithm with the traditional GVF snake. Experiments show that the DGVF snakes increases the FOM values yielded by the traditional GVF B-spline snake and the number of successfully segmented frames given by the traditional GVF B-spline snake.

The accurate surface tracking possible with the DGVF snake allows us to use the tracking results obtained to construct a 3-D model of the articular cartilage, which is used to compute the thickness of the cartilage and the volume of the cartilage. In order to make the thickness measurement more reproducible, a new thickness computation approach is proposed. Experimental results have shown that the new thickness computation approach is more effective than the existing methods. The precise reproducible measurements of quantitative parameters such as thickness that are possible when using the DGVF snake provides a useful tool to monitor changes in the articular cartilage typically seen in degenerative diseases such as posttraumatic osteoarthritis of the ankle.

References

[1] E. Yelin and L. F. Callahan, "The economic cost and social and psychological impact of musculoskeletal conditions. National arthritis data work groups," *Arthritis Rheum.*, vol. 38, no. 10, pp. 1351–1362, Oct. 1995.

[2] R. Burgkart, C. Glaser, A. Hyhlik-Durr, K. H. Englmeier, M. Reiser, and F. Eckstein, "Magnetic resonance imaging-based assessment of cartilage loss in severe osteoarthritis: accuracy, precision, and diagnostic value," *Arthritis Rheum.*, vol. 44, no. 9, pp. 2072–2077, Sept. 2001.

[3] R. Burgkart, C. Glaser, S. Hinterwimmer, M. Hudelmaier, K. H. Englmeier, M. Reiser, and F. Eckstein, "Feasibility of T and Z scores from magnetic resonance imaging data for quantification of cartilage loss in osteoarthritis," *Arthritis Rheum.*, vol. 48, no. 10, pp. 2829–2835, Oct. 2003.

[4] F. Eckstein, M. Reiser, K. H. Englmeier, and R. Putz, "*In vivo* morphometry and functional analysis of human articular cartilage with quantitative magnetic resonance imaging—from image to data, from data to theory," *Anat. Embryol. (Berlin)*, vol. 203, no. 3, pp. 147–173, Mar. 2001.

Appendix 2

[5] F. Eckstein, L. Heudorfer, S. C. Faber, R. Burgkart, K. H. Englmeier, and M. Reiser, "Long-term and resegmentation precision of quantitative cartilage MR imaging (qMRI)," *Osteoarthritis. Cartilage.*, vol. 10, no. 12, pp. 922–928, Dec. 2002.

[6] C. G. Peterfy and H. K. Genant, "Emerging applications of magnetic resonance imaging in the evaluation of articular cartilage," *Radiol. Clin. North Am.*, vol. 34, no. 2, pp. 195–213, Mar. 1996, ix.

[7] D. Al Ali, H. Graichen, S. Faber, K. H. Englmeier, M. Reiser, and F. Eckstein, "Quantitative cartilage imaging of the human hind foot: precision and inter-subject variability," *J. Orthop. Res.*, vol. 20, no. 2, pp. 249–256, Mar. 2002.

[8] F. Eckstein, H. Sittek, S. Milz, R. Putz, and M. Reiser, "The morphology of articular cartilage assessed by magnetic resonance imaging (MRI). Reproducibility and anatomical correlation," *Surg. Radiol. Anat.*, vol. 16, no. 4, pp. 429–438, 1994.

[9] F. Eckstein, H. Sittek, S. Milz, E. Schulte, B. Kiefer, M. Reiser, and R. Putz, "The potential of magnetic resonance imaging (MRI) for quantifying articular cartilage thickness—a methodological study," *Clin. Biomech. (Bristol., Avon.)*, vol. 10, no. 8, pp. 434–440, Dec. 1995.

[10] H. Graichen, V. Springer, T. Flaman, T. Stammberger, C. Glaser, K. H. Englmeier, M. Reiser, and F. Eckstein, "Validation of high-resolution water-excitation magnetic resonance imaging for quantitative assessment of thin cartilage layers," *Osteoarthritis. Cartilage.*, vol. 8, no. 2, pp. 106–114, Mar. 2000.

[11] Z. A. Cohen, D. M. McCarthy, S. D. Kwak, P. Legrand, F. Fogarasi, E. J. Ciaccio, and G. A. Ateshian, "Knee cartilage topography, thickness, and contact areas from MRI: *in-vitro* calibration and *in-vivo* measurements," *Osteoarthritis. Cartilage.*, vol. 7, no. 1, pp. 95–109, Jan. 1999.

[12] S. C. Faber, F. Eckstein, S. Lukasz, R. Muhlbauer, J. Hohe, K. H. Englmeier, and M. Reiser, "Gender differences in knee joint cartilage thickness, volume and articular surface areas: assessment with quantitative three-dimensional MR imaging," *Skeletal Radiol.*, vol. 30, no. 3, pp. 144–150, Mar. 2001.

[13] S. Lukasz, R. Muhlbauer, S. Faber, K. H. Englmeier, M. Reiser, and F. Eckstein, "[Sex-specific analysis of cartilage volume in the knee joint—a quantitative MRI-based study]," *Anat. Anz.*, vol. 180, no. 6, pp. 487–493, Dec. 1998.

[14] C. G. Peterfy, C. F. van Dijke, D. L. Janzen, C. C. Gluer, R. Namba, S. Majumdar, P. Lang, and H. K. Genant, "Quantification of articular cartilage in the knee with pulsed saturation transfer subtraction and fat-suppressed MR imaging: optimization and validation," *Radiology*, vol. 192, no. 2, pp. 485–491, Aug. 1994.

[15] L. Pilch, C. Stewart, D. Gordon, R. Inman, K. Parsons, I. Pataki, and J. Stevens, "Assessment of cartilage volume in the femorotibial joint with magnetic resonance imaging and 3D computer reconstruction," *J. Rheumatol.*, vol. 21, no. 12, pp. 2307–2321, Dec. 1994.

[16] M. Schnier, F. Eckstein, J. Priebsch, M. Haubner, H. Sittek, C. Becker, R. Putz, K. H. Englmeier, and M. Reiser, "[Three-dimensional thickness and volume measurements of the knee joint cartilage using MRI: validation in an anatomical specimen by CT arthrography]," *Rofo*, vol. 167, no. 5, pp. 521–526, Nov. 1997.

[17] K. Jonsson, K. Buckwalter, M. Helvie, L. Niklason, and W. Martel, "Precision of hyaline cartilage thickness measurements," *Acta Radiol.*, vol. 33, no. 3, pp. 234–239, May 1992.

[18] J. C. Waterton, V. Rajanayagam, B. D. Ross, D. Brown, A. Whittemore, and D. Johnstone, "Magnetic resonance methods for measurement of disease progression in rheumatoid arthritis," *Magn. Reson. Imag.*, vol. 11, no. 7, pp. 1033–1038, 1993.

[19] M. D. Robson, R. J. Hodgson, N. J. Herrod, J. A. Tyler, and L. D. Hall, "A combined analysis and magnetic resonance imaging technique for computerised automatic measurement of cartilage thickness in the distal interphalangeal joint," *Magn. Reson. Imag.*, vol. 13, no. 5, pp. 709–718, 1995.

[20] S. Solloway, C. Hutchison, J. Waterton, and C. Taylor, "The use of active shape models for making thickness measurements of articular cartilage from MR images," *Magn. Reson. Med.*, vol. 36, pp. 943–952, 1997.

[21] F. Eckstein, J. Westhoff, H. Sittek, K. P. Maag, M. Haubner, S. Faber, K. H. Englmeier, and M. Reiser, "*In vivo* reproducibility of three-dimensional cartilage volume and thickness measurements with MR imaging," *AJR Am. J. Roentgenol.*, vol. 170, no. 3, pp. 593–597, Mar. 1998.

[22] M. Haubner, F. Eckstein, M. Schnier, A. Losch, H. Sittek, C. Becker, H. Kolem, M. Reiser, and K. H. Englmeier, "A noninvasive technique for 3-dimensional assessment of articular cartilage thickness based on MRI. Part 2: Validation using CT arthrography," *Magn. Reson. Imag.*, vol. 15, no. 7, pp. 805–813, 1997.

[23] A. Losch, F. Eckstein, M. Haubner, and K. H. Englmeier, "A noninvasive technique for 3-dimensional assessment of articular cartilage thickness based on MRI. Part 1: Development of a computational method," *Magn. Reson. Imag.*, vol. 15, no. 7, pp. 795–804, 1997.

[24] M. Kass, A. Witkin, and D. Terzopolous, "Snakes: active contour models," *Int. J. Comput. Vis.*, vol. 1, no. 4, pp. 321–331, 1987.

[25] C. Xu and J. L. Prince, "Snakes, shapes, and gradient vector flow," *IEEE Trans. Image Process.*, vol. 7, no. 3, pp. 359–369, Mar. 1998.

[26] ——, "Generalized gradient vector flow external force for active contours," *Signal Process.*, vol. 71, no. 2, pp. 131–139, 1998.

[27] D. H. Chung and G. Sapiro, "Segmenting skin lesions with partial-differential-equations-based image processing algorithms," *IEEE Trans. Med. Imag.*, vol. 19, no. 7, pp. 763–767, Jul. 2000.

[28] P. Brigger, J. Hoeg, and M. Unser, "B-spline snakes: a flexible tool for parametric contour detection," *IEEE Trans. Image Process.*, vol. 9, no. 9, pp. 1484–1496, Sep. 2000.

[29] A. Blake and M. Isard, *Active Contours: The Application of Techniques From Graphics, Vision, Control Theory and Statistics to Visual Tracking of Shapes in Motion.* Berlin, Germany: Springer-Verlag, 1998.

[30] A. K. Klein, F. Lee, and A. A. Amini, "Quantitative coronary angiography with deformable spline models," *IEEE Trans. Med. Imag.*, vol. 16, no. 5, pp. 468–482, Oct. 1997.

[31] F. Heuer, M. Sommers, III, J. R. , and M. Bottlang, "Estimation of cartilage thickness from joint surface scans: comparative analysis of comparative analysis of computational methods," in *Proc. 2001 Bioengineering Conf. ASME 2001*, 2001, vol. 50, pp. 569–570.

[32] G. Gerig, O. Kubler, R. Kikinis, and F. A. Jolesz, "Nonlinear anisotropic filtering of MRI data," *IEEE Trans. Med. Imag.*, vol. 11, no. 2, pp. 221–232, Jun. 1992.

[33] Y. Yu and S. T. Acton, "Speckle reducing anisotropic diffusion," *IEEE Trans. Image Process.*, vol. 11, no. 11, pp. 1260–1270, Nov. 2002.

[34] J. Foley, A. Dam, S. Feiner, and J. Hughes, *Computer Graphics: Principles and Practice.* Reading, MA: Addison Wesley, 1996.

[35] W. Pratt, *Digital Image Processing.* New York: Wiley, 1978, pp. 495–501.

[36] C. C. Gluer, G. Blake, Y. Lu, B. A. Blunt, M. Jergas, and H. K. Genant, "Accurate assessment of precision errors: how to measure the reproducibility of bone densitometry techniques," *Osteoporos. Int.*, vol. 5, no. 4, pp. 262–270, 1995.

[37] A. A. Kshirsagar, P. J. Watson, J. A. Tyler, and L. D. Hall, "Measurement of localized cartilage volume and thickness of human knee joints by computer analysis of three-dimensional magnetic resonance images," *Invest. Radiol.*, vol. 33, no. 5, pp. 289–299, May 1998.

[38] T. Stammberger, F. Eckstein, K. H. Englmeier, and M. Reiser, "Determination of 3D cartilage thickness data from MR imaging: computational method and reproducibility in the living," *Magn. Reson. Med.*, vol. 41, no. 3, pp. 529–536, Mar. 1999.

[39] T. C. Tan, D. M. Wilcox, L. Frank, C. Shih, D. J. Trudell, D. J. Sartoris, and D. Resnick, "MR imaging of articular cartilage in the ankle: comparison of available imaging sequences and methods of measurement in cadavers," *Skeletal Radiol.*, vol. 25, no. 8, pp. 749–755, Nov. 1996.

Jinshan Tang (M'00–SM'03) received the Ph.D. degree from Beijing University of Posts and Telecommunications, Beijing, China, in 1998.

From September 1998 to June 2000, he worked as an invited researcher in ATR Media Integration and Communications Research Laboratories (MIC), Kyoto, Japan. In June 2000, he went to Harvard Medical School to work on image enhancement technology. From December 2001 to September 2004, he worked as a Research Scientist in Department of Electrical and Computer Engineering, University of Virginia, Charlottesville. From September to June 2005, he worked on medical imaging for cancer detection in National Cancer Institute, National Institute of Health, Bethesda, MD. Currently, he is working on imaging technology at Intel, Boston, MA. His research interests are medical image analysis and medical imaging, computer-aided diagnosis and detection, medical image database and data mining, and multimedia technology and applications.

Appendix 2

Steven Millington received the M.D. degree from the University of Nottingham, Nottingham, U.K., in 1998.

He is with the Department of Trauma Surgery at the Medical University of Vienna, Vienna, Austria. He previously worked as an Orthopaedic Research Fellow at the University of Virginia, Charlottesville, and was an Orthopaedic and Trauma Surgeon, at the Technical University of Graz, Graz, Austria. He has a keen interest in articular cartilage imaging and biomechanics.

Dr. Millington is a member of the Royal College of Surgeons of Edinburgh since 2002.

Scott T. Acton (S'88–M'93–SM'99) received the M.S. degree in electrical and computer engineering and the Ph.D. degree in electrical and computer engineering from the University of Texas at Austin in 1990 and 1993, respectively, where he was a Microelectronics and Computer Development Fellow. He received the B.S. degree in electrical engineering from Virginia Tech, Blacksburg, in 1988 as a Virginia Scholar and Marshall Hahn Fellow.

He has worked in industry for AT&T, Oakton, VA., the MITRE Corporation, McLean, VA. and Motorola, Inc., Phoenix, AZ. and in academia for Oklahoma State University, Stillwater. Currently, he is a Professor at the University of Virginia (U.Va.), Charlottesville, where he is a member of the Charles L. Brown Department of Electrical and Computer Engineering and the Department of Biomedical Engineering.

He is an active participant in the IEEE, served as Associate Editor for the IEEE TRANSACTIONS ON IMAGE PROCESSING and as Associate Editor the IEEE SIGNAL PROCESSING LETTERS. He is the 2004 Technical Program Chair and the 2006 General Chair for the *Asilomar Conference on Signals, Systems and Computers*. His research interests include anisotropic diffusion, basketball, active contours, biomedical segmentation problems, and biomedical tracking problems.

At U.Va., Dr. Acton was named the Outstanding New Teacher in 2002 and was elected a Faculty Fellow in 2003. He was a 2005 finalist in the Florida First Coast Novel Contest.

Jeff Crandall received the Ph.D. degree in mechanical and aerospace engineering from the University of Virginia, Charlottesville, in 1994.

He is an Associate Professor in the Departments of Mechanical and Aerospace Engineering and Biomedical Engineering at the University of Virginia, Charlottesville. In addition, he serves as the Director of the University's Center for Applied Biomechanics. His research focuses on understanding the human body's response and injury mechanisms during dynamic loading. Applications of his research include impact biomechanics, transportation safety, orthopedic studies, military and blast trauma, and sports-related injuries. His investigations focus primarily on the extremities, thorax, and head with an emphasis on neurological and musculoskeletal trauma.

Dr. Crandall is a member of the Society of Automotive Engineers, the American Society of Biomechanics, and the American Society of Mechanical Engineers. He is past-president of the Association for the Advancement of Automotive Medicine and is currently a member of the board for the International Research Committee on the Biomechanics of Impact.

Shepard Hurwitz received the M.D. degree from Columbia University College of Physicians and Surgeons, New York, in 1976. He completed postdoctoral fellowships in trauma surgery and foot/ankle. He has also taken advanced study in orthopaedic biomechanics, focusing on gait mechanics and fracture characteristics of bones.

He is the S. Ward Casscells Professor of Orthopaedic Surgery at the University of Virginia Health System, Charlottesville. He is also Adjunct Professor of Mechanical Engineering at the University of Virginia School of Engineering and Applied Science, and is Medical Director of the Center for Applied Biomechanics at the University of Virginia (U.Va.), Charlottesville. He is an Orthopaedic Surgeon with a specialty practice in problems of the foot and ankle. His past experience includes faculty positions at George Washington University, the University of Rochester, and Cornell University.

Appendix 3. 2-D Quantitative segmentation study

Quantitative and Topographical Evaluation of Ankle Articular Cartilage Using High Resolution MRI

Steven A. Millington,[1] Bing Li,[2] Jinshan Tang,[2] Siegfried Trattnig,[1] Jeff R. Crandall,[3] Shepard R. Hurwitz,[4] Scott T. Acton[2]

[1]Centre of Excellence, High Field MR, Medical University of Vienna, Leitermayergasse 31/20, A1180, Vienna, Austria

[2]Department of Electrical and Computer Engineering, University of Virginia, Charlottesville, Virginia 22904

[3]Center for Applied Biomechanics, University of Virginia, Charlottesville, Virginia 22902

[4]Department of Orthopaedic and Trauma Surgery, University of Virginia, Charlottesville, Virginia 22908

Received 23 February 2006; accepted 19 May 2006

Published online 3 October 2006 in Wiley InterScience (www.interscience.wiley.com). DOI 10.1002/jor.20267

ABSTRACT: The objectives of this study were to quantitatively evaluate the articular cartilage layers of the ankle and describe the cartilage topographical distribution across the joint surfaces using high resolution MRI and image segmentation. An anisotropic diffusion noise reduction algorithm and a directional gradient vector flow (dGVF) snake segmentation algorithm were applied to cartilage sensitive MR images. Eight cadaveric ankles were studied. Six repeated data sets were acquired in five of the ankles. Quantitative parameters were calculated for each cartilage layer; coefficients of variation (CV) were calculated from the six repeated data sets; and 3D thickness distribution maps were generated. The noise reduction algorithm produced marked image enhancement. Mean cartilage thickness ranged from 0.91 ± 0.08 mm in the fibula to 1.34 ± 0.14 mm in the talus. Mean cartilage volume was 3.32 ± 0.55 ml, 1.72 ± 0.25 ml, and 0.35 ± 0.06 ml for the talus, tibia, and fibula, respectively. Mean CV ranged 2.82%–5.04% for quantitative parameters in the talus and tibia. The reported noise reduction and segmentation technique allow precise extraction of ankle cartilage and 3D reconstructions show that the thickest cartilage occurs over the talar shoulders, where osteochondritits dissecans (OCD) lesions commonly occur. © 2006 Orthopaedic Research Society. Published by Wiley Periodicals, Inc. J Orthop Res 25:143–151, 2007

Keywords: ankle; articular cartilage; MRI; image segmentation

INTRODUCTION

Unlike other major joints of the lower limb, the ankle is rarely affected by primary osteoarthritis. However, the ankle appears to have a greater predisposition to the development of posttraumatic osteoarthritis than the hip and knee joints.[1,2] Furthermore, ankle posttraumatic osteoarthritis often develops in a younger population and more rapidly than in other joints.[3–5] Another challenging problem in the ankle is osteochondritits dissecans (OCD) of the talar body, which typically occurs over the anterior-lateral or posterior-medial shoulders of the talus.[6] Talar OCD lesions are a well known cause of pain, recurrent synovitis, loose bodies, and altered joint mechanics.[7]

Precise evaluation of a patient's degenerative joint(s), qualitatively and quantitatively is technically demanding, especially in highly congruent joints with thin articular cartilage. However, in order to clinically evaluate present and future treatments, we must be able to precisely and reproducibly image and quantify the articular cartilage of these joints.[8–12]

Magnetic resonance imaging (MRI) of articular cartilage is becoming a useful tool for the assessment and monitoring of articular cartilage injury and degeneration. It is an excellent research instrument for articular tissue and there is considerable potential for expansion of the role of MRI in clinical practice.[13–16]

Extensive work by Eckstein et al.[17–20] has shown spoiled 3D gradient echo (FLASH) sequences with water excitation to be particularly useful. However, most articular cartilage imaging

Correspondence to: Steven A. Millington (Telephone: +43 650 962 0402; Fax: +43 316 873 9402; E-mail: steven.millington@meduniwien.ac.at)

Appendix 3

work has concentrated on the knee joint,[21–26] which displays the thickest articular cartilage layers in the human body. There have been a few notable investigations[17,20,27,28] that have examined joints with thinner articular cartilage layers (<3 mm thick), which are more typical for joints of the human body.

The accuracy of the segmentation of thin cartilage layers in congruent joints can have a significant effect on the percentage errors in quantitative measurements of the articular cartilage (e.g., thickness and volume). Previous studies have performed segmentation using a variety of techniques including: manual segmentation,[18,21,29–32] seed point and region growing algorithms,[33–35] and edge detection followed by spline-based smoothing,[21] all of which have limitations in noisy images of thin cartilage layers of highly congruent joints. Fully manual surface extraction and segmentation[18,21,29–32] is tedious, time consuming, and prone to subjective judgment. Fully automated processes[36,37] at present cannot accurately and reproducibly extract and segment articular cartilage layers in areas where the boundary is not sufficiently distinct or in noisy images.

Trattnig et al.[38] and Ba-Ssalamah et al.[39] reported sequences with the potential for a fourfold reduction in image acquisition time. They showed that fat suppressed multi-shot echo planar imaging sequences were comparable to fat suppressed gradient recalled images for detection of lesions. Unfortunately, the resolution of the sequence for the ankle joint ($0.625 \times 0.625 \times 1.5$ mm[39]) is not suitable for precise quantification of cartilage thickness and volume. Similarly, the sequence used by Tan et al.[40] lacked sufficient resolution ($0.83 \times 0.625 \times 3.0$ mm) which combined with the use of a thresholding technique to measure thickness led to errors of $\pm 100\%$ in their measurements. Al-Ali et al.[17] and Eckstein et al.[41] used a B-spline snake image segmentation program and reconstructed the cartilage layers of the talar dome and tibial plafond after image interpolation. However, a nonisotropic sequence was used; therefore, their measurements do not include the shoulders of the talus or the malleolar surfaces, and a subjective decision was required to determine the edges of the talar dome.

The purpose of this study was firstly to evaluate quantitative parameters of the cartilage layers of the entire ankle joint using high resolution MRI. Secondly, to test the precision (reproducibility) of the quantitative measurements made using our recently described semi-automated directional gradient vector flow (dGVF) snake segmentation algorithm.[42] The final aim was to describe the topographical distribution of articular cartilage over the surfaces of the ankle joint.

MATERIALS AND METHODS

Ethical approval for this study was provided by the Human Usage Review Panel and the University of Virginia Human Investigations Committee. Eight fresh frozen human, male cadaveric lower leg and foot complexes harvested from five cadavers, were studied. The mean age was 52.3 years. From the available medical histories, there were no reports of trauma to the lower limbs or musculoskeletal disease in the ankle(s) of the subjects.

The MR images were acquired using a 1.5 T MR scanner (Magnetom vision, Siemens, Erlangen, Germany) with a circularly polarized transmit and receive extremity coil. A sagittal spoiled 3D gradient echo sequence, fast low angle shot (FLASH), with selective water excitation imaging sequence was used, TR of 18 ms, TE 7.65 ms, flip angle 25°, in-plane resolution 0.3 mm × 0.3 mm, slice thickness 0.3 mm, field of view 160 mm, and a 512^2 matrix. The acquisition time was 17 min 14 s. As the image resolution was isotropic, we were able to reconstruct the images in three perpendicular planes (sagittal, coronal, and axial).

In five cadaveric ankles, six repeated data sets were acquired with repositioning of the ankle and re-shimming of the magnet between acquisitions. In all other specimens, a single data set was acquired.

All image data sets were then transferred and stored on a desktop work station for postprocessing and segmentation. For this study, coronal images were chosen for segmentation as they allow visualization of all the relevant cartilage. The postprocessing and segmentation procedures consist of a number of steps. First, the image volume is cropped to a smaller volume containing all the cartilage layers of the ankle, but excluding unnecessary image data such as the distal tibial shaft. Secondly, the images are linearly interpolated (doubling the number of voxels in each row and column of each slice) to an in-plane resolution of 0.15 mm × 0.15 mm. The third step was to run an anisotropic diffusion "denoising" algorithm.[43] The anisotropic diffusion technique preserves the quality of edges within the images by using a nonlinear filtering method that encourages smoothing in homogeneous regions while inhibiting smoothing across the edges. The anisotropic diffusion algorithm increases the robustness of the dGVF snake to noise. In the presence of noise, the dGVF snake may produce a boundary which requires considerable manual editing. However, the use of the anisotropic diffusion algorithm prior to segmentation improves the performance of the dGVF snake by enhancing the cartilage and bone boundaries, and reduces the need for manual editing (Fig. 1).

DOI 10.1002/jor

Appendix 3

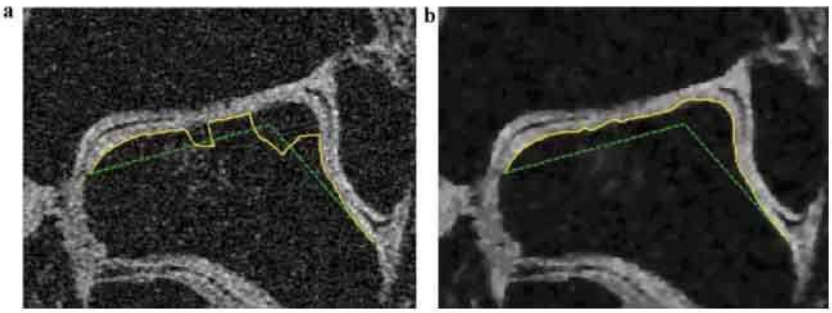

Figure 1. A typical coronal MRI slice acquired using the isotropic cartilage sequence. (a) Before noise reduction and (b) after noise reduction using the anisotropic diffusion denoising algorithm. The dashed line represents a very simple approximate initialization for the bone boundary and the solid line represents the boundary detected by the dGVF snake.

The fourth step was to segment the talar, tibia, and fibula cartilage layers using a semi-automated directional gradient vector flow (dGVF) snake algorithm.[43] Briefly, a manual initialization is required for each border in the first image segmented, the dGVF snake algorithm is then applied, and the resulting contours serve as the initialization for the borders in the next image. The snake is an active contour that is optimized with respect to curve smoothness and collocation with the strong image edges. This approach takes account of the 3D context of the image data and facilitates segmentation in regions where the cartilage surfaces are closely apposed. The system is interactive and allows manual editing of the segmentation lines in each image if required. After completing the full segmentation, the final step was to interpolate the data to an isotropic resolution of 0.15 mm^3 and generate 3D reconstructions of each cartilage layer.

For ground truth data, expert manual tracings were used in order to evaluate the border positioning of the computer-aided segmentation. The Pratt figures of merit (FOM),[44] calculated using Equation 1, were computed to assess the computer-aided border positioning compared to manual segmentation. The FOM is given by:

$$FOM = \frac{\sum_{i=1}^{I_A} \frac{1}{1+\alpha(d(i)^2)}}{\max(I_A, I_M)}. \quad (1)$$

In Equation 1, I_A is the number of boundary pixels delineated by the computer-aided segmentation method, I_M is the number of boundary pixels delineated by manual segmentation. $d(i)$ is the Euclidean distance between a boundary pixel delineated by the expert and the nearest boundary pixel delineated by dGVF snake segmentation algorithm and α is a scaling constant, with a suggested value of 1/9.[44] A FOM = 1 represents a perfect match between the boundary pixels delineated by computer-aided segmentation method and the boundary pixels delineated by manual segmentation. The relationship between the FOM and the average distance between the computer-aided segmentation boundary and a ground truth derived boundary is shown in Figure 2.

Two image stacks each containing 20 contiguous image slices through the middle of the talus in the region of cartilage-to-cartilage contact were selected from the image data set. Each image stack was manually segmented by an expert, experienced in cartilage segmentation, who was blinded to the results of the dGVF snake segmentation. The FOM values were then calculated using Equation 1.

Three-dimensional reconstructions were used to make quantitative measurements and visualize the thickness distribution of the articular cartilage. Thickness was determined at each voxel on the cartilage surface (4,444 sites/cm^2) using a 3D Euclidean distance transformation.[45] Cartilage surface area and bone cartilage interface (BCI) area were measured from the triangulated mesh[46] and the cartilage volume of each layer was determined by integration of the voxels.[30]

In order to evaluate the precision (reproducibility) of our approach, we determined the mean, standard deviation (SD) and coefficients of variation (CV%), for each of the quantitative parameters studied from the six repeated data sets in five ankles. The root mean square (RMS) average[47] of the CVs and SD from the individual joints were used to calculated for each of the parameters measured in the talar, tibia, and fibula cartilage layers.

The performance of the anisotropic diffusion algorithm was evaluated quantitatively by measuring the variance reduction ratio.[48,49] The variance reduction ratio is defined as the ratio of variance reduction due following noise reduction and the original variance in a defined region of interest. A value of 0 means no noise reduction, and a value of 1 means perfect noise reduction. We used this test in order to quantify the improvement given by the anisotropic diffusion process, thus avoiding

DOI 10.1002/jor

Appendix 3

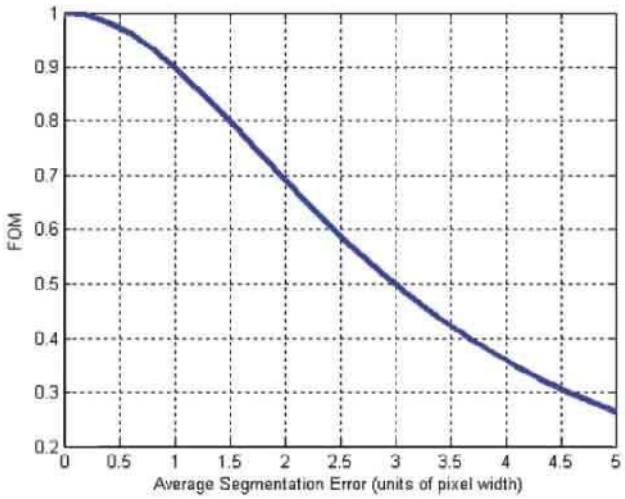

Figure 2. A plot of Pratt figure of merit (FOM) vs. "average segmentation error" in units of pixel width. The segmentation error is defined here as the average distance between the computed boundary and the ground truth boundary.

absolute computation of signal and noise power for a given image. For these reduction computations, five contiguous slices from the central part of the joint were selected from every data set. The variance reduction was calculated for two regions of interest (ROIs), one in the bone, one in the cartilage. A total of 165 images were evaluated.

Statistical analysis was performed using an analysis of variance (ANOVA) with repeated measures (mixed model) and post hoc Tukey tests. Results were considered significant at the $p < 0.05$ level.

RESULTS

The mean number of images segmented (±SD) per data set was 110 ± 6. From the eight ankles imaged, the mean values (±SD) for thickness, maximum thickness, cartilage surface area, cartilage bone interface area, and volume are shown in Table 1. The results show that, for each of the parameters measured, the talar cartilage had the largest values and the fibula cartilage gave the lowest values.

There were significant differences between the talus, tibia, and fibula for all quantitative parameters: mean thickness, $p < 0.001$; maximum thickness, $p < 0.005$; cartilage surface area, $p < 0.001$; cartilage bone interface area, $p < 0.001$; and cartilage volume, $p < 0.001$.

In order to compare the superior part of the ankle joint (tibia-fibula complex) to the inferior part of the ankle joint, we compared values for surface areas and volume in the talar cartilage to the combined tibia and fibula values. The talar cartilage layer has a significantly larger cartilage surface area

Table 1. Absolute Mean Values (±SD), from the Eight Subjects, for Each of the Quantitative Parameters Measured for the Talar, Tibial, and Fibula Cartilage Layers

Variable	Mean Thickness (mm ± SD)	Max Thickness (mm ± SD)	Cartilage Area (cm^2 ± SD)	BCI Area (cm^2 ± SD)	Cartilage Volume (ml ± SD)
Talus	1.34 ± 0.14	2.67 ± 0.25	28.03 ± 2.56	24.53 ± 2.16	3.32 ± 0.55
Tibia	1.21 ± 0.14	2.44 ± 0.58	15.30 ± 1.69	14.87 ± 1.48	1.72 ± 0.25
Fibula	0.91 ± 0.08	1.68 ± 0.18	4.21 ± 0.63	3.75 ± 0.56	0.35 ± 0.06

BCI, bone cartilage interface.

Appendix 3

$p < 0.001$, cartilage bone interface $p < 0.001$, and cartilage volume $p = 0.002$, than the superior part of the joint with which it is articulated.

The mean FOM value for the border positioning between the expert manually defined borders and the borders obtained with dGVF snake segmentation algorithm was 0.88 ± 0.06. From Figure 2, it can be seen that a FOM = 0.9 represents approximately a one pixel (0.15 mm) "average" Euclidean distance between the boundary pixels delineated by computer-aided segmentation method and the boundary pixels delineated by manual segmentation. Figure 3 shows a sample image with an expert traced border and the corresponding border detected by the dGVF snake algorithm.

When evaluating the precision of our approach using the six repeated data sets from five ankles (Table 2), the RMS average coefficient of variation (min–max) ranged from 2.82% (1.21%–4.21%) for the talar cartilage bone interface area to 9.62% (5.08%–12.0%) for the fibula volume. Segmentation of the talar cartilage was the most precise in terms of all measured parameters followed by the tibial cartilage; the fibula gave the largest mean CVs for all the parameters assessed.

The color 3D thickness distribution maps of each segmented cartilage layer show clear characteristic thickness distributions. In all the tali studied, there were two distinct areas, one anterior-laterally and one posterior-medially, over the talar shoulders where the thickest cartilage occurred (Fig. 4). For the tibial cartilage layers, the cartilage thickness appeared to be more evenly distributed; however, two areas, the central part of the anterior tibial plafond and the curved region at the transition between the tibial plafond and the medial malleolus, were typically thicker than the other regions (Fig. 5). The fibula cartilage was typically more homogeneous, but slight valgus angulation of the distal articular surface was seen, as shown in Figure 6.

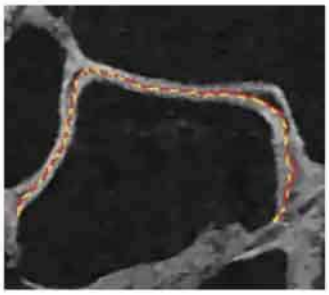

Figure 3. Talar cartilage borders detected by the dGVF snake (solid red line) and manual expert segmentation (dashed yellow line), with an FOM value of 0.937.

The evaluation of the anisotropic diffusion denoising algorithm showed that the technique produced marked enhancement of the images with a clear improvement in the definition of the edges in the images. The variance reduction ratios were 0.98 ± 0.01 and 0.74 ± 1.38 for the bone and cartilage, respectively.

DISCUSSION

The objectives of this study were: to evaluate the quantitative geometric parameters of the cartilage layers of the ankle joint; to test the precision of our segmentation technique; and to describe the topographic distribution of the cartilage over the ankle joint surfaces. To our knowledge, this is the first study to quantify the articular cartilage of the entire ankle joint, including the fibula and high curved regions over the talar shoulders and the medial malleolus, using MRI.

Our results show that the mean thickness ranged from 0.91 ± 0.08 mm in the fibula to 1.35 ± 0.14 mm in the talus, and maximum thickness ranged from 1.68 ± 0.18 mm in the fibula to 2.69 ± 0.25 mm in the talus. The figure of merit values show that the border positioning achieved with the dGVF snake, relative to expert manual segmentation, is better than the border positioning obtained with standard snake techniques.[42] Furthermore, the high FOM values obtained are encouraging since the images analyzed were in the middle of the joint and showed extensive cartilage-to-cartilage contact which represents some of the most challenging regions to segment in the ankle joint (Fig. 3). However, in some images, the dGVF snake failed and it was necessary to manually edit the borders detected by the dGVF snake; this typically occurred where there were large areas of continuous cartilage-to-cartilage contact with indistinct borders. We found the coefficients of variation for the quantitative geometric parameters studied varied from 2.82% to 9.62% in the different cartilage layers. The inter-subject variability in this study was slightly smaller than reported by Al-Ali et al.[17]; moreover, it was notably larger than the variability seen in the serial measurements.

Appendix 3

Table 2. Mean CVs (Min–Max) from the Six Repeated Measurements in Five Subjects for Each of the Quantitative Parameters

Variable	Mean Thickness %	Max Thickness %	Cartilage Area %	BCI area %	Volume %
Talus	3.49 (2.67–4.75)	4.47 (3.26–6.24)	3.23 (2.01–4.48)	2.82 (1.21–4.21)	4.95 (2.57–7.48)
Tibia	4.57 (3.26–5.75)	6.33 (3.77–11.35)	4.51 (2.41–7.71)	3.99 (2.27–6.96)	5.04 (3.29–6.98)
Fibula	4.67 (2.62–7.40)	7.44 (4.14–9.51)	9.28 (7.29–11.96)	9.46 (8.21–11.10)	9.62 (5.08–12.00)

CVs, coefficients of variation; BCI, bone cartilage interface.

Quantitative MRI of thin congruent cartilage layers has, to date, been challenging because of the trade-off between maintaining an acceptable scan time and signal to noise ratio (SNR) while obtaining a sufficient resolution required for accurate quantitative measurements. The scan time, 17 min 14 s, used in this study is relatively long; however, Al Ali et al. used a longer sequence on volunteers, reported no motion artefacts, and suggested that the scan time is acceptable for routine in vivo use.[17] We believe the scan time used in this study is acceptable for research use however it is unclear whether this would be well tolerated by symptomatic patients, who may experience discomfort and have difficultly remaining motionless. We felt that it was acceptable to sacrifice some of the SNR by using one image acquisition in order to obtain high resolution, isotropic image data and maintain a suitable scan time. By using isotropic image data reconstructions can be made in all three planes while the resolution was sufficiently high to avoid partial volume effects. Furthermore, the variance reduction ratio values show that it is possible to effectively counteract the reduced SNR by applying the anisotropic diffusion algorithm to enhance the images while preserving edges with the image. Through the combination of the anisotropic diffusion algorithm and the dGVF snake segmentation algorithm, we have been able to segment images that others believed lacked sufficient definition for reliable segmentation.[17]

The coefficients of variation reported in this study are approaching those observed in quantitative studies of knee articular cartilage,[30,33,45,50,51] which is very encouraging. Unfortunately, the CV values for the fibula are slightly higher due to the much smaller area and thickness of the layer which makes measurements more sensitive to small variations.

Further improvements in precision will be possible in the future through a number of technological advancements. Current and ongoing development of higher field strength can be observed and a new clinical standard of 3.0 Tesla seems to be being established.[22,23,52–54] High-field MRI allows increased resolution while maintaining

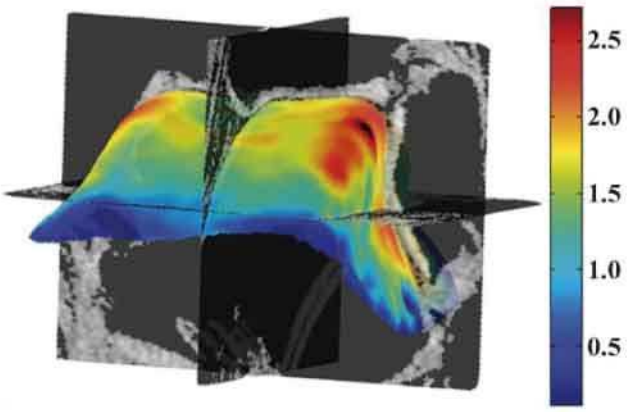

Figure 4. A typical 3D thickness distribution map of a talar cartilage layer in context with the original 3D MRI data.

Appendix 3

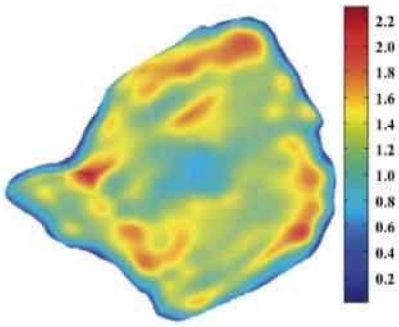

Figure 5. A typical tibial cartilage 3D thickness distribution map.

the same scan time. In addition, the development of parallel imaging allows shorter scan times. Multi-element coils can reduce the scan time by a factor of 2–4.[55] Furthermore, there has been renewed interest in SNR efficient imaging sequences for cartilage, including forms of steady-state precession as well as driven equilibrium and Turbo Spin Echo (TSE) imaging. These new sequences offer the possibility to acquire 3D data sets with isotropic voxels, which provides excellent segmentation possibilities.[56,57]

The values for mean and maximum cartilage thickness of the talus, tibia, and fibula measured using this approach are greater than those previously reported using a number of different techniques including A-mode ultrasound,[58] MRI,[17,40] and force-needle probes.[59,60] However, it is important to note that these studies excluded the highly curved regions over the talar shoulders, which have been shown to be the site of maximum cartilage thickness.[61,62] Notably, the values obtained in this study are congruent with values reported using a high resolution stereophotography technique that evaluated the entire cartilage layers of the talus, tibia, and fibula, and which should be considered as a reference standard for the "true" cartilage thickness.[61]

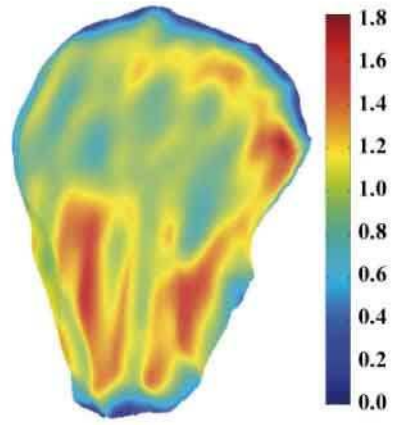

Figure 6. A typical fibula cartilage layer 3D thickness distribution map.

The 3D thickness distribution maps demonstrate a characteristic distribution pattern which is most marked in the talus. It is widely believed that the thickest cartilage in the ankle occurs at the center of the talar dome and tibial plafond,[59,60,63] but thickness maps clearly show the thickest cartilage occurred over the anterior-lateral and posterior-medial shoulders of the talus which corresponds to the most common site of OCD lesions in the ankle joint[6] and corresponds to measurements from anatomical sections.[62] Furthermore, the thick cartilage over the anterior border of the tibia corresponds to cartilage injury sites seen in dorsiflexion testing.[64]

CONCLUSIONS

In this study, we have quantified the geometric parameters of the talar, tibial, and fibula cartilage layers. We have demonstrated that the mean and maximum thickness of each layer of ankle cartilage exceed the measurements previously reported.[17,40,58–60] We have shown that, by using a dGVF snake segmentation algorithm combined with an anisotropic diffusion denoising algorithm, we can extract the cartilage layer more precisely than previously achieved[17] in the ankle joint. Finally, the 3D thickness distribution maps have shown a characteristic pattern with the thickest cartilage occurring over the anterior-lateral and posterior-medial talar shoulders, where OCD lesions commonly occur.[6]

ACKNOWLEDGMENTS

Partial funding for this study was provided by Zimmer Inc., Warsaw, Indiana, USA.

REFERENCES

1. Marsh JL, Buckwalter J, Gelberman R, et al. 2002. Articular fractures: does an anatomic reduction really

Appendix 3

change the result? J Bone Joint Surg [Am] 84-A:1259–1271.
2. Marsh JL, Weigel DP, Dirschl DR. 2003. Tibial plafond fractures. How do these ankles function over time? J Bone Joint Surg [Am] 85-A:287–295.
3. Buckwalter JA, Saltzman CL. 1999. Ankle osteoarthritis: distinctive characteristics. Instr Course Lect 48:233–241.
4. Dieppe P, Kirwan J. 1994. The localization of osteoarthritis. Br J Rheumatol 33:201–203.
5. Funk FJ. 1976. Osteoarthritis of the foot and ankle. In: American Academy of Surgeons Symposiums on Osteoarthritis. St. Louis: CV Mosby.
6. O'Farrell TA, Costello BG. 1982. Osteochondritis dissecans of the talus. The late results of surgical treatment. J Bone Joint Surg [Br] 64:494–497.
7. Hangody L. 2003. The mosaicplasty technique for osteochondral lesions of the talus. Foot Ankle Clin 8:259–273.
8. Burgkart R, Glaser C, Hinterwimmer S, et al. 2003. Feasibility of T and Z scores from magnetic resonance imaging data for quantification of cartilage loss in osteoarthritis. Arthritis Rheum 48:2829–2835.
9. Burgkart R, Glaser C, Hyhlik-Durr A, et al. 2001. Magnetic resonance imaging-based assessment of cartilage loss in severe osteoarthritis: accuracy, precision, and diagnostic value. Arthritis Rheum 44:2072–2077.
10. Eckstein F, Heudorfer L, Faber SC, et al. 2002. Long-term and resegmentation precision of quantitative cartilage MR imaging (qMRI). Osteoarthritis Cartilage 10:922–928.
11. Eckstein F, Reiser M, Englmeier KH, et al. 2001. In vivo morphometry and functional analysis of human articular cartilage with quantitative magnetic resonance imaging—from image to data, from data to theory. Anat Embryol (Berl) 203:147–173.
12. Peterfy CG, Genant HK. 1996. Emerging applications of magnetic resonance imaging in the evaluation of articular cartilage. Radiol Clin North Am 34:195–213.
13. Eckstein F, Glaser C. 2004. Measuring cartilage morphology with quantitative magnetic resonance imaging. Semin Musculoskelet Radiol 8:329–353.
14. Gray ML, Eckstein F, Peterfy C, et al. 2004. Toward imaging biomarkers for osteoarthritis. Clin Orthop 427(suppl):S175–S181.
15. Recht M, Bobic V, Burstein D, et al. 2001. Magnetic resonance imaging of articular cartilage. Clin Orthop 391(suppl):S379–S396.
16. Trattnig S, Millington SA, Szomolanyi P, et al. 2006. MR imaging of osteochondral grafts and autologous chondrocyte implantation. European Radiology Epub ahead of print. DOI. 10.1007/s00330-006-0333z.
17. Al Ali D, Graichen H, Faber S, et al. 2002. Quantitative cartilage imaging of the human hind foot: precision and inter-subject variability. J Orthop Res 20:249–256.
18. Eckstein F, Sittek H, Milz S, et al. 1994. The morphology of articular cartilage assessed by magnetic resonance imaging (MRI). Reproducibility and anatomical correlation. Surg Radiol Anat 16:429–438.
19. Eckstein F, Sittek H, Milz S, et al. 1995. The potential of magnetic resonance imaging (MRI) for quantifying articular cartilage thickness—a methodological study. Clin Biomech (Bristol, Avon) 10:434–440.
20. Graichen H, Springer V, Flaman T, et al. 2000. Validation of high-resolution water-excitation magnetic resonance imaging for quantitative assessment of thin cartilage layers. Osteoarthritis Cartilage 8:106–114.
21. Cohen ZA, McCarthy DM, Kwak SD, et al. 1999. Knee cartilage topography, thickness, and contact areas from MRI: in-vitro calibration and in-vivo measurements. Osteoarthritis Cartilage 7:95–109.
22. Eckstein F, Charles HC, Buck RJ, et al. 2005. Accuracy and precision of quantitative assessment of cartilage morphology by magnetic resonance imaging at 3.0T. Arthritis Rheum 52:3132–3136.
23. Eckstein F, Hudelmaier M, Wirth W, et al. 2006. Double echo steady state (DESS) magnetic resonance imaging of knee articular cartilage at 3 tesla—a pilot study for the osteoarthritis initiative. Ann Rheum Dis 65:433–441.
24. Faber SC, Eckstein F, Lukasz S, et al. 2001. Gender differences in knee joint cartilage thickness, volume and articular surface areas: assessment with quantitative three-dimensional MR imaging. Skeletal Radiol 30:144–150.
25. Raynauld JP. 2003. Quantitative magnetic resonance imaging of articular cartilage in knee osteoarthritis. Curr Opin Rheumatol 15:647–650.
26. Raynauld JP, Martel-Pelletier J, Berthiaume MJ, et al. 2004. Quantitative magnetic resonance imaging evaluation of knee osteoarthritis progression over two years and correlation with clinical symptoms and radiologic changes. Arthritis Rheum 50:476–487.
27. Nishii T, Sugano N, Sato Y, et al. 2004. Three-dimensional distribution of acetabular cartilage thickness in patients with hip dysplasia: a fully automated computational analysis of MR imaging. Osteoarthritis Cartilage 12:650–657.
28. Peterfy CG, van Dijke CF, Lu Y, et al. 1995. Quantification of the volume of articular cartilage in the metacarpophalangeal joints of the hand: accuracy and precision of three-dimensional MR imaging. AJR Am J Roentgenol 165:371–375.
29. Jonsson K, Buckwalter K, Helvie M, et al. 1992. Precision of hyaline cartilage thickness measurements. Acta Radiol 33:234–239.
30. Peterfy CG, van Dijke CF, Janzen DL, et al. 1994. Quantification of articular cartilage in the knee with pulsed saturation transfer subtraction and fat-suppressed MR imaging: optimization and validation. Radiology 192:485–491.
31. Pilch L, Stewart C, Gordon D, et al. 1994. Assessment of cartilage volume in the femorotibial joint with magnetic resonance imaging and 3D computer reconstruction. J Rheumatol 21:2307–2321.
32. Waterton JC, Rajanayagam V, Ross BD, et al. 1993. Magnetic resonance methods for measurement of disease progression in rheumatoid arthritis. Magn Reson Imaging 11:1033–1038.
33. Eckstein F, Westhoff J, Sittek H, et al. 1998. In vivo reproducibility of three-dimensional cartilage volume and thickness measurements with MR imaging. AJR Am J Roentgenol 170:593–597.
34. Haubner M, Eckstein F, Schnier M, et al. 1997. A noninvasive technique for 3-dimensional assessment of articular cartilage thickness based on MRI. Part 2: Validation using CT arthrography. Magn Reson Imaging 15:805–813.
35. Losch A, Eckstein F, Haubner M, et al. 1997. A noninvasive technique for 3-dimensional assessment of articular cartilage thickness based on MRI. Part 1: Development of a computational method. Magn Reson Imaging 15:795–804.

Appendix 3

36. Robson MD, Hodgson RJ, Herrod NJ, et al. 1995. A combined analysis and magnetic resonance imaging technique for computerised automatic measurement of cartilage thickness in the distal interphalangeal joint. Magn Reson Imaging 13:709–718.
37. Solloway S, Hutchison C, Waterton J, et al. 1997. The use of active shape models for making thickness measurements of articular cartilage from MR images. Magn Reson Med 36:943–952.
38. Trattnig S, Huber M, Breitenseher MJ, et al. 1998. Imaging articular cartilage defects with 3D fat-suppressed echo planar imaging: comparison with conventional 3D fat-suppressed gradient echo sequence and correlation with histology. J Comput Assist Tomogr 22:8–14.
39. Ba-Ssalamah A, Schibany N, Puig S, et al. 2002. Imaging articular cartilage defects in the ankle joint with 3D fat-suppressed echo planar imaging: comparison with conventional 3D fat-suppressed gradient echo imaging. J Magn Reson Imaging 16:209–216.
40. Tan TC, Wilcox DM, Frank L, et al. 1996. MR imaging of articular cartilage in the ankle: comparison of available imaging sequences and methods of measurement in cadavers. Skeletal Radiol 25:749–755.
41. Eckstein F, Siedek V, Glaser C, et al. 2004. Correlation and sex differences between ankle and knee cartilage morphology determined by quantitative magnetic resonance imaging. Ann Rheum Dis 63:1490–1495.
42. Tang J, Millington SA, Acton ST, et al. 2006. Surface extraction and thickness measurement of the articular cartilage from MR images using directional gradient vector flow snakes. IEEE Trans Biomed Eng 53:896–907.
43. Tang JS, Millington SA, Acton ST, et al. 2004. Ankle cartilage surface tracking using directional gradient vector flow snakes. IEEE Int Conf Image Process 4:2745–2748.
44. Pratt W. 1978. Digital image processing. New York: Wiley.
45. Stammberger T, Eckstein F, Englmeier KH, et al. 1999. Determination of 3D cartilage thickness data from MR imaging: computational method and reproducibility in the living. Magn Reson Med 41:529–536.
46. Eckstein F, Winzheimer M, Hohe J, et al. 2001. Interindividual variability and correlation among morphological parameters of knee joint cartilage plates: analysis with three-dimensional MR imaging. Osteoarthritis Cartilage 9:101–111.
47. Gluer CC, Blake G, Lu Y, et al. 1995. Accurate assessment of precision errors: how to measure the reproducibility of bone densitometry techniques. Osteoporos Int 5:262–270.
48. Acton ST, Bovik AC. 1998. Order statistics in image processing. In: Balakrishnan N, Rao CR, editors. Handbook of statistics 17: order statistics and their applications. New York: Elsevier Science; p 603–641.
49. Acton ST, Wei D, Bovik AC. 1999. Image enhancement. In: Webster J, editor. Encyclopedia of electrical and electronics engineering. New York: Wiley-Interscience; p 550–559.
50. Hyhlik-Durr A, Faber S, Burgkart R, et al. 2000. Precision of tibial cartilage morphometry with a coronal water-excitation MR sequence. Eur Radiol 10:297–303.
51. Kshirsagar AA, Watson PJ, Tyler JA, et al. 1998. Measurement of localized cartilage volume and thickness of human knee joints by computer analysis of three-dimensional magnetic resonance images. Invest Radiol 33: 289–299.
52. Craig JG, Go L, Blechinger J, et al. 2005. Three-tesla imaging of the knee: initial experience. Skeletal Radiol 34:453–461.
53. Schibany N, Ba-Ssalamah A, Marlovits S, et al. 2005. Impact of high field (3.0 T) magnetic resonance imaging on diagnosis of osteochondral defects in the ankle joint. Eur J Radiol 55:283–288.
54. Schmitt F, Grosu D, Mohr C, et al. 2004. [3 Tesla MRI: successful results with higher field strengths]. Radiologe 44:31–47.
55. Heidemann RM, Griswold MA, Muller M, et al. 2004. [Feasibilities and limitations of high field parallel MRI]. Radiologe 44:49–55.
56. Hargreaves BA, Gold GE, Beaulieu CF, et al. 2003. Comparison of new sequences for high-resolution cartilage imaging. Magn Reson Med 49:700–709.
57. Menzel M, Horger W, Welsh GH, et al. 2005. Proceedings of the 13th International Society of Magnetic Resonance in Medicine meeting. Miami Beach, Florida International Society of Magnetic Resonance in Medicine.
58. Adam C, Eckstein F, Milz S, et al. 1998. The distribution of cartilage thickness within the joints of the lower limb of elderly individuals. J Anat 193(Pt 2):203–214.
59. Athanasiou KA, Niederauer GG, Schenck RC Jr. 1995. Biomechanical topography of human ankle cartilage. Ann Biomed Eng 23:697–704.
60. Shepherd DE, Seedhom BB. 1999. Thickness of human articular cartilage in joints of the lower limb. Ann Rheum Dis 58:27–34.
61. Millington SA, Grabner M, Hurwitz SR, et al. 2004. A stereophotographic study of ankle cartilage thickness; distribution and surface topography. Osteoarthritis Cartilage 12:S64.
62. Muller-Gerbl M, Putz R. 1995. Functional anatomy of the ankle joint. In: The tibial pilon fracture, Heim U, editor. 1st ed. Philadelphia: Saunders; p 3–25.
63. Adam C, Eckstein F, Milz S, et al. 1998. The distribution of cartilage thickness in the knee-joints of old-aged individuals—measurement by A-mode ultrasound. Clin Biomech (Bristol, Avon) 13:1–10.
64. Rudd R, Crandall J, Millington SA, et al. 2004. Injury tolerance and response of the ankle joint in dynamic dorsiflexion. Stapp Car Crash J 48:1–26.

Appendix 4. Automated 3-D segmentation study

Simultaneous Segmentation of Multiple Closed Surfaces Using Optimal Graph Searching

Kang Li[1], Steven Millington[2], Xiaodong Wu[3],
Danny Z. Chen[4], and Milan Sonka[3]

[1] Dept. of Electrical and Computer Engineering, Carnegie Mellon University,
5000 Forbes Ave, Pittsburgh, PA 15213, USA
kangl@cmu.edu
[2] Frank Stronach Institute, Infeldgasse 21B/II, A8010 Graz, Austria
steven.millington@tugraz.at
[3] Dept. of Electrical and Computer Engineering, The University of Iowa,
4016 Seamans Center, Iowa City, IA 52242-1595, USA
{xiaodong-wu, milan-sonka}@uiowa.edu
[4] Dept. of Computer Science and Engineering, The University of Notre Dame
Notre Dame, IN 46556, USA
dchen@cse.nd.edu

Abstract. This paper presents a general graph-theoretic technique for simultaneously segmenting multiple closed surfaces in volumetric images, which employs a novel graph-construction scheme based on triangulated surface meshes obtained from a topological presegmentation. The method utilizes an efficient graph-cut algorithm that guarantees global optimality of the solution under given cost functions and geometric constraints. The method's applicability to difficult biomedical image analysis problems was demonstrated in a case study of co-segmenting the bone and cartilage surfaces in 3-D magnetic resonance (MR) images of human ankles. The results of our automated segmentation were validated against manual tracings in 55 randomly selected image slices. Highly accurate segmentation results were obtained, with signed surface positioning errors for the bone and cartilage surfaces being 0.02 ± 0.11mm and 0.17 ± 0.12mm, respectively.

1 Introduction

Optimal segmentation of surfaces representing object boundaries in volumetric datasets is important and challenging for many medical image analysis applications. Recently, we proposed an efficient algorithm for d-D ($d \geq 3$) optimal hyper-surface detection with hard smoothness constraints, making globally optimal surface segmentation in volumetric images practical [1, 2]. By modeling the problem with a *geometric graph*, the method transforms the segmentation problem into computing the minimum s-t graph cut that is well-studied in graph theory, and makes the problem solvable in a low-order polynomial time. The solution is guaranteed to be globally optimal in the considered region by theoretical

G.E. Christensen and M. Sonka (Eds.): IPMI 2005, LNCS 3565, pp. 406–417, 2005.

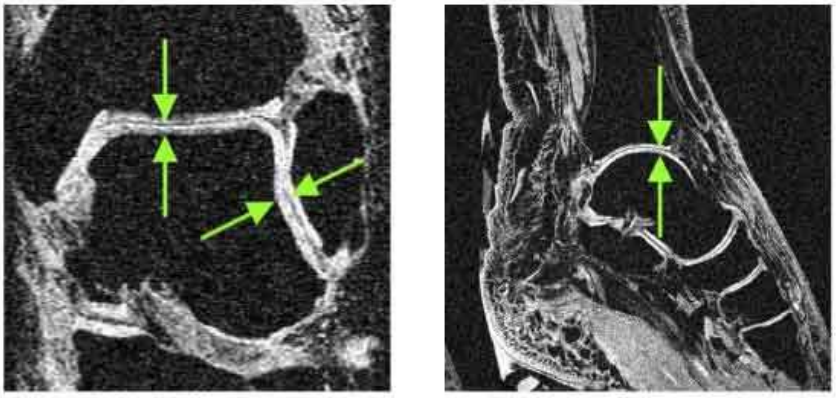

(a) Coronal view (b) Sagittal view

Fig. 1. Two sample slices of a 3-D MR image of human ankle

proofs [1]. We have also developed a multi-surface segmentation algorithm [3]. However, these methods were both limited to segmenting height-field or cylindrical surfaces in regular grids.

In this paper, we present a non-trivial extension of our previous work. We focus on the problem of segmenting *optimal multiple closed* surfaces in 3-D. The new method for multiple surfaces segmentation is motivated by the need to accurately segment cartilage layers in diseased joints. In this application, the articular cartilage and corresponding subchondral bone surfaces can be imaged by 3-D high-resolution MRI (Fig. 1). However, no segmentation method exists that would allow a rapid, accurate, and reproducible segmentation for quantitative evaluation of articular cartilage.

The main contribution of our work is that it extends the optimal graph-searching techniques to closed surfaces, while the backbone of our approach – graph-cuts – is radically different from traditional graph searching. Consequently, many existing problems that were tackled using graph-searching in a slice-by-slice manner can be migrated to our new framework with little or no change to the underlying objective function formulation.

2 Methods

The proposed method allows segmenting multiple inter-related surfaces in volumetric images and facilitates subsequent quantitative analysis. We will utilize the bone–cartilage segmentation task to help make the method description intuitively clear. The general strategy of our method is to achieve the final segmentation in two stages. The initial stage provides approximate segmentation of the three-dimensional object (in our case, of the bone), and the final segmentation is achieved by accurate and simultaneous segmentation of its multiple surfaces

of interest. The outputs of the algorithm are triangulated meshes that are ready for visualization and quantitative measurement.

The method consists of the following three main steps:

1. *Bone surface presegmentation.* A level set based algorithm is used. Starting from several seed-spheres, the method uses the image-derived edge and regional information to evolve a smooth surface toward the bone boundary. The presegmented surface serves as an initialization to the subsequent segmentation.
2. *Mesh generation and optimization.* The presegmentation results in an implicit surface that is the zero level set of a 4-D function embedded in a volumetric digital grid. An isosurfacing algorithm (e.g., marching cubes) is used to convert the implicit surface into an explicit triangulated mesh. The mesh is optimized by removing or merging isolated and redundant triangles. The resolution of the mesh can be increased or decreased using progressive level of detail approaches when necessary.
3. *Co-segmentation of the cartilage and bone surfaces.* The mesh generated by the second step is used to initialize a graph in a narrow-band around the presegmented bone surface. A novel multi-surfaces graph search algorithm is used to simultaneously obtain the precise positions of the bone and cartilage surfaces based on two cost functions separately designed for the two surfaces while considering specific geometric constraints.

Since the mesh manipulation step involves largely standard techniques in graphics, only the first and third steps are described in detail.

2.1 Bone Surface Presegmentation

The presegmentation algorithm is based on the *MetaMorphs* deformable shape and texture model presented in [4]. The method provides a unified gradient-descent framework for modeling both the boundary and texture information in an image, and is relatively efficient in computation.

Let Ω denote the image domain, and $\partial\Omega$ be the surface represented by the model, which is the zero level set of a signed distance function ϕ. ϕ is positive in the model interior, denoted Ω^+. Instead of directly evolving the function ϕ, the deformation of the surface is controlled by a set of uniformly-spaced control points artificially embedded in the image domain. The motion of the control points is computed using image-derived information. The deformation at any voxel location can then be derived using the cubic B-spline based Free Form Deformation (FFD). As such, the level set function ϕ can be updated using a geometric transformation of itself at each descent step. The motion of the control points is determined by minimizing the weighted combination of two edge-based cost terms and two region-based cost terms. For more detail of the cost terms and the model evolution, we refer to reader to [4].

Particularly, in [4], the authors suggested a Gaussian kernel-based nonparametric approach for modeling image pixel (voxel) intensity distributions. This approach, however, is computationally expensive in 3-D. Considering our

application domain and taking advantage of the physical properties of the MR images, voxel intensities in the bone region are approximated by a Rayleigh distribution:

$$P(I|b) = \frac{Ie^{-I^2/2b^2}}{b^2}, \quad I \geq 0, \;\; b > 0 \tag{1}$$

with I being the pixel intensity. This distribution has only one free parameter b, which is estimated using the sample mean μ of voxel intensities inside the initializing spheres, as:

$$b = \mu\sqrt{\frac{2}{\pi}} \tag{2}$$

2.2 Simultaneous Segmentation of Cartilage and Bone Surfaces

After the bone surface is presegmented and converted into a triangulated mesh, a novel graph-based algorithm is applied to co-optimize the cartilage and bone surfaces. Note that anatomically, the cartilage only covers certain parts of the bone surface. To simplify the problem, we assume the cartilage extends the full surface area of the bone. However, in some areas the "cartilage" surface merges with the bone, so that the cartilage thickness is effectively zero in those areas.

Preliminaries. A triangulated mesh consists of a set of *vertices* connected by *edges*. We use $\mathcal{M}(\mathcal{V}, \mathcal{E})$ to denote a mesh with vertex set $\mathcal{V}$ and edge set $\mathcal{E}$. Two vertices are said to be *adjacent* if they are connected by an edge. Each vertex has an associated surface *normal*, which is perpendicular to the surface that the mesh represents at the vertex.

A graph $\mathcal{G}(\mathcal{N}, \mathcal{A})$ is a structure that consists of a set of *nodes* $\mathcal{N}$ and a set of *arcs* $\mathcal{A}$. The arc connecting two nodes n_1 and n_2 is denoted by $\langle n_1, n_2\rangle$. For *undirected* arcs, the notations $\langle n_1, n_2\rangle$ and $\langle n_2, n_1\rangle$ are considered equivalent. For a *directed* arc, they are considered distinct. The former one denotes the arc from n_1 to n_2, and the latter one from n_2 to n_1. In addition, a *geometric* graph is a graph whose nodes have certain geometric positions in space.

Graph Construction. Since the bone and cartilage surfaces are to be segmented simultaneously, two spatially-coincident *columns* of equidistant nodes are constructed along the normal at each vertex of the triangular mesh obtained from the presegmentation (Fig. 2). The number of nodes in each column is determined by the required resolution, and the extent of each column depends on the width of the region where the cartilage and bone surfaces are expected – a narrow-band around the presegmented surface. A set of arcs is carefully constructed between the nodes to ensure the geometric constraints, including the *smoothness constraint*, which controls the stiffness of the output surfaces, and the surface *separation constraint*, which defines the relative positioning and the distance range of the two surfaces.

Suppose there are N vertices on the mesh, and let v_i be one of them ($i \in \{0, \ldots, N-1\}$). The two columns of nodes constructed along the normal at v_i are denoted by $\mathcal{K}_0(v_i) \equiv \{n_{0i}^0, \ldots, n_{0i}^{K-1}\}$ and $\mathcal{K}_1(v_i) \equiv \{n_{1i}^0, \ldots, n_{1i}^{K-1}\}$,

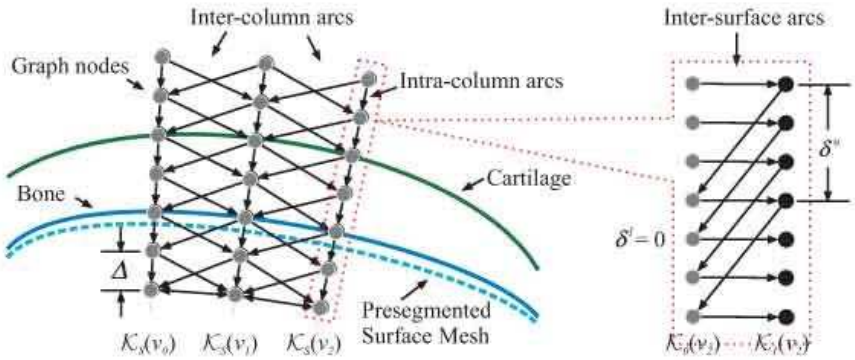

Fig. 2. Graph construction

respectively, where K is the number of nodes in each column. The collection of columns $\bigcup \mathcal{K}_s(v_i)$ with $s = 0, 1$ and $i = 1, \ldots, N-1$ constitutes the node set $\mathcal{N}$.

Next, assuming that each column $\mathcal{K}_0(v_i)$ intersects with the bone surface at exactly one node, denoted n^*_{0i}, and each column $\mathcal{K}_1(v_i)$ intersects with the cartilage surface at exactly one node n^*_{1i}, the collections of nodes $\mathcal{N}^*_0 \equiv \{n^*_{0i} : i = 0, \ldots, N-1\}$ and $\mathcal{N}^*_1 \equiv \{n^*_{1i} : i = 0, \ldots, N-1\}$ will represent discretizations of the bone surface and the cartilage surface, respectively. In this way, the segmentation problem is converted to a graph search problem, in which the node sets $\mathcal{N}^*_0$ and $\mathcal{N}^1_1$ are to be identified.

Apparently, the choices of $\mathcal{N}^*_0$ and $\mathcal{N}^*_1$ are not arbitrary. Cost values are assigned to the graph nodes according to two cost functions constructed specifically for the bone and cartilage surfaces. $\mathcal{N}^*_0$ and $\mathcal{N}^*_1$ will correspond to the set of nodes with the minimum total cost in the graph. Furthermore, several constraints are imposed on the geometric relations of the nodes in $\mathcal{N}^*_0$ and $\mathcal{N}^*_1$. These constraints are enforced by the graph arcs, constructed as follow.

- *Intra-column arcs* $\mathcal{A}^a$: Along each column $\mathcal{K}_s(v_i)$, every node n^k_{si} has a directed arc to the node n^{k-1}_{si}, i.e.,

$$\mathcal{A}^a = \{\langle n^k_{si}, n^{k-1}_{si}\rangle : k = 1, \ldots, K-1; \forall i, s\} \tag{3}$$

- *Inter-column arcs* $\mathcal{A}^r$: The inter-column arcs encode the smoothness constraint, which is imposed between each pair of adjacent columns. Two columns $\mathcal{K}_s(v_i)$ and $\mathcal{K}_s(v_j)$ $(s \in \{0, 1\},\ i \neq j)$ are said to be adjacent if the two vertices v_i and v_j are adjacent on the mesh. Suppose one of the sought surfaces intersects with two adjacent columns $\mathcal{K}_s(v_i)$ and $\mathcal{K}_s(v_j)$ at nodes $n^{k_i}_{si}$ and $n^{k_j}_{sj}$, respectively. If the surface is smooth, k_i and k_j should not differ too much. The smoothness constraint Δ defines the maximum allowed difference between k_i and k_j, i.e., $\Delta = \max |k_i - k_j|$. Smaller Δ forces the surface to be smoother. To encode the smoothness constraint in the graph, the following directed arcs are constructed:

$$\mathcal{A}^r = \{\langle n^k_{si}, n^{\max(0,k-\Delta)}_{sj}\rangle : \forall s, k;\ v_i, v_j \text{ adjacent}\} \tag{4}$$

– *Inter-surface arcs* $\mathcal{A}^s$: These arcs model the separation constraint between the two surfaces. Suppose the bone and cartilage surfaces intersect $\mathcal{K}_0(v_i)$ and $\mathcal{K}_1(v_i)$ at nodes $n_{0i}^{k_0}$ and $n_{1i}^{k_1}$, respectively. Because the thickness of the cartilage is within some known range, $n_{0i}^{k_0}$ and $n_{1i}^{k_1}$ are at least δ^l, and at most δ^u nodes apart, i.e., $\delta^l \leq k_1 - k_0 \leq \delta^u$. The inter-surface arcs are constructed between columns $\mathcal{K}_0(v_i)$ and $\mathcal{K}_1(v_i)$ for all $v_i \in \mathcal{V}$ as:

$$\mathcal{A}^s = \{\langle n_{1i}^k, n_{0i}^{\max(0,k-\delta^u)}\rangle, \langle n_{0i}^k, n_{1i}^{\min(K-1,k+\delta^l)}\rangle : \forall i, k\} \tag{5}$$

For more than two surfaces, the separation constraint is specified pairwisely.

Cost Functions. The cost functions are crucial for accurate surface localization. For this pilot study, relatively simple cost functions are used. Specifically, the cost function for the bone surface, C_{bone}, is the negated gradient magnitude of the Gaussian-smoothed image G,

$$C_{bone} = -|\nabla G| \equiv -\sqrt{G_x^2 + G_y^2 + G_z^2} \tag{6}$$

where $G_x \equiv \frac{\partial}{\partial x}G$, $G_y \equiv \frac{\partial}{\partial y}G$ and $G_z \equiv \frac{\partial}{\partial z}G$ are partial derivatives of the image. The cost function for the cartilage surface is computed as a weighted combination of the response of a 3-D "sheet filter" [5] and the directional image gradients. The sheet filter is formulated using the Hessian matrix $\nabla^2 G$ of the image intensity. Let the eigenvalues of $\nabla^2 G$ be λ_0, λ_1 and λ_2, $(\lambda_0 \geq \lambda_1 \geq \lambda_2)$. The sheet filter is defined as:

$$F_{sheet}(G) = \begin{cases} |\lambda_2| \cdot \omega(\lambda_1, \lambda_2) \cdot \omega(\lambda_0, \lambda_2), & \lambda_2 < 0, \\ 0, & \text{otherwise.} \end{cases} \tag{7}$$

The function ω is given by:

$$\omega(\lambda_a, \lambda_b) = \begin{cases} (1 + \frac{\lambda_a}{|\lambda_b|})^\gamma, & \lambda_b \leq \lambda_a \leq 0, \\ (1 - \alpha\frac{\lambda_a}{|\lambda_b|})^\gamma, & \frac{|\lambda_b|}{\alpha} > \lambda_a > 0, \\ 0, & \text{otherwise,} \end{cases} \tag{8}$$

where α, γ are parameters. In our experiments, we chose $\alpha = 0.25$ and $\gamma = 0.5$.

In summary, the cost function for cartilage surface is computed as:

$$C_{cartilage} = \begin{cases} -F_{sheet}(-G) - \tau_x G_x, & \text{if } G_x > 0, \\ -F_{sheet}(-G) & \text{otherwise,} \end{cases} \tag{9}$$

where the value of τ_x is chosen to be 1.0 in our experiments.

The above cost functions are computed in the image domain. The node costs are assigned using spatial interpolation based on the positions of the nodes. Specifically, the costs of nodes n_{0i}^k are assigned according to C_{bone}, and the costs of nodes n_{1i}^k are computed from $C_{cartilage}$.

Optimization. Once the graph is constructed and the node costs assigned, we can use the same technique described in [3] to transform the graph into an s-t graph $\mathcal{G}_{st}$ that has a source node s and a sink node t, and apply a minimum s-t cut algorithm to compute the optimal surfaces. The final surfaces will correspond to the upper envelope of the set of nodes that can be reached from s in $\mathcal{G}_{st}$, i.e., the source set of $\mathcal{G}_{st}$.

3 Case Study

Osteoarthritis and articular cartilage injuries are very common – one in six people in the USA is affected by some form of arthritis. The socio-economic impact of degenerative joint diseases is massive, with an estimated annual cost of $65 billion in the USA during the 1990's. As such, there is a huge research interest in the field of chondro-protective and chondro-restorative treatments.

The proposed method allows segmenting the articular cartilage surface and the corresponding subchondral bone surface in volumetric MRI images that facilitates subsequent quantitative analysis. The segmentation is initiated by a few (normally 3 or less) roughly-placed seed points in the bone region, but is otherwise fully automated.

Data. The method was tested in 8 high-resolution 3-D MR data sets of human ankles. The images were acquired using a 1.5T MR scanner, with in plane resolution 0.3×0.3 mm^2 and slice thickness 0.3 mm. The acquisition time was 17 minutes and 14 seconds. Overall, each MR image data set consisted of approximately $512 \times 512 \times 150$ voxels.

Independent Standard. In the 8 MR images, 55 coronal or sagittal slices were randomly selected to be manually traced by an expert observer (orthopedic surgeon) and formed the independent standard. The selection of coronal as well as sagittal slices allows assessing the performance of the inherently 3-D segmentation method using 2-D manual tracings.

Comparisons with the Independent Standard. Computer segmentation of the talus bone and the cartilage surfaces was performed in 3-D. Consequently, the segmented surfaces were available for the entire closed 3-D object. The automated segmentation method locally failed in 5 of the 55 image slices for which independent standard was available due to local pre-segmentation errors. The segmentation accuracy was assessed in the 50 image slices by computing signed, unsigned, and RMS surface positioning errors. The positioning errors were defined as the shortest distances between the manually traced borders and the computer-determined surfaces in the coronal and sagittal MR slices for which the independent standard was available. The errors are reported on a per-slice basis as mean $\pm$ standard deviation.

Reproducibility. To assess the reproducibility of cartilage segmentation, the method was independently initialized 5 times and the mean and maximum car-

Appendix 4

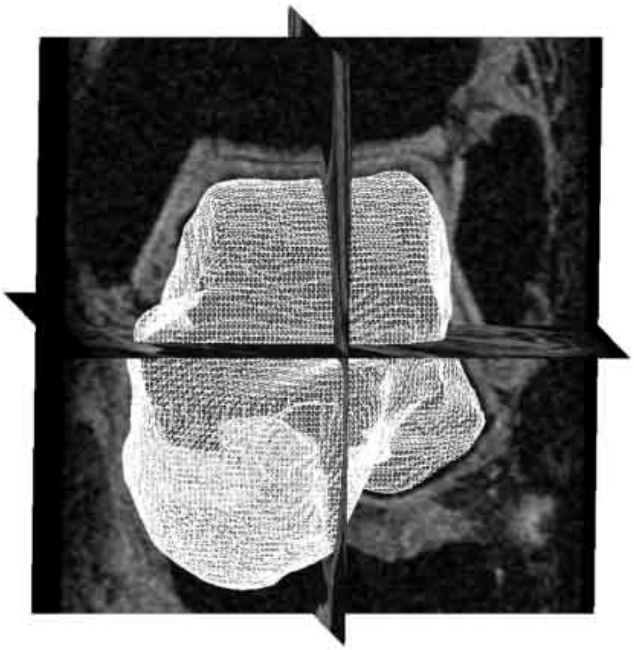

(a) Presegmented talus surface

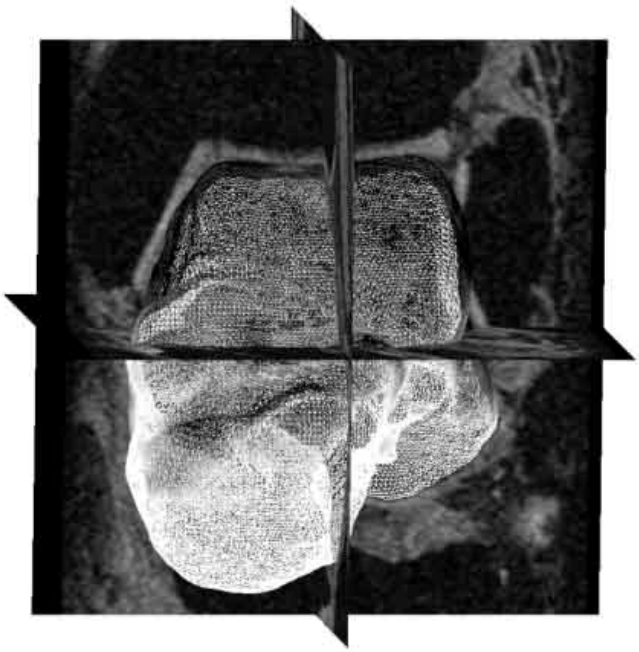

(b) Segmented talus and cartilage

Fig. 3. Presegmentation and segmentation. Cartilage surfaces are color-coded, with darker shadings depicting thicker cartilage

tilage thicknesses were determined for each of the 8 talus cartilages. The reproducibility was assessed by calculating mean ± standard deviation of differences between the average values obtained in the 5 reproducibility runs and the individual results.

Results. All experiments were performed on a workstation with dual 3.0GHz processors and 4GB of RAM. For each data set, we used 3 seed-spheres inside the

Table 1. Overall surface positioning accuracy

	Signed Error (mm)	Unsigned Error (mm)	RMS Error (mm)
Bone	0.02 ± 0.11	0.25 ± 0.08	0.03 ± 0.01
Cartilage	0.17 ± 0.12	0.39 ± 0.09	0.04 ± 0.01

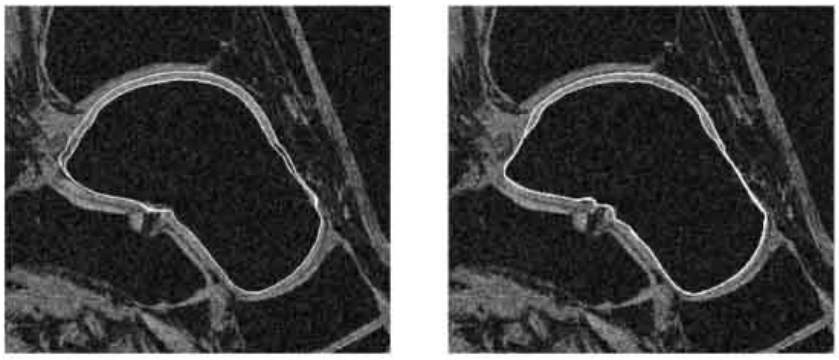

(a) Computer (b) Manual

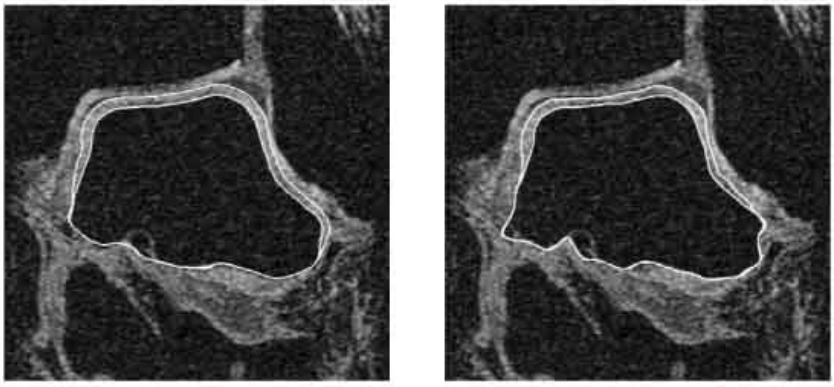

(c) Computer (d) Manual

Fig. 4. Comparison of computer and manual segmentations

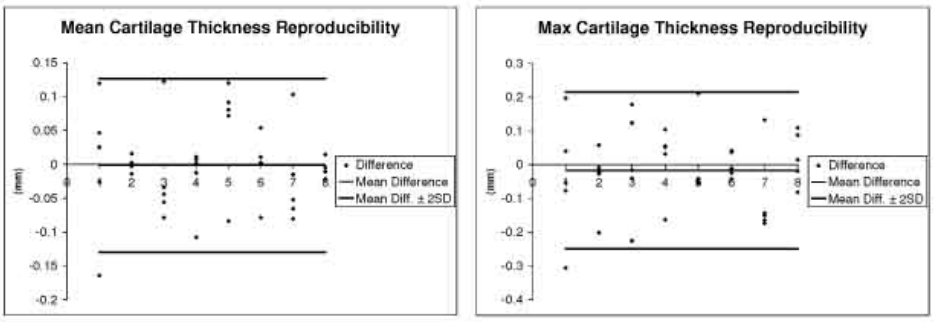

(a) Mean cartilage thickness (b) Max cartilage thickness

Fig. 5. Bland-Altman plots of cartilage thickness reproducibility

bone region to initialize the presegmentation. To reduce running time, the regions containing the talus bones were cropped from the original MR images to form smaller images of approximately 250×250×150 voxels each. The presegmentation was performed on 2-times downsampled copies of the cropped images, while the final segmentation was performed on the original full-resolution images.

The parameters used for final segmentations were $K = 30$, $\delta^l = 0$, $\delta^u = 12$ and $\Delta = 1$. For each data set, the average execution times of the presegmentation and segmentation stages were about 200 seconds and 70 seconds, respectively. The overall surface positioning errors of the computer-segmented talus bone and its cartilage surfaces are shown in Table 1. Examples of computer-segmented and manually-traced bone and cartilage contours are shown in Fig. 4.

The mean cartilage thickness measurements achieved a signed error of 0.08 ± 0.07mm, and an unsigned error of 0.09 ± 0.06mm. The corresponding measurements of maximum cartilage thicknesses have signed and unsigned errors of 0.01 ± 0.19mm and 0.16 ± 0.10mm, respectively. All border positioning errors show subvoxel accuracy (voxel size $0.3 \times 0.3 \times 0.3$ mm^3).

In the reproducibility experiment, the initializing spheres were modified from the original settings by adding up to 10% of random perturbations to their radii and 2 to 5 voxels of random translations to each coordinate of their positions. The Bland-Altman plots of the signed differences between each individual measurement and the average measurements are shown in Fig. 5 demonstrating that repeated measurement of cartilage thickness is unbiased and reproducible.

4 Discussion and Conclusion

Traditional techniques such as manual segmentation and gradient based edge detection are not suitable for automated, accurate, reproducible detection of the cartilage and subchondral bone surfaces in thin congruent cartilage layers. The objective of this study was to provide a proof of concept that the cartilage

and subchondral bone surfaces can be accurately detected simultaneously in 3-D, using a novel segmentation method, and perform its pilot validation in comparison with an independent standard.

Properties of the Method. The graph-based segmentations utilized hard geometric constraints, which are intuitive and easily controllable. The definition of the smoothness constraint, however, requires that the edges in the surface mesh be as equidistant as possible. This could be achieved by using sophisticated mesh optimization algorithms. An alternative and simpler way is to make the smoothness constraint vary between graph columns by modulating it according to the corresponding edge length. When the mesh is dense enough, however, the effect of unequal edge length could be ignored for our application. Therefore, neither approach was used in the reported experiments. A drawback of the presented graph-search approach is its dependence on presegmentation, which is crucial for obtaining good final results. However, a one-shot approach using either numerical or discrete mathematical tools alone could be difficult to design, computationally inefficient and may not yield a satisfactory outcome. In addition, its reliance on surface normals makes the method suffer from surface self-intersections. However, this problem is avoidable by detecting spatially intersecting node columns and pruning the affected nodes during the graph-construction.

The employed presegmentation method uses free form deformation, with which one can use large step size for surface evolution. Moreover, in practice, the number of control points required for the FFD is usually much fewer than the number of image voxels. These make the method computationally efficient.

Overall, the method was shown to be highly reproducible in our experiments. However, the initialization of the presegmentation is quite strategic. As a rule of thumb, the seed-spheres should be roughly centered at the maxima of the "shape image" in the bone interior. Automatic initialization methods can be designed following this strategy.

Cartilage Segmentation. A variety of 2-D image segmentation techniques have been utilized on articular cartilage images in the past, including manual segmentation, seed point and region growing algorithms, fully automated 2-D shape recognition, interpolated B-splines, B-spline snakes, and directional gradient vector flow snakes [6, 7, 8]. All of these techniques have limitations as they require an accurate initialization. Manual surface segmentation is both labor intensive and prone to error and is influenced by subjective judgment of the operator leading to inter-observer variability. Moreover, the accuracy and reproducibility of existing fully automated and semi-automated algorithms in noisy images of cartilage layers are often suboptimal. This poses particular problems in thin highly congruent, curved cartilage layers, which require subvoxel measurement accuracy. Previous studies utilizing computer-assisted techniques suffer from measurement errors of up to 100% or exclude large areas of the joint surface. As a result there has been a return to manual segmentation techniques with the focus being on the development of time saving devices such as touch screen interactive segmentation. The reported 3-D approach addresses a number

of the existing challenges and carries a substantial promise for the future utility of automated quantitative analysis of cartilage in 3-D.

Conclusion. A novel method for simultaneously segmenting multiple closed surfaces was demonstrated. The method utilizes an efficient graph-based algorithm that produces optimal solutions according to certain cost functions and geometric constraints. The proposed method achieved highly accurate results in segmenting cartilage and bone surfaces in MR images of human ankles. Although this paper concentrated on closed surfaces, the presented method can segment surfaces of other topologies according to different initializing meshes.

References

1. X. Wu and D. Z. Chen, "Optimal net surface problems with applications," in *Proc. of the 29th International Colloquium on Automata, Languages and Programming (ICALP)*, July 2002, pp. 1029–1042.
2. K. Li, X. Wu, D. Z. Chen, and M. Sonka, "Efficient optimal surface detection: Theory, implementation and experimental validation," in *Proc. SPIE International Symposium on Medical Imaging: Image Processing*, vol. 5370, May 2004, pp. 620–627.
3. ——, "Globally optimal segmentation of interacting surfaces with geometric constraints," in *Proc. IEEE Computer Society Conference on Computer Vision and Pattern Recognition (CVPR)*, vol. I, June 2004, pp. 394–399.
4. X. Huang, D. Metaxas, and T. Chen, "Metamorphs: Deformable shape and texture models," in *Proc. IEEE Computer Society Conference on Computer Vision and Pattern Recognition (CVPR)*, vol. I, June 2004, pp. 496–503.
5. Y. Sato, C.-F. Westin, A. Bhalerao, S. Nakajima, N. Shiraga, S. Tamura, and R. Kikinis, "Tissue classification based on 3D local intensity structure for volume rendering," *IEEE Trans on Visualization and Computer Graphics*, vol. 6, no. 2, pp. 160–180, 2000.
6. C. G. Peterfy, C. F. van Dijke, D. L. Janzen, C. C. Gluer, R. Namba, S. Majumdar, P. Lang, and H. K. Genant, "Quantification of articular cartilage in the knee with pulsed saturation transfer subtraction and fat-suppressed MR imaging: optimization and validation," *Radiology*, vol. 192, pp. 485–491, 1994.
7. A. Stammberger, F. Eckstein, M. Michaelis, K. H. Englmeier, and M. Reiser, "Interobserver reproducibility of quantitative cartilage measurement: comparison between B-spline snakes and manual segmentation," *Magnetic Resonance Imaging*, vol. 17, pp. 1033–1042, 1999.
8. J. Tang, S. Millington, S. Acton, J. Crandall, and S. Hurwitz, "Cartilage surface tracking using directional gradient vector flow snakes," in *IEEE Int. Conf. on Image Processing*, Singapore, 2004.

Appendix 5. Ankle Joint contact area study

A Stereophotographic Study of Ankle Joint Contact Area

Stephen Millington, Markus Grabner, Ralph Wozelka, Shepard Hurwitz, Jeff Crandall

Medical University of Vienna, Währinger Gürtel 18-20, Wein, 1090, Germany

Received 4 September 2006; accepted 15 March 2007

Published online ? ? ? ? in Wiley InterScience (www.interscience.wiley.com). DOI 10.1002/jor.20425

ABSTRACT: The purpose of this study was to measure the ankle joint contact area under physiological load magnitudes using a stereophotography technique that allows accurate analysis of the entire joint surface without disrupting the joint during loading. Ten cadaveric foot and ankle specimens were loaded to 1000 N in neutral, and 20° dorsiflexion, supination, pronation, and plantarflexion. Photo targets rigidly fixed to each of the bones were imaged in the loaded joint position using a high-resolution stereophotography system. After testing, each ankle was disarticulated and the joint surfaces imaged relative to the photo targets. The photo targets were then used to spatially register the joint surfaces into the loaded joint position; the overlap of the surfaces was used to determine the joint contact area. The mean talo–tibia contact area was greatest in dorsiflexion $7.34 \pm 1.69\ cm^2$ and was significantly larger than in plantar flexion ($p < 0.05$), which showed the smallest joint contact area $4.39 \pm 1.41\ cm^2$. Considering talo–fibula, the maximum contact area was measured in dorsiflexion, $2.02 \pm 0.78\ cm^2$, and the minimum contact area occurred in pronation, $0.77 \pm 0.49\ cm^2$, respectively ($p < 0.05$). The reported stereophotography technique allows measurement of the joint contact area without disrupting the joint during loading. The contact area is larger than previously reported, as the entire joint surface was analyzed. Joint contact extends over both the talar dome and the talar shoulders where osteochondritis dissecans lesions commonly occur. © 2007 Orthopaedic Research Society. Published by Wiley Periodicals, Inc. J Orthop Res 25:1–9, 2007

Keywords: ankle; joint contact area; stereophotography; joint loading

INTRODUCTION

The ankle joint is one of the three major joints of the lower limb; however, unlike the hip and knee joints, the ankle is rarely affected by primary osteoarthritis but is particularly sensitive to posttraumatic osteoarthritis.[1] Knowledge of the joint contact area under physiological loads and throughout the range of motion is essential for understanding the biomechanics of the ankle joint; furthermore, it is beneficial for understanding the pathogenesis of joint degeneration as well as improving prosthetic design and ligament reconstruction surgery. Importantly, cartilage restoration and repair therapies, such as mosaicoplasty and autologous chondrocyte implantation (ACI), are becoming more common for talar articular cartilage lesions.[2–5] Lesions occurring on the talus that are amenable to surgical treatment commonly occur over the anterior–medial or posterior–lateral talar shoulders,[6] therefore, the joint contact characteristics in these regions under different loading conditions are of particular interest.

There have been several reported experimental studies of ankle joint contact characteristics with wide variations in methodology and loading conditions resulting in varying reports of the extent and location of the contact area.[7–13] The most widely used technique for measuring joint contact area in the ankle has been Fuji film.[7,8,12,14,15] Fuji film has several well-established limitations; it requires dissection of the joint so the film can be inserted, it is prone to crinkling, slippage and shearing can produce erroneous results, and it has a thickness on the order 0.3 mm, which can alter the joint contact characteristics in highly congruent curved joints such as the ankle.[16] Other methods that have been applied to study the joint contact area include: reversible cartilage staining,[17] silicone oil–carbon black powder suspension squeeze, known as the 'A3S technique',[18] dye injection,[13] silicone rubber molding,[10] stereophotography,[19] and more recently, roentgen stereophotography.[20]

Using Fuji film, Calhoun et al.[7] and Driscoll et al.[8] reported that the contact area of the ankle joint was located over the central region of the talar dome; Kimizuka et al.[10] reported a similar

Correspondence to: Stephen Millington (Telephone: 0043-1-40400-1771; Fax: 0043-1-40400-7631; E-mail: steven.millington@reseed.ac.uk)

Appendix 5

distribution from silicone rubber moldings. In contrast, studies using reversible staining[9] and roentgen stereophotography combined with a 3D digitizer[20] reported the ankle joint contact area to be located over the lateral and medial margins of the talus.

Previous studies of ankle joint contact area have used a range of different joint load magnitudes varying from to 490 N to 3200 N,[7,18] and have measured contact area with the ankle joint in variety of positions,[7,10,15] which has substantially influenced the results previously reported. However, these earlier studies have not assessed the joint contact area under load at the extremes of ankle movement where injury may be more likely to occur.

Ateshian et al.[19] published an elegant study using a stereophotogrammetry technique and compared it to a number of different techniques for measuring joint contact area in an incongruent and a congruent joint. Dye staining technique consistently overestimated the contact area, especially in congruent joints. Silicone casting produced the smallest contact areas; this probably occurs for two reasons. First, the silicone 'film' cannot be squeezed out of the contact area in a finite time. Second, the viscosity of the silicone rapidly increases as it turn from liquid to solid state relatively rapidly. Furthermore, dye staining and silicone molding also require extensive joint dissection prior to testing, which may significantly affect joint stability and hence joint contact area. Fuji film and the stereophotography proximity techniques produced consistent result in both the congruent and incongruent joints. Although Fuji film gives the benefit of also allowing pressure measurement, as described above, it has considerable disadvantages. On the other hand, stereophotography proximity experiments do not require disruption of the joint prior to testing, and the experiments can be performed relatively quickly.

The specific objectives of this study were first to measure the joint contact area in intact ankle joints under a physiological load in a variety of positions including neutral and the extremes of dorsiflexion, supination, pronation, and plantar flexion. Second, to describe the distribution of the contact area across the joint surfaces, and last, to demonstrate a technique that allows analysis of the entire ankle joint surface with greater accuracy and fewer limitations than other techniques.

MATERIALS AND METHODS

Ethical approval for the study was provided by the University of Virginia institutional review board and human usage review panel. All specimens were acquired in accordance with state and federal laws.

Specimen Preparation

Ten lower leg specimens (six right and four left legs) were obtained from nine fresh-frozen cadavers, mean age 64.6 years (six male, three female). From the available medical histories there were no reports of trauma to the lower limbs or musculoskeletal disease in the ankle(s) of the subjects. The specimens were stored at −25°C; prior to testing each specimen was allowed to thaw at room temperature for 24 h. A normal range of movement and ligamentous stability were confirmed by physical examination prior to testing performed by an orthopedic surgeon.

Each lower leg specimen was transected approximately 20 cm proximal to the ankle joint. The soft tissues were stripped from the proximal tibia and fibula and the two bones were then rigidly fixed into potting cup using a fast setting resin (R1 Fastcast, Goldenweest Manufacturing Inc., CA) with the leg in an anatomically neutral position.

Two Steinmann pins were inserted into the tibia approximately 1 cm proximal to the joint line, via minimal incisions; a further two pins were inserted into each of the talar neck and the distal fibula. Forty-five degree bevelled frames with mounted photo targets were then rigidly fixed to Steinmann pins using polymethylmetharcrylate (PMMA). The range of movement was once again examined to ensure that the reference frames did not come into contact with each other or impinge the range of motion at the ankle joint. The foot was then rigidly mounted to a foot plate using three screws into the calcaneous, one screw into the distal part of the first metatarsal, and taping across the forefoot (Fig. 1).

Specimen Loading

In the next step the foot plate was rigidly fixed to the base of the test fixture. The actuator of the hydraulic materials testing machine (Tinius Olsen, Horsham, PA, USA) was lowered and the base of the potting cup was positioned flat against the actuator plate. This configuration ensured that the axial compressive load was applied along the vertical axis of the tibia and fibula. For testing in positions other than neutral, a 20° angled aluminium block was incorporated between the foot plate and the base of the test rig (Fig. 1).

Each ankle was tested in five positions: neutral, 20° plantar flexion, 20° supination, 20° pronation, and 20° dorsiflexion, which reflect the more extreme ends of movement where the ankle may be more susceptible to injury.[21] The specimen was steadily loaded over 3 min to a peak load of 1000 N, the actuator was then held in a stationary position, for approximately 20 s while the photo targets were imaged using the stereophotogrammatric system. The load was then released and the specimen was repositioned. The process was repeated for each of the joint positions studied.

DOI 10.1002/jor

Appendix 5

Figure 1. A lower leg specimen mounted in the test rig in 20° plantarflexion. Bevelled frames with the mounted photo targets are rigidly attached to each of the bones. The foot is rigidly attached to the foot plate by screws in the calcaneus the first metatarsal Additionally the forefoot was tapped to the foot plate prior to loading.

Stereophotogrammetry System

The Advanced TOpometric System (ATOS II SO, Capture 3-d, Costa Mesa, CA, USA), consists of two high-resolution CCD cameras, a fringe pattern projector, and digital imaging processing software. The ATOS™ system has a measurement noise (accuracy) of ±2 μm and point spacing of 0.03 mm (http://www.gom.com/EN/measuring.systems/atos/system/variations). It functions by projecting a fringe pattern onto the specimen and the fixed photo targets. The system automatically detects the photo targets within the images captured by the two CCD cameras, therefore it is not necessary to know the exact spatial relationship of the photo targets before imaging. The system then uses triangulation and digital image post processing to assign 3D coordinates to each pixel and generates a dense point cloud. Multiple point clouds taken from different views are automatically combined into one measurement project within a common coordinate system defined by the photo targets. By combining multiple point clouds a full detailed 3D model of each surface can be generated in the form of a triangulated mesh.

At peak load the photo targets were imaged and formed the spatial coordinate frame for the subsequent registration of the tibia, talus, and fibula surfaces together. Once the loading studies were completed the ankle joint was disarticulated and inspected by an orthopedic surgeon for signs of surface fibrillation or degeneration using the India ink technique. Each articular surface was then imaged relative to the photo targets rigidly fixed to the relevant bone, using the ATOS™ system.

The surfaces of the three ankle bones were then realigned into the positions assumed in each of the joint loading configurations. This was performed using software incorporated into the ATOS™ system. First, the photo targets associated with an individual cartilage surface were identified and then the same photo targets in the loaded configuration were identified. An automated transformation to position the photo targets and the associated surface into the loaded joint position was performed and the point cloud data was saved. The procedure was performed for each bone, hence providing the relative positions of the joint surfaces when under load. The procedure was repeated for each of the five joint positions evaluated.

Postprocessing Technique

The force applied to the cartilage layers during the loading phase causes cartilage deformation to occur; however, the force is then removed, the ankle joint is disarticulated, and the joint surfaces are independently imaged with the stereophotography system in the undeformed state. When the undeformed surfaces of the talus, tibia, and fibula are transformed into the common coordinate system formed by the photo targets in the loaded state the undeformed cartilage surfaces overlap. This overlapping region is a good approximation of the true contact area according to the Winkler elastic foundation model.[22] However, determining the overlapping regions is not straightforward, because the surfaces are not closed, so heuristics must be applied to decide which part of the surface should be considered in contact (i.e., overlapping) with the opposite surface.

We define two constants, ε_1 and ε_2, and treat all triangles on mesh A with a distance of less than $<\varepsilon_1$ from the corresponding triangle on the opposite mesh B as part of the contact area. Moreover, overlapping regions are considered in contact for distances up to ε_2 to account for a certain amount of deformation (Fig. 2). We set $\varepsilon_1 > 0$, because in the deformed state a greater area of cartilage will be in contact with its opposing surface than compared to the overlap of undeformed surfaces; furthermore, ε_1 allows for a small amount of uncertainty in the surface due to the surface preparation. To ensure that only valid solutions are yielded, and erroneous results at the peripheries of the joint surfaces are avoided, the value of ε_2 should not exceed the maximum expected value of overlap. The values of ε_2 may theoretically be up to the combined cartilage thickness of the opposing surfaces. For this study we set $\varepsilon_1 = 0.03$ mm and $\varepsilon_2 = 1$ mm. To distinguish overlapping and nonoverlapping regions, we examine the surface normal vector $\mathbf{n}$. In the nonoverlapping case, $\mathbf{n}$ points toward the opposite surface, while the opposite surface is found in the negative direction $-\mathbf{n}$ in the overlapping case (Fig. 2). Finally, we ignore ε_2 in regions that extend beyond the opposite surface's border as previously described.[23]

Appendix 5

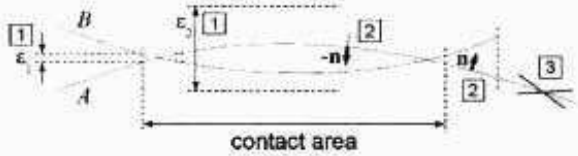

Figure 2. Contact area post processing steps: [1] Values of ε_1 and ε_2 are set to allow for the surface uncertainty and the maximum deformation; [2] the direction from one surface to the other is determined, which is the surface normal vector [n] in nonoverlapping regions and [−n] in overlapping regions; [3] regions of the surface extending beyond the border of the opposing surface are excluded.

because we know in advance that such regions cannot contribute to the contact area (Fig. 2).

Because the surface areas and contact areas are measured from the triangulated mesh, created from the point cloud data, noise in the vertex locations could result in local variations in the surface normals, which may subsequently increase the size of the measured area. Although this effect is small for any given vertex, the cumulative effect across the total surface area or joint contact area maybe considerable; however, the area error is small if the vertex displacement is small compared to the triangle edge length. To assess whether vertex location noise produced a marked effect on the area measurements, the change in the total surface area and normalized joint contact area following consecutive iterations of a previously described denoising method[24] was measured for a talus in the neutral position.

Statistical Analysis

Parameters were assessed for statistical differences between joint loading positions using an ANOVA with a post hoc Tukey's test, $p < 0.05$ was considered statistically significant. All statistical analysis was performed using SPSS 13.0 (SPSS Inc. Chicago, IL).

RESULTS

The results of multiple iterations of the denoising method show that the contact area error due to vertex location noise is negligibly low; therefore, mesh denoising was not used for the purposes of these tests (Table 1).

The absolute size of the joint surface area for each bone, the talo–tibia joint contact area, talo–fibula contact area, and total joint contact area were calculated for each joint position. To compensate for variations in the size of the joint contact area caused by differences in the size of the specimen donors we also determined the normalized joint contact area.

The joint surface area measurements are shown in Table 2. The mean talo–tibia contact area was greatest in dorsiflexion 7.34 ± 1.69 cm^2, and was significantly larger than in plantar flexion ($p < 0.05$), which showed the smallest joint contact area 4.39 ± 1.41 cm^2. When considering the talo–fibula contact area, the maximum joint contact occurred in dorsiflexion, 2.02 ± 0.78 cm^2, and the minimum joint contact area occurred in pronation, 0.77 ± 0.49 cm^2, respectively ($p < 0.05$). Mean total talar, tibia, and fibula contact areas for the different loading positions are shown in Figure 3. The total talar contact area in dorsiflexion and neutral were both significantly larger than the total contact area in plantarflexion, $p < 0.005$ and $p < 0.05$, respectively. Furthermore, the total contact area in dorsiflexion was significantly larger than in pronation, $p < 0.05$.

The joint contact area for each measurement was normalized to the joint surface area of the appropriate bone, that is, the talus, tibia, or fibula for each specimen. The mean normalized total talar, tibia, and fibula contact areas for the different loading positions are shown in Figure 4.

The normalized plantarflexion contact area was significantly smaller than in dorsiflexion, $p < 0.05$, neutral, $p < 0.05$ and supination, $p < 0.05$. The normalized dorsiflexion contact area was also significantly greater than in pronation, $p < 0.05$.

Table 1. Impact on Surface Area and Normalized Contact Area Measurements for Consecutive Iterations of the Noise Reduction Procedure

Number of Iterations	% Reduction of Total Surface Area	Normalised Contact Area (%)
0	—	39.86
1	0.23	39.83
2	0.30	39.83
3	0.36	39.84
4	0.40	39.82
5	0.44	39.83

Reductions in total surface area a reported relative to the unprocessed mesh.

DOI 10.1002/jor

Appendix 5

Table 2. Mean, Standard Deviation and Range of Joint Surface Areas for Each Bone in the Ankle Joint ($N = 10$)

Bone	Mean Surface Area, cm^2	Standard Deviation, cm^2	Minimum Surface Area, cm^2	Maximum Surface Area, cm^2
Talus	20.0	2.3	16.3	24.1
Tibia	10.4	1.2	8.7	12.8
Fibula	3.0	0.5	2.4	4.0

The results show that as the ankle joint rotated in the sagittal plane and moved from plantar flexion to dorsiflexion the tibio–talar normalized contact area increased by $15.74 \pm 7.95\%$, whereas when the ankle rotated in the coronal plane moving from pronation to supination the tibio–talar normalized contact area increased by only $5.02 \pm 6.86\%$.

Characteristic pattern of joint contact were seen in each of the respective loading positions; typical examples of the shape and location of the joint contact area in each of the five positions tested are shown in Figure 5. Notable features are the broad contact area in dorsiflexion distributed especially over the medial and lateral talar shoulders. However, in 20° plantarflexion the contact area on the tibia is narrower and more centrally located as the talus is narrower posteriorly. When the limbs were loaded in supination typically the area where the greatest overlap of the surfaces and therefore the region of greatest deformation under load occurred at the site where the medial talar shoulder contacts the tibial plafond. In supination, the contact area was more medially located than in

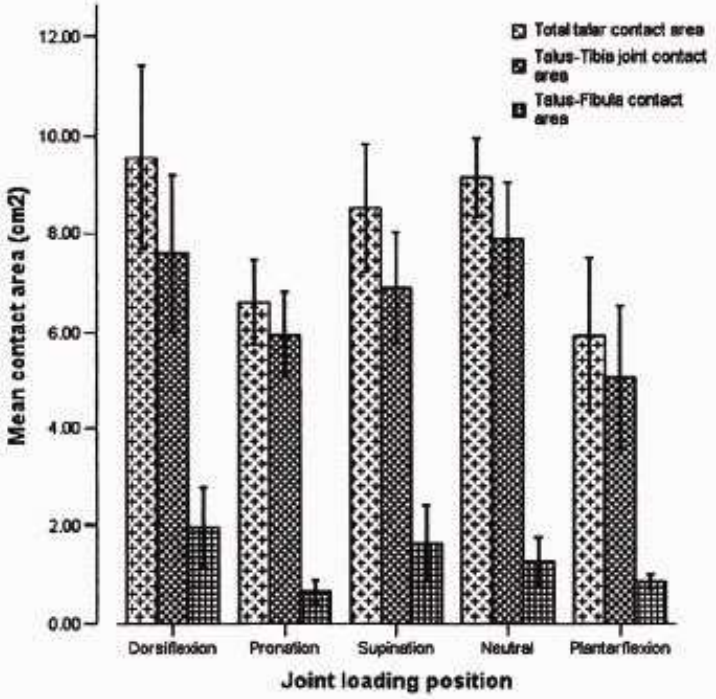

Figure 3. Bar chart of the mean joint contact area (cm^2) over the surface of each of the talus, tibia, and fibula in five different loading positions. Error bars represent ±1 SD.

Appendix 5

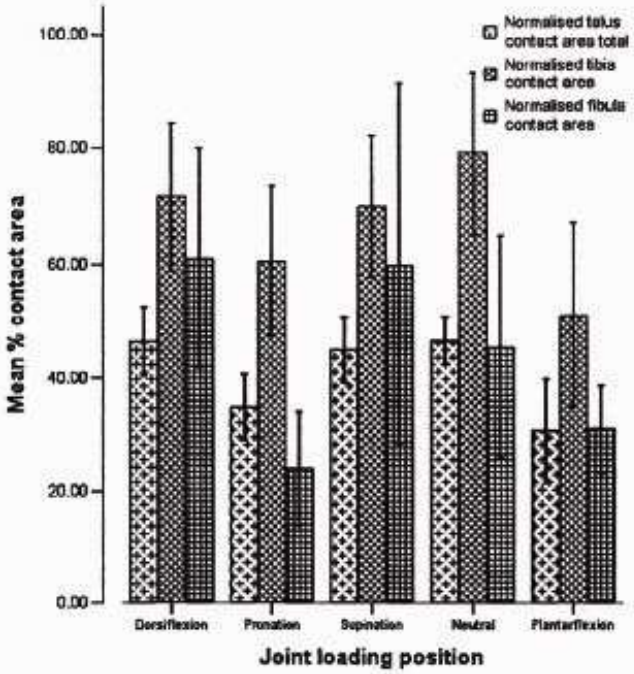

Figure 4. Mean normalized joint contact area over the surface of the talus, tibia, and fibula in each of the five loading positions. Error bars represent ±1 SD.

neutral or pronation (Fig. 5). In contrast, the region of maximum cartilage surface overlap in pronation occurred at the site corresponding to the contact between the lateral talar shoulder and the tibial plafond. The region of contact in pronation was clearly more laterally located than in neutral loading (Fig. 5).

The contact pattern between the talus and fibula displayed a relatively consistent pattern; there was a noticeable difference, as anticipated, between supination and pronation. Under loading in 20° of supination the contact area occurred over the proximal part of the fibula surface, mainly centrally and anteriorly (Fig. 6). The corresponding contact on the talar surface over the anterior superior aspect of the lateral talar facet (Fig. 6). When the specimens were loaded in the pronated position the contact area was distributed over the inferior part of the fibula surface where it has a valgus angulation (Fig. 7). The corresponding contact area on the talar surface occurred slightly posteriorly over the distal valgus angulated part of the lateral talar facet (Fig. 7).

DISCUSSION

In this study we have described a modification of a stereophotogrammetric technique, previously used to determine cartilage thickness and distribution, for measuring and describing joint contact area in the ankle joint. The objective of the study was to quantitatively evaluate the joint contact area and its topographical distribution under loading with the foot positioned in neutral and at extremes of dorsiflexion, planter flexion, supination, and pronation, that is, in positions where the ankle maybe more susceptible to injury. The system allows rapid acquisition and processing of large volumes of geometric data with high measurement accuracy (±2 μm). The versatility and accuracy of the technique has enabled us to study the joint contact characteristics of the highly congruent ankle joint without having to disrupt the joint integrity prior to the loading phase.

Our results show that the largest talo–tibia and talo–fibula contact area occurred in dorsiflexion,

 DOI 10.1002/jor

Appendix 5

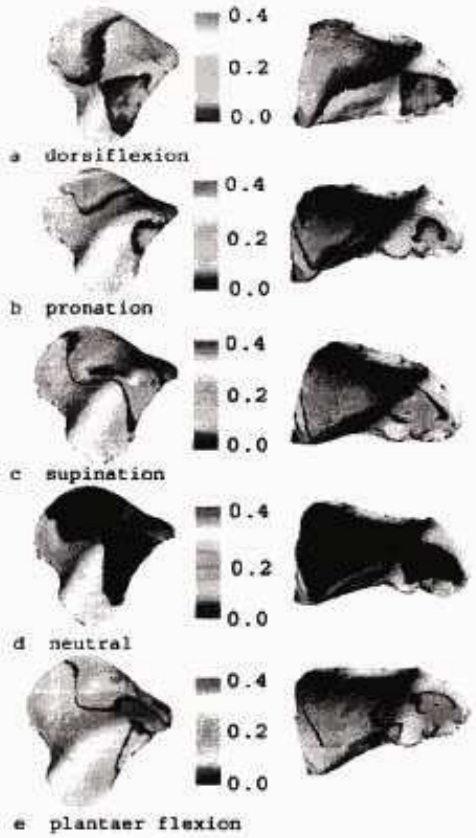

Figure 5. Typical talar–tibia joint contact distribution patterns displayed on the talar and tibial surfaces in (a) dorsiflexion, (b) pronation, (c) supination, (d) neutral, and (e) plantarflexion. Color coding shows the extent of overlap, in millimeters, of the surfaces in the loaded position indicating the areas of greatest cartilage deformation.

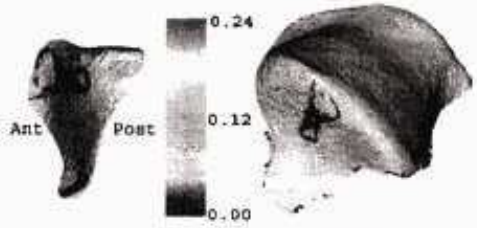

Figure 6. Characteristic joint contact distribution patterns between the talus and fibula in 20° supination displayed on the talar and fibula surfaces.

DOI: 10.1002/jor

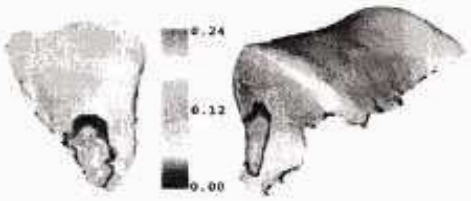

Figure 7. Examples of the joint contact between the talus and fibula in 20° pronation, displayed on the talar and fibula surfaces.

7.34 ± 1.69 cm^2 and 2.02 ± 0.78 cm^2, respectively. The smallest talo–tibia contact area occurred in plantarflexion, 4.39 ± 1.41 cm^2 and the smallest talo–fibula contact area occurred when the foot was pronated, 0.77 ± 0.49 cm^2; both are significantly smaller than in dorsiflexion ($p < 0.05$).

Additionally, the assessment of the noise reduction algorithm showed that the surface area and joint contact area errors occurring due to vertex noise was negligible, and that the method used does not require noise reduction as part of the postprocessing procedure.

Direct comparison to earlier studies is difficult due to the variety of loads and joint positions used in previously reported tests. Calhoun et al.[7] reported the contact area normalized to joint surface area; their results show the greatest contact area (15%) occurred at the maximum applied dorsiflexion (10°), and that medial and lateral facet contact increased with inversion and eversion, respectively. Yao and Seedhom[13] applied the highest load (3200 N $\pm$ 562.5) and measured the tibio–talar contact area to be 4.839 ± 0.986 cm^2, using the '3S technique.' Christensen et al.[15] applied an 800 N load, similar to the loading range used by Calhoun,[7] which are the lowest loads reported in the ankle literature; they measured a mean contact area of 3.25 ± 0.52 cm^2, but found considerable variation with position.

Unfortunately, these earlier ankle studies were unable to reliably evaluate contact area over highly curved surfaces with complex 3D topography such as occurs over the shoulders of the talus, and therefore it was extremely challenging to accurately quantify the total surface area of the joint. On the other hand, the reported stereophotography approach allows easy evaluation of the entire surface and measurement of surface and contact areas by triangulation. As a result, the mean normalized total talar contact area measured in this study was considerably higher than that measured by Calhoun et al.,[7] who reported the

Appendix 5

maximum normalized contact as 15% at 10° dorsiflexion. Moreover, the total talar contact area measured in this study exceeds values reported using the 'A3S technique'[13] and Fuji film.[15]

Calhoun et al.[7,11] obtained joint contact areas with the foot in a variety of positions and reported the their values as inversion and eversion; in this study we used a similar method for positioning the foot but we favor the terms pronation and supination because this movement affects several joints, and in supination is a combination of inversion, flexion and adduction at the ankle, whereas in pronation it is a combination of eversion extension and abduction.

In pronation, we found that the mean talo–fibula contact area was significantly smaller than in dorsiflexion. In contrast to earlier studies,[7,11] the talo–fibula contact area in pronation was smaller than in supination; however, the difference was not statistically significant. This was an unexpected finding, but is explained by examining the distribution pattern of the talo–fibula contact area over the joint surfaces. When the ankle joint is loaded in pronation the fibula tip comes into contact with the distal angulated section of the lateral talar facet, which forces the distal fibula more laterally. This results in a small localized contact between the distal part of the fibula surface and the distal part of the lateral talar facet (Fig. 7). In supination, the distal part of the lateral talar facet assumes a more vertical orientation; this, combined with the compressive load and the ligamentotaxis pulling the fibula inferiorly, result in a larger contact area between the lateral talar shoulder region and the broader proximal part of the fibula joint surface (Fig. 6).

The regions where we measured the greatest surface overlap, corresponding to the regions where the greatest cartilage deformation occurred and therefore presumably the greatest load transfer, correspond to the shoulders of the talar cartilage. This is interesting as the cartilage thickness and the subchondral bone mineral density are highest over the talar shoulders,[23,25,28] and these finding may be a response to the prevailing mechanical conditions occurring in the ankle joint.

The distribution of the contact area over the joint surfaces seen in this study support the finding of earlier studies using roentgen stereophotography and reversible staining[20] and reversible staining,[9] which indicated that joint contact was predominantly over the margins of the talar dome. However, our results differ from studies that required the insertion of Fuji film into the joint space and reported that the contact area to be over the central talar dome.[7,8,10] Fuji film studies of highly curved and congruent joints must be interpreted with caution as the Fuji film itself can alter the join mechanics and is prone to crinkling in highly curved areas, such as the talar shoulders.

It is important to bear in mind that in this study, as in many of the earlier studies, the fixation of the foot and the tibia constrain movements in particular rotation of the tibia, which occurs during dorsiflexion and plantar flexion in the gait cycle.[27] This restriction of rotation could have prevented the ankle joint from obtaining maximal congruence in dorsiflexion and plantar flexion; hence, the joint contact area reported my still be an under estimation of the in vivo situation.

Given that cartilage surfaces deform in regions of contact it should be appreciated that the 'true' in vivo contact area is not directly measured by this technique because a proximity analysis of the non-deformed surfaces is used to determine the joint contact area. Additionally, the technique used in this study can only be used in vitro, and it is important to appreciate that in cadaveric experiments there is no muscle tension and the stiffness of ligamentous tissue is different from that of living people.

Despite these shortcomings, the reported stereophotogrammetric technique has the advantage that during the loading phase of the study no extensive dissection of the joint structures is required and no foreign material is inserted into the joint, which may alter the joint contact pattern. Moreover, the described method allows accurate 3D reconstructions of the entire articular surface of each bone in the joint, facilitating joint contact analysis in highly curved regions and automating quantitative measurements. The versatility of the technique addresses many of the difficulties associated with previous methods used for measuring ankle joint contact area.

The in vitro method described in this study will be helpful for comparative studies and validation of loading devices and image analysis algorithms that are being developed for measuring joint contact area from magnetic resonance images. In the future it will be particularly interesting to remove the constraints on tibial rotation during loading and assess the effect on contact area. Furthermore, it will be interesting to assess sex differences, as it has been show there are differences in the bone sizes and radii of curvature between men and women, with a greater potential for adduction in women;[28] unfortunately, this was not possible in this study due to the small numbers of specimens. Importantly, this method provides

DOI 10.1002/jor

Appendix 5

useful input data for computational models of the ankle joint, which facilitate in-depth analysis of joint biomechanics.

CONCLUSIONS

A high-resolution stereophotographic technique that does not violate the joint structures or require insertion of foreign material into the joint during loading and allows analysis of the entire ankle joint surface has been described. The largest contact area occurred in dorsiflexion, the smallest contact area occurred in plantarflexion, but in all cases the contact area appears to be larger than previously reported. Furthermore, the contact distribution was located more over the talar shoulders where the cartilage is thickest, the subchondral bone most dense, and OCD lesions most commonly occur[6] as opposed to contact over the center of the talar dome and tibial plafond as reported in some earlier studies.

ACKNOWLEDGMENTS

Partial funding for this study was provided by Zimmer Inc. USA.

REFERENCES

1. Saltzman CL, Salamon ML, Blanchard GM, et al. 2005. Epidemiology of ankle arthritis: report of a consecutive series of 639 patients from a tertiary orthopaedic center. Iowa Orthop J 25:44–46.
2. Hangody L, Feczko P, Bartha L, et al. 2001. Mosaicplasty for the treatment of articular defects of the knee and ankle. Clin Orthop Relat Res 391:Suppl:S328–S336.
3. Hangody L. 2003. The mosaicplasty technique for osteochondral lesions of the talus. Foot Ankle Clin 8:259–273.
4. Mandelbaum BR, Gerhardt MB, Peterson L. 2003. Autologous chondrocyte implantation of the talus. Arthroscopy 19 (Suppl 1):129–137.
5. Whittaker JP, Smith G, Makwana N, et al. 2005. Early results of autologous chondrocyte implantation in the talus. J Bone Joint Surg Br 87:179–183.
6. O'Farrell TA, Costello BG. 1982. Osteochondritis dissecans of the talus. The late results of surgical treatment. J Bone Joint Surg Br 64:494–497.
7. Calhoun JH, Li F, Ledbetter BR, Viegas SF. 1994. A comprehensive study of pressure distribution in the ankle joint with inversion and eversion. Foot Ankle Int 15:125–133.
8. Driscoll HL, Christensen JC, Tencer AF. 1994. Contact characteristics of the ankle joint. Part 1. The normal joint. J Am Podiatr Med Assoc 84:491–498.
9. Greenwald AS, Matejczyk MB, Keppler L, et al. 1977. Articular cartilage contact areas of the ankle. 23rd Annual meeting of the orthopaedic research society. Las Vegas, NV: Orthopaedic Research Society.
10. Kimizuka M, Kurosawa H, Fukubayashi T. 1980. Load-bearing pattern of the ankle joint. Contact area and pressure distribution. Arch Orthop Trauma Surg 96:45–49.
11. Kura H, Kitaoka HB, Luo ZP, An KN. 1998. Measurement of surface contact area of the ankle joint. Clin Biomech (Bristol, Avon) 13:365–370.
12. Macko VW, Matthews LS, Zwirkoski P, Goldstein SA. 1991. The joint-contact area of the ankle. The contribution of the posterior malleolus. J Bone Joint Surg Am 73:347–351.
13. Yao JQ, Seedhom BB. 1991. A new technique for measuring contact areas in human joints—the 'A3S technique'. Proc Inst Mech Eng [H] 205:69–72.
14. Choung D, Christensen JC. 2002. Mosaicplasty of the talus: a joint contact analysis in a cadaver model. J Foot Ankle Surg 41:65–75.
15. Christensen JC, Driscoll HL, Tencer AF. 1994. William J. Stickel Gold Award. Contact characteristics of the ankle joint. Part 2. The effects of talar dome cartilage defects. J Am Podiatr Med Assoc 84:537–547.
16. Wu JZ, Herzog W, Epstein M. 1998. Effects of inserting a pressensor film into articular joints on the actual contact mechanics. J Biomech Eng 120:655–659.
17. Black JD, Matejczyk MB, Greenwald AS. 1981. Reversible cartilage staining technique for defining articular weight-bearing surfaces. Clin Orthop 265–267.
18. Yao JQ, Seedhom BB. 1993. Mechanical conditioning of articular cartilage to prevalent stresses. Br J Rheumatol 32:956–965.
19. Ateshian GA, Kwak SD, Soslowsky LJ, Mow VC. 1994. A stereophotogrammetric method for determining in situ contact areas in diarthrodial joints, and a comparison with other methods. J Biomech 27:111–124.
20. Corazza F, Stagni R, Castelli VP, Leardini A. 2005. Articular contact at the tibiotalar joint in passive flexion. J Biomech 38:1205–1212.
21. Rudd R, Crandall J, Millington S, et al. 2004. 2004-22-0001 Injury tolerance and response of the ankle joint in dynamic dorsiflexion. Stapp Car Crash J 48:1–26.
22. Johnson KL. 1965. Contact mechanics. Cambridge: Cambridge University Press.
23. Millington SA, Grabner M, Wozelka R, et al. 2007. Quantification of ankle articular cartilage topography and thickness using a high resolution stereophotography system. Osteoarthritis Cartilage 15:205–211.
24. Fleishman S, Drori I, Cohen-Or D. 2003. Bilateral mesh denoising. In: Hodgins J, editor. SIGGRAPH 03 Conference Proceedings. San Diego, CA: Assoc. for Computing Machinary.
25. Millington SA, Li B, Trattnig S, et al. 2006. A quantitative and topographical evaluation of ankle articular cartilage using high resolution MRI. J Orthop Res 25: 143–151.
26. Muller-Gerbl M, Putz R., 1995. Functional anatomy of the ankle joint. In: Heim U, editor. The tibial pilon fracture. 1st ed. Philadelphia, PA: Saunders.
27. Mann RA. 1993. Biomechanics of the foot and ankle. Surgery of the foot and ankle. St. Louis, MO: C.V. Mosby Co.
28. Ferrari J, Hopkinson DA, Linney AD. 2004. Size and shape differences between male and female foot bones: Is the female foot predisposed to hallux abducto valgus deformity? J Am Podiatr Med Assoc 94:434–452.

Chapter 10. References

Acton, S. T., Bovik, A. C., (1998). Order statistics in image processing. In: Balakrishnan, N., Rao, C. R. (Eds.), Handbook of Statistics 17: Order Statistics and Their Applications. Elsevier Science, New York, pp. 603-641.

Acton, S. T., Wei, D., Bovik, A. C., (1999). Image enhancement. In: Webster, J. (Ed.), Encyclopedia of Electrical and Electronics Engineering. Wiley - Interscience, New York.

Adam, C., Eckstein, F., Milz, S., Putz, R., (1998a). The distribution of cartilage thickness within the joints of the lower limb of elderly individuals. J.Anat. 193 (Pt 2)**,** 203-214.

Adam, C., Eckstein, F., Milz, S., Schulte, E., Becker, C., Putz, R., (1998b). The distribution of cartilage thickness in the knee-joints of old-aged individuals -- measurement by A-mode ultrasound. Clin.Biomech.(Bristol., Avon.) 13**,** 1-10.

Al Ali, D., Graichen, H., Faber, S., Englmeier, K. H., Reiser, M., Eckstein, F., (2002). Quantitative cartilage imaging of the human hind foot: precision and inter-subject variability. J.Orthop.Res. 20**,** 249-256.

Anderson, D. D., Goldsworthy, J. K., Shivanna, K., Grosland, N. M., Pedersen, D. R., Thomas, T. P., Tochigi, Y., Marsh, J. L., Brown, T. D., (2006). Intra-articular contact stress distributions at the ankle throughout stance phase-patient-specific finite element analysis as a metric of degeneration propensity. Biomech.Model.Mechanobiol. 5**,** 82-89.

Ateshian, G. A., (1993). A B-spline least-squares surface-fitting method for articular surfaces of diarthrodial joints. J.Biomech.Eng 115**,** 366-373.

Ateshian, G. A., Kwak, S. D., Soslowsky, L. J., Mow, V. C., (1994). A stereophotogrammetric method for determining in situ contact areas in diarthrodial joints, and a comparison with other methods. Journal of Biomechanics 27**,** 111-124.

Ateshian, G. A., Soslowsky, L. J., Mow, V. C., (1991). Quantitation of articular surface topography and cartilage thickness in knee joints using stereophotogrammetry. Journal of Biomechanics 24**,** 761-776.

Ateshian, G. A., Warden, W. H., Kim, J. J., Grelsamer, R. P., Mow, V. C., (1997). Finite deformation biphasic material properties of bovine articular cartilage from confined compression experiments. Journal of Biomechanics 30**,** 1157-1164.

Athanasiou, K. A., Niederauer, G. G., Schenck, R. C., Jr., (1995). Biomechanical topography of human ankle cartilage. Ann.Biomed.Eng 23**,** 697-704.

References

Atkinson, T. S., Haut, R. C., Altiero, N. J., (1998). Impact-induced fissuring of articular cartilage: an investigation of failure criteria. J.Biomech.Eng 120**,** 181-187.

Ba-Ssalamah, A., Schibany, N., Puig, S., Herneth, A. M., Noebauer-Huhmann, I. M., Trattnig, S., (2002). Imaging articular cartilage defects in the ankle joint with 3D fat-suppressed echo planar imaging: comparison with conventional 3D fat-suppressed gradient echo imaging. J.Magn Reson.Imaging 16**,** 209-216.

Bashir, A., Gray, M. L., Boutin, R. D., Burstein, D., (1997). Glycosaminoglycan in articular cartilage: in vivo assessment with delayed Gd(DTPA)(2-)-enhanced MR imaging. Radiology 205**,** 551-558.

Bashir, A., Gray, M. L., Hartke, J., Burstein, D., (1999). Nondestructive imaging of human cartilage glycosaminoglycan concentration by MRI. Magn Reson.Med. 41**,** 857-865.

Black, J. D., Matejczyk, M. B., Greenwald, A. S., (1981). Reversible cartilage staining technique for defining articular weight-bearing surfaces. Clinical Orthopaedics and Related Research 265-267.

Borrelli, J., Jr., Tinsley, K., Ricci, W. M., Burns, M., Karl, I. E., Hotchkiss, R., (2003). Induction of chondrocyte apoptosis following impact load. J.Orthop.Trauma 17**,** 635-641.

Brittberg, M., Lindahl, A., Nilsson, A., Ohlsson, C., Isaksson, O., Peterson, L., (1994). Treatment of deep cartilage defects in the knee with autologous chondrocyte transplantation. N.Engl.J.Med. 331**,** 889-895.

Brown, T. D., Anderson, D. D., Nepola, J. V., Singerman, R. J., Pedersen, D. R., Brand, R. A., (1988). Contact stress aberrations following imprecise reduction of simple tibial plateau fractures. J.Orthop.Res. 6**,** 851-862.

Buckwalter, J. A., (1992). Mechanical injuries of articular cartilage. In: Finerman, G. (Ed.), Biology and biomechanics of te traumatised synovial joint. American Academy of Orthopaedic Surgeons, Park Ridge, IL, pp. 83-96.

Buckwalter, J. A., (1995). Osteoarthritis and articular cartilage use, disuse, and abuse: experimental studies. J.Rheumatol.Suppl 43**,** 13-15.

Buckwalter, J. A., (2002). Articular cartilage injuries. Clinical Orthopaedics and Related Research 21-37.

Buckwalter, J. A., Mankin, H. J., (1997). Articular cartilage .2. Degeneration and osteoarthrosis, repair, regeneration, and transplantation. Journal of Bone and Joint Surgery-American Volume 79A**,** 612-632.

Buckwalter, J. A., Martin, J., Mankin, H. J., (2000). Synovial joint degeneration and the syndrome of osteoarthritis. Instr.Course Lect. 49**,** 481-489.

References

Buckwalter, J. A., Saltzman, C. L., (1999). Ankle osteoarthritis: distinctive characteristics. Instr.Course Lect. 48**,** 233-241.

Bullough, P. G., Jagannath, A., (1983). The morphology of the calcification front in articular cartilage. Its significance in joint function. J Bone Joint Surg.Br. 65**,** 72-78.

Burgkart, R., Glaser, C., Hinterwimmer, S., Hudelmaier, M., Englmeier, K. H., Reiser, M., Eckstein, F., (2003). Feasibility of T and Z scores from magnetic resonance imaging data for quantification of cartilage loss in osteoarthritis. Arthritis Rheum. 48**,** 2829-2835.

Burgkart, R., Glaser, C., Hyhlik-Durr, A., Englmeier, K. H., Reiser, M., Eckstein, F., (2001). Magnetic resonance imaging-based assessment of cartilage loss in severe osteoarthritis: accuracy, precision, and diagnostic value. Arthritis Rheum. 44**,** 2072-2077.

Burstein, D., Gray, M., (2003). New MRI techniques for imaging cartilage. Journal of Bone and Joint Surgery 85-A Suppl 2**,** 70-77.

Calhoun, J. H., Li, F., Ledbetter, B. R., Viegas, S. F., (1994). A comprehensive study of pressure distribution in the ankle joint with inversion and eversion. Foot Ankle Int. 15**,** 125-133.

Chen, C. T., Burton-Wurster, N., Borden, C., Hueffer, K., Bloom, S. E., Lust, G., (2001). Chondrocyte necrosis and apoptosis in impact damaged articular cartilage. J.Orthop.Res. 19**,** 703-711.

Cheung, J. T., Zhang, M., (2005). A 3-dimensional finite element model of the human foot and ankle for insole design. Arch.Phys.Med.Rehabil. 86**,** 353-358.

Choung, D., Christensen, J. C., (2002). Mosaicplasty of the talus: a joint contact analysis in a cadaver model. J.Foot Ankle Surg. 41**,** 65-75.

Christensen, J. C., Driscoll, H. L., Tencer, A. F., (1994). 1994 William J. Stickel Gold Award. Contact characteristics of the ankle joint. Part 2. The effects of talar dome cartilage defects. J.Am.Podiatr.Med.Assoc. 84**,** 537-547.

Cohen, Z. A., McCarthy, D. M., Kwak, S. D., Legrand, P., Fogarasi, F., Ciaccio, E. J., Ateshian, G. A., (1999). Knee cartilage topography, thickness, and contact areas from MRI: in-vitro calibration and in-vivo measurements. Osteoarthritis.Cartilage. 7**,** 95-109.

Cohen, Z. A., Mow, V. C., Henry, J. H., Levine, W. N., Ateshian, G. A., (2003). Templates of the cartilage layers of the patellofemoral joint and their use in the assessment of osteoarthritic cartilage damage. Osteoarthritis.Cartilage. 11**,** 569-579.

Corazza, F., Stagni, R., Castelli, V. P., Leardini, A., (2005). Articular contact at the tibiotalar joint in passive flexion. Journal of Biomechanics 38**,** 1205-1212.

Craig, J. G., Go, L., Blechinger, J., Hearshen, D., Bouffard, J. A., Diamond, M., van Holsbeeck, M. T., (2005). Three-tesla imaging of the knee: initial experience. Skeletal Radiol. 34**,** 453-461.

Cushnaghan, J., Dieppe, P., (1991). Study of 500 patients with limb joint osteoarthritis. I. Analysis by age, sex, and distribution of symptomatic joint sites. Ann.Rheum.Dis. 50**,** 8-13.

DeCoster, T. A., Willis, M. C., Marsh, J. L., Williams, T. M., Nepola, J. V., Dirschl, D. R., Hurwitz, S. R., (1999). Rank order analysis of tibial plafond fractures: does injury or reduction predict outcome? Foot Ankle Int. 20**,** 44-49.

Dieppe, P., Kirwan, J., (1994). The localization of osteoarthritis. British Journal of Rheumatology 33**,** 201-203.

Donohue, J. M., Buss, D., Oegema, T. R., Jr., Thompson, R. C., Jr., (1983). The effects of indirect blunt trauma on adult canine articular cartilage. Journal of Bone and Joint Surgery 65**,** 948-957.

Driscoll, H. L., Christensen, J. C., Tencer, A. F., (1994). Contact characteristics of the ankle joint. Part 1. The normal joint. J.Am.Podiatr.Med.Assoc. 84**,** 491-498.

Eckstein, F., Adam, C., Sittek, H., Becker, C., Milz, S., Schulte, E., Reiser, M., Putz, R., (1997). Non-invasive determination of cartilage thickness throughout joint surfaces using magnetic resonance imaging. Journal of Biomechanics 30**,** 285-289.

Eckstein, F., Charles, H. C., Buck, R. J., Kraus, V. B., Remmers, A. E., Hudelmaier, M., Wirth, W., Evelhoch, J. L., (2005b). Accuracy and precision of quantitative assessment of cartilage morphology by magnetic resonance imaging at 3.0T. Arthritis Rheum. 52**,** 3132-3136.

Eckstein, F., Charles, H. C., Buck, R. J., Kraus, V. B., Remmers, A. E., Hudelmaier, M., Wirth, W., Evelhoch, J. L., (2005a). Accuracy and precision of quantitative assessment of cartilage morphology by magnetic resonance imaging at 3.0T. Arthritis Rheum. 52**,** 3132-3136.

Eckstein, F., Gavazzeni, A., Sittek, H., Haubner, M., Losch, A., Milz, S., Englmeier, K. H., Schulte, E., Putz, R., Reiser, M., (1996). Determination of knee joint cartilage thickness using three-dimensional magnetic resonance chondro-crassometry (3D MR-CCM). Magn Reson.Med. 36**,** 256-265.

Eckstein, F., Glaser, C., (2004). Measuring cartilage morphology with quantitative magnetic resonance imaging. Semin.Musculoskelet.Radiol. 8**,** 329-353.

Eckstein, F., Heudorfer, L., Faber, S. C., Burgkart, R., Englmeier, K. H., Reiser, M., (2002). Long-term and resegmentation precision of quantitative cartilage MR imaging (qMRI). Osteoarthritis.Cartilage. 10**,** 922-928.

Eckstein, F., Hudelmaier, M., Wirth, W., Kiefer, B., Jackson, R., Yu, J., Eaton, C., Schneider, E., (2005c). Double Echo Steady State (DESS) Magnetic Resonance Imaging of Knee Articular Cartilage at 3 Tesla - a Pilot Study for the Osteoarthritis Initiative. Ann.Rheum.Dis.

Eckstein, F., Reiser, M., Englmeier, K. H., Putz, R., (2001a). In vivo morphometry and functional analysis of human articular cartilage with quantitative magnetic resonance imaging--from image to data, from data to theory. Anat.Embryol.(Berl) 203**,** 147-173.

Eckstein, F., Schnier, M., Haubner, M., Priebsch, J., Glaser, C., Englmeier, K. H., Reiser, M., (1998a). Accuracy of cartilage volume and thickness measurements with magnetic resonance imaging. Clinical Orthopaedics and Related Research 137-148.

Eckstein, F., Sittek, H., Milz, S., Putz, R., Reiser, M., (1994). The morphology of articular cartilage assessed by magnetic resonance imaging (MRI). Reproducibility and anatomical correlation. Surg.Radiol.Anat. 16**,** 429-438.

Eckstein, F., Sittek, H., Milz, S., Schulte, E., Kiefer, B., Reiser, M., Putz, R., (1995). The potential of magnetic resonance imaging (MRI) for quantifying articular cartilage thickness -- a methodological study. Clin.Biomech.(Bristol., Avon.) 10**,** 434-440.

Eckstein, F., Westhoff, J., Sittek, H., Maag, K. P., Haubner, M., Faber, S., Englmeier, K. H., Reiser, M., (1998b). In vivo reproducibility of three-dimensional cartilage volume and thickness measurements with MR imaging. AJR Am.J.Roentgenol. 170**,** 593-597.

Eckstein, F., Winzheimer, M., Hohe, J., Englmeier, K. H., Reiser, M., (2001b). Interindividual variability and correlation among morphological parameters of knee joint cartilage plates: analysis with three-dimensional MR imaging. Osteoarthritis.Cartilage. 9**,** 101-111.

Eyre, D. R., (1980). Collagen: molecular diversity in the body's protein scaffold. Science 207**,** 1315-1322.

Faber, S. C., Eckstein, F., Lukasz, S., Muhlbauer, R., Hohe, J., Englmeier, K. H., Reiser, M., (2001). Gender differences in knee joint cartilage thickness, volume and articular surface areas: assessment with quantitative three-dimensional MR imaging. Skeletal Radiol. 30**,** 144-150.

Ferrari, J., Hopkinson, D. A., Linney, A. D., (2004). Size and shape differences between male and female foot bones: is the female foot predisposed to hallux abducto valgus deformity? J.Am.Podiatr.Med.Assoc. 94**,** 434-452.

Fitzpatrick, D. C., Otto, J. K., McKinley, T. O., Marsh, J. L., Brown, T. D., (2001). Dynamic contact stress aberrations after simulateed posterior malleolar fracture of the ankle. In Transactions of the orthopaedic trauma association. Orthopaedic Trauma Association, San Diego, CA.

Fitzpatrick, D. C., Otto, J. K., McKinley, T. O., Marsh, J. L., Brown, T. D., (2004). Kinematic and contact stress analysis of posterior malleolus fractures of the ankle. Journal of Orthopaedic Trauma 18**,** 271-278.

Fleishman, S., Drori, I., Cohen-Or, D., (2003). Bilateral mesh denoising. In SIGGRAPH. Assoc. for Computing Machinary, San Diego.

Fukubayashi, T., Kurosawa, H., (1980). The contact area and pressure distribution pattern of the knee. A study of normal and osteoarthrotic knee joints. Acta Orthop.Scand. 51**,** 871-879.

Funk, F. J., (1976). Osteoarthritis of the Foot and Ankle. In American Academy of Surgeons

Symposiums on Osteoarthritis. CV Mosby , St Louis MO.

Glaser, C., Faber, S., Eckstein, F., Fischer, H., Springer, V., Heudorfer, L., Stammberger, T., Englmeier, K. H., Reiser, M., (2001). Optimization and validation of a rapid high-resolution T1-w 3D FLASH water excitation MRI sequence for the quantitative assessment of articular cartilage volume and thickness. Magn Reson.Imaging 19**,** 177-185.

Gluer, C. C., Blake, G., Lu, Y., Blunt, B. A., Jergas, M., Genant, H. K., (1995). Accurate assessment of precision errors: how to measure the reproducibility of bone densitometry techniques. Osteoporos.Int. 5**,** 262-270.

Gold, G. E., Besier, T. F., Draper, C. E., Asakawa, D. S., Delp, S. L., Beaupre, G. S., (2004). Weight-bearing MRI of patellofemoral joint cartilage contact area. J.Magn Reson.Imaging 20**,** 526-530.

Graichen, H., Springer, V., Flaman, T., Stammberger, T., Glaser, C., Englmeier, K. H., Reiser, M., Eckstein, F., (2000). Validation of high-resolution water-excitation magnetic resonance imaging for quantitative assessment of thin cartilage layers. Osteoarthritis.Cartilage. 8**,** 106-114.

Gray, M. L., Eckstein, F., Peterfy, C., Dahlberg, L., Kim, Y. J., Sorensen, A. G., Smith, R. L., (2004). Toward imaging biomarkers for osteoarthritis. Clinical Orthopaedics and Related Research S175-S181.

Greenwald, A. S., Matejczyk, M. B., Keppler, L., Black, J. D., Moran, J. M., Porritt, D., Beck, R. D., Wilde, A. H., (1977). Articular cartilage contact areas of the ankle. Orthopaedic Research Society, Las Vegas, Nevada.

Hall, F. M., Wyshak, G., (1980). Thickness of articular cartilage in the normal knee. Journal of Bone and Joint Surgery 62**,** 408-413.

Han, B., Cole, A. A., Shen, Y., Brodie, T., Williams, J. M., (2002). Early alterations in the collagen meshwork and lesions in the ankles are associated with spontaneous osteoarthritis in guinea-pigs. Osteoarthritis.Cartilage. 10**,** 778-784.

Hangody, L., (2003). The mosaicplasty technique for osteochondral lesions of the talus. Foot Ankle Clin. 8**,** 259-273.

Hangody, L., Feczko, P., Bartha, L., Bodo, G., Kish, G., (2001). Mosaicplasty for the treatment of articular defects of the knee and ankle. Clin.Orthop.Relat Res. S328-S336.

Hangody, L., Kish, G., Karpati, Z., Udvarhelyi, I., Szigeti, I., Bely, M., (1998). Mosaicplasty for the treatment of articular cartilage defects: application in clinical practice. Orthopedics 21**,** 751-756.

Hargreaves, B. A., Gold, G. E., Beaulieu, C. F., Vasanawala, S. S., Nishimura, D. G., Pauly, J. M., (2003). Comparison of new sequences for high-resolution cartilage imaging. Magn Reson.Med. 49**,** 700-709.

Haubner, M., Eckstein, F., Schnier, M., Losch, A., Sittek, H., Becker, C., Kolem, H., Reiser, M., Englmeier, K. H., (1997). A non-invasive technique for 3-dimensional assessment of articular cartilage thickness based on MRI. Part 2: Validation using CT arthrography. Magn Reson.Imaging 15**,** 805-813.

Haut, R. C., (1989). Contact pressures in the patellofemoral joint during impact loading on the human flexed knee. J.Orthop.Res. 7**,** 272-280.

Haut, R. C., Ide, T. M., De Camp, C. E., (1995). Mechanical responses of the rabbit patello-femoral joint to blunt impact. J.Biomech.Eng 117**,** 402-408.

Heidemann, R. M., Griswold, M. A., Muller, M., Breuer, F., Blaimer, M., Kiefer, B., Schmitt, M., Jakob, P. M., (2004). [Feasibilities and limitations of high field parallel MRI]. Radiologe 44**,** 49-55.

Hlavacek, M., (1995). The role of synovial fluid filtration by cartilage in lubrication of synovial joints--IV. Squeeze-film lubrication: the central film thickness for normal and inflammatory synovial fluids for axial symmetry under high loading conditions. J Biomech. 28**,** 1199-1205.

Huber-Betzer, H., Brown, T. D., Mattheck, C., (1990). Some effects of global joint morphology on local stress aberrations near imprecisely reduced intra-articular fractures. Journal of Biomechanics 23**,** 811-822.

Hyhlik-Durr, A., Faber, S., Burgkart, R., Stammberger, T., Maag, K. P., Englmeier, K. H., Reiser, M., Eckstein, F., (2000). Precision of tibial cartilage morphometry with a coronal water-excitation MR sequence. Eur.Radiol. 10**,** 297-303.

Imhof, H., Nobauer-Huhmann, I. M., Krestan, C., Gahleitner, A., Sulzbacher, I., Marlovits, S., Trattnig, S., (2002). MRI of the cartilage. Eur.Radiol. 12**,** 2781-2793.

Jeffrey, J. E., Thomson, L. A., Aspden, R. M., (1997). Matrix loss and synthesis following a single impact load on articular cartilage in vitro. Biochim.Biophys.Acta 1334**,** 223-232.

Johnson, K. L., (1985). Contact mechanics. Cambridge University Press, Cambridge.

Jonsson, K., Buckwalter, K., Helvie, M., Niklason, L., Martel, W., (1992). Precision of hyaline cartilage thickness measurements. Acta Radiol. 33**,** 234-239.

Jurvelin, J., Kiviranta, I., Arokoski, J., Tammi, M., Helminen, H. J., (1987). Indentation study of the biochemical properties of articular cartilage in the canine knee. Eng Med. 16**,** 15-22.

Jurvelin, J. S., Rasanen, T., Kolmonen, P., Lyyra, T., (1995). Comparison of optical, needle probe and ultrasonic techniques for the measurement of articular cartilage thickness. Journal of Biomechanics 28**,** 231-235.

Karvonen, R. L., Negendank, W. G., Teitge, R. A., Reed, A. H., Miller, P. R., Fernandez-Madrid, F., (1994). Factors affecting articular cartilage thickness in osteoarthritis and aging. J.Rheumatol. 21**,** 1310-1318.

Kempson, G. E., (1979). Mechanical properties of articular cartilage. In: Freeman, M. A. (Ed.), Adult articular cartilage. Pitman Medical, Tunbridge Wells, England, pp. 333-414.

Kim, H. A., Lee, Y. J., Seong, S. C., Choe, K. W., Song, Y. W., (2000). Apoptotic chondrocyte death in human osteoarthritis. J.Rheumatol. 27**,** 455-462.

Kim, Y. J., Jaramillo, D., Millis, M. B., Gray, M. L., Burstein, D., (2003). Assessment of early osteoarthritis in hip dysplasia with delayed gadolinium-enhanced magnetic resonance imaging of cartilage. Journal of Bone and Joint Surgery 85-A**,** 1987-1992.

Kimizuka, M., Kurosawa, H., Fukubayashi, T., (1980). Load-bearing pattern of the ankle joint. Contact area and pressure distribution. Arch.Orthop.Trauma Surg. 96**,** 45-49.

Kshirsagar, A. A., Watson, P. J., Tyler, J. A., Hall, L. D., (1998). Measurement of localized cartilage volume and thickness of human knee joints by computer analysis of three-dimensional magnetic resonance images. Invest Radiol. 33**,** 289-299.

Kura, H., Kitaoka, H. B., Luo, Z. P., An, K. N., (1998). Measurement of surface contact area of the ankle joint. Clin.Biomech.(Bristol., Avon.) 13**,** 365-370.

Kurosawa, H., Fukubayashi, T., Nakajima, H., (1980). Load-bearing mode of the knee joint: physical behavior of the knee joint with or without menisci. Clin.Orthop.Relat Res. 283-290.

Lane, J. M., Weiss, C., (1975). Review of articular cartilage collagen research. Arthritis Rheum. 18**,** 553-562.

Li, K., Wu, X., Chen, D., Sonka, M., (2004). Globally Optimal Segmentation of Interacting Surfaces with Geometric Constraints. IEEE Computer Society Conference On Computer Vision And Pattern Recognition Vol 1**,** 394-399.

Llinas, A., McKellop, H. A., Marshall, G. J., Sharpe, F., Kirchen, M., Sarmiento, A., (1993). Healing and remodeling of articular incongruities in a rabbit fracture model. Journal of Bone and Joint Surgery 75**,** 1508-1523.

Loening, A. M., James, I. E., Levenston, M. E., Badger, A. M., Frank, E. H., Kurz, B., Nuttall, M. E., Hung, H. H., Blake, S. M., Grodzinsky, A. J., Lark, M. W., (2000). Injurious mechanical compression of bovine articular cartilage induces chondrocyte apoptosis. Arch.Biochem.Biophys. 381**,** 205-212.

Losch, A., Eckstein, F., Haubner, M., Englmeier, K. H., (1997). A non-invasive technique for 3-dimensional assessment of articular cartilage thickness based on MRI. Part 1: Development of a computational method. Magn Reson.Imaging 15**,** 795-804.

Lovasz, G., Llinas, A., Benya, P. D., Park, S. H., Sarmiento, A., Luck, J. V., Jr., (1998). Cartilage changes caused by a coronal surface stepoff in a rabbit model. Clinical Orthopaedics and Related Research 224-234.

Lukasz, S., Muhlbauer, R., Faber, S., Englmeier, K. H., Reiser, M., Eckstein, F., (1998). [Sex-specific analysis of cartilage volume in the knee joint--a quantitative MRI-based study]. Anat.Anz. 180**,** 487-493.

Macko, V. W., Matthews, L. S., Zwirkoski, P., Goldstein, S. A., (1991). The joint-contact area of the ankle. The contribution of the posterior malleolus. Journal of Bone and Joint Surgery 73**,** 347-351.

Mandelbaum, B. R., Gerhardt, M. B., Peterson, L., (2003). Autologous chondrocyte implantation of the talus. Arthroscopy 19 Suppl 1**,** 129-137.

Mann, R. A., (1993). Biomechanics of the foot and ankle. Surgery of the foot and ankle. C.V. Mosby Co, St Louis, pp. 3-43.

Maroudas, A., (1968). Physicochemical properties of cartilage in the light of ion exchange theory. Biophys.J 8**,** 575-595.

Maroudas, A., (1975). Biophysical chemistry of cartilaginous tissues with special reference to solute and fluid transport. Biorheology 12**,** 233-248.

Maroudas, A., (1979). Physiochemical properties of articular cartilage. In: Freeman, M. A. (Ed.), Adult articular cartilage. Pitman Medical, Tunbridge Wells, England, pp. 215-290.

Marsh, J. L., Buckwalter, J., Gelberman, R., Dirschl, D., Olson, S., Brown, T., Llinias, A., (2002). Articular fractures: does an anatomic reduction really change the result? Journal of Bone and Joint Surgery 84-A**,** 1259-1271.

Marsh, J. L., Weigel, D. P., Dirschl, D. R., (2003). Tibial plafond fractures. How do these ankles function over time? Journal of Bone and Joint Surgery 85-A**,** 287-295.

Marsh, J. L., williams, T., Nepola, J. V., DeCoster, T. A., Hurwitz, S., Dirschl, D., (1997). Tibial plafond fractures: Does articular reduction and/or injury pattern predict outcome? Orthopaedic Transactions 21**,** 563.

Martin, J. A., Buckwalter, J. A., (2000). The role of chondrocyte-matrix interactions in maintaining and repairing articular cartilage. Biorheology 37**,** 129-140.

Martin, J. A., Buckwalter, J. A., (2001). Roles of articular cartilage aging and chondrocyte senescence in the pathogenesis of osteoarthritis. Iowa Orthop.J. 21**,** 1-7.

Martin, J. A., Ellerbroek, S. M., Buckwalter, J. A., (1997). Age-related decline in chondrocyte response to insulin-like growth factor-I: the role of growth factor binding proteins. J.Orthop.Res. 15**,** 491-498.

Meachim, G., (1975). Cartilage fibrillation at the ankle joint in Liverpool necropsies. J.Anat. 119**,** 601-610.

Menzel, M., et al, (2005). Proceedings of the 13th international society of magnetic resonance in medicine meeting.

Michelson, J. D., (1995). Fractures about the ankle. Journal of Bone and Joint Surgery 77**,** 142-152.

Millington, S., Grabner, M., Wozelka, R., Hurwitz, S., Crandall, J., (2007a). A stereophotographic study of ankle joint contact area. J Orthop.Res.

Millington, S. A., Grabner, M., Hurwitz, S. R., Crandall, J. R., (2004). A stereophotographic study of ankle cartilage thickness; distribution and surface topography. Osteoarthritis and Cartilage 12**,** S64.

Millington, S. A., Grabner, M., Wozelka, R., Anderson, D. D., Hurwitz, S. R., Crandall, J. R., (2007b). Quantification of ankle articular cartilage topography and thickness using a high resolution stereophotography system. Osteoarthritis Cartilage 15**,** 205-211.

Millington, S. A., Li, B., Tang, J., Trattnig, S., Crandall, J. R., Hurwitz, S. R., Acton, S. T., (2007c). Quantitative and topographical evaluation of ankle articular cartilage using high resolution MRI. J Orthop.Res. 25**,** 143-151.

Minas, T., Nehrer, S., (1997). Current concepts in the treatment of articular cartilage defects. Orthopedics 20**,** 525-538.

Mosher, T. J., Dardzinski, B. J., Smith, M. B., (2000). Human articular cartilage: influence of aging and early symptomatic degeneration on the spatial variation of T2--preliminary findings at 3 T. Radiology 214**,** 259-266.

Mow, V. C., Ateshian, G. A., (1997). Lubrication and wear of diarthrodial joints. In: Mow, V. C., Hayes, W. C. (Eds.), Basic biomechanics. Lippincott-Raven, Philadelphia, pp. 275-315.

Mow, V. C., Ratcliffe, A., (1997). Structure and function of articular cartilage and meniscus. In: Mow, V. C., Hayes, W. C. (Eds.), Basic orthopaedic biomechanics. lippincott-Raven, Philadelphia, pp. 113-177.

Mow, V. C., Holmes, M. H., Lai, W. M., (1984). Fluid transport and mechanical properties of articular cartilage: a review. J Biomech. 17**,** 377-394.

Mow, V. C., Kuei, S. C., Lai, W. M., Armstrong, C. G., (1980). Biphasic creep and stress relaxation of articular cartilage in compression? Theory and experiments. J.Biomech.Eng 102**,** 73-84.

Muir, H., (1983). Proteoglycans as organizers of the intercellular matrix. Biochem.Soc.Trans. 11**,** 613-622.

Muller-Gerbl, M., Putz, R., (1995). Functional anatomy of the ankle joint. In: Heim, U. (Ed.), Saunders, Philadelphia, pp. 3-25.

Nakagawa, S., Kadoya, Y., Kobayashi, A., Tatsumi, I., Nishida, N., Yamano, Y., (2003). Kinematics of the patella in deep flexion. Analysis with magnetic resonance imaging. Journal of Bone and Joint Surgery 85-A**,** 1238-1242.

Nieminen, M. T., Toyras, J., Laasanen, M. S., Silvennoinen, J., Helminen, H. J., Jurvelin, J. S., (2004). Prediction of biomechanical properties of articular cartilage

with quantitative magnetic resonance imaging. Journal of Biomechanics 37**,** 321-328.

Nishii, T., Sugano, N., Sato, Y., Tanaka, H., Miki, H., Yoshikawa, H., (2004). Three-dimensional distribution of acetabular cartilage thickness in patients with hip dysplasia: a fully automated computational analysis of MR imaging. Osteoarthritis Cartilage 12**,** 650-657.

O'Farrell, T. A., Costello, B. G., (1982). Osteochondritis dissecans of the talus. The late results of surgical treatment. J.Bone Joint Surg.Br. 64**,** 494-497.

Patel, V. V., Hall, K., Ries, M., Lindsey, C., Ozhinsky, E., Lu, Y., Majumdar, S., (2003). Magnetic resonance imaging of patellofemoral kinematics with weight-bearing. Journal of Bone and Joint Surgery 85-A**,** 2419-2424.

Peterfy, C. G., Genant, H. K., (1996). Emerging applications of magnetic resonance imaging in the evaluation of articular cartilage. Radiol.Clin.North Am. 34**,** 195-213, ix.

Peterfy, C. G., van Dijke, C. F., Janzen, D. L., Gluer, C. C., Namba, R., Majumdar, S., Lang, P., Genant, H. K., (1994). Quantification of articular cartilage in the knee with pulsed saturation transfer subtraction and fat-suppressed MR imaging: optimization and validation. Radiology 192**,** 485-491.

Peterfy, C. G., van Dijke, C. F., Lu, Y., Nguyen, A., Connick, T. J., Kneeland, J. B., Tirman, P. F., Lang, P., Dent, S., Genant, H. K., (1995). Quantification of the volume of articular cartilage in the metacarpophalangeal joints of the hand: accuracy and precision of three-dimensional MR imaging. AJR Am.J.Roentgenol. 165**,** 371-375.

Pilch, L., Stewart, C., Gordon, D., Inman, R., Parsons, K., Pataki, I., Stevens, J., (1994). Assessment of cartilage volume in the femorotibial joint with magnetic resonance imaging and 3D computer reconstruction. J.Rheumatol. 21**,** 2307-2321.

Poole, A. R., Kojima, T., Yasuda, T., Mwale, F., Kobayashi, M., Laverty, S., (2001). Composition and structure of articular cartilage - A template for tissue repair. Clinical Orthopaedics and Related Research S26-S33.

Pratt, W., (1978). Digital Image Processing. Wiley, New York, pp. 495-501.

Ratcliffe, A., Tyler, J. A., Hardingham, T. E., (1986). Articular cartilage cultured with interleukin 1. Increased release of link protein, hyaluronate-binding region and other proteoglycan fragments. Biochem.J 238**,** 571-580.

Recht, M., Bobic, V., Burstein, D., Disler, D., Gold, G., Gray, M., Kramer, J., Lang, P., McCauley, T., Winalski, C., (2001). Magnetic resonance imaging of articular cartilage. Clinical Orthopaedics and Related Research S379-S396.

Repo, R. U., Finlay, J. B., (1977). Survival of articular cartilage after controlled impact. Journal of Bone and Joint Surgery 59**,** 1068-1076.

Robson, M. D., Hodgson, R. J., Herrod, N. J., Tyler, J. A., Hall, L. D., (1995). A combined analysis and magnetic resonance imaging technique for computerised automatic measurement of cartilage thickness in the distal interphalangeal joint. Magn Reson Imaging 13**,** 709-718.

Rudd, R., Crandall, J., Millington, S. A., Hurwitz, S. R., Hoglund, N., (2004). Injury Tolerance and Response of the Ankle Joint in Dynamic Dorsiflexion. Stapp Car Crash Journal 48**,** 1-26.

Schibany, N., Ba-Ssalamah, A., Marlovits, S., Mlynarik, V., Nobauer-Huhmann, I. M., Striessnig, G., Shodjai-Baghini, M., Heinze, G., Trattnig, S., (2005). Impact of high field (3.0 T) magnetic resonance imaging on diagnosis of osteochondral defects in the ankle joint. Eur.J.Radiol. 55**,** 283-288.

Schmitt, F., Grosu, D., Mohr, C., Purdy, D., Salem, K., Scott, K. T., Stoeckel, B., (2004). [3 Tesla MRI: successful results with higher field strengths]. Radiologe 44**,** 31-47.

Schnier, M., Eckstein, F., Priebsch, J., Haubner, M., Sittek, H., Becker, C., Putz, R., Englmeier, K. H., Reiser, M., (1997). [Three-dimensional thickness and volume measurements of the knee joint cartilage using MRI: validation in an anatomical specimen by CT arthrography]. Rofo 167**,** 521-526.

Setton, L. A., Gu, W. Y., Lai, W. M., et al, (1995). Predictions of the swelling induced pre-stress in articular cartilage. In: Selvadurai, A. P. S. (Ed.), Mechanics of porous media. Kluwer Academic Publishers, Dordrecht, The Netherlands, pp. 299-322.

Seul, M., O'Gormal, L., Sammon, M. J., (2000). Practical algorithms for image analysis. Cambridge.Cambridge University Press 101-105.

Shepherd, D. E., Seedhom, B. B., (1999). Thickness of human articular cartilage in joints of the lower limb. Ann.Rheum.Dis. 58**,** 27-34.

Solloway, S., Hutchison, C., Waterton, J., Taylor, C., (1997). The use of active shape models for making thickness measurements of articular cartilage from MR images. Magn Reson Med 36**,** 943-952.

Stammberger, T., Eckstein, F., Englmeier, K. H., Reiser, M., (1999a). Determination of 3D cartilage thickness data from MR imaging: computational method and reproducibility in the living. Magn Reson.Med. 41**,** 529-536.

Stammberger, T., Eckstein, F., Michaelis, M., Englmeier, K. H., Reiser, M., (1999b). Interobserver reproducibility of quantitative cartilage measurements: comparison of B-spline snakes and manual segmentation. Magn Reson.Imaging 17**,** 1033-1042.

Stockwell, R. S., (1979). Biology of cartilage cells. Cambridge University Press, Cambridge.

Tan, T. C., Wilcox, D. M., Frank, L., Shih, C., Trudell, D. J., Sartoris, D. J., Resnick, D., (1996). MR imaging of articular cartilage in the ankle: comparison of available imaging sequences and methods of measurement in cadavers. Skeletal Radiol. 25**,** 749-755.

Tang, J., Millington, S. A., Acton, S. T., Crandall, J. R., Hurwitz, S. R., (2006). Surface Extraction and Thickness measurement of the articular Cartilage from MR images using Directional Gradient Vector Flow Snakes. IEEE transaction on biomedical engineering 53**,** 896-907.

Tang, J. S., Millington, S. A., Acton, S. T., Crandall, J., Hurwitz, S. R., (2004). Ankle cartilage surface tracking using directional gradient vector flow snakes. IEEE International Conference on Image Processing 4**,** 2745-2748.

Thompson, R. C., Jr., Oegema, T. R., Jr., Lewis, J. L., Wallace, L., (1991). Osteoarthrotic changes after acute transarticular load. An animal model. Journal of Bone and Joint Surgery 73**,** 990-1001.

Torzilli, P. A., Grigiene, R., Borrelli, J., Jr., Helfet, D. L., (1999). Effect of impact load on articular cartilage: cell metabolism and viability, and matrix water content. J.Biomech.Eng 121**,** 433-441.

Trattnig, S., Huber, M., Breitenseher, M. J., Trnka, H. J., Rand, T., Kaider, A., Helbich, T., Imhof, H., Resnick, D., (1998). Imaging articular cartilage defects with 3D fat-suppressed echo planar imaging: comparison with conventional 3D fat-suppressed gradient echo sequence and correlation with histology. J.Comput.Assist.Tomogr. 22**,** 8-14.

Trattnig, S., Mlynarik, V., Breitenseher, M., Huber, M., Zembsch, A., Rand, T., Imhof, H., (1999). MRI visualization of proteoglycan depletion in articular cartilage via intravenous administration of Gd-DTPA. Magn Reson.Imaging 17**,** 577-583.

Treppo, S., Koepp, H., Quan, E. C., Cole, A. A., Kuettner, K. E., Grodzinsky, A. J., (2000). Comparison of biomechanical and biochemical properties of cartilage from human knee and ankle pairs. J.Orthop.Res. 18**,** 739-748.

Walter, J. H., Jr., Spector, A., (1991). Traumatic osteoarthrosis of the ankle joint secondary to ankle fractures. J.Am.Podiatr.Med Assoc. 81**,** 399-405.

Wehrli, F. W., Hwang, S. N., Song, H. K., (1998). New architectural parameters derived from micro-MRI for the prediction of trabecular bone strength. Technol.Health Care 6**,** 307-320.

Whittaker, J. P., Smith, G., Makwana, N., Roberts, S., Harrison, P. E., Laing, P., Richardson, J. B., (2005). Early results of autologous chondrocyte implantation in the talus. J.Bone Joint Surg.Br. 87**,** 179-183.

Wilson, M. G., Michet, C. J., Jr., Ilstrup, D. M., Melton, L. J., III, (1990). Idiopathic symptomatic osteoarthritis of the hip and knee: a population-based incidence study. Mayo Clin.Proc. 65**,** 1214-1221.

Woo, S. L. Y., Mow, V. C., Lai, W. M., (1987). Biomechanical properties of articular cartilage. Handbook of bioengineering. McGraw-Hill, New York, p. 4.1-4.44.

Yao, J. Q., Seedhom, B. B., (1991). A new technique for measuring contact areas in human joints--the '3S technique'. Proc.Inst.Mech.Eng [H.] 205**,** 69-72.

Yao, J. Q., Seedhom, B. B., (1993). Mechanical conditioning of articular cartilage to prevalent stresses. British Journal of Rheumatology 32**,** 956-965.

Yao, J. Q., Seedhom, B. B., (1999). Ultrasonic measurement of the thickness of human articular cartilage in situ. Rheumatology.(Oxford) 38**,** 1269-1271.

Yelin, E., Callahan, L. F., (1995). The economic cost and social and psychological impact of musculoskeletal conditions. National Arthritis Data Work Groups. Arthritis Rheum. 38**,** 1351-1362.